

REPORT DOCUMENTATION PAGE

Public reporting burden for this collection of information is estimated to average 1 hour per response, including the time for reviewing instructions, searching existing data sources, gathering the required data, reviewing the collected information, completing and reviewing the collection of information. Send comments regarding this burden estimate or any other aspect of this collection of information, including suggestions for reducing the burden, to Washington Headquarters Services, Directorate for Information Operations and Reports, 1215 Jefferson Davis Highway, Suite 1204, Arlington, VA 22202-4302, and to the Office of Management and Budget, Paperwork Project, Washington, DC 20503.

AFRL-SR-BL-TR-00-

Rating and reviewing rate for information

1. AGENCY USE ONLY (Leave blank)		2. REPORT DATE December, 1997		3. 0963	
4. TITLE AND SUBTITLE 1997 Summer Research Program (SRP), Graduate Student Research Program (GSRP), Final Reports, Volume 8, Phillips Laboratory				5. FUNDING NUMBERS F49620-93-C-0063	
6. AUTHOR(S) Gary Moore					
7. PERFORMING ORGANIZATION NAME(S) AND ADDRESS(ES) Research & Development Laboratories (RDL) 5800 Uplander Way Culver City, CA 90230-6608				8. PERFORMING ORGANIZATION REPORT NUMBER	
9. SPONSORING/MONITORING AGENCY NAME(S) AND ADDRESS(ES) Air Force Office of Scientific Research (AFOSR) 801 N. Randolph St. Arlington, VA 22203-1977				10. SPONSORING/MONITORING AGENCY REPORT NUMBER	
11. SUPPLEMENTARY NOTES					
12a. DISTRIBUTION AVAILABILITY STATEMENT Approved for Public Release				12b. DISTRIBUTION CODE	
13. ABSTRACT (Maximum 200 words) The United States Air Force Summer Research Program (USAF-SRP) is designed to introduce university, college, and technical institute faculty members, graduate students, and high school students to Air Force research. This is accomplished by the faculty members (Summer Faculty Research Program, (SFRP)), graduate students (Graduate Student Research Program (GSRP)), and high school students (High School Apprenticeship Program (HSAP)) being selected on a nationally advertised competitive basis during the summer intersession period to perform research at Air Force Research Laboratory (AFRL) Technical Directorates, Air Force Air Logistics Centers (ALC), and other AF Laboratories. This volume consists of a program overview, program management statistics, and the final technical reports from the GSRP participants at the Phillips Laboratory.					
14. SUBJECT TERMS Air Force Research, Air Force, Engineering, Laboratories, Reports, Summer, Universities, Faculty, Graduate Student, High School Student				15. NUMBER OF PAGES	
				16. PRICE CODE	
17. SECURITY CLASSIFICATION OF REPORT Unclassified	18. SECURITY CLASSIFICATION OF THIS PAGE Unclassified	19. SECURITY CLASSIFICATION OF ABSTRACT Unclassified	20. LIMITATION OF ABSTRACT UL		

UNITED STATES AIR FORCE
SUMMER RESEARCH PROGRAM -- 1997
GRADUATE STUDENT RESEARCH PROGRAM FINAL REPORTS

VOLUME 8

PHILLIPS LABORATORY

RESEARCH & DEVELOPMENT LABORATORIES

5800 Uplander Way

Culver City, CA 90230-6608

Program Director, RDL
Gary Moore

Program Manager, AFOSR
Major Linda Steel-Goodwin

Program Manager, RDL
Scott Licoscas

Program Administrator, RDL
Johnetta Thompson

Program Administrator
Rebecca Kelly-Clemmons

Submitted to:

AIR FORCE OFFICE OF SCIENTIFIC RESEARCH

Bolling Air Force Base

Washington, D.C.

December 1997

20010321 045

AQM 01-00 1264

PREFACE

Reports in this volume are numbered consecutively beginning with number 1. Each report is paginated with the report number followed by consecutive page numbers, e.g., 1-1, 1-2, 1-3; 2-1, 2-2, 2-3.

This document is one of a set of 16 volumes describing the 1997 AFOSR Summer Research Program. The following volumes comprise the set:

<u>VOLUME</u>	<u>TITLE</u>
1	Program Management Report
	<i>Summer Faculty Research Program (SFRP) Reports</i>
2A & 2B	Armstrong Laboratory
3A & 3B	Phillips Laboratory
4A & 4B	Rome Laboratory
5A , 5B & 5C	Wright Laboratory
6	Arnold Engineering Development Center, United States Air Force Academy and Air Logistics Centers
	<i>Graduate Student Research Program (GSRP) Reports</i>
7A & 7B	Armstrong Laboratory
8	Phillips Laboratory
9	Rome Laboratory
10A & 10B	Wright Laboratory
11	Arnold Engineering Development Center, United States Air Force Academy, Wilford Hall Medical Center and Air Logistics Centers
	<i>High School Apprenticeship Program (HSAP) Reports</i>
12A & 12B	Armstrong Laboratory
13	Phillips Laboratory
14	Rome Laboratory
15A & 15B	Wright Laboratory
16	Arnold Engineering Development Center

GSRP FINAL REPORT TABLE OF CONTENTS	i-x
--	------------

1. INTRODUCTION	1
2. PARTICIPATION IN THE SUMMER RESEARCH PROGRAM	2
3. RECRUITING AND SELECTION	3
4. SITE VISITS	4
5. HBCU/MI PARTICIPATION	4
6. SRP FUNDING SOURCES	5
7. COMPENSATION FOR PARTICIPATIONS	5
8. CONTENTS OF THE 1995 REPORT	6

APPENDICIES:

A. PROGRAM STATISTICAL SUMMARY	A-1
B. SRP EVALUATION RESPONSES	B-1

GSRP FINAL REPORTS

SRP Final Report Table of Contents

Author	University/Institution Report Title	Armstrong Laboratory Directorate	Vol-Page
MR Benedict N Arrey	Univ of Texas at San Antonio , San Antonio , TX Identification and Quantitation of N-menthyl-1-(3,4 Methylenedioxyhenyl)-2- Butanamine Together wiht	AL/AOT	7- 1
MS JoAnne E Bates	University of North Dakota , Grand Forks , ND A Way to Condense the Time Consuming Procedure of Cognitive Task Analysis	AL/HRCT	7- 2
MR Brandon B Boke	Trinity University , San Antonio , TX Effects of Brain Temperature on Fatugue in Rats due to maximal Exercise an Millimeter Microwave Radi	AL/OER	7- 3
MS Constance R Buford	Alabama A&M University , Normal , AL Assessment of Coagulant Agents on The Reduction of Aqueous Film Forming Foam (AFFF) in Wastewater	AL/OEB	7- 4
MS Dawn D Burnett	Wright State University , Dayton , OH The Effects of Individual Differences and Team Processed ofn Team Member Schema Similarity and Task	AL/CFHI	7- 5
MR Bradley E Collie	Arizona State University , Mesa , AZ Perception of Velocity as a Function of the Oculomotor State of the Eyes	AL/HRA	7- 6
MR Gerald W DeWolfe	Univ of Texas at Austin , Austin , TX Investigation and Validation of Submaximal Cycle Ergometry Protocols Used to Assess the Aerobic Capa	AL/PSP	7- 7
Kea U Duckenfield	The Virginia Institute of Marine Science , Gloucester Point , VA Direct Measurment of DNAPL/Water Contact Area in the Subsurace: One-And three-Dimensional Studies	AL/EQL	7- 8
MR Phillip T Dunwoody	University of Georgia , Athens , GA The Effects of Task Structure on Cognitive Organizing Principles: Implicatins	AL/CFTO	7- 9
MR Daniel X Hammer	Univ of Texas at Austin , Austin , TX Measurement of Dispersive Curves for Ocular Media by white-light Interferometry	AL/OEO	7- 10
MS Catherine R Harrison	Univ of Illinois Urbana/Champaign , Champaign , IL Gender effects in Wayfinding Strategy: Implications for Teamand Individual Trainging	AL/HRCC	7- 11

SRP Final Report Table of Contents

Author	University/Institution Report Title	Armstrong Laboratory Directorate	Vol-Page
MS Laura J Hott	Wright State University , Dayton , OH Examination of an Organizational Climate Measure and the Relationship with Grievances and Turnover	AL/HRG	7- 12
MS Vanessa D Le	Univ of Texas at Austin , Austin , TX A Clearance Study of Nitrotyrosine From a Prostate Cancer Cell Line	AL/OER	7- 13
MS Kavita Mahajan	Trinity University , San Antonio , TX the Effect of 2.06 GHz Microwave Irraditation on The Permeability of the Blood Brain Barrier	AL/OER	7- 14
MR Thomas R Mertz (Jr.)	Univ of Scranton , Scranton , PA Protocol for Development of Amplicons for a Rapid & Efficient Method of Genotyping Hepatitis C Virus	AL/AOEL	7- 15
MR Michael J Miller	Texas A & M Univ-College Station , College Station , TX An Psycholmetric Examination of the Multidimensional work ethic Profile among Air Force enlisted per	AL/HRCF	7- 16
MR Miguel A Moreno	Arizona State University , Tempe , AZ The Effect of Size Disparity on Perception of Surface Slant in Steroscopic Moving Images	AL/HRA	7- 17
MR Brian W Moroney	University of Cincinnati , Cincinnati , OH The Role of Multi-Modal Adaptive Interfaces in Providing Flight Path Guidance	AL/CFHI	7- 18
MR Randy J Mueller	University of Connecticut , Storrs , CT Desorption and Biodegradation of Dinitrotoluenes in Aged soils	AL/EQL	7- 19
MR Mark A Murphy	Ohio University , Athens , OH Implementation of Freflex/merlin Teleoperation	AL/CFBA	7- 20
MS Cynthia J Musante	North Carolina State U-Raleigh , Raleigh , NC Well-Posedness for a Class of Nonlinear Distributed Parameter Models wiht Time Delay Arising in Adva	AL/OES	7- 21
MR David C Powell	The College of William and Mary , Gloucester , VA Investigaatioon of the Iron-Bearing Phases of the Columbus AFB Aquifer	AL/EQL	7- 22

SRP Final Report Table of Contents

Author	University/Institution Report Title	Armstrong Laboratory Directorate	Vol-Page
MR Christopher S Schreiner	Miami University , Oxford , OH The Effect of Visual Similarity and Reference Frame Alignment on the Recognition of Military Aircra	AL/HRCT	7- 23
MR John N Sempeles	University of Florida , Gainesville , FL OH Radical Reaction Rate Constant & Product Study of 2-Propoxyethanol	AL/EQL	7- 24
MS Julie A Stiles-Shipley	Bowling Green State University , Bowling Green , OH The Effects of Observation and Training Schedule on The Acquisition of a complex Computer Based	AL/HRCT	7- 25
MR Robert S Tannen	University of Cincinnati , Cincinnati , OH Integrating Multisensory Displays for an Adaptive Target Leading Interface	AL/CFHP	7- 26
MR Paul J Taverna	Tulane University , New Orleans , LA A Preliminary Examination of ECL Activity Geared Toward a CD+2 Sensor	AL/EQL	7- 27
MR James M Tickner	Univ of Scranton , Scranton , PA Molecular typing of Cndida Parasilosis Via Amplified Fragment Length Polymorphism and Repetitive S	AL/AOEL	7- 28
MS Deanne L Westerman	Case Western Reserve Univ , Cleveland , OH A Test of the Misattributed-Activation Hypothesis of the Revelatin Effect in Memory	AL/HRCC	7- 29

SRP Final Report Table of Contents

Author	University/Institution Report Title	Phillips Laboratory Directorate	Vol-Page
MR Joshua C Bienfang	University of New Mexico , Albuquerque , NM Frequency Stabilization of an Nd; Yag Laser	AFRL/DEL _____	8- 1
MR Marc L Breen	Tulane University , New Orleans , LA A Study of Defects and Dark Current Mechanisms in Triple-Junction GaInP2/GaAs/Ge Photovoltaic Cells	PL/VTV _____	8- 2
MR Jerome T Chu	University of Florida , Gainesville , FL The Characterization of High Performance Quantum Well Infrared Photodetectors for Low Background O	PL/VTMR _____	8- 3
MR Theodore S Elicker	University of N. C.- Charlotte , Charlotte , NC Simulation and Modeling of Nanoelectronic Materials	PL/VTMR _____	8- 4
MR Jeffery M Ganley	University of New Mexico , Albuquerque , NM A Preliminary Study of the Causes of Spring-IN in A Unidirectional Carbon Fiber/EPOXY Composite	PL/VTV _____	8- 5
Johnelle L Koriath	Univ of Texas at Dallas , Richardson , TX A Preliminary analysis of Stacked Blumleins Used in Pulsed power Devices	PL/WSQ _____	8- 6
Kelly K Lau	Univ of Texas at Arlington , Arlington , TX Experimental Validation of Three-Dimensional Reconstruction of Inhomogeneity Images in turbid Media	PL/LIMI _____	8- 7
MS Ruthie D Lyle	Polytechnic University , Farmingdale , NY A Quasi-Particle Analysis of Amplitude Scintillation	PL/GPS _____	8- 8
MR Shaun L Meredith	Massachusetts Inst of Technology , Cambridge , MA Research on Plasma Diagnostics for Versatile Toroidal Facility: Gridded energy Analyzers	PL/GPS _____	8- 9

SRP Final Report Table of Contents

Author	University/Institution Report Title	Phillips Laboratory Directorate	Vol-Page
MR Eric J Paulson	Univ of Colorado at Boulder , Boulder , CO A Study of Atomospheric Perturbations On a Suborbital Space Plane Skipping Trajectory	AFRL/PR _____	8- 10
MR Christopher W Peters	Univ of Michigan , Ann Arbor , MI A New "Technique Used to Dertemine the Time Evolutin of The Frequency in Heterodyne Systems	PL/WSQN _____	8- 11
MR Michael J Rowlands	Massachusetts Inst of Technology , Cambridge , MA Ducted Whistler waves and Emissions in the Laboratory and the Ionosphere	PL/GPS _____	8- 12
MS Lorena L Sanchez	University of New Mexico , Albuquerque , NM A Preliminary Study of the Effects of Process Conditions on Curvature in Graphite/EPoxy Pultruded Ro	PL/VTV _____	8- 13
MR John H Schilling	Univ of Southern California , Los Angeles , CA "A Study of Alternate Propellants for Pulsed Plasma Thrusters	PL/RKEE _____	8- 14
MR Kenneth F Stephens II	University of North Texas , Denton , TX Investigation of an Explosively Formed Fus Using Mach2	AFRL/DEH _____	8- 15
MS Jane A Vladimer	Boston University , Boston , MA Low Latitude Ionospheric Tec Measured by Nasa Topex	PL/GPS _____	8- 16
MR Michael V Wood	Pennsylvania State University , University Park , PA Characterization of Spatial Light Modulator For Application to real-time Hlography	PL/LIMS _____	8- 17
MR. Mark C Worthy	Univ of Alabama at Huntsville , Huntsville , AL Library of the Natural Frequency Responses for Cylindrical & Rectangular Shaped Plastic Mines	PL/WSQW _____	8- 18
MR John Yoon	University of Florida , Gainesville , FL Simulating Transient Temperature Distributions in Optically Pumped Multilayer Laser Structures	PL/LIDA _____	8- 19

SRP Final Report Table of Contents

Author	University/Institution Report Title	Rome Laboratory Directorate	Vol-Page
MR Tony M Adami	Ohio University , Athens , OH	RL/C3	9- 1
MR Richard S Andel	SUNY Binghamton , Binghamton , NY Visual Target Tracking and Extraction from a Sequence of Images	RL/IRRE	9- 2
MR Patrick M Garrity	Central Michigan University , Mt. Pleasant , MI An Examination of Java and CORBA Security	RL/CA-II	9- 3
MR Walter I Kaechele	Rensselaer Polytechnic Instit , Troy , NY Operational Analysis of an Actively Mode-Locked Fiber Laser	RL/OCPA	9- 5
MR William J Kostis	Cornell University , Ithaca , NY	RL/OCSS	9- 6
MS Helen Lau	Syracuse University , Syracuse , NY A Simulati9n Study on a Partitioning Procedure for Radar Signal processing Problems	RL/OCSS	9- 7
MR Myron R Mychal	Illinois Inst of Technology , Chicago , IL Simulaton of a Robust Locally Optimum Receiver in Correlated Noise Using Autoregressive Modeling	RL/C3BB	9- 8
MS Maryanne C Nagy	SUNY OF Tech Utica , Utica , NY	RL/TWT	9- 9
DR Luke J Olszewski	Georgia Southern University , Statesboro , GA Software Veification Guide Using PVS	RL/ERDD	9- 12
MR Charles M Palmer	George Washington University , Washington , DC A Technique for locating and characterizing crystalline regions in simulated solids	RL/ERDR	9- 10
MR Dsunte L Wilson	Brown University , Providence , RI System-Level Hardware/Software Partitioning of Hetergeneous Embedded Systems	RL/ERDD	9- 11

SRP Final Report Table of Contents

Author	University/Institution Report Title	Wright Laboratory Directorate	Vol-Page
MR Mark L Adams	Auburn University , Auburn , AL A Study of Laser Induced Plasma Damage of Thin Metal Foils	WL/MNMF _____	10- 1
MR James T Belich	Bethel College , St. Paul , MN Contribution of a scene Projecotr's Non-Uniformity to a test Article's output Image Non-Uniformity	WL/MNGI _____	10- 2
MR Jason W Bitting	Louisiana State University , Baton Rouge , LA Visualization and Two-Color Digital PIV Measurements in Circular and Square Coaxial Nozzles	WL/POSC9 _____	10- 3
MR Lawrence L Brott	University of Cincinnati , Cincinnati , OH Synthesis of a Novel Second Order Nonlinear Optical Polymer	WL/MLBP _____	10- 4
MS Danielle E Brown	Wright State University , Dayton , OH An Experimental and Computational Analysis of the Unsteady Blade Row Potential Interaction in a Tran	WL/POTF _____	10- 5
MS Angela M Cannon	Pennsylvania State University , University Park , PA the Synthesis of a Protected Carboxylic Acid Derivative for Attachment To C60	WL/MLPJ _____	10- 6
MR Charles C Conklin	Florida State University , Tallahassee , FL Vision Algorithms For Military Image Processing	WL/MNMF _____	10- 7
MR Mitchell G Dengler	University of Missouri - Rolla , Rolla , MO	WL/MLIM _____	10- 8
MR James D Drummond	University of Cincinnati , Cincinnati , OH Invesstigation of Conductive Cladding Layers for Improved Polimg in Non-Linear Optical Polymer waveg	WL/MLPO _____	10- 9
MR Gary W Dulaney	Brown University , Providence , RI Computer Simulation of Fire Suppression in Aircraft Engine Nacelles	WL/FIVS _____	10- 10

SRP Final Report Table of Contents

Author	University/Institution Report Title	Wright Laboratory Directorate	Vol-Page
MR Robert L Parkhill	Oklahoma State University , Stillwater , OK Organically modified Silicate Films as Corrosion Resistant Treatments for 2024-T3 Aluminum Alloy	WL/MLBT	10- 23
MS Annie R Pearce	Georgia Inst of Technology , Atlanta , GA Cost-Based Risk Prediction and Identification of Project Cost Drives Using Artificial neural Network	WL/FIVC-	10- 24
MR Dax B Pitts	University of Cincinnati , Cincinnati , OH A Study of Intra-Class Variability in ATR Systems	WL/AACR	10- 25
MR Jonathan M Protz	Massachusetts Inst of Technology , Cambridge , MA An LPV Controller for a Tailless Fighter Aircraft Simulation	WL/FIGC	10- 26
MR Jason E Riggs	Clemson University , Clemson , SC	WL/MLPJ	10- 27
MR Thomas W Scott	University of Missouri - Rolla , Rolla , MO Iso-Octane and N-Heptane Laminar Flame Numerical Study	WL/POPS	10- 28
MR Steven R Stanfill	University of Florida , Gainesville , FL A study of HRR Super Resolution Analysis for Possible ATR Performance Enhancement	WL/AACR	10- 29
Adedokun W Sule-Koiki	Howard University , Washington , DC Detection Techniques use in Forward-Lookeng Radar Signal A Literature Review	WL/AAMR	10- 30
MR. Robert M Taylor	Purdue University , West Lafayette , IN Rapid Modeling for Aircraft Design Synthesis	WL/FIBD	10- 31
MS Laura E Williams	Georgia Inst of Technology , Atlanta , GA Data Simulation Supporting Range Estimating for Research and Sevelopment Alternatives	WL/FIVC-	10- 32

SRP Final Report Table of Contents

Author	University/Institution Report Title	Wright Laboratory Directorate	Vol-Page
MR Cornelious W Williams Jr.	University of Cincinnati , Cincinnati , OH Allyl & Propargyl Resins	WL/MLBC _____	10- 33
MS Melissa R Wilson	University of Missouri - Rolla , Rolla , MO A Study of The Particulate Emissions of A Well-Stirred Reactor	WL/POSC _____	10- 34
Sami Zendah	Wright State University , Dayton , OH Develop an Explosive simulated Testing Apparatus for Impact Physics Research at Wright Laboratory	WL/FIV _____	10- 35

SRP Final Report Table of Contents

Author	University/Institution Report Title	Wright Laboratory Directorate	Vol-Page
MR David W Fanjoy	Purdue University , West Lafayette , IN Demonstration of Genetic Algorithms for Wngineering Optimization Problems	WL/FIIB	10- 11
		WL/MLPJ	10- 12
	Western Michigan University , Kalamazon , MI Comparison of self-assembled monolayers and chitosan as functional substrates for deposition fo ultr		
MR Carl C Hoff	Wright State University , Dayton , OH Similarity Measures for pattern Recognition	WL/AACA	10- 13
MR Adam R Hoffman	Wright State University , Dayton , OH Evaluation and Integratin of Electrodynamic Simulation Packages for Madmel Program	WL/POOX	10- 14
MR. George W Jarriel, Jr.	Auburn University , Auburn , AL Exploding Foil Initiator Flyer Velocity Measurement Using VISAR	WL/MNMF	10- 15
MR Brett A Jordan	Wright State University , Dayton , OH Capacitor Based DC Backup Power Supply with Integrated Cahrging Circuit	WL/POOC	10- 16
MR Edward L Kiely	Ohio State University , Columbus , OH	WL/FIBD	10- 17
MS Janae N Lockett	University of Toledo , Toledo , OH A Study of Electronics Design Environments in Terms of Computer aided Design A Psychological Persper	WL/AAST	10- 18
MS Stephanie Luetjering	University of Dayton , Dayton , OH Fatigue Crack GrowthBehavior of Ti-22A1-23Nb	WL/MLLN	10- 19
MR Alfred L Malone	Auburn University , Auburn , AL Electrical and Mathematical Characterization of th Semiconductor	WL/MNMF	10- 20
MR Herbert F Miles II	Tulane University , New Orleans , LA	WL/MLLN	10- 21
Dawn H Miller	Georgia Inst of Technology , Atlanta , GA	WL/FIVC	10- 22

SRP Final Report Table of Contents

Author	University/Institution Report Title	Arnold Engineering Development Center Directorate	Vol-Page
MS Jessica L Thomas	Tennessee Univ Space Institute , Tullahoma , TN Incorporating Condensation into Nastd	AEDC	11- 1
MR Derek E Lang	University of Washington , Seattle , WA Hue Analysis Factors For Liquid Crystal Transient Heat Tranasfer Measurements	USAFA	11 - 2
MS Bridget V McGrath	Univ of Colorado at Colorado Springs , Colorado Spring , CO A Setup for Photoassociation of cold, Trapped Cesium Atoms	USAFA	11 - 3
MS Donna M Lehman	Univ of Texas Health Science Center , San Antonio , TX Relationship between Growth Hormone and Myelin Basic Protein Expression in Vivo	WHMC	11 - 4

1. INTRODUCTION

The Summer Research Program (SRP), sponsored by the Air Force Office of Scientific Research (AFOSR), offers paid opportunities for university faculty, graduate students, and high school students to conduct research in U.S. Air Force research laboratories nationwide during the summer.

Introduced by AFOSR in 1978, this innovative program is based on the concept of teaming academic researchers with Air Force scientists in the same disciplines using laboratory facilities and equipment not often available at associates' institutions.

The Summer Faculty Research Program (SFRP) is open annually to approximately 150 faculty members with at least two years of teaching and/or research experience in accredited U.S. colleges, universities, or technical institutions. SFRP associates must be either U.S. citizens or permanent residents.

The Graduate Student Research Program (GSRP) is open annually to approximately 100 graduate students holding a bachelor's or a master's degree; GSRP associates must be U.S. citizens enrolled full time at an accredited institution.

The High School Apprentice Program (HSAP) annually selects about 125 high school students located within a twenty mile commuting distance of participating Air Force laboratories.

AFOSR also offers its research associates an opportunity, under the Summer Research Extension Program (SREP), to continue their AFOSR-sponsored research at their home institutions through the award of research grants. In 1994 the maximum amount of each grant was increased from \$20,000 to \$25,000, and the number of AFOSR-sponsored grants decreased from 75 to 60. A separate annual report is compiled on the SREP.

The numbers of projected summer research participants in each of the three categories and SREP "grants" are usually increased through direct sponsorship by participating laboratories.

AFOSR's SRP has well served its objectives of building critical links between Air Force research laboratories and the academic community, opening avenues of communications and forging new research relationships between Air Force and academic technical experts in areas of national interest, and strengthening the nation's efforts to sustain careers in science and engineering. The success of the SRP can be gauged from its growth from inception (see Table 1) and from the favorable responses the 1997 participants expressed in end-of-tour SRP evaluations (Appendix B).

AFOSR contracts for administration of the SRP by civilian contractors. The contract was first awarded to Research & Development Laboratories (RDL) in September 1990. After completion of the

1990 contract, RDL (in 1993) won the recompetition for the basic year and four 1-year options.

2. PARTICIPATION IN THE SUMMER RESEARCH PROGRAM

The SRP began with faculty associates in 1979; graduate students were added in 1982 and high school students in 1986. The following table shows the number of associates in the program each year.

YEAR	SRP Participation, by Year			TOTAL
	SFRP	GSRP	HSAP	
1979	70			70
1980	87			87
1981	87			87
1982	91	17		108
1983	101	53		154
1984	152	84		236
1985	154	92		246
1986	158	100	42	300
1987	159	101	73	333
1988	153	107	101	361
1989	168	102	103	373
1990	165	121	132	418
1991	170	142	132	444
1992	185	121	159	464
1993	187	117	136	440
1994	192	117	133	442
1995	190	115	137	442
1996	188	109	138	435
1997	148	98	140	427

Beginning in 1993, due to budget cuts, some of the laboratories weren't able to afford to fund as many associates as in previous years. Since then, the number of funded positions has remained fairly constant at a slightly lower level.

3. RECRUITING AND SELECTION

The SRP is conducted on a nationally advertised and competitive-selection basis. The advertising for faculty and graduate students consisted primarily of the mailing of 8,000 52-page SRP brochures to chairpersons of departments relevant to AFOSR research and to administrators of grants in accredited universities, colleges, and technical institutions. Historically Black Colleges and Universities (HBCUs) and Minority Institutions (MIs) were included. Brochures also went to all participating USAF laboratories, the previous year's participants, and numerous individual requesters (over 1000 annually).

RDL placed advertisements in the following publications: *Black Issues in Higher Education*, *Winds of Change*, and *IEEE Spectrum*. Because no participants list either *Physics Today* or *Chemical & Engineering News* as being their source of learning about the program for the past several years, advertisements in these magazines were dropped, and the funds were used to cover increases in brochure printing costs.

High school applicants can participate only in laboratories located no more than 20 miles from their residence. Tailored brochures on the HSAP were sent to the head counselors of 180 high schools in the vicinity of participating laboratories, with instructions for publicizing the program in their schools. High school students selected to serve at Wright Laboratory's Armament Directorate (Eglin Air Force Base, Florida) serve eleven weeks as opposed to the eight weeks normally worked by high school students at all other participating laboratories.

Each SFRP or GSRP applicant is given a first, second, and third choice of laboratory. High school students who have more than one laboratory or directorate near their homes are also given first, second, and third choices.

Laboratories make their selections and prioritize their nominees. AFOSR then determines the number to be funded at each laboratory and approves laboratories' selections.

Subsequently, laboratories use their own funds to sponsor additional candidates. Some selectees do not accept the appointment, so alternate candidates are chosen. This multi-step selection procedure results in some candidates being notified of their acceptance after scheduled deadlines. The total applicants and participants for 1997 are shown in this table.

1997 Applicants and Participants			
PARTICIPANT CATEGORY	TOTAL APPLICANTS	SELECTEES	DECLINING SELECTEES
SFRP	490	188	32
(HBCU/MI)	(0)	(0)	(0)
GSRP	202	98	9
(HBCU/MI)	(0)	(0)	(0)
HSAP	433	140	14
TOTAL	1125	426	55

4. SITE VISITS

During June and July of 1997, representatives of both AFOSR/NI and RDL visited each participating laboratory to provide briefings, answer questions, and resolve problems for both laboratory personnel and participants. The objective was to ensure that the SRP would be as constructive as possible for all participants. Both SRP participants and RDL representatives found these visits beneficial. At many of the laboratories, this was the only opportunity for all participants to meet at one time to share their experiences and exchange ideas.

5. HISTORICALLY BLACK COLLEGES AND UNIVERSITIES AND MINORITY INSTITUTIONS (HBCU/MIIs)

Before 1993, an RDL program representative visited from seven to ten different HBCU/MIIs annually to promote interest in the SRP among the faculty and graduate students. These efforts were marginally effective, yielding a doubling of HBCU/MI applicants. In an effort to achieve AFOSR's goal of 10% of all applicants and selectees being HBCU/MI qualified, the RDL team decided to try other avenues of approach to increase the number of qualified applicants. Through the combined efforts of the AFOSR Program Office at Bolling AFB and RDL, two very active minority groups were found, HACU (Hispanic American Colleges and Universities) and AISES (American Indian Science and Engineering Society). RDL is in communication with representatives of each of these organizations on a monthly basis to keep up with their activities and special events. Both organizations have widely-distributed magazines/quarterlies in which RDL placed ads.

Since 1994 the number of both SFRP and GSRP HBCU/MI applicants and participants has increased ten-fold, from about two dozen SFRP applicants and a half dozen selectees to over 100 applicants and two dozen selectees, and a half-dozen GSRP applicants and two or three selectees to 18 applicants and 7 or 8 selectees. Since 1993, the SFRP had a two-fold applicant increase and a two-fold selectee increase. Since 1993, the GSRP had a three-fold applicant increase and a three to four-fold increase in selectees.

In addition to RDL's special recruiting efforts, AFOSR attempts each year to obtain additional funding or use leftover funding from cancellations the past year to fund HBCU/MI associates. This year, 5 HBCU/MI SFRPs declined after they were selected (and there was no one qualified to replace them with). The following table records HBCU/MI participation in this program.

SRP HBCU/MI Participation, By Year				
YEAR	SFRP		GSRP	
	Applicants	Participants	Applicants	Participants
1985	76	23	15	11
1986	70	18	20	10
1987	82	32	32	10
1988	53	17	23	14
1989	39	15	13	4
1990	43	14	17	3
1991	42	13	8	5
1992	70	13	9	5
1993	60	13	6	2
1994	90	16	11	6
1995	90	21	20	8
1996	119	27	18	7

6. SRP FUNDING SOURCES

Funding sources for the 1997 SRP were the AFOSR-provided slots for the basic contract and laboratory funds. Funding sources by category for the 1997 SRP selected participants are shown here.

1997 SRP FUNDING CATEGORY	SFRP	GSRP	HSAP
AFOSR Basic Allocation Funds	141	89	123
USAF Laboratory Funds	48	9	17
HBCU/MI By AFOSR (Using Procured Addn'l Funds)	0	0	N/A
TOTAL	9	98	140

SFRP - 188 were selected, but thirty two canceled too late to be replaced.

GSRP - 98 were selected, but nine canceled too late to be replaced.

HSAP - 140 were selected, but fourteen canceled too late to be replaced.

7. COMPENSATION FOR PARTICIPANTS

Compensation for SRP participants, per five-day work week, is shown in this table.

1997 SRP Associate Compensation

PARTICIPANT CATEGORY	1991	1992	1993	1994	1995	1996	1997
Faculty Members	\$690	\$718	\$740	\$740	\$740	\$770	\$770
Graduate Student (Master's Degree)	\$425	\$442	\$455	\$455	\$455	\$470	\$470
Graduate Student (Bachelor's Degree)	\$365	\$380	\$391	\$391	\$391	\$400	\$400
High School Student (First Year)	\$200	\$200	\$200	\$200	\$200	\$200	\$200
High School Student (Subsequent Years)	\$240	\$240	\$240	\$240	\$240	\$240	\$240

The program also offered associates whose homes were more than 50 miles from the laboratory an expense allowance (seven days per week) of \$50/day for faculty and \$40/day for graduate students. Transportation to the laboratory at the beginning of their tour and back to their home destinations at the end was also reimbursed for these participants. Of the combined SFRP and GSRP associates, 65 % (194 out of 286) claimed travel reimbursements at an average round-trip cost of \$776.

Faculty members were encouraged to visit their laboratories before their summer tour began. All costs of these orientation visits were reimbursed. Forty-three percent (85 out of 188) of faculty associates took orientation trips at an average cost of \$388. By contrast, in 1993, 58 % of SFRP associates took

orientation visits at an average cost of \$685; that was the highest percentage of associates opting to take an orientation trip since RDL has administered the SRP, and the highest average cost of an orientation trip. These 1993 numbers are included to show the fluctuation which can occur in these numbers for planning purposes.

Program participants submitted biweekly vouchers countersigned by their laboratory research focal point, and RDL issued paychecks so as to arrive in associates' hands two weeks later.

This is the second year of using direct deposit for the SFRP and GSRP associates. The process went much more smoothly with respect to obtaining required information from the associates, only 7% of the associates' information needed clarification in order for direct deposit to properly function as opposed to 10% from last year. The remaining associates received their stipend and expense payments via checks sent in the US mail.

HSAP program participants were considered actual RDL employees, and their respective state and federal income tax and Social Security were withheld from their paychecks. By the nature of their independent research, SFRP and GSRP program participants were considered to be consultants or independent contractors. As such, SFRP and GSRP associates were responsible for their own income taxes, Social Security, and insurance.

8. CONTENTS OF THE 1997 REPORT

The complete set of reports for the 1997 SRP includes this program management report (Volume 1) augmented by fifteen volumes of final research reports by the 1997 associates, as indicated below:

1997 SRP Final Report Volume Assignments

LABORATORY	SFRP	GSRP	HSAP
Armstrong	2	7	12
Phillips	3	8	13
Rome	4	9	14
Wright	5A, 5B	10	15
AEDC, ALCs, WHMC	6	11	16

APPENDIX A -- PROGRAM STATISTICAL SUMMARY

A. Colleges/Universities Represented

Selected SFRP associates represented 169 different colleges, universities, and institutions, GSRP associates represented 95 different colleges, universities, and institutions.

B. States Represented

SFRP -Applicants came from 47 states plus Washington D.C. Selectees represent 44 states.

GSRP - Applicants came from 44 states. Selectees represent 32 states.

HSAP - Applicants came from thirteen states. Selectees represent nine states.

Total Number of Participants	
SFRP	189
GSRP	97
HSAP	140
TOTAL	426

Degrees Represented			
	SFRP	GSRP	TOTAL
Doctoral	184	0	184
Master's	2	41	43
Bachelor's	0	56	56
TOTAL	186	97	298

SFRP Academic Titles	
Assistant Professor	64
Associate Professor	70
Professor	40
Instructor	0
Chairman	1
Visiting Professor	1
Visiting Assoc. Prof.	1
Research Associate	9
TOTAL	186

Source of Learning About the SRP		
Category	Applicants	Selectees
Applied/participated in prior years	28 %	34 %
Colleague familiar with SRP	19 %	16 %
Brochure mailed to institution	23 %	17 %
Contact with Air Force laboratory	17 %	23 %
<i>IEEE Spectrum</i>	2 %	1 %
<i>BIIHE</i>	1 %	1 %
Other source	10 %	8 %
TOTAL	100 %	100 %

APPENDIX B – SRP EVALUATION RESPONSES

1. OVERVIEW

Evaluations were completed and returned to RDL by four groups at the completion of the SRP. The number of respondents in each group is shown below.

Table B-1. Total SRP Evaluations Received

Evaluation Group	Responses
SFRP & GSRPs	275
HSAPs	113
USAF Laboratory Focal Points	84
USAF Laboratory HSAP Mentors	6

All groups indicate unanimous enthusiasm for the SRP experience.

The summarized recommendations for program improvement from both associates and laboratory personnel are listed below:

- A. Better preparation on the labs' part prior to associates' arrival (i.e., office space, computer assets, clearly defined scope of work).
- B. Faculty Associates suggest higher stipends for SFRP associates.
- C. Both HSAP Air Force laboratory mentors and associates would like the summer tour extended from the current 8 weeks to either 10 or 11 weeks; the groups state it takes 4-6 weeks just to get high school students up-to-speed on what's going on at laboratory. (Note: this same argument was used to raise the faculty and graduate student participation time a few years ago.)

2. 1997 USAF LABORATORY FOCAL POINT (LFP) EVALUATION RESPONSES

The summarized results listed below are from the 84 LFP evaluations received.

1. LFP evaluations received and associate preferences:

Table B-2. Air Force LFP Evaluation Responses (By Type)

Lab	Evals Recv'd	How Many Associates Would You Prefer To Get ?								(% Response)			
		SFRP				GSRP (w/ Univ Professor)				GSRP (w/o Univ Professor)			
		0	1	2	3+	0	1	2	3+	0	1	2	3+
AEDC	0	-	-	-	-	-	-	-	-	-	-	-	-
WHMC	0	-	-	-	-	-	-	-	-	-	-	-	-
AL	7	28	28	28	14	54	14	28	0	86	0	14	0
USAFA	1	0	100	0	0	100	0	0	0	0	100	0	0
PL	25	40	40	16	4	88	12	0	0	84	12	4	0
RL	5	60	40	0	0	80	10	0	0	100	0	0	0
WL	46	30	43	20	6	78	17	4	0	93	4	2	0
Total	84	32%	50%	13%	5%	80%	11%	6%	0%	73%	23%	4%	0%

LFP Evaluation Summary. The summarized responses, by laboratory, are listed on the following page. LFPs were asked to rate the following questions on a scale from 1 (below average) to 5 (above average).

2. LFPs involved in SRP associate application evaluation process:
 - a. Time available for evaluation of applications:
 - b. Adequacy of applications for selection process:
3. Value of orientation trips:
4. Length of research tour:
5.
 - a. Benefits of associate's work to laboratory:
 - b. Benefits of associate's work to Air Force:
6.
 - a. Enhancement of research qualifications for LFP and staff:
 - b. Enhancement of research qualifications for SFRP associate:
 - c. Enhancement of research qualifications for GSRP associate:
7.
 - a. Enhancement of knowledge for LFP and staff:
 - b. Enhancement of knowledge for SFRP associate:
 - c. Enhancement of knowledge for GSRP associate:
8. Value of Air Force and university links:
9. Potential for future collaboration:
10.
 - a. Your working relationship with SFRP:
 - b. Your working relationship with GSRP:
11. Expenditure of your time worthwhile:

(Continued on next page)

12. Quality of program literature for associate:
 13. a. Quality of RDL's communications with you:
 b. Quality of RDL's communications with associates:
 14. Overall assessment of SRP:

Table B-3. Laboratory Focal Point Responses to above questions

	<i>AEDC</i>	<i>AL</i>	<i>USAFA</i>	<i>PL</i>	<i>RL</i>	<i>WHMC</i>	<i>WL</i>
<i># Evals Recv'd</i>	0	7	1	14	5	0	46
<i>Question #</i>							
2	-	86 %	0 %	88 %	80 %	-	85 %
2a	-	4.3	n/a	3.8	4.0	-	3.6
2b	-	4.0	n/a	3.9	4.5	-	4.1
3	-	4.5	n/a	4.3	4.3	-	3.7
4	-	4.1	4.0	4.1	4.2	-	3.9
5a	-	4.3	5.0	4.3	4.6	-	4.4
5b	-	4.5	n/a	4.2	4.6	-	4.3
6a	-	4.5	5.0	4.0	4.4	-	4.3
6b	-	4.3	n/a	4.1	5.0	-	4.4
6c	-	3.7	5.0	3.5	5.0	-	4.3
7a	-	4.7	5.0	4.0	4.4	-	4.3
7b	-	4.3	n/a	4.2	5.0	-	4.4
7c	-	4.0	5.0	3.9	5.0	-	4.3
8	-	4.6	4.0	4.5	4.6	-	4.3
9	-	4.9	5.0	4.4	4.8	-	4.2
10a	-	5.0	n/a	4.6	4.6	-	4.6
10b	-	4.7	5.0	3.9	5.0	-	4.4
11	-	4.6	5.0	4.4	4.8	-	4.4
12	-	4.0	4.0	4.0	4.2	-	3.8
13a	-	3.2	4.0	3.5	3.8	-	3.4
13b	-	3.4	4.0	3.6	4.5	-	3.6
14	-	4.4	5.0	4.4	4.8	-	4.4

3. 1997 SFRP & GSRP EVALUATION RESPONSES

The summarized results listed below are from the 257 SFRP/GSRP evaluations received.

Associates were asked to rate the following questions on a scale from 1 (below average) to 5 (above average) - by Air Force base results and over-all results of the 1997 evaluations are listed after the questions.

1. The match between the laboratories research and your field:
2. Your working relationship with your LFP:
3. Enhancement of your academic qualifications:
4. Enhancement of your research qualifications:
5. Lab readiness for you: LFP, task, plan:
6. Lab readiness for you: equipment, supplies, facilities:
7. Lab resources:
8. Lab research and administrative support:
9. Adequacy of brochure and associate handbook:
10. RDL communications with you:
11. Overall payment procedures:
12. Overall assessment of the SRP:
13.
 - a. Would you apply again?
 - b. Will you continue this or related research?
14. Was length of your tour satisfactory?
15. Percentage of associates who experienced difficulties in finding housing:
16. Where did you stay during your SRP tour?
 - a. At Home:
 - b. With Friend:
 - c. On Local Economy:
 - d. Base Quarters:
17. Value of orientation visit:
 - a. Essential:
 - b. Convenient:
 - c. Not Worth Cost:
 - d. Not Used:

SFRP and GSRP associate's responses are listed in tabular format on the following page.

Table B-4. 1997 SFRP & GSRP Associate Responses to SRP Evaluation

	Arnold	Brooks	Edwards	Eglin	Griffis	Hanscom	Kelly	Kirtland	Lackland	Robins	Tyndall	WPAFB	average
# res	6	48	6	14	31	19	3	32	1	2	10	85	257
1	4.8	4.4	4.6	4.7	4.4	4.9	4.6	4.6	5.0	5.0	4.0	4.7	4.6
2	5.0	4.6	4.1	4.9	4.7	4.7	5.0	4.7	5.0	5.0	4.6	4.8	4.7
3	4.5	4.4	4.0	4.6	4.3	4.2	4.3	4.4	5.0	5.0	4.5	4.3	4.4
4	4.3	4.5	3.8	4.6	4.4	4.4	4.3	4.6	5.0	4.0	4.4	4.5	4.5
5	4.5	4.3	3.3	4.8	4.4	4.5	4.3	4.2	5.0	5.0	3.9	4.4	4.4
6	4.3	4.3	3.7	4.7	4.4	4.5	4.0	3.8	5.0	5.0	3.8	4.2	4.2
7	4.5	4.4	4.2	4.8	4.5	4.3	4.3	4.1	5.0	5.0	4.3	4.3	4.4
8	4.5	4.6	3.0	4.9	4.4	4.3	4.3	4.5	5.0	5.0	4.7	4.5	4.5
9	4.7	4.5	4.7	4.5	4.3	4.5	4.7	4.3	5.0	5.0	4.1	4.5	4.5
10	4.2	4.4	4.7	4.4	4.1	4.1	4.0	4.2	5.0	4.5	3.6	4.4	4.3
11	3.8	4.1	4.5	4.0	3.9	4.1	4.0	4.0	3.0	4.0	3.7	4.0	4.0
12	5.7	4.7	4.3	4.9	4.5	4.9	4.7	4.6	5.0	4.5	4.6	4.5	4.6
Numbers below are percentages													
13a	83	90	83	93	87	75	100	81	100	100	100	86	87
13b	100	89	83	100	94	98	100	94	100	100	100	94	93
14	83	96	100	90	87	80	100	92	100	100	70	84	88
15	17	6	0	33	20	76	33	25	0	100	20	8	39
16a	-	26	17	9	38	23	33	4	-	-	-	30	
16b	100	33	-	40	-	8	-	-	-	-	36	2	
16c	-	41	83	40	62	69	67	96	100	100	64	68	
16d	-	-	-	-	-	-	-	-	-	-	-	0	
17a	-	33	100	17	50	14	67	39	-	50	40	31	35
17b	-	21	-	17	10	14	-	24	-	50	20	16	16
17c	-	-	-	-	10	7	-	-	-	-	-	2	3
17d	100	46	-	66	30	69	33	37	100	-	40	51	46

4. 1997 USAF LABORATORY HSAP MENTOR EVALUATION RESPONSES

Not enough evaluations received (5 total) from Mentors to do useful summary.

5. 1997 HSAP EVALUATION RESPONSES

The summarized results listed below are from the 113 HSAP evaluations received.

HSAP apprentices were asked to rate the following questions on a scale from
1 (below average) to 5 (above average)

1. Your influence on selection of topic/type of work.
2. Working relationship with mentor, other lab scientists.
3. Enhancement of your academic qualifications.
4. Technically challenging work.
5. Lab readiness for you: mentor, task, work plan, equipment.
6. Influence on your career.
7. Increased interest in math/science.
8. Lab research & administrative support.
9. Adequacy of RDL's Apprentice Handbook and administrative materials.
10. Responsiveness of RDL communications.
11. Overall payment procedures.
12. Overall assessment of SRP value to you.
13. Would you apply again next year? Yes (92 %)
14. Will you pursue future studies related to this research? Yes (68 %)
15. Was Tour length satisfactory? Yes (82 %)

	Arnold	Brooks	Edwards	Eglin	Griffiss	Hanscom	Kirtland	Tyndall	WPAFB	Totals
# resp	5	19	7	15	13	2	7	5	40	113
1	2.8	3.3	3.4	3.5	3.4	4.0	3.2	3.6	3.6	3.4
2	4.4	4.6	4.5	4.8	4.6	4.0	4.4	4.0	4.6	4.6
3	4.0	4.2	4.1	4.3	4.5	5.0	4.3	4.6	4.4	4.4
4	3.6	3.9	4.0	4.5	4.2	5.0	4.6	3.8	4.3	4.2
5	4.4	4.1	3.7	4.5	4.1	3.0	3.9	3.6	3.9	4.0
6	3.2	3.6	3.6	4.1	3.8	5.0	3.3	3.8	3.6	3.7
7	2.8	4.1	4.0	3.9	3.9	5.0	3.6	4.0	4.0	3.9
8	3.8	4.1	4.0	4.3	4.0	4.0	4.3	3.8	4.3	4.2
9	4.4	3.6	4.1	4.1	3.5	4.0	3.9	4.0	3.7	3.8
10	4.0	3.8	4.1	3.7	4.1	4.0	3.9	2.4	3.8	3.8
11	4.2	4.2	3.7	3.9	3.8	3.0	3.7	2.6	3.7	3.8
12	4.0	4.5	4.9	4.6	4.6	5.0	4.6	4.2	4.3	4.5
Numbers below are percentages										
13	60%	95%	100%	100%	85%	100%	100%	100%	90%	92%
14	20%	80%	71%	80%	54%	100%	71%	80%	65%	68%
15	100%	70%	71%	100%	100%	50%	86%	60%	80%	82%

FREQUENCY STABILIZATION OF AN Nd:YAG LASER

Joshua C. Bienfang
Graduate Student
Department of Physics and Astronomy

University of New Mexico
Yale Boulevard
Albuquerque, NM 87106

Final Report for:
Graduate Student Research Program
Phillips Laboratory

Sponsored by:
Air Force Office of Scientific Research
Bolling AFB, Washington DC

and

Phillips Laboratory

FREQUENCY STABILIZATION OF AN Nd:YAG LASER

Joshua C. Bienfang
Graduate Student
Department of Physics and Astronomy
University of New Mexico

Abstract

A frequency stabilization technique based on locking to the reflection mode of a high finesse cavity is described. The experimental apparatus for locking two lasers to adjacent modes of the cavity was designed and built based on this technique. A feedback control loop was assembled, including the design and construction of a highly variable servo with maximum bandwidth and desirable response at unity gain. The noise characteristics of the control loop are investigated, and the most significant component is found to be the discriminator. The discriminator error signal was observed and showed superior performance and low noise density. The discriminator constant was measured to be 4.100V/MHz, and the actuator constant was found to be 4.517 MHz/V. This work is part of a project to develop a high powered laser with narrow linewidth for use in spectroscopy and the development of optical time standards.

FREQUENCY STABILIZATION OF AN Nd:YAG LASER

Joshua C. Bienfang

As a measurement tool the frequency stabilized laser offers accuracies which are orders of magnitude greater than almost all other devices. Modern stabilization techniques have achieved sub-Hertz linewidths for lasers in the optical range. This corresponds to accuracies better than one part in one hundred trillion! Such sensitive devices have applications in high resolution spectroscopy, gravitational wave detection, and the development of new time standards. Furthermore, the long coherence length of these lasers makes them very attractive for atmospheric researchers and coherent communications techniques. Modern techniques have made it possible to stabilize a wide range of lasers with fantastic accuracy, each having its own advantages and disadvantages. Our research is directed towards developing a highly frequency stabilized Nd:YAG laser which operates at high power. Such a laser would be able to probe weak atomic transitions, and may make new transitions of narrower linewidth available for use as frequency standards, but also has potential applications in atmospheric spectroscopy. Nd:YAG lasers are particularly attractive for researchers since they are easily controlled, and the lasing transition corresponds to well known transitions in iodine and carbon dioxide; molecules which are used in a variety of systems, particularly in time standards.

A high power injection locked Nd:YAG laser has been built capable of powers up to 30 W. The master oscillator of this system is a nonplanar ring Nd:YAG equipped with temperature tuning, and piezo electric tuning. The goal of this project is to use another laser, identical to the master oscillator of the injection locked laser, to lock to a resonant longitudinal mode of a very high finesse Fabry-Perot interferometer. The master oscillator of the injection locked system will then be locked to an adjacent mode of the cavity. The spectral characteristics of the master oscillator will be transferred to the high power slave, and the output of the slave will be compared to that of the first laser. One should observe a heterodyne beatnote between the two lasers at roughly 6 GHz. With the two lasers heterodyned together one can measure the relative stability of the injection locked system. The result being a high powered laser with

narrow linewidth and a well known relative frequency stability. Since the master oscillator is identical to the other laser locked to the cavity, it is sufficient to describe the locking technique for a single laser in this report.

The optics for the two lasers locked to the cavity is shown in figure 0. Care was taken to match to the longitudinal cavity mode accurately, and we had only 1% of the optical power in the transverse modes. Also, to avoid significant intensity noise a total of 110dB of isolation from reflected beams was put on each laser; 30dB with a Faraday isolator, and 80 dB with an acousto-optic modulator. The lasers were made by Lightwave, model #122 diode-pumped NPRO Nd:YAG lasers at 1064nm. They have can be tuned with

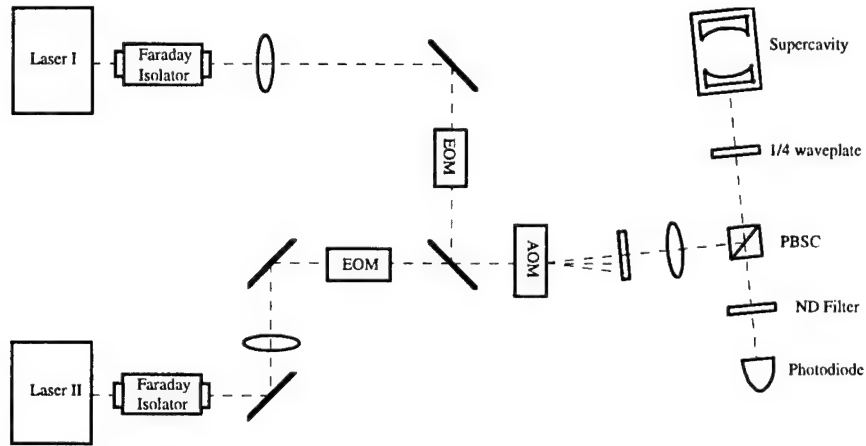


Figure 0: The Optics Table. Two lasers are matched to adjacent longitudinal modes of a high finesse cavity. 110dB of isolation from reflection is used.

temperature variation, or by applying a voltage to the piezo electric crystal bonded to the laser crystal. The high finesse cavity is a Newport SuperCavity, model SC-150C. It has a free spectral range of roughly 6.2 GHz, and a finesse close to 40,000. The photodetector is a New Focus model 1611 low noise detector with a DC-coupled bandwidth of 1 GHz. The locking technique described below involves phase modulating the laser beams. This was done with New Focus electro-optic modulators resonant at 15 MHz and 21 MHz. The two lasers are modulated at different frequencies to avoid interference on the photodetector. Although it is not shown in the diagram, one of the lasers is also used as the master oscillator of the injection locked system.

The most fundamental source of noise in a laser is the spontaneous emission rate of the laser transition. Photons from this process build up in the laser cavity and cause random phase fluctuations in the

output beam, thereby introducing white noise and broadening the spectrum of the laser. This is an unavoidable noise source in any laser, and defines the so called Schawlow-Townes limit to the spectral density of frequency noise, given by¹

$$S_{f,ST} = \delta\nu_L \sqrt{\frac{2h\nu}{P}} \quad (1)$$

where $\delta\nu_L$ is the laser cavity linewidth, and P is the laser output power. Note that $S_{f,ST}$ has units $\text{Hz} / \sqrt{\text{Hz}}$ (the subscript 'f' denotes frequency noise), and shows that the quantum limit for the laser linewidth is

$$\Delta\nu_L = \pi S_{f,ST}^2 = \frac{2\pi h\nu (\delta\nu_L)^2}{P} \quad (2)$$

Because Nd:YAG lasers have a very narrow laser cavity linewidths, this quantum limit can be as low as 1Hz, even for powers on the order of 1mW.² Quantum noise is not the prevailing noise source in the laser, but rather defines the limit at which other sources have been removed. Noise sources such as thermal fluctuation and vibration, which directly affect the laser cavity length, usually dominate the laser linewidth at low frequencies (up to 50kHz), and have a spectral character like $\frac{1}{f^\alpha}$. To reduce these noise sources researchers often go to great lengths to isolate their systems from vibrations and temperature fluctuations in the local environment, however, high quality frequency stabilization requires the use of active noise suppression.

An active control system is typically broken up in to four distinct parts: the system under control, a discriminator, a servo, and an actuator. It is simply a feedback loop; the discriminator measures the system parameter of interest (in this case, the frequency), and compares it to a reference value, the servo tailors the 'error signal' from the discriminator, usually inverting it, amplifying, etc., and the actuator imposes the appropriate change on the system to make the measured parameter equal the reference value. In our system the reference value of the frequency is a resonant frequency of a very high finesse optical cavity. The discriminator compares the instantaneous laser frequency with the resonant frequency of the cavity, and converts the difference in frequency to an error signal voltage with a conversion factor $D(\text{V/Hz})$. The servo

applies a frequency dependent gain to the error signal (low pass filter), and creates a feedback voltage with a conversion $G(\omega)(V/V)$. The actuator is a piezo electric crystal bonded to the top of the Nd:YAG laser crystal driven directly by the servo. Since the laser cavity is in a non-planar ring configuration, changing the height of the crystal with the piezo changes the laser cavity length, thereby tuning the laser frequency with a conversion factor $K(Hz/V)$. A schematic of the control loop is shown in figure 1.

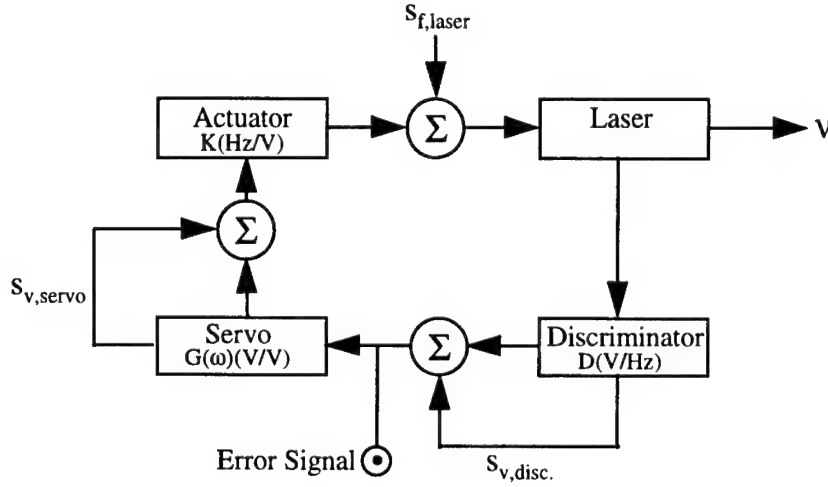


Figure 1: The Control Loop. Each element of the loop contributes noise to the signal as shown. Actuator noise is indistinguishable from laser noise, and is included in $S_{f,Laser}$.

Each element of the feedback loop contributes a certain amount of noise to the feedback signal. For the discriminator and the servo this noise is voltage noise. The actuator noise, arising mainly from thermal fluctuations and Johnson noise in the piezo, cannot be distinguished from the frequency noise of the laser itself. The linear spectral density of frequency noise at the laser of the entire control loop can be written with the understanding that the linear spectral density is the root of the power spectral density, and the power spectral density is simply the sum of contributions of each element of the loop.³

$$S_{f,loop} = \frac{\sqrt{S_{f,laser}^2 + |KS_{v,servo}|^2 + |KG(\omega)S_{v,disc.}|^2}}{|1 + KG(\omega)D|} \quad (3)$$

This result can be simplified when one considers the gain of the servo, $G(\omega)$ to be large relative to the actuator constant, K (see below). In this limit the minimum linear spectral density of frequency noise is seen

to be

$$S_{f,loop} = \frac{S_{v,disc.}}{D} \quad (4)$$

Noise in the discriminator arises mainly from variations in the reference frequency, amplifier noise, and photodetector shot noise. It is evident that a discriminator with a low noise contribution, and a large conversion factor, D , will yield optimal frequency stabilization of the laser, and thus much effort has been devoted to developing discriminators with these characteristics.

Many discrimination techniques have been developed since work in laser (actually, maser) frequency stabilization began, the most prominent of these are referenced in the endnotes⁴⁻⁶. All of these are based on referencing the laser to a resonance of a high finesse cavity. The method we use is based on work by Drever et al.⁷, and will be referred to as the Pound-Drever-Hall, or PDH technique. In this technique the laser is mode matched to a high finesse cavity and phase modulated with a sinusoidal modulation at a RF frequency, ω_m , much larger than the cavity bandwidth. Phase modulating the laser beam creates sidebands on the carrier, or original laser frequency, as follows

$$e^{i\nu t} \xrightarrow{\omega_m \text{ modulation}} e^{i(\nu t + \alpha \sin(\omega_m t))}.$$

The generating function for the Bessel function of the first kind is⁸:

$$e^{\frac{1}{2}z\left(x - \frac{1}{x}\right)} = \sum_{k=-\infty}^{\infty} x^k J_k(z), \quad (5)$$

so the phase modulated beam can be written as

$$e^{i(\nu t + \alpha \sin(\omega_m t))} = e^{i\nu t} \sum_{k=-\infty}^{\infty} e^{ik\omega_m t} J_k(\alpha). \quad (6)$$

Since α , the depth of the phase modulation, is small, we need only keep up to the first order Bessel function, leaving

$$e^{i(\nu t + \alpha \sin(\omega_m t))} \cong J_0(\alpha)e^{i\nu t} + J_1(\alpha)\left[e^{i(\nu + \omega_m)t} - e^{i(\nu - \omega_m)t}\right]. \quad (7)$$

Thus one can see that there is energy at the carrier frequency ν , and at the symmetrically placed sideband frequencies $(\nu \pm \omega)$. In the experiment we were able to see the second order sidebands at $\pm 2\omega_m$, but

their amplitude ($\propto J_2(\alpha)$) was so small as to be neglected. When the beam is sent in to the cavity, the sidebands are completely reflected, since they lie well outside the cavity bandwidth. The carrier, on the other hand, experiences a phase shift when it is close to the cavity resonant frequency, according to the reflection coefficient for a Fabry-Perot interferometer with no absorption⁹:

$$R(\nu) = \frac{r \left(1 - e^{-i \frac{2L\nu}{c}} \right)}{1 - r^2 e^{-i \frac{2L\nu}{c}}}, \quad (8)$$

where r is the reflection coefficient of the cavity mirrors (for simplicity the cavity mirrors are taken to have the same reflectivity), and L is the cavity length. Note that when the laser frequency is exactly resonant (i.e. is equal to an integer times $\pi c/L$) the reflectivity is zero. When the phase shifted carrier is mixed with the sidebands on the photodetector, the detector signal will be sinusoidal with frequency equal to the modulation frequency, and with amplitude equal to the sine of the round trip phase shift of the cavity. When ν is close to resonance this amplitude is directly proportional to the difference between the laser frequency and the cavity resonance:

$$\text{amplitude} = \frac{4\pi L(\nu - \nu_{\text{cavity}})}{c}. \quad (9)$$

Another way to understand this effect is to understand that if there is *no* phase shift on the carrier, then the mixing products $(\nu, \nu + \omega_m)$ and $(\nu, \nu - \omega_m)$ will exactly cancel, but when the carrier is phase shifted, these two terms will not cancel, and the AM signal will appear. The error signal is recovered by mixing in quadrature the AM signal from the detector with a portion of the RF phase modulation signal, resulting in a voltage directly proportional to the difference between the instantaneous laser frequency and the cavity resonant frequency when the laser is close to resonance. It should be noted that the mixing also yields voltages at twice the modulation frequency, and at DC. These are removed with a notch filter, and an AC coupled amplifier, respectively. Figure 2 shows a theoretical error signal when the carrier is swept over a large range of frequencies, well beyond the cavity bandwidth and the modulation frequency. The large slope at the centre of the plot is linear, as expected from the results above for frequencies close to

resonance. This slope is the discriminator constant $D(V/Hz)$. Since it is desirable to have a large discriminator constant, and equation (9) shows that the discriminator constant is inversely proportional to the free spectral range of the cavity, $c/2L$, it is best to use long cavity lengths.

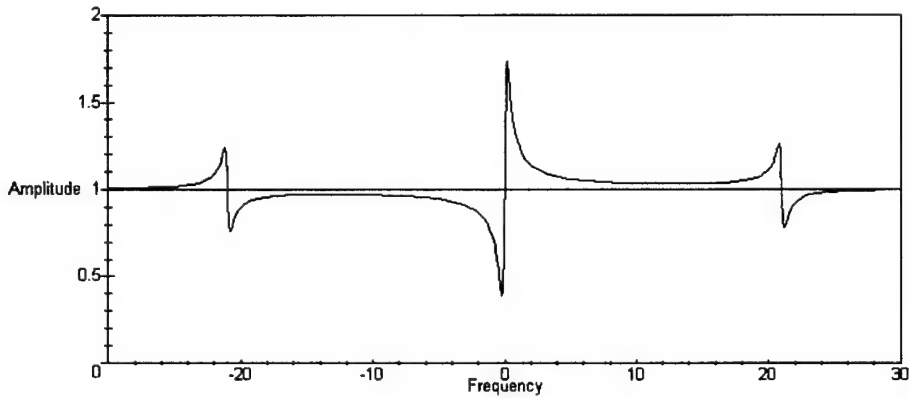


Figure 2: Theoretical Error Signal (Amplitude in arbitrary units, Frequency in MHz). The carrier frequency is swept over a large range, showing the phase sidebands at 21MHz, and the discriminator slope when close to resonance(0MHz).

This theoretical prediction was verified experimentally by applying a low frequency triangle wave to the piezo electric crystal. The modulation frequency was 21 MHz, and the laser was swept through roughly 60MHz by the voltage ramp. The error signal was monitored on an oscilloscope, and is shown in figure 3.

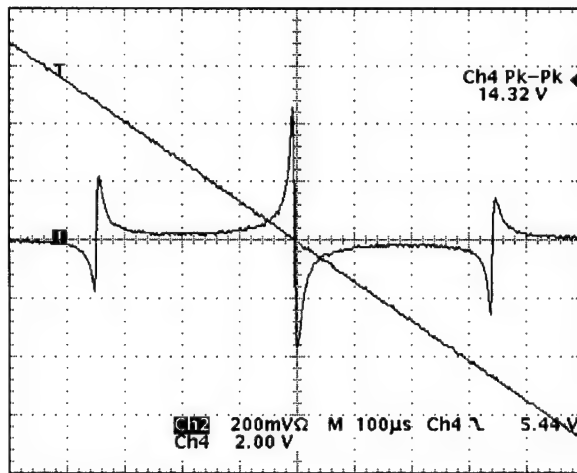


Figure 3: Experimental Error Signal. The voltage ramp applied to the piezo is shown along with the error signal. The sidebands are known to be 42MHz apart, allowing the actuator constant, K , and the discriminator slope D to be measured. This signal has been inverted by the input stage of the servo (see circuit diagram).

This data shows the discriminator slope to be 4.100 V/MHz. The actuator constant was found to be 4.517 MHz/V. This data also allows us to measure the phase modulation depth from the relative heights of the carrier and sideband signals. The modulation depth was found to be 1.171 radians.

For the frequencies of the control signal in our experiment, the discriminator and the actuator have an essentially flat frequency response. Thus the response of the control loop is determined by that of the servo. Since the environmental noise sources which have spectral densities like $\frac{1}{f^\alpha}$ dominate up to about 50kHz, our servo was designed to have large gain at low frequencies. Ideally one would like to have a servo with an infinite bandwidth to suppress the white noise from spontaneous emission in the laser, but the response time of the actuator limits the bandwidth. This can be understood by considering the response of a piezo to a square voltage pulse; the mass of the piezo and the laser crystal will not allow instantaneous changes in the cavity length. Rather there is some finite time delay between when the servo tells the actuator to change the laser frequency, and when the actuator accomplishes the task. This time delay means that in order to avoid applying positive feedback (driving the laser in the wrong way), the loop bandwidth must be limited to frequencies whose corresponding periods are less than twice the time delay. This cutoff frequency is referred to as the unity gain point; beyond which the feedback signal is attenuated to avoid positive feedback. The unity gain point in our servo was set to be roughly 25 kHz. Furthermore, to avoid large phase delays in the feedback loop, but have as large a bandwidth as possible, one should tailor the signal such that the slope of the gain is less than 6 dB/Octave at the unity gain point¹⁰.

The servo circuit diagram and frequency response are shown in figure 4. The input is impedance matched to 50Ω cable, and provides an inverting gain of 10. The error signal is monitored at this point, as shown in the diagram. One should note that the definition of which elements are part of the servo and which are part of the discriminator is somewhat subjective. The next two op-amps are low pass active filters (integrators) which have been tailored to give the appropriate gain at low frequencies, and to set the unity gain point. The output stage is a voltage follower OP633; since the piezo is a capacitive load, and the LF356N op-amps have low slew rates, another op-amp was chosen to drive the actuator. At low frequencies, the gain slope is 12 dB/Octave, rolling off to 6dB/Octave at about 100 Hz. The slope at unity

gain is approaching 3 dB/Octave. We added a 12dB/Octave attenuation for very high frequencies to avoid instability, and reduce noise. It should be noted that these values have not yet been adjusted for optimal performance, but rather serve as nominal values for functional purposes.

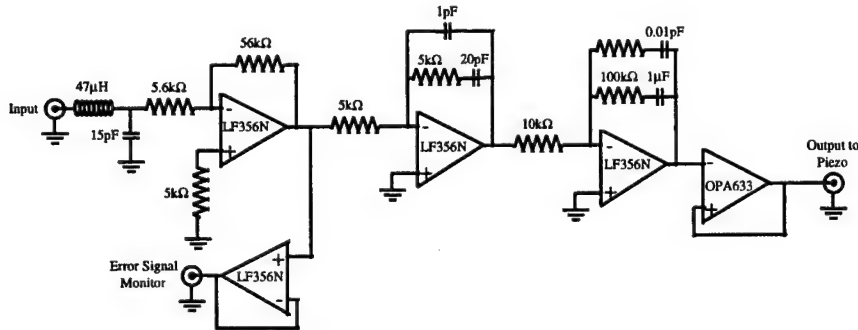


Figure 4a: The Servo Circuit. An impedance matched input stage, amplifier, two low pass filters, and an output buffer tailor the error signal for the appropriate frequency response and drive the piezo electric crystal on the laser.

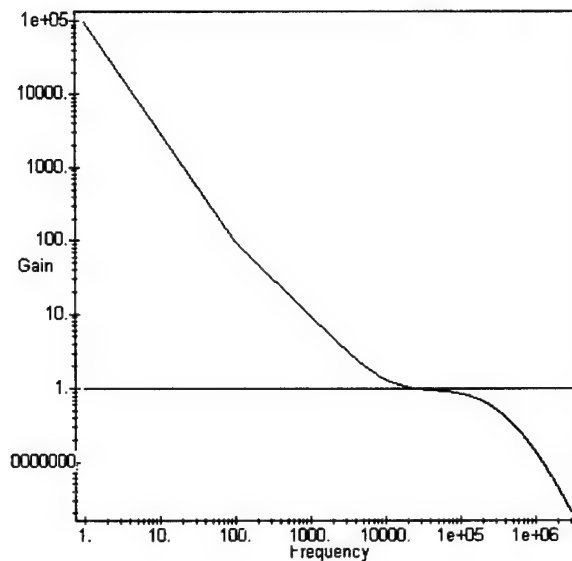


Figure 4b: Servo Frequency Response. 12 dB/Oct. gain slope at low frequencies rolls off to 6dB/Oct. up to unity gain where the feedback becomes positive. High frequencies are attenuated strongly.

We hope to add an integration stage after the output buffer of the servo circuit. This integrator will have a very large RC constant, and will be used to drive the slow temperature control on the Nd:YAG laser. It is

hoped that this will yield superior long term stability to the laser system.

This summer a great deal of progress was made on the laser stabilization project. The optics were assembled, the lasers matched to the cavity, the discriminator was built, the servo circuit was designed and built, and the actuator and discriminator constants were measured. Our system shows an excellent signal to noise ratio on the error signal well above 80, and shows a significant improvement over previous applications of the PDH technique. This is partly due to the care with which the discriminator was designed for our system, and partly due to the availability of high quality materials and equipment. The servo we designed will also be used for other control techniques which will be used for iodine spectroscopy and the development of a highly stable standardized frequency source for the lab. The investigation of CO₂ as a possible new frequency standard will be a significant contribution to the time standards community, and the progress made in this project brings that work nearer to being realized.

References

- (1) A. Yariv, *Quantum Electronics 3rd Edition*, Capter 21, (New York: John Wiley and Sons, 1989).
- (2) D.S. Elliot, R. Roy, and S.J. Smith, "Extracavity laser band-shape and bandwidth modifications", *Phys. Rev. A*, **26**, 12-18 (1982).
- (3) T. Day Ph.D. dissertation (Dept. of Physics, Stanford University, Stanford California, 1990).
- (4) A.D. White, "Frequency stabilization of gas lasers", *IEEE J. Quant. Electron.*, **QE-1**, 349-357, (1965).
- (5) T.W. Hansch, B. Couillaud, "Laser frequency stabilisation by polarization spectroscopy of a reflecting reference cavity", *Opt. Comm.*, **35**, 441-444 (1980).
- (6) R.V. Pound, "Electronic frequency stabilization of microwave oscillators", *Rev. Sci. Instrum.*, **17**, 490-505 (1946).
- (7) R.W.P. Drever, J.L. Hall, F.V. Kowalski, J. Hough, G.M. Ford, A.J. Munley, and H. Ward, "Laser phase and frequency stabilization using and optical resonator", *Appl. Phys. B*, **31**, 97-105 (1983).
- (8) M. Abramowitz and I. Stegun, *Handbook Of Mathematical Functions 9th Printing* page 361 (New York: Dover Pub. Inc., 1972).
- (9) A.E. Siegamn, *Lasers*, Chapter 11, (Mill Valley: University Science Books, 1986).
- (10) G. Franklin, J.D. Powell, and A. Emami-Naeini, *Feedback Control of Dynamic Systems*, Chapter 3, (Menlo Park: Addison-Wesley Publishing 1988).

**A Study of Defects and Dark Current Mechanisms
in Triple-Junction GaInP₂/GaAs/Ge Photovoltaic Cells**

**Marc L. Breen
Graduate Student
Department of Chemistry**

**Tulane University
New Orleans, LA 70118**

**Final Report for:
Summer Graduate Student Research Program
Phillips Laboratory**

**Sponsored by:
Air Force Office of Scientific Research
Bolling Air Force Base, DC**

and

**Phillips Laboratory
Kirtland AFB
Albuquerque, NM 87117**

August 1997

**A Study of Defects and Dark Current Mechanisms
in Triple-Junction GaInP₂/GaAs/Ge Photovoltaic Cells**

**Marc L. Breen
Graduate Student
Department of Chemistry
Tulane University**

Abstract

Triple-junction GaInP₂/GaAs/Ge n⁺/p photovoltaic cells, monolithically grown by metal-organic vapor deposition, were studied by optical and electronic microscopy to look for defects responsible for dark currents in the cell. Physical abnormalities introduced during the manufacturing process indicated the need for more careful handling of the cells. Forward-bias dark current measurements were consistent with recombination theory at the cell's maximum power point. Two, "2 1/2"-junction GaInP₂/GaAs/Ge, single-junction GaAs/Ge and single-junction GaAs/GaAs cells also showed similar dark current mechanisms.

**A Study of Defects and Dark Current Mechanisms
in Triple-Junction GaInP₂/GaAs/Ge Photovoltaic Cells**

**Marc L. Breen
Graduate Student
Department of Chemistry
Tulane University**

Abstract

Triple-junction GaInP₂/GaAs/Ge n⁺/p photovoltaic cells, monolithically grown by metal-organic vapor deposition, were studied by optical and electronic microscopy to look for defects responsible for dark currents in the cell. Physical abnormalities introduced during the manufacturing process indicated the need for more careful handling of the cells. Forward-bias dark current measurements were consistent with recombination theory at the cell's maximum power point. Two, "2 1/2"-junction GaInP₂/GaAs/Ge, single-junction GaAs/Ge and single-junction GaAs/GaAs cells also showed similar dark current mechanisms.

A Study of Defects and Dark Current Mechanisms in Triple-Junction GaInP₂/GaAs/Ge Photovoltaic Cells

Marc L. Breen

Introduction

The triple-junction GaInP₂/GaAs/Ge solar cell is currently the highest efficiency photovoltaic cell in production with a one sun, AM0 efficiency of 24-25%. It is composed of thin-films of GaInP₂ and GaAs grown monolithically on top of a germanium substrate. Work in this area began in earnest after Olsen *et al.*¹ first reported a GaInP₂/GaAs two-junction solar cell with a one sun, AM1.5 efficiency of 27.3% in 1990. Subsequently a number of groups have attempted to improve cell quality and develop reliable methods for demonstrating the performance capabilities of these systems (eg. precise and accurate modeling of AM0 conditions).

Dark current-voltage behavior is known to limit solar cell open-circuit voltage, fill factor, and conversion efficiency. A number of papers can be found in the literature which describe methods for identifying and reducing dark current in Si and GaAs solar cells²⁻⁵, but few studies have examined GaInP₂ diodes. In two notable exceptions, Reinhardt *et al.* investigated efficiency losses through dark current mechanisms in 2-junction GaInP₂/GaAs cells before⁶ and after 1 MeV electron irradiation⁷.

In the 3-junction cells discussed herein, germanium replaces GaAs as the substrate because of its cheaper cost (ca. \$5/in² vs. \$25/in²), durability and the marginal increase in efficiency it provides by absorbing some of the longer wavelengths below the bandgap of GaAs. When the three materials of GaInP₂/GaAs/Ge, with bandgaps of 1.83, 1.42 and 0.67 eV, are combined, a broad section of the solar spectrum is absorbed. Therefore, the multi-junction cells realize a greater overall efficiency than could be achieved with any single material.

Since this was one of the most promising solar cell designs available, a joint ManTech program was organized in 1995 between USAF Phillips and Wright-Patterson Laboratories, NASA Lewis Research Center, and two industry contractors. Through this partnership, the group is concentrating on an effective technology transfer to scale-up cell size and quantity to production levels in order to meet the future needs of America's spacecraft industry. This 4 year program builds on earlier ManTech initiatives to develop single-junction GaAs/GaAs and GaAs/Ge solar cells which began in the early 1980's.

The objectives of the ManTech program are to produce a high efficiency 24-26% cell which could directly replace GaAs/Ge cells in existing array designs (Table I)⁸. Therefore, the cells need to be similar in size and contact strength with similar or superior radiation resistance and mass savings over GaAs/Ge cells. Experimental 2 x 2 cm² cells will need to be scaled up to 16 cm² without decreases in efficiency and for ² 1.15 X the cost of state-of-the-art GaAs/Ge cells. The realization of these goals will lead to a 33% increase in solar array specific power (W/kg), a 25% decrease in array size and a 15% reduction in the total array cost per watt (\$/W) over GaAs/Ge cells.

Table I. Multi-junction GaInP₂/GaAs/Ge ManTech Program Requirements

Parameter	Requirement
Lot Average Efficiency (bare, glass optimized AR coating)	24%
p/p ₀ @ 1 x 10 ¹⁵ 1 MeV electrons	0.75
Cell Area	16 cm ²
Thickness	5.5 mm
Contact Integrity, Ag/Kovar weld	>300g w/<0.2% loss

Two basic designs were utilized by Spectrolab, Inc. and TECSTAR/Applied Solar to produce the multi-junction solar cells (Table II)⁸. Primarily the two systems differ in the formation of the bottom Ge layer. Spectrolab reversed the polarity of the Ge layer from p/n, which was used in earlier single junction ManTech cells, to n/p. Whereas TECSTAR forms a controlled n/n AlGaAs/Ge heterointerface at the Ge substrate to give the cell a voltage boost. The Spectrolab cell is a true 3-junction cell, while the TECSTAR cell is referred to as a "2 1/2"-junction cell since the Ge layer is only partially activated.

Table II. Cell comparison between 3 and 2 1/2-Junction cells

	Spectrolab	TECSTAR
Baseline cell decision	n/p triple-junction	p/n 2 1/2-junction
Ge cell formation	n/p Ge junction	n/n AlGaAs/Ge heterointerface, voltage boost
Best dual junction cell efficiency	23.7%	22.8%
Best triple junction cell efficiency	25.5%	24.1%
Best large area cell efficiency	24.3% (13.78 cm ²)	22.1% (16.6 cm ²)
Lot average of Phase I deliverables	24.2%	22.4%

A variety of methods were used to evaluate the performance of Spectrolab and TECSTAR cells by members of the Phillips Laboratory Space Power and Thermal Management Branch. One technique for

detecting defects takes advantage of the cells' observed electroluminescence. When a forward-bias is applied to the triple-junction cells, red light is emitted from the top, GaInP₂ layer. Some defects negate this effect and appear as "dark spots" on the cells during illumination.

There are several types of defects which could possibly be found in monolithically grown solar cells. The simplest to understand are physical scratches, chips, or marks which indicate some form of trauma to the cells in the manufacturing and handling processes. A more serious concern is crystal lattice mismatch. This problem arises when the faces of two different crystals don't align properly leaving some angle between the two crystal faces. There will always be some mismatch between different crystals with different lattice parameters, but these deficiencies can be minimized in some cases. For instance, two materials with similar lattice parameters in the cubic crystal system could align their crystal faces relatively closely. However, if one of the materials had a hexagonal form which was close in energy to that of the cubic, then hexagonal crystals could form in the lattice and distort the bulk crystal sending ripples throughout the structure. Such defects could appear anywhere in the cell.

Even if one layer of material was made up entirely of the same crystal type, each crystal has different lattice faces (except for crystals in the cubic system). At a heterointerface between two different materials, some of those lattice faces will align with more or less mismatch than others.

Temperatures in excess of 600°C are required for the vapor deposition of GaInP₂. Under these conditions there may be diffusion of Ge into the GaAs layer and mobility of dopants and other atoms in the cells. The formation of quaternary GaInAsP has also been observed in GaInP₂/GaAs/GaInP₂ cells grown between 610 and 670°C⁹.

The purpose of this investigation was to look for the aforementioned "dark spots" seen through electroluminescence and then attempt to correlate these and other defects to the formation of dark currents which decrease cell efficiencies. Cells were examined by optical and electronic microscopy. Junction dark current was measured as a function of forward-bias voltages.

Experimental Procedure

The GaInP₂/GaAs/Ge triple-junction mesa diodes and solar cells were grown by metal-organic chemical vapor deposition, MOCVD, and coated with a thin-layer of TiO₂ anti-reflective coating.

Eleven cells were electro-illuminated by applying a forward-bias of 0.5 A and 3.0 V. Contact was made by either soldering leads directly to the cells or touching the back and front bus bar with electrode probes.

A Nikon Optihot optical microscope was used to examine the dark spots up to 1000X magnification. Pictures were taken using a Pulnix TMC-74 video camera and a Polaroid FreezeFrame

video recorder equipped with a Polaroid 35 mm camera attachment. Additionally, the cells were examined under an AMRAY 1830 scanning electron microscope.

Dark current measurements were collected using an HP 4145B semiconductor parameter analyzer integrated with a Macintosh 7500 computer. A custom designed LabView interface was utilized to acquire and analyze data. Low current measurements, up to 0.1 A, were taken directly while higher current measurements required the use of a Kepco bipolar amplifier. The resolution of the voltage and current meters were 1 mV and 10 μ A, respectively. High current measurements, up to 1 A, experienced slightly lower resolutions of 1 mV and 1 A. Dozens of single-junction GaAs/GaAs and GaAs/Ge, double-junction GaInP₂/GaAs/Ge, triple and 2 ¹/₂-junction GaInP₂/GaAs/Ge cells were studied with this apparatus. All measurements were made at room temperature, approximately 23°C, on a brass block, heat sink to minimize temperature fluctuations.

Results and Discussion

A. Physical inspection by optical and electronic microscopy

In response to a forward bias, the GaInP₂ layer radiated a brilliant red light except in certain areas which remained dark. The dark spots manifested themselves in three forms (1) spots, (2) lines, (3) and columns following either side of a grid line. In every case, the dark spots corresponded with a scratch, chip or physical depression on the surface of the solar cells. Most scratches were perpendicular to the grid lines, while a few extended over five or more lines. The scratches were jagged and discontinuous, as if a probe were bouncing as it was dragged across the surface. The systematic accumulation of material on the right side of most of the scratches (with the cell lying flat and the bus bar away from the viewer) gives the appearance that the scratches were made from left to right. The dark spots, were small scratches (<0.5 mm) running parallel to the grid lines.

When dark columns were viewed along either side of a grid line, physical breaks were found in the wire. Obviously, this caused an interruption of current to those areas of the cell which remained dark. In several cases, the cell was illuminated along the grid line from the bus bar to the defect, then dark alongside the rest of the wire. The damage was either in the form of a piece missing from a section of the wire, or a deep groove cut perpendicular to it.

Both high and low efficiency cells had some of these defects, therefore a single scratch isn't enough to defeat the efficiency of a cell. Also, not all the low efficiency cells had scratches or chips.

There were some additional physical flaws observed in the cells. On some of the cells the grid lines were frayed, with hairs of the material hanging off from the surface. At 1000X magnification, dark "veins" were visible in the grid lines of some cells. These may be due to impurities or thermal stressing.

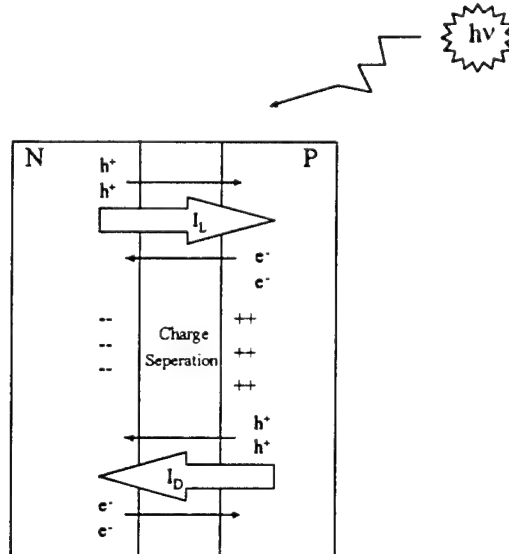
Although frayed wires and dark veins were seen on both high and low efficiency cells, these flaws were far more common in the poorer performing cells.

The manufacturer described a drying cycle during which wipers were swiped across the surface of the wafer to remove excess liquid prior to the deposition process. It is likely that particles trapped under the wipers as they were dragged over the surface of the cells produced the observed scratches.

B. Dark current measurements

The typical dark current-voltage response of a middoped GaInP₂/GaAs/Ge diode is shown in Figure 1. Dark current (I_D) is produced as a thermodynamic response to light current (I_L) generation. As light current produces a separation of charge across the p/n junction, the charges attempt to equilibrate back to neutrality by processes of diffusion, recombination and quantum mechanical tunneling (Fig. 1).

Figure 1. Solar cell diode



Consequently, the total current produced is the light current minus the dark current. Thus the observed current for a single-junction cell can be described by equation 1.

$$I_T = I_L - I_D = I_L - \left[I_{diff} \exp\left(\frac{qV}{A_1 kT}\right) + I_{rec} \exp\left(\frac{qV}{A_2 kT}\right) + I_0 \exp(\beta V) \right] \quad (1)$$

Here, I_T represents the total forward-bias current and V is the applied junction voltage. The term in eq. 1 containing I_{diff} represents the classic Shockley diode equation which accounts for diffusion of carriers across the junction barrier¹⁰. The second term in brackets describes the recombination of electrons and holes via deep energy levels within the junction's space-charge region as first treated by Sah, Noyce, and

Shockley¹¹ and later by Choo¹². Note the third term, which accounts for current due to tunneling^{13,14} is not dependent on temperature.

The parameters I_0 and β in eq. 1 are empirical, but have a theoretical basis related to tunneling in heterojunctions^{13,14}. Expressions for diffusion and recombination are given as^{10,11}

$$I_{diff} = qS(D_n n_p / L_n + D_p p_n / L_p) \quad (2)$$

and

$$I_{rec} = \frac{qS n_i W_d \times f(b)}{(\tau_{p0} \tau_{n0})^{1/2} (V_{bi} - V) / (kT / q)} \quad (3)$$

where the factors D_n and D_p , n_p and p_n , and L_n and L_p refer to the diffusion coefficients, minority carrier densities and diffusion lengths of electrons and holes, respectively. The expression $f(b)$ is a complicated factor involving the recombination trap center energy level, E_t , and electron and hole minority carrier lifetimes, τ_{n0} and τ_{p0} respectively^{11,12}. The value of $f(b)$ can be calculated by numerical integration and has a maximum of $\pi/2$.

The dark current was measured by placing a forward-bias across the cells in the absence of light. Current was then plotted logarithmically with respect to voltage. Since the slope of the curve is a function of the diode ideality factors A_1 , A_2 and β , it is possible to determine the contribution of each of the three mechanisms towards the total amount of dark current present. When a single mechanism is dominant, the slope of a given I-V curve can be represented by equation 4.

$$f(x) = \exp\left(\frac{qV}{kTA_{obs}}\right) \quad (4)$$

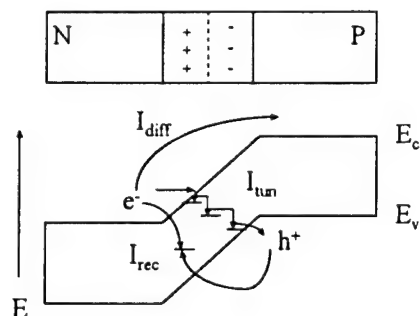
For a single-junction cell, an ideality factor, $A_{obs} = 1$, is seen for ideal diffusion. Recombination dominates when $A_{obs} \cong 2$ and tunneling takes over for any value $A_{obs} > 2$.

In the case of double and triple-junction cells, it is necessary to consider the total current with respect to the light and dark currents for all of the layers. The GaInP₂/GaAs/Ge cell may be subject to 3 mechanisms of dark current generation for each of its three layers. Therefore, there can be a total of nine mechanisms of dark current active in the cell.

Of the three types of dark current, diffusion is always present. Recombination and tunneling are enabled by defects within the material which provide additional energy levels between the valence and

conduction bands. Through these intermediate levels, electrons can recombine with positive holes or relax by tunneling back down to the valence band (Fig. 2).

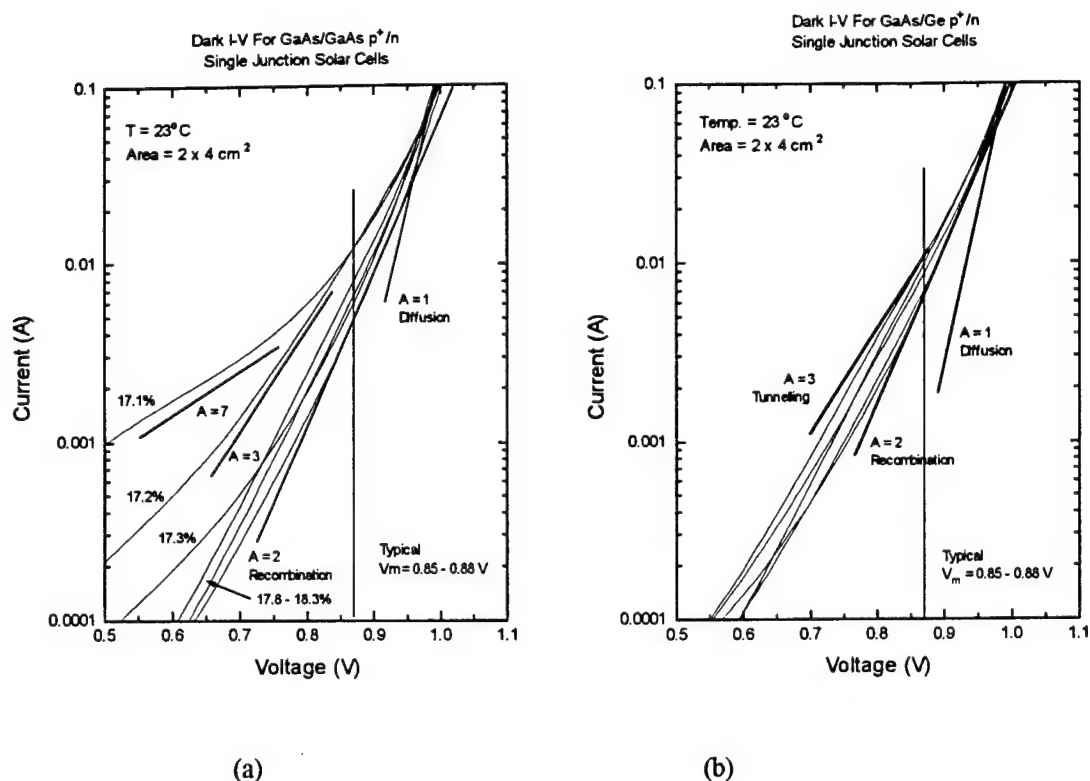
Figure 2. Dark current transport mechanisms



In order to simplify our measurements and the above model, dark current I-V curves were first generated for single-junction GaAs/GaAs and GaAs/Ge cells. The cells were prepared for an earlier ManTech program and share similar design features to that of the triple-junction solar cells.

As demonstrated in Fig. 3, the slope of I-V curves of both single junction GaAs/GaAs and GaAs/Ge cells have ideality factors of $A = 2$ at the maximum power point voltage ($V_m = 0.85$ - 0.88). This indicates that recombination is the dominant mechanism for cells of $\sim 17.8\%$ efficiency. Diffusion takes over at higher voltages. A few examples of lower efficiency cells are also shown (Fig. 3a) where defects are beginning to produce tunneling currents.

Figure 3. Dark I-V for single junction solar cells



Numerous dual, 2 ¹/₂, and triple-junction GaInP₂/GaAs/Ge cells were also examined. Analysis of the dark I-V curves is not as straightforward for the multi-junction cells as it is for the single-junction, but initial calculations suggest that tunneling is not occurring in the former nor the latter. Rather, dark currents are controlled by recombination for all four cell types at their maximum power points.

Conclusion

The absence of tunneling currents in the high efficiency GaInP₂/GaAs/Ge cells shows that the process for depositing the semiconductor films is well developed with a minimum of crystal lattice defects. The presence of physical scratches on high and low performing samples raises a concern for more delicate handling of the cells during processing. However, a small scratch alone isn't enough to dramatically lower the efficiency of the solar cells and crystal defects may well play a role in decreasing the

performance of some of the poorer cells. Deposition conditions must be carefully controlled and monitored to improve the overall yield of high quality triple-junction cells and lower the cost of this exceptional new device.

References

- ¹ J. M. Olson, S. R. Kurtz, A. E. Kibbler, and P. Fain, *Appl. Phys. Lett* **56**, 623 (1990)
- ² M. Wolf, G. T. Noel, and R. J. Stirn, *IEEE Trans. Electron Device* **24**, 419 (1977)
- ³ B. B. Rao, S. Banerjee, W. A. Anderson, and M. K. Han, *IEEE Trans. Electron Device* **32**, 817 (1985)
- ⁴ P. D. DeMoulin, S. P. Tobin, M.S. Lundstrom, M. S. Carpenter, and M. R. Melloch, *IEEE Electron Device Lett.* **9**, 368 (1988)
- ⁵ P. D. DeMoulin, C. S. Kyono, M. S. Lundstrom, and M. R. Melloch, *Proceedings of the 19th IEEE Photovoltaics Specialists Conference* (IEEE, New York, 1987), p. 93
- ⁶ K. C. Reinhardt, Y. K. Yeo and R. L. Hengehold, *J. Appl. Phys.* **77**, No. 11 (1995)
- ⁷ K. C. Reinhardt, Y. K. Yeo, P. H. Ostdiek and R. L. Hengehold, *J. Appl. Phys.* **81**, No. 8 (1997)
- ⁸ Capt. D. N. Keener, D. Marvin, D. J. Brinker, H. B. Curtis, *Proceedings of the XV SPRAT Conference*, June 1997
- ⁹ K. Uchida, T. Arai, K. Matsumoto, *J. Appl. Phys.* **81**, No. 2 (1997) 771
- ¹⁰ S. M. Sze, *Physics of Semiconductor Devices*, 2nd ed. (Wiley, New York, 1981) 358
- ¹¹ C. T. Sah, R. N. Noyce, and W. Shockley, *Proc. IRE* **45**, 1228 (1957)
- ¹² S. C. Choo, *Solid-State Electron* **11**, 1069 (1968)
- ¹³ H. J. Hovel, *Semiconductors and Semimetals*, ed. R. K. Willardson and A. C. Bear (Academic, New York, 1975) vol. 11
- ¹⁴ A. R. Riben and D. L. Feucht, *Solid-State Electron* **9**, 1055 (1966)

**THE CHARACTERIZATION OF HIGH PERFORMANCE QUANTUM WELL INFRARED
PHOTODETECTORS FOR LOW BACKGROUND OPERATION**

**Jerome T. Chu
Ph.D. Candidate
Department of Electrical and Computer Engineering**

**University of Florida
588 New Engineering Building
Gainesville, FL 32611**

**Final Report for:
Graduate Student Research Program
Phillips Laboratory**

**Sponsored by:
Air Force Office of Scientific Research
Bolling Air Force Base, DC**

and

**Phillips Laboratory
Kirtland Air Force Base, NM**

September 1997

THE CHARACTERIZATION OF HIGH PERFORMANCE QUANTUM WELL INFRARED PHOTODETECTORS FOR LOW BACKGROUND OPERATION

Jerome T. Chu
Ph.D. Candidate
Department of Electrical and Computer Engineering
University of Florida

Abstract

The design and characterization of a number of quantum well infrared photodetectors (QWIPs) was carried out. The devices studied over the course of the summer program include: (1) a compressively strained p-type superlattice (SL-) QWIP with a spectral responsivity peak at 19.2 μm with a corresponding cut-off wavelength of greater than 20 μm , (2) a truly voltage tunable unstrained SL-QWIP with a spectral responsivity peak at either 9.2 or 6.5 μm and (3) an InP based QWIP with tensile strain (TS-) layers that responds at 4.4 μm and 6.5 μm as a function of applied bias. All of these devices were grown by molecular beam epitaxy on GaAs, except for the InP based TS-QWIP. The exact performance in terms of dark current, background photocurrent, noise, responsivity, detectivity and quantum efficiency gain product will be discussed in this report.

THE CHARACTERIZATION OF HIGH PERFORMANCE QUANTUM WELL INFRARED PHOTODETECTORS FOR LOW BACKGROUND OPERATION

Jerome T. Chu

Introduction

With the proliferation of molecular beam epitaxy (MBE) technologies, device structures that use heterostructures or quantum wells have been extensively investigated in the last few decades. N-type quantum well infrared photodetectors (QWIPs) grown by MBE have been intensively studied in recent years [1,2,3]. These devices use either the GaAs/AlGaAs/InGaAs or the InP/InGaAs/InAlAs material systems for detection in the 3-5 μm mid-wavelength infrared (MWIR) or 8-14 μm long-wavelength infrared (LWIR) atmospheric transmission windows. Since n-type GaAs/AlGaAs/InGaAs and InP/InGaAs/InAlAs QWIPs have inherently low electron effective masses and high electron mobilities, they offer excellent infrared (IR) detection properties. But, because the quantum mechanical selection rules prohibit normal incidence intersubband absorption, focal plane arrays (FPAs) using n-type QWIPs must use either metal or dielectric gratings to couple normal incidence IR radiation into the quantum well [2,4,5]. In contrast, because of the mixing between the light and heavy hole states under either biaxial tension or compressive strain, normal incidence illumination is absorbed for the intersubband transition in p-type QWIPs; thus eliminating the need for metal or dielectric grating couplers and simplifying the design of p-type QWIPs.

Device Processing

In order to electrically and optically characterize these devices, a wet chemical etch of 8:1:1 $\text{H}_2\text{O}:\text{H}_2\text{O}_2:\text{H}_3\text{PO}_4$ was used to fabricate $216 \times 216 \mu\text{m}^2$ mesas. Then, Cr/Au (100 \AA /1500 \AA)

was deposited on top of and around the mesas to form the top and bottom ohmic contacts, respectively. Since these devices respond to normal incidence radiation, except for the n-type broadband QWIP, a ring contact around the mesa edge was used to allow light to pass through to most of the mesa top surface, which simplifies the processing requirements while still maintaining a 75% fill factor. For the n-type broadband QWIP, a 45° edge was polished on the substrate for illumination. The chips were then bonded onto 68 pin chip carriers and wired to the contact pads via ultrasonic wedge bonding. For cryogenic testing, the chips were mounted into open cycle dewars which were capable of being mounted with KRS-5 windows and a variety of apertures to limit the field of view (FOV) from 40° to 0°.

Device Characterization

For the measurement of the responsivity, a blackbody source at 1243 K is used as the light source into a ¼ m Oriel MS257 monochrometer with various grating and filters to allow testing from 3-21 µm. The device under test (DUT) is held at cryogenic temperatures by an open cycle dewar using liquid helium as the coolant. The output from the DUT is then amplified by a Keithley 428 transimpedance amplifier with a variable gain, after which the output is sent to an Oriel Merlin DSP lock-in amplifier. The output from the DUT is normalized against a reference sensor (an Oriel 70129 pyroelectric detector) to determine the relative photoresponsivity. Then, the output of the detector at a specific chopped frequency was analyzed with a Stanford Research 770 FFT network analyzer to determine the integrated optical response. For this measurement, the field of view was limited to 1.78° and the chopped blackbody source was set at 800 K. Using the same experimental setup, but without the chopped blackbody source, we were also able to measure the noise of the device at various temperatures under a limited field of view (1.78°) with a 295 K background. The dark current was measured with the devices in the open cycle dewars with a

Keithley 236 source measure unit sensitive to about 10 femtoamps, while the background photocurrent was measured using the same Keithley 236, while maintaining a 1.78° FOV.

19.2 μm p-type Superlattice Quantum Well Infrared Photodetector

Little research has focused on the wavelengths longer than 12 to 14 μm , since detectors that operate in the very long-wavelength infrared (VLWIR) band would have very strict cooling requirements and for terrestrial environments, the lack of a transmission window through the atmosphere and the relatively low flux of photons would diminish resolution and range. But for space-based platforms, the cooling requirements are easily met and the lack of atmospheric absorption gives an opportunity to observe VLWIR photons without serious attenuation. Levine, *et al.*, designed and characterized a simple bound-to-continuum n-QWIP [6] with a detection peak at 16.6 μm and a cut-off wavelength of 19 μm . We have designed a novel p-type QWIP which exhibits normal incidence response that utilizes four closely spaced $\text{In}_x\text{Ga}_{1-x}\text{As}$ quantum wells in series separated by very thin $\text{Al}_y\text{Ga}_{1-y}\text{As}$ barriers (a superlattice) to effectively create a large absorption thickness while maximizing the oscillator strength by using the ground heavy hole (HH1) to first excited heavy hole (HH2) intersubband transition, in contrast with current p-type QWIPs which utilize the HH1 to HH3 intersubband transition for optical absorption [10]. These superlattice (SL) layers are then separated by thick GaAs barriers to minimize the tunneling current which dominates the dark current at sub-liquid nitrogen temperatures.

Originally, the SL-QWIP was designed to exhibit a peak photoresponse in the 8-14 μm LWIR band, but because of strain relaxation [7] in the thin superlattice layers between the $\text{In}_x\text{Ga}_{1-x}\text{As}$ and the $\text{Al}_y\text{Ga}_{1-y}\text{As}$, the effective barrier height and the corresponding energy gap between the HH1 and HH2 states was reduced from 120 meV to 65 meV, which shifted the response peak to a predicted value of 18 μm . The calculated transmission coefficient for the SL-QWIP with

compressive strain relaxation is shown in Fig. 1. When comparing the experimental results and the theoretical prediction of the transfer matrix method (TMM) [8] for the relaxed case, we see very good agreement and an error of only 5 meV. Shown in the inset of figure 1 is the idealized band diagram for the SL-QWIP.

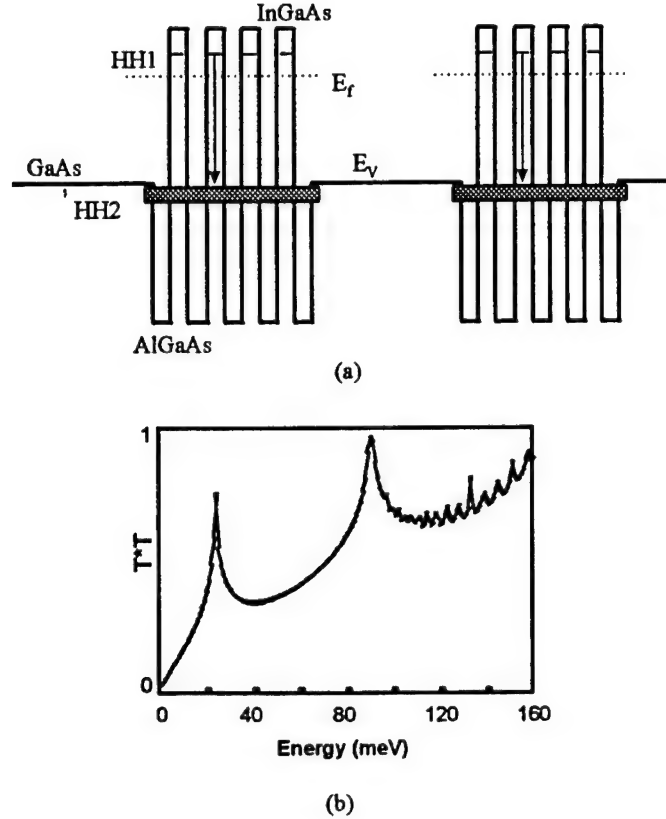


Figure 1. The (a) idealized band diagram and (b) calculated transmission coefficient from TMM.

Figure 2 shows the responsivity of the p-type SL-QWIP as a function of incident radiation wavelength and device temperature for $V_b = 20$ mV under high flux illumination under a FOV=1.78°. The FWHM spectral bandwidth of the 19.2 μm VLWIR peak is $\Delta\lambda/\lambda_p=12\%$. This narrow spectral bandwidth is in excellent agreement with the value predicted by the TMM calculation, since the FWHM energy spread of the VLWIR peak is only 8 meV (see figure 1). At $T=40$ K and $V_b=20$ mV, the peak absolute photoresponse at $\lambda_p=19.2$ μm was found to be $R_A=49.8$

mA/W. From this responsivity, the quantum efficiency gain product (ηg) was determined to be 0.325%. The variation of peak absolute responsivity as a function of bias and operating temperature is shown in figure 3. The decrease in the responsivity as the applied bias reaches the 50 mV point has been attributed to the breakdown of the resonance between the bound HH2 states, which results in the photoexcited heavy holes having a much lower probability of tunneling out of the SL quantum wells and registering as photocurrent. In figure 3, note that at 0 V bias there is a significant photoresponse of 32.5 mA/W at T=40 K, denoting photovoltaic (PV) operation. This mode of operation has been attributed to the large oscillator strength of the HH1 to HH2 intervalence band optical transition. Note that all of the photoresponse measurements did not take into account the 75% fill factor of these DUTs. Therefore, slightly higher (33% higher) responsivities would be expected for backside illuminated devices.

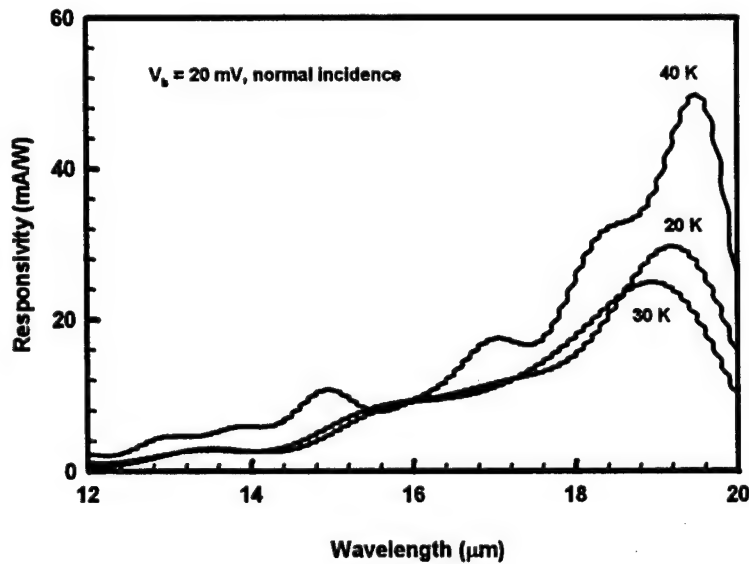


Figure 2. Absolute responsivity as a function of detector temperature at $V_b=20$ mV.

Figure 4 shows the measured dark current as a function of temperature and applied bias for the p-type SL-QWIP. Overlaid on top of the dark I-V curves is the FOV limited (1.78°)

background photocurrent. This shows that the device is under background limited performance (BLIP) operation at $T=40$ K or lower under a narrow field of view. The slight asymmetry in the dark current can be attributed to band bending as an effect of dopant migration [11], since the mobile p-type dopant beryllium was used in the quantum well layers.

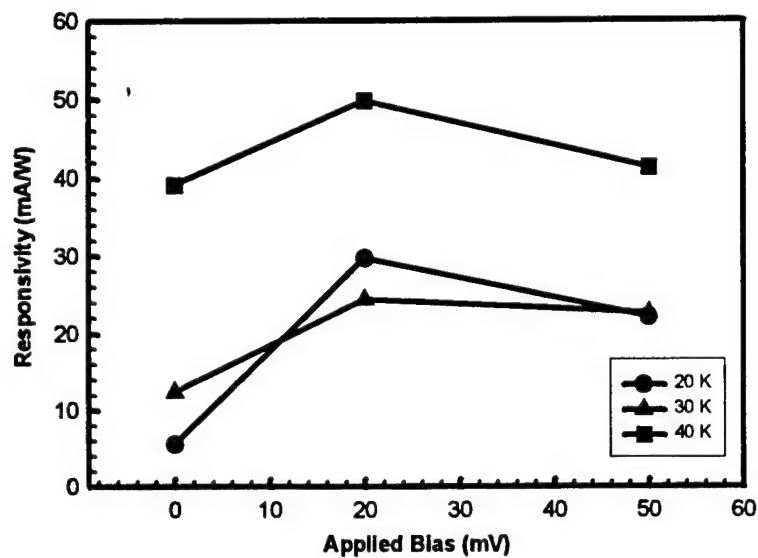


Figure 3. Responsivity as a function of applied bias and device temperature.

Table 1 illustrates the variation of the responsivity, noise, quantum efficiency gain product and measured detectivity as a function of applied bias and device operating temperature. Note the rapid increase of responsivity as the device temperature is increased. The increase of responsivity from 0 to 20 mV has been attributed to the cancellation of the built-in field caused by dopant migration during layer growth [11] and the resonant lining up of the HH2 states to form a miniband. The decrease in the responsivity as the bias is increased from 20 to 50 mV is attributed to the breakdown of the resonant miniband formed by the combination of the superlattice quantum wells, which causes the tunneling probability of the carriers through the thin superlattice barriers to

dramatically decrease. Note that these two trends are consistent throughout at each temperature from 20 to 40 K, and that the noise current and ηg product also follow the same trend. It has been postulated that the decrease in the ηg product as the temperature declines could be due to a reduction of the quantum efficiency at very low temperatures ($T \leq 30$ K) due to carrier freeze out. Further study of this phenomenon should be conducted. The calculated detectivity as a function of bias and device temperature is also shown in table 1.

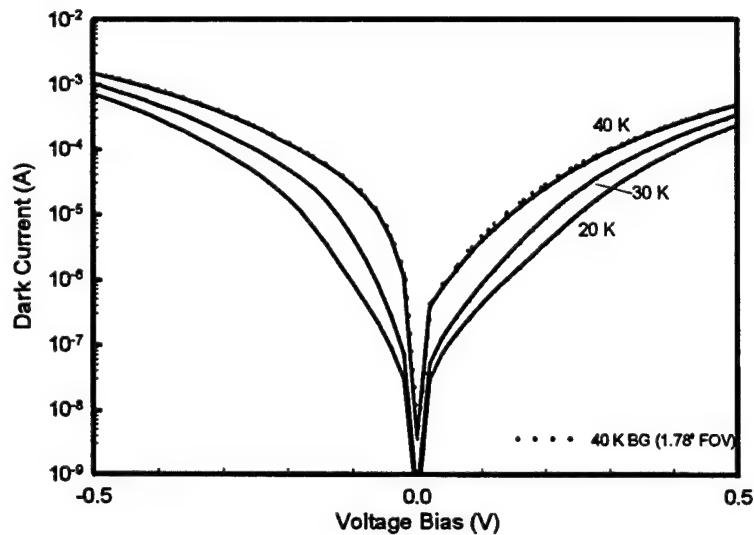


Figure 4. The dark I-V characteristic of the p-type QWIP as a function of applied bias and device temperature. The 40 K background photocurrent (FOV=1.78°) is superimposed on the figure.

We have demonstrated a novel p-type QWIP which has normal incidence response in the VLWIR band. Operation at up to 40 K is obtained for a variety of biases in the photoconductive (PC) mode and PV mode. An absolute responsivity of 49.8 mA/W and an $\eta g = 0.325\%$ was achieved at $T = 40$ K under 20 mV of bias with FWHM spectral bandwidth of $\Delta\lambda/\lambda_p = 12\%$. This SL-QWIP was under BLIP operation at $T = 40$ K for a 1.78° field of view for the biases tested. Further refinements can be made to this structure to tailor the peak responsivity wavelength and

FWHM spectral bandwidths by altering the layer composition and material thicknesses. In addition, we can use slightly strained quantum well layers (indium concentrations of up to about 6-7%) to reduce the effective mass of the ground heavy hole states [9], increasing heavy hole mobility, which increases intersubband absorption and improves transport characteristics. The results of this study are being prepared for publication and will be presented at the 1997 ECS conference in Paris, France in September.

Temp. & Bias	R_A (mA/W)	I_{dark} (A/Hz ^{1/2})	ηg (%)	D^* (cm-Hz ^{1/2} /W)
20 K				
0 V	5.6	1.36×10^{-11}	0.035	8.86×10^6
20 mV	29.7	2.47×10^{-11}	0.192	2.58×10^7
50 mV	22.1	2.51×10^{-11}	0.142	1.90×10^7
30 K				
0 V	12.4	3.46×10^{-11}	0.079	7.78×10^6
20 mV	24.4	3.89×10^{-11}	0.157	1.33×10^7
50 mV	22.6	4.03×10^{-11}	0.142	1.20×10^7
40 K				
0 V	39.1	3.96×10^{-11}	0.249	2.13×10^7
20 mV	49.8	5.83×10^{-11}	0.317	1.84×10^7
50 mV	41.3	6.90×10^{-11}	0.263	1.29×10^7

Table 1. Summary of the VLWIR p-QWIP optical, gain and noise.

Truly Voltage Tunable p-type Superlattice QWIP

Since the inception of the quantum well infrared photodetector (QWIP), various methods have been used to increase the flexibility of this simple device. Among these have been the use of stacks of different QWIP layers to increase the number of wavelengths or wavebands which the pixel is sensitive [12-14] or a voltage tuning scheme which shifts the detection peak around in a single waveband as a function of applied bias [15,16]. We have designed and characterized a novel p-type superlattice quantum well infrared photodetector (SL-QWIP) which maximizes the flexibility of the QWIP design by exhibiting normal incidence detection and true voltage tuning,

where the changing applied bias changes the detection peak by allowing one peak and suppressing another. Uses for such devices range from single pixel two color imaging to two color temperature resolution.

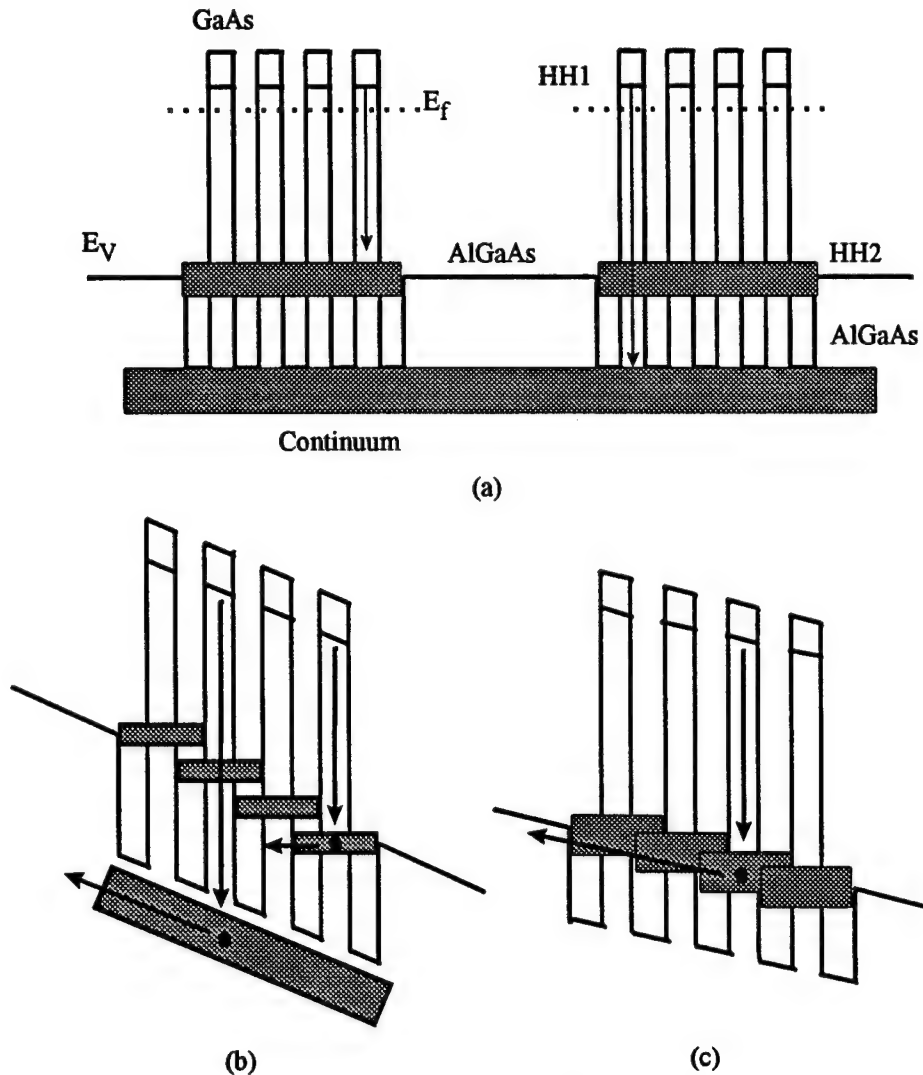


Figure 5. (a) Schematic band diagram of the SL-QWIP, (b) the transport mechanism at high fields and (c) at moderate fields.

Because of the quantum mechanical selection rules, p-QWIPs are allowed normal incidence detection. Because of this, p-QWIPs are simpler to design and fabricate since complex dielectric or metallic grating structures are not necessary. This SL-QWIP was designed with GaAs (3.0 nm) quantum wells and $\text{Al}_{0.4}\text{Ga}_{0.6}\text{As}$ (3.5 nm) superlattice barriers, as seen schematically in

figure 5(a). The thick (50 nm) barriers separating the sets of four GaAs quantum wells are also grown with $\text{Al}_{0.3}\text{Ga}_{0.7}\text{As}$. Figures 5(b) and 5(c) illustrate the two intersubband transitions and how the applied bias is used to tune the detection peak. Note that the $9.2\text{ }\mu\text{m}$ peak can be seen only when the superlattice miniband is resonantly lined up at moderate biases, while at higher applied biases, the breakdown of the miniband resonance limited the detection at this peak. From the transfer matrix method, we calculated two responsivity peaks at 9.6 and $6.4\text{ }\mu\text{m}$, which is in excellent agreement with the measured results.

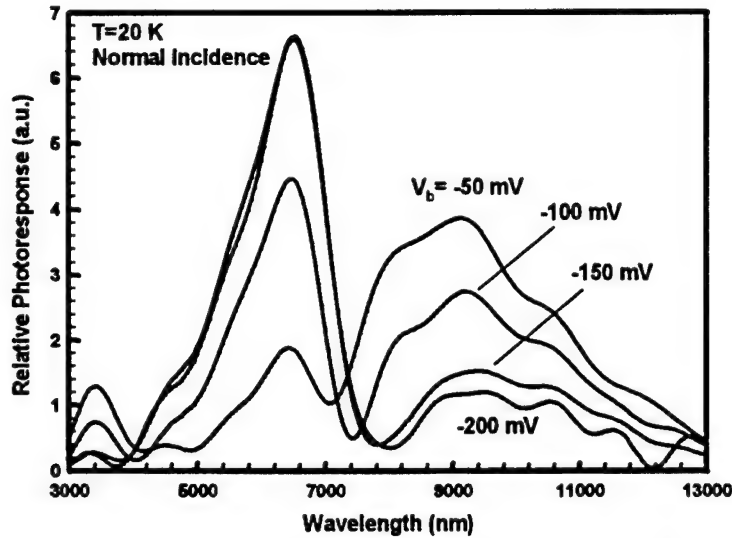


Figure 6. Relative photoresponse of the unstrained SL-QWIP as a function of applied bias at $T=20\text{ K}$.

Figure 6 shows the responsivity of the p-type SL-QWIP as a function of incident radiation wavelength and negative applied bias. As the bias is increased from 0 to -50 mV , the response of the LWIR peak ($9.3\text{ }\mu\text{m}$) rapidly increases, while the $6.5\text{ }\mu\text{m}$ peak is effectively suppressed. As the bias is increased to -100 mV and greater, the superlattice miniband on which the photoexcited LWIR hole transport depends, loses resonance which causes the loss of responsivity for the $9.2\text{ }\mu\text{m}$

peak. This effect gives rise to the voltage tuning capability of this QWIP structure. Note that at these higher applied biases, the 6.5 μm peak dominates and saturates at $V_b \leq -200$ mV with a maximum absolute responsivity of 6 mA/W. The lack of LWIR photoresponse in the positive bias regime can be attributed to the built-in field in the superlattice region arising from dopant migration [11], which causes the breakdown of the miniband resonance when positive bias is applied and can be seen in figure 7.

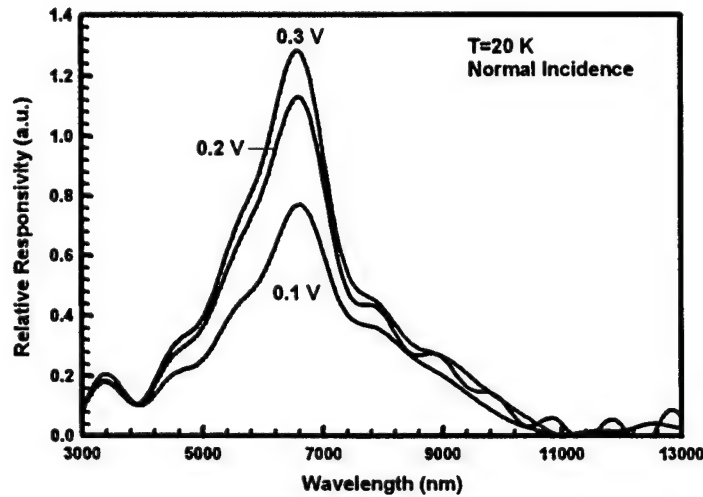


Figure 7. Forward bias photoresponse for the unstrained SL-QWIP at $T=20$ K.

Figure 8 shows the measured dark current as a function of temperature and applied bias for the p-type SL-QWIP. Overlaid on top of the dark I-V curves is the FOV limited (1.78°) background photocurrent. This shows that the device is under background limited performance (BLIP) operation at $T=35$ K or lower under this narrow field of view for a broad range of applied bias. The slight asymmetry in the dark current can be attributed to band bending as an effect of dopant migration [11], since the mobile p-type dopant beryllium was used in the quantum well layers.

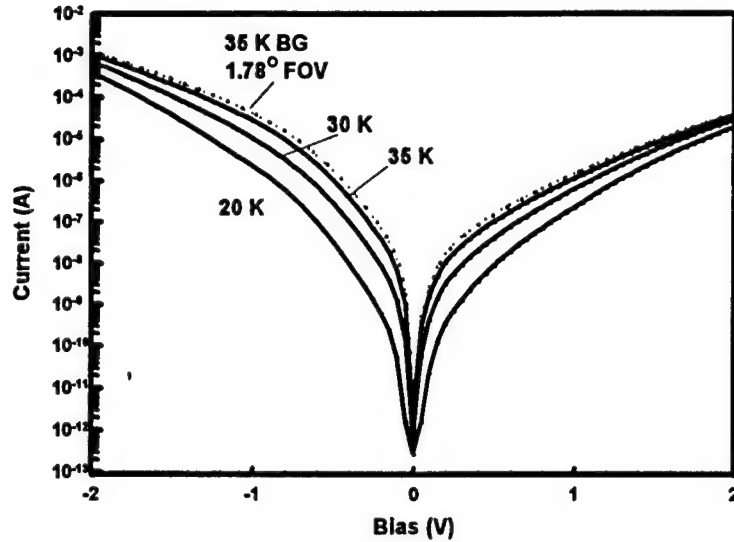


Figure 8. Dark current as a function of temperature with the 300 K background photocurrent superimposed (1.78° FOV).

We have designed and characterized a new normal incidence p-type quantum well infrared photodetector (QWIP) which exhibits two distinct spectral responsivity peaks at 6.5 and 9.2 μm . The FWHM bandwidth of each peak is $\Delta\lambda/\lambda_p=28\%$ and 39% respectively. This unstrained p-QWIP is capable of BLIP operation at up to 35 K under the proper operating bias. Further improvements can be made in terms of increasing responsivity by introducing compressive strain in the absorbing layers by adding indium into the GaAs layers [9] and by shortening the detection wavelength of the bound-to-continuum peak by means of increasing the superlattice barrier height, which also should lower the effective dark current by decreasing the tunneling probability through the superlattice slightly. The results of this study are being prepared for publication.

Tensile Strained p-type Quantum Well Infrared Photodetector

Efforts have been made in recent years to use materials other than the familiar GaAs/AlGaAs/InGaAs system to fabricate quantum well infrared photodetectors. Examples are GaAs/GaInP [17], GaAs/GaInAsP [18] and GaSb/AlSb [20]. But very few attempts have been

made to use tensile strain in the quantum wells to enhance the photoresponse [19], especially in III-V material systems. The inducement to use the InGaAs/InAlAs/InP system is due to the potential of the tensile strained p-type material. For the p-doped quantum wells, the ground state under tensile strain is the lowest light hole state, which exhibits an effective mass similar to that of electrons. Since the absorption coefficient is inversely proportional to the effective mass, the absorption and responsivity should increase with decreasing effective mass.

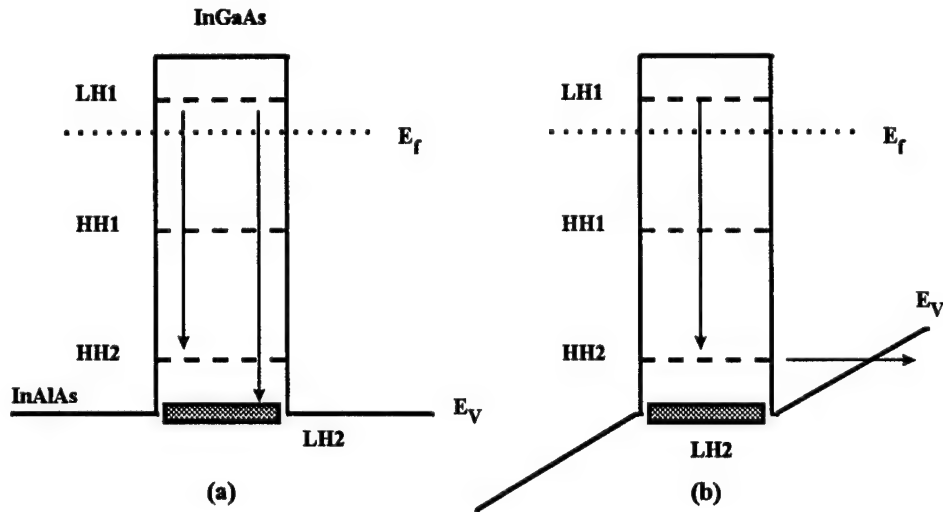


Figure 9. (a) the schematic energy band diagram for the TS-QWIP and (b) the bound-to-bound intersubband transition ($6.5 \mu\text{m}$).

The TS-QWIP consists of 20 periods of $\text{In}_{0.4}\text{Ga}_{0.6}\text{As}$ (7.0 nm) quantum wells separated by 50 nm thick $\text{In}_{0.52}\text{Al}_{0.48}\text{As}$ barriers and are p-doped to $3 \times 10^{18} \text{ cm}^{-3}$. The schematic band diagram is shown in figure 9(a), which illustrates the two essential intersubband transitions for each detection peak.

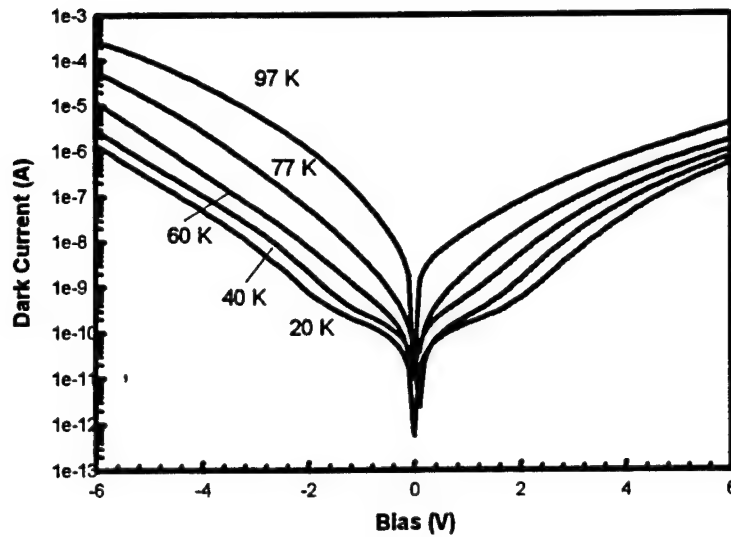


Figure 10. The dark current as a function of bias and temperature for the TS-QWIP.

Shown in figure 10 is the dark current of the p-type tensile strained QWIP (TS-QWIP). The asymmetrical dark current can be attributed to dopant migration during layer growth. As seen by the slight increase between the 20 and 60 K dark currents, it seems that the dark current is mainly due to tunneling or thermally assisted tunneling at under temperatures 60 K.

Shown in figure 11 is the responsivity of the p-type TS-QWIP. Note the two color response of this device at high applied biases. This has been tentatively attributed to the close spacing of the HH2 and LH2 energy levels near the barrier edge (see figure 9). Since the LH1 to LH2 transition is a bound-to-continuum transition, the 4.4 μm peak is visible under all applied biases. Note that the LH1 (ground state) to HH2 transition at 6.5 μm is strong only when the applied bias is large (greater than 2 V), due to the bound-to-bound nature of this transition, as seen in figure 9(b).

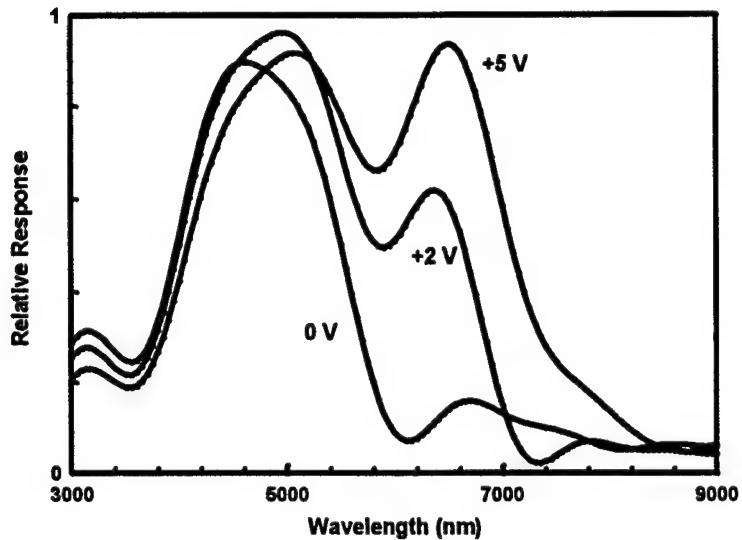


Figure 11. The relative photoresponse of the TS-QWIP as a function of bias at $T=20$ K with a 40 degree field of view.

Work in Progress and Future Work

We are currently exploring the usefulness of the QWIP technology as applied to broadband detectors and as the base absorbing region in a heterojunction phototransistor. The broadband (BB-) QWIP seems very promising after some preliminary measurements with low dark current and a large optical response at $T=77$ K. The QWIP phototransistor theoretically has the ability to provide very high performance at liquid nitrogen temperatures, given that this device structure can exhibit optical gain along with suppressed dark current.

Other structures to be tested in the future are the p-type broadband QWIPs and further refinements in the heterojunction phototransistor once the proof-of-concept device has been fully characterized. All of these devices will be characterized through a wide range in temperatures and at various photon backgrounds.

Acknowledgments

I wish to thank AFOSR for the opportunity to perform this research this summer at Phillips Lab (PL) at Kirtland AFB, NM. I would also like to thank Drs. Anjali Singh and David Cardimona for their support and helpful discussions throughout my assignment at PL, and Jon Syverson and Ryan Sharp for helping me with setting up and running my experiments.

REFERENCES

1. B. F. Levine, R. J. Malik, J. Walker, K. K. Choi, C. G. Bethea, D. A. Kleinman and J. M. Vandenberg, *Appl. Phys. Lett.* **50**, 273 (1987).
2. L. S. Yu and S. S. Li, *Appl. Phys. Lett.* **59**, 1332 (1991).
3. B. F. Levine, *J. Appl. Phys.* **74**, R1 (1993).
4. G. Hasnain, B. F. Levine, C. G. Bethea, R. A. Logan, J. Walker and R. J. Malik, *Appl. Phys. Lett.* **54**, 2515 (1989).
5. J. Y. Andersson and L. Lundqvist, *J. Appl. Phys.* **71**, 3600 (1992).
6. B. F. Levine, A. Zussman, J. M. Kuo and J. deJong, *J. Appl. Phys.* **71**(10), 5130 (1992).
7. J. W. Matthews and A. E. Blakeslee, *J. Cryst. Growth* **27**, 188 (1974) **29**, 273 (1975) **32**, 265 (1976).
8. A. K. Ghatak, K. Thyagarajan and M. R. Shenoy, *IEEE J. Quantum Electron.* **24**, 1524 (1988).
9. K. Hirose, T. Mizutani and K. Nishi, *J. Cryst. Growth* **81**, 130 (1987).
10. Y. H. Wang, S. S. Li, J. Chu and Pin Ho, *J. Appl. Phys.* **76**(10), 6009 (1994).
11. H. C. Liu, Z. R. Wasilewski and M. Buchanan, *Appl. Phys. Lett.* **63**, 761 (1993).
12. Y. H. Wang, J. C. Chiang, S. S. Li and P. Ho, *J. Appl. Phys.* **76**(4), 2538 (1994).
13. J. Chu, S. S. Li and P. Ho, *J. Cryst. Growth* **175/176**, 964 (1997).
14. M. Z. Tidrow, J. C. Chiang, S. S. Li and K. Bacher, *Appl. Phys. Lett.* **70**(7), 859 (1997).
15. J. C. Chiang, S. S. Li, M. Z. Tidrow, P. Ho, M. Tsai and C. P. Lee, *Appl. Phys. Lett.* **69**(16), 2412 (1996).
16. L. C. Lenchyshyn, H. C. Liu, M. Buchanan and Z. R. Wasilewski, *J. Appl. Phys.* **79**(10), 8091 (1996).
17. C. Jelen, S. Slivken, J. Hoff, M. Razeghi and G. J. Brown, *Appl. Phys. Lett.* **70**(3), 360 (1997).
18. J. Hoff, S. Kim, M. Erdtmann, R. Williams, J. Piotrowski, E. Bigan, M. Razeghi and G. J. Brown, *Appl. Phys. Lett.* **67**(1), 22 (1995).
19. Y. H. Wang, S. S. Li, J. Chu and P. Ho, *Appl. Phys. Lett.* **64**(6), 727 (1994).
20. B. Brar, L. Samoska, H. Kroemer and J. H. English, *J. Vac. Sci. & Tech. B* **12**(2), 1242 (1994).

SIMULATION AND MODELING OF
NANOELECTRONIC MATERIALS

T. Sean Elicker
Research Assistant/Graduate Student
Department of Electrical Engineering

University of North Carolina at Charlotte
9201 University City Boulevard
Charlotte, NC 28223-0001

Final Report for:
Graduate Student Research Program
Phillips Laboratory

Sponsored by:
Air Force Office of Scientific Research
Bolling Air Force Base, DC

and

Phillips Laboratory, Kirtland AFB

August 1997

SIMULATION AND MODELING OF NANOELECTRONIC MATERIALS

T. Sean Elicker
Research Assistant/Graduate Student
Department of Electrical Engineering
University of North Carolina at Charlotte

Abstract

We designed and developed two computational tools for use in the study of radiation effects in nanoelectronic materials and devices. The first of these tools was a non-orthogonal tight-binding molecular dynamics code. A basic shell was completed, onto which specific modifications will be added to increase applicability to irregular cluster geometries. Both the shell and future modifications are being designed to maximize data parallelism, and we are using a recently-published algorithm that results in $O(N)$ scaling. The second tool is a code for modeling self-organization/self-assembly in nanoelectronic materials. This code uses ideas from the modeling of molecular assembly in biology and polymer chemistry--independent, interacting agents, interactions governed by effective parameters. In our case, these interaction parameters will be determined by small-scale, highly accurate quantum-chemical data.

SIMULATION AND MODELING OF NANOELECTRONIC MATERIALS

T. Sean Elicker

Introduction

Reduction of device size has always been a concern of the electronics industry. Currently, electronics fabrication is poised to leave the realm of "microelectronics" and enter the realms of "nanoelectronics." This new size regime consists of two distinct areas: one is the extension of conventional lithographic techniques to allow design rules of 0.1 microns--100 nanometers--or less[1]; the other area is often referred to as "molecular electronics," and deals with novel device architectures that make use of zeolites, fullerenes, and other supramolecular structures[2].

My work this summer focused on the issues of simulation and modeling in nanoelectronics research. The nature of the field--combined with recent advances in computing machinery--has presented some unique challenges.

Computer models have a well-defined role in microelectronics research, and this role consists of several standard methodologies. Atomistic modeling used either finite clusters of atoms or periodic systems such as crystals to provide insight into electronic structure. Device modeling was on a much larger scale, employing empirically-determined parameters and dealing with bulk-level behavior. Both of these approaches have proved to be quite successful in determining properties of microelectronics. Moving into the nanometer regime introduces complications, primarily due to size- and morphology-dependent properties[3]. Nanoelectronic devices constructed of familiar materials such as silicon[4] and gallium arsenide[5] can display properties that are not seen in bulk devices of the same composition; these properties are often coupled very strongly to the size and shape of the structures involved. Furthermore, control of physical parameters of fabricated devices is statistical in nature, and the amount of direct control continues to shrink with device size. Thus, creation of actual prototypes for material/device characterization is becoming more expensive and less reliable as the size of the devices shrinks--and the nanoelectronics industry of tomorrow will have a need for robust and accurate computer simulation tools, even moreso than the microelectronics industry of today.

Another important issue is the advent, over the last decade, of massively parallel

processing(MPP). There are many demonstrations of how the computing power of linked groups of smaller processors can rival--even outperform, in certain instances--traditional, large-scale serial (and even vector) supercomputers such as the Cray Y-MP. The flexibility and reduced maintenance of these parallel networks make them appealing for use in future research, and it is therefore important to develop software that fully exploits the advantages of parallel computing. While many types of modeling(artificial life, cellular automata, etc.) have an inherent, data-level parallelism that makes them ideal for implementation on MPP platforms[6], the non-local nature of Hartree-Fock calculations may ultimately limit the degree to which such codes can be parallelized.

My goal for this internship was to identify fertile areas for new simulation tools, and to construct such tools with the aforementioned issues in mind: the codes should be specifically designed to address the specific difficulties of nanoelectronic materials modeling, and the completed programs should be capable of fully exploiting MPP systems. I made progress on two different programming projects in the course of the summer: a non-orthogonal, tight-binding molecular dynamics code, and a mesoscopic simulator that uses effective interaction parameters based on quantum-chemical data.

Results and Discussion, Pt. 1

As previously mentioned, finite-cluster methods are often ineffective in nanoelectronic modeling, due to the effects of high-level order and mesoscopic geometry. This limits the usefulness of ab initio electronic-structure calculations, since most nanostructures contain hundreds, even thousands, of atoms. The implementation of less accurate large-scale models involving pseudopotentials, effective parameters, etc. is therefore a viable option[7]; the recovery of size-related "emergent" effects offsets somewhat the inherent lack of accuracy.

My choice to work on a tight-binding molecular dynamics(TBMD) code was due primarily to recent advances concerning adaptation of TBMD to parallel hardware[8]. Newly-developed algorithms allow these programs' computational needs to scale linearly with the size of the system[9]. This $O(N)$ scaling--compared to the $O(N^3)$ or $O(N^4)$ for other electronic-structure codes--makes tight-binding a perfect example of a model that fully exploits MPP to permit atomic-scale modeling of nanostructures.

Conventional tight-binding theory was designed for the study of periodic systems, and the universal parameters(of Harrison[10], e.g.) are generally inapplicable to aperiodic

structures. While some nanostructures are regular pseudo-crystalline arrays with large clusters as unit cells, this inapplicability was a problem which I took several steps to circumvent. The underlying model for my code is the nonorthogonal TBMD of Menon and Subbaswamy[11], which has shown greater portability to isolated clusters. The basic shell for this code was written this summer, and two additional modifications are in the pseudo-code stage of development: self-consistency[12], and the "environmental dependence"[13] of Tang et. al. The former reduces errors due to charge transfer, while the latter employs a type of screening parameter to further improve portability to clusters.

When completed, this code will provide electronic structure data on nanostructures that comes out of a complex system of interacting atoms, so that emergent properties at all levels will be accessible. During the summer, a program shell was completed that performed all necessary data manipulation, and used matrix inversion to determine basic energy levels. Current work involves calculation of band structure for regular structures, and the aforementioned modifications.

Results and Discussion, Pt. 2

The idea for a mesoscopic simulation code was originally motivated by a collaboration with Josef Michl et. al., at the University of Colorado. I was attempting some ab initio calculations on certain components of their "molecular Tinkertoy" grid polymers[14]. Even small components required extensive computational resources simply to determine equilibrium geometries using a reasonably accurate model chemistry[15]; applying such methods to even subsections of an actual grid would be impossible. Moreover, my intent was to investigate the effects of defects(intrinsic and radiation-induced) on properties of the grid itself, and the mesoscopic configuration of the grid seemed as important as point defects in individual components. I began work on a code that was to be a compromise--a model based on accurate quantum-chemical data that focused on large-scale phenomena like self-organization, structural defects, and emergent order.

The resulting program represents each grid component--rods and connectors, usually--as a unique data object, or "agent," which contains spatial data for that component. These agents move in a two-dimensional milieu, interacting with the milieu and each other. The agent-agent interactions are governed by a set of effective parameters; it is these parameters that are determined by quantum-chemical calculations. For example, one fundamental

interaction in grid formation is the joining of two components by a chemical bond. Using an accurate model chemistry(ab initio with size-consistent correlation corrections), energies are found for the optimized geometries of a rod-connector complex; the sole parameter in the optimization is the intercomponent separation. These energies can be used--via the typical Boltzmann occupation argument--to determine probabilities of bond formation; a set of data points is fit to a function $P(d)$, a distance-dependent formation probability. At each time step of the simulation, the agents are compared pairwise, and if a rod and connector are close enough, there is a chance that the bond will form. This basic probability is further modified by relative motion and other factors.

These probabilities govern the combination of agents into larger complexes. The experimentalists are studying the feasibility of using solvents to create a reversible assembly process[16], so future versions of the simulator will include "dissociation probabilities" as well. If agents do combine, the resulting collective becomes a single "agent" in the simulation, with physical data adapted from that of its constituents. The simulation terminates when all components have combined into a single agent, which is the completed grid.

Although originally conceived as a way to simulate self-assembly in grid polymers, I plan to expand this program into a flexible tool with a broad range of applications. There is nothing in the simulation that specifies the scale, so that "agents" could be molecules, atoms, supramolecular complexes, or even device components. The milieu is currently flat and homogeneous, but will be modified to include phenomena such as electromagnetic fields and solvent distributions, which would manifest themselves via spatial dependence in the interaction parameters. At certain scales, external agents like solvent molecules and heavy ions will be agents themselves, interacting with the standard agent population to create localized defects.

This model bears draws inspiration from certain models in artificial life[17] and computational cognitive science[18]. Like them, it is naturally well-adapted for parallel implementation. With the computational resources we have available, the program will be capable of modeling systems with hundreds of agents; large populations should increase the model's capacity for representing large-scale, emergent phenomena.

Conclusion

The shift to nanoscale electronics will, combined with the advent of molecular electronic devices, bring about fundamental changes in device applications, as well as the area of electronic materials research. This "new frontier" demands new computational tools, and my summer's work was to identify problems amenable to novel simulation codes, and also to begin construction of those tools. A working shell was developed for the tight-binding code, and extensive pseudocoding brought the mesoscopic simulator to a point where coding can begin; due to their complexity, this summer was used to lay the groundwork for these two projects, and work continues on both.

References

- [1] H.L. Hartnagel, R. Richter, A. Grub, *Electronics and Communications Engineering Journal* **3**, 119(91).
- [2] R.M. Metzger and C.A. Panetta, in Molecular Electronic Devices, ed. by F.L. Carter, Dekker, New York, 1987.
- [3] Y. Wang and N. Herron, *Journal of Physical Chemistry* **95**, 525(1991); L.E. Brus, *Journal of Physical Chemistry* **90**, 2555(1986).
- [4] L. Brus, *Journal of Physical Chemistry* **98**, 3575(94).
- [5] H. Nakashima, M Takeuchi, D. Bimberg, *Physica B: Condensed Matter* **227**, 291(96).
- [6] C. Langton, Artificial Life: an overview, MIT Press, Cambridge, 1995.
- [7] Dr. Deborah Evans, private communication.
- [8] A. Canning, G. Galli, R. Car, *Computer Physics Communications* **94**, 89(1996); L. Colombo, W. Sawyer, *Materials Science and Engineering B* **37**, 228(1996).
- [9] X.-P. Li, R.W. Nunes, and D. Vanderbilt, *Physical Review(B)* **47**, 10891(1993).
- [10] W.A. Harrison, Electronic Structure and the Properties of Solids: The Physics of the Chemical Bond, Freeman, San Francisco, 1980.
- [11] P. Ordejon, D. Lebedenko, M. Menon, *Physical Review(B)* **50**, 5645(1994).
- [12] F. Lui, *Physical Review(B)* **52**, 10677(1995).
- [13] M.S. Tang, C.Z. Wang, C.T. Chan, K.M. Ho, *Physical Review(B)* **53**, 979(1996).
- [14] There are many articles on this topic; a good example is P. Kasynski, A.C. Friedli, J. Michl, *Journal of the American Chemical Society* **114**, 601(1992).
- [15] Dr. Henry Kurtz, private communication.
- [16] R.M. Harrison, T.F. Magnera, J. Vacek, J. Michl, "Towards Designer Solids: An Approach to Tinkertoy-like Molecular Grids and Scaffolds" submitted for publication.
- [17] See the TIERRA project by Ray in Artificial Life II: Proceedings on the Second Conference on Artificial Life, ed by C. Langton et al, Addison-Wesley Pub. Co., Reading, Mass., 1992.
- [18] D. Hofstadter and the Fluid Analogies Research Group, Fluid Concepts and Creative Analogies: Computer Models of the Fundamental Mechanisms of Thought, Basic Books, New York, 1995.

**A PRELIMINARY STUDY OF THE CAUSES OF SPRING-IN IN A
UNIDIRECTIONAL CARBON FIBER / EPOXY COMPOSITE**

**Jeff M Ganley
Graduate Research Assistant**

**University of New Mexico
Department of Civil Engineering
Albuquerque, NM 87131-1351**

**Final Report for:
Graduate Student Research Program**

**Sponsored by:
Air Force Office of Scientific Research,
Bolling AFB, Washington D.C.**

and

**Phillips Labs
Kirtland AFB, Albuquerque, NM**

August 1997

A PRELIMINARY STUDY OF THE CAUSES OF SPRING-IN IN A
UNIDIRECTIONAL CARBON FIBER / EPOXY COMPOSITE

Jeff M Ganley
Graduate Research Assistant
Department of Civil Engineering
University of New Mexico

Abstract

Composite materials are advantageous for space applications due to their light weight and high stiffness/weight ratio. However, curved composite parts which are autoclave cured tend to exhibit “spring-in”, a permanent deformation due to residual stresses [1], which must be understood to ensure dimensional accuracy of the final part. The purpose of this research is to determine and, if possible, to quantify the principle causes of spring-in in a unidirectional carbon fiber/epoxy composite. This project is intended to form the basis of further research into the spring-in effect to assist the Advanced Grid Stiffened (AGS) Composite Shroud Program at Phillips Labs, Albuquerque, NM. For this first stage of the research, three series of ICI Fiberite IM7/977-2 carbon fiber/epoxy cylindrical hoops were wound on a three-axis winder and autoclave cured according to the manufacturer’s recommended cure cycle [2]. These cylindrical parts were then cut to determine the effect of varying parameters such as winding tension and part thickness on the measured spring-in. The findings in this paper are preliminary and represent work to date. Additional research and testing on the spring-in effect in curved composite parts is planned to further clarify the relevant factors involved.

A PRELIMINARY STUDY OF THE CAUSES OF SPRING-IN IN A UNIDIRECTIONAL CARBON FIBER / EPOXY COMPOSITE

Jeff M Ganley

Introduction

Composite materials are advantageous for space applications due to their light weight and high stiffness/weight ratio. However, curved composite parts which are autoclave cured tend to exhibit "spring-in", a permanent deformation due to residual stresses [1], which must be understood and accounted for to ensure dimensional accuracy of the final part. For this project, three series of ICI Fiberite IM7/977-2 carbon fiber/epoxy cylindrical hoops were wound and autoclave cured. These cylindrical parts were then cut to determine the effect of varying parameters such as winding tension and part thickness on the measured spring-in. The goal of this research is to determine the relevant variables which cause spring-in, then attempt to quantify each relevant variable's effect on total spring-in.

Discussion of Problem

The Advanced Grid Stiffened (AGS) Composite Shroud Program at Phillips Laboratories, Albuquerque, NM plans to fabricate a carbon fiber/epoxy composite shroud for a future satellite launch. As part of the mission specification, the shroud must be able to be cut in half and then rejoined with mechanical fasteners. However, it is known that an autoclave cured composite part of this nature will exhibit spring-in with permanent deformations when cut. The goal of this research is to develop a methodology for the Advanced Grid Stiffened (AGS) Composite Shroud Program to counteract the spring-in effect to produce a shroud with zero spring-in when cut. As a first step, this research will attempt to identify the causes of and, if possible, to quantify the contributing factors to spring-in in a unidirectional, cylindrical IM7/977-2 carbon fiber/epoxy composite part.

Methodology

The intent of these experiments is to measure the spring-in while varying two parameters: winding tension and part thickness. In addition, a third parameter, the fiber/matrix distribution after cure, was studied to determine its effect on spring-in. In order to isolate and quantify these parameters, three series of four unidirectional cylindrical hoops were wound using IM7/977-2 prepreg tow. Each series of four parts was wound on a 5.5 inch diameter by 36 inch long stainless steel mandrel on an En-tec three-axis winder. The parts had a width along the mandrel of 6 inches. The series were then vacuum bagged and cured in an autoclave according to the manufacturer's recommended cure cycle [2]. Upon removal from the mandrel the parts were measured and cut into three 1.5 inch wide pieces. These 1.5 inch wide pieces were then cut a second time, parallel to the axis of the hoop, and the spring-in was measured. For each part, the thickness and inside diameter before and after cutting were measured to quantify the total spring-in.

The first series of hoops involved varying the winding tension. Each of the four parts had a thickness of 10 layers, and the winding tension was varied as follows: 2lb., 4lb., 6lb., and 8lb. The second series of hoops involved varying the part thickness while holding the winding tension constant. Each of the four parts had a winding tension of 4 lb. while the part thickness was varied as follows: 5 layers, 10 layers, 15 layers, and 20 layers. The third series provided additional data points to supplement the first two series. The parts were wound as follows: 2 lb./2 layers; 4 lb./2 layers; 4lb./10 layers; and 4lb./30 layers.

In addition to the spring-in measurements, a qualitative scanning electron microscope (SEM) analysis was performed to determine the distribution of fiber/resin through the thickness of the cured parts. According to Radford [3], the distribution of fiber/resin through the thickness of the part can effect the spring-in. Specifically, locally resin rich regions on the outside of the part can reduce the total spring-in. The scanning electron microscope was used to evaluate the cross section of the parts to determine the fiber/resin distribution through the thickness of the part.

Results

Three variables were studied to determine their effect on spring-in in a unidirectional composite part: winding tension, part thickness and fiber/resin distribution. As can be seen in the tables and graphs which follow, a variation in each of the three variables produced a measurable change in the spring-in.

It was observed that, when cut, all of the hoops sprung-in with pure bending strains. This was confirmed by the use of strain gages mounted on the inside and outside of three representative pieces. The readings from the strain gages very closely matched (with compressive strains on the inside of the piece and tensile strains on the outside of the piece, as expected) the bending formula for an elastic material. For this reason, the bending formula was used to derive the strains in the remainder of the cut parts. In addition, these strains were used as a relative measure of total spring-in.

The formula for bending in an elastic material is as follows:

$$\epsilon = y * (1/R_o - 1/R_f)$$

Where:

ϵ = strain at the extreme fiber (inside or outside, in this case)

y = distance from neutral axis (N.A.) to extreme fiber = thickness of the part/2 (in.)

R_o = Original (uncut) radius to N.A. (in.)

R_f = Final (after cut) radius to N.A. (in.)

The results of the variation in winding tension and part thickness versus spring-in are summarized in the tables and graphs on the following two pages.

Table 1: Variation in Winding Tension

Part	y (in.)	R _o (in.)	R _i (in.)	Strain ($\mu\epsilon$)
2lb. tension / 10 layers	0.0320	2.7845	2.5190	1211.265
4lb. tension / 10 layers	0.0320	2.7840	2.4690	1466.460
6lb. tension / 10 layers	0.0320	2.7860	2.4190	1742.605
8lb. tension / 10 layers	0.0315	2.7855	2.4270	1670.424

Figure 1: Winding Tension -vs- Measured Spring-In (Bending Strain)

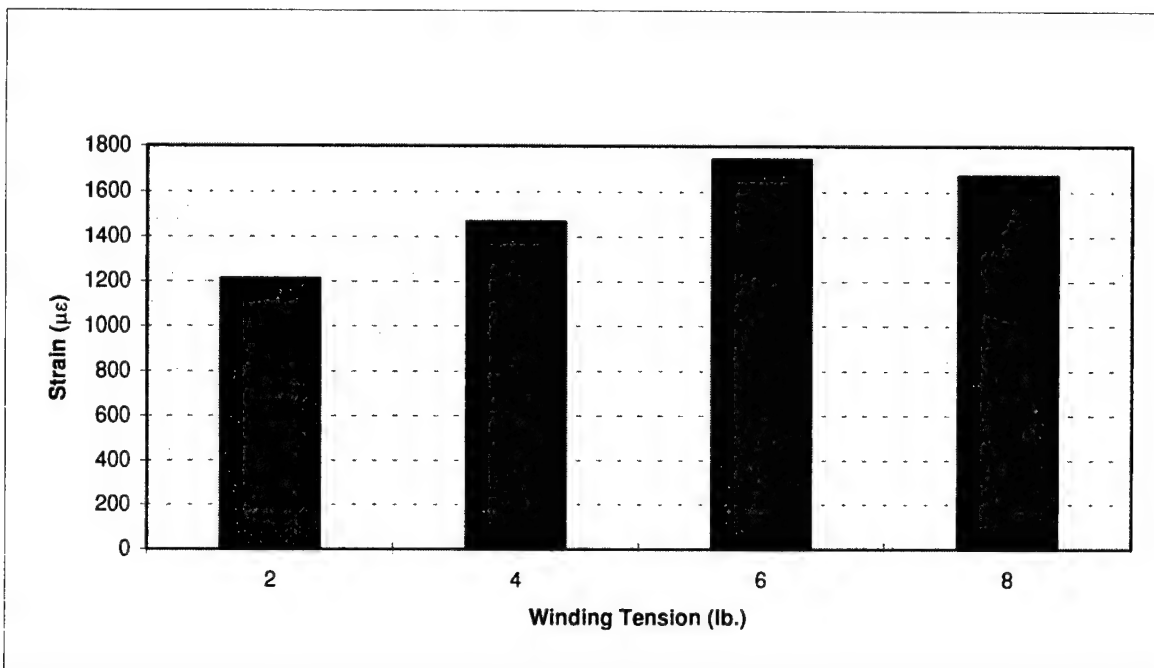
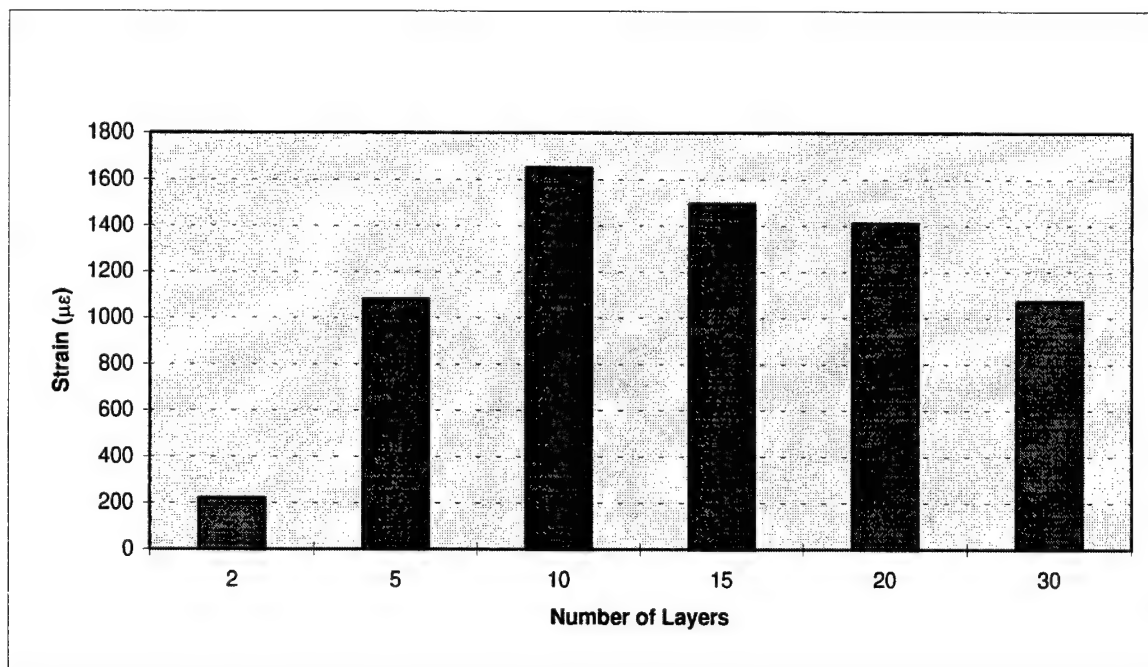


Table 2: Variation in Part Thickness

Part	y (in.)	R _o (in.)	R _f (in.)	Strain (μϵ)
4lb. tension / 2 layers	0.0065	2.7580	2.5205	222.073
4lb. tension / 5 layers	0.0145	2.7660	2.2930	1081.367
4lb. tension / 10 layers	0.0300	2.7830	2.4135	1650.347
4lb. tension / 15 layers	0.0445	2.7975	2.5570	1496.147
4lb. tension / 20 layers	0.0615	2.8150	2.6440	1412.965
4lb. tension / 30 layers	0.0785	2.8315	2.7260	1072.951

Figure 2: Thickness Variation -vs- Measured Spring-In (Bending Strain)



The results of the scanning electron microscope analysis suggest that the cured parts possess a resin rich outer surface which varies according to the type of release film which is used during cure. The remainder of the part displays a uniform, densely packed fiber/resin distribution. A slightly different release film combination was used in each of the three wound series. For uniformity, the spring-in in the 10 layer/4 lb

parts on each of the three series was measured to determine if there is a correlation between measured spring-in and the amount of resin bleed-off which is allowed by the release system. Refer to table 3 below for a summary of the release system (and corresponding resin bleed-out) versus measured spring-in.

Table 3: Spring-In as a Function of Release System (Resin Bleed Out)

Wind No.	Release System	y (in.)	R _o (in.)	R _i (in.)	Strain (με)
First Wind	Plastic perforated release with caul plates, most restrictive for resin flow	0.0320	2.7840	2.4690	1466.460
Second Wind	Plastic perforated release film only, moderately restrictive for resin flow	0.0300	2.7830	2.4135	1650.347
Third Wind	Teflon release film, least restrictive for resin flow	0.0260	2.7785	2.3595	1661.717

Conclusions

The results of experiments completed to date suggest that both winding tension and part thickness are significant factors which contribute to spring-in in composite parts. As can be seen in figure 1 and figure 2, a variation in either winding tension or part thickness will produce a corresponding change in measured spring-in. However, the change does not appear to be linear and appears to alter dramatically in the thin two layer piece. This suggests that winding tension and part thickness are contributing factors to spring-in, but that at least one other variable is also contributing to the observed spring-in. It is believed, at this point, that the other variable involved is either thermal expansion of the mandrel during cure or compaction of the composite part during cure, or both. The lack of spring-in in the 2 layer thin part could be explained by the fact that the part is too thin to experience appreciable compaction like the thicker parts and/or that the thermal expansion of the mandrel effects the full thickness of the thin part, whereas it would only effect the inner layers of thicker parts. It is believed that these two variables could interact with winding tension and part thickness to produce the variation in bending strains observed thus far. Further experiments are planned to help clarify the interactions between winding tension, part thickness, part compaction and

mandrel thermal expansion.

With the exception of extremely thin parts, as the thickness of a composite part is increased the total measured spring-in (dimensional change) decreases due to the fact that the bending stiffness (i.e. moment of inertia) is greater. However, the total force involved in the spring-in increases. Thus, if reducing total spring-in is the goal, then a thicker part may be advantageous. However, the total force required to return a thicker part to it's original shape is much greater than that of a thinner part.

As mentioned previously, in the case of varying the part thickness the thin 2 layer pieces behaved much differently than the thicker 5-30 layer parts. This is believed to be due to the contribution of mandrel thermal expansion and/or part compaction, which effect a thinner part much differently than the thicker parts. Further testing is planned to attempt to isolate the spring-in contributions of mandrel thermal expansion and part compaction.

The contribution to spring-in from fiber/resin distribution was examined in a qualitative way. From table 3 it is apparent that a release system which allows more resin bleed off will lead to a greater measured spring-in in the final cured part. This agrees with the mechanism that Radford [3] proposes: a resin rich outer surface will reduce spring-in. However, the increased spring-in with increased resin bleed off could also be due to increased compaction of the part. As was stated before, compaction could produce the bending stresses required for increased part spring-in which were observed in table 3. Further study is required to determine if fiber/resin distribution and/or part compaction are significant variables effecting part spring-in. The spring-in variation with resin bleed out system appears to have a contribution to spring-in which is an order of magnitude smaller than the total spring-in observed in the experiments thus far. Therefore, it may not be a significant factor in trying to reduce or eliminate total spring-in. Further experiments are planned to determine if the contribution of resin bleed out (release system) is significant to the total measured spring-in, and if so, to more precisely quantify the contribution.

References

- [1] Stover, Debbie, "Coping with Spring-In in Composite Tools and Parts," *Advanced Composites*, March/April 1993, pp. 38-45.
- [2] "ICI Fiberite Data Sheet, 977-2 Toughened Epoxy Resin," Fiberite Recommended Cure for 977-2, Page 13, November 15, 1995 (Rev. E).
- [3] Radford, Donald W., "Cure Shrinkage Induced Warpage in Flat Uni-Axial Composites," *Journal of Composites Technology and Research*, Vol. 15, No. 4, Winter 1993, pp. 290-296.
- [4] Hahn, H.T. and White, S.R., "Process Modeling of Composite Materials: Residual Stress Development During Cure. Part I. Model Formulation," *Journal of Composite Materials*, Vol. 26, No. 16/1992, pp. 2402-2422.
- [5] Kim, K.S. and Hahn, H.T., "Residual Stress Development During Processing of Graphite/Epoxy Composites," *Composites Science and Technology*, 36, 1989, pp. 121-132.
- [6] Daniel, I.M., Wang, T.M., Karalekas, D. and Gotro, J., "Determination of Chemical Cure Shrinkage in Composite Laminates," *Journal of Composites Technology and Research*, Vol. 12, No. 3/Fall 1990, pp. 172-176.

A PRELIMINARY ANALYSIS OF STACKED BLUMLEINS
USED IN PULSED POWER DEVICES

Johnelle L. Koriath
Department of Physics

University of Texas at Dallas
2601 N. Floyd Rd.
Richardson, TX 75080

Final Report for:
Graduate Student Research Program
Phillips Laboratory

Sponsored by:
Air Force Office of Scientific Research
Bolling Air Force Base, DC

and

Phillips Laboratory

September 1997

A PRELIMINARY ANALYSIS OF STACKED BLUMLEINS USED IN PULSED POWER DEVICES

Johnelle L. Koriath
Department of Physics
University of Texas at Dallas

Abstract

A computational model of stacked Blumleins used in pulsed power devices was initiated. Moment method calculations were completed using MATLAB in order to determine the charge densities of the flat, parallel conducting plates comprising the Blumleins. Preliminary findings indicate that fringing electric fields do exist and should affect the output of the pulser, especially in the high-frequency regime. Further analysis is required for a more decisive and complete picture of pulse propagation along the Blumleins.

A PRELIMINARY ANALYSIS OF STACKED BLUMLEINS USED IN PULSED POWER DEVICES

Johnelle L. Koriath

Introduction

Pulsed power technology largely involves the creation of high-power electromagnetic pulses. The relatively slow storage of energy, which is later discharged at a rapid rate, effectively transforms long, low-power pulses into shorter, more intense ones. These techniques are employed to provide energy sources for a wide variety of applications. The excitation of atomic and nuclear fluorescence, the generation of electron and ion beams¹, the pumping of laser media², and the production of high-power microwaves are but a few.

Transmission lines have long been an integral part of this technology. There is, however, a major drawback for their use in the high-voltage regime. When the impedance of the load is matched to that of the transmission line, only one half of the initial charging voltage is seen across the load. Thus, in 1948, A. D. Blumlein patented a structure commonly known as a "Blumlein" line³. This device consists of two transmission lines with a common charged conductor which, in the matched case, allows the propagation of the full voltage pulse. Several Blumleins can then be connected in series, or stacked, across the load in order to obtain a higher output voltage.

Theoretical Considerations

An excellent description of the operation of a Blumlein constructed of coaxial cable is given by Stanley Humphries⁴. Applying this theory to a Blumlein consisting of three flat conducting plates yields a similar explanation. Consider, for instance, that the three horizontally stacked plates are separated by a distance d , as in Fig. 1. A dielectric is placed between adjacent conductors. If these plates are infinitely wide, there is no mutual coupling between the top and bottom conductors. The top plate is connected to the bottom one through the load resistance. In order to prevent any reflections at the output, the impedance of the load is matched to the characteristic impedance of the Blumlein. Thus, if each of the component transmission lines has an impedance of Z_c , the impedance of the Blumlein as seen from the load is ideally

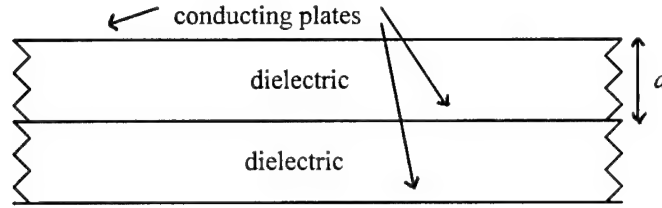


Figure 1. A cross sectional view of a portion of an infinitely wide single Blumlein.

$2Z_c$. The middle and bottom plates are joined by way of the voltage source and a protective, possibly infinite, source resistance. This allows the middle, common conductor to be charged to a high voltage, V_0 . If the two outer conductors are at a ground potential of zero, a potential difference of V_0 exists between the plates of each transmission line. Completing the circuit is a fast shorting switch, such as a spark gap, a thyatron or a semiconducting photoconductive GaAs or Si wafer, located between the top and middle plates.

Closure of the switching element initiates pulse propagation along the Blumlein, as shown in Fig. 2. As with a single transmission line, it takes twice the one-way transit time, τ_l , in order to fully form the pulse. Recall that $\tau_l = l/v$, where v is the speed of light in the dielectric medium and l is the length of the Blumlein. The standing voltage waveforms that are present in each of the constituent transmission lines before commutation are composed of two oppositely directed propagating pulses. Each of these square waves have a maximum voltage of $V_0/2$. During the first transit time, the waves traveling toward the load completely dissipate their energy into the matched resistive load, resulting in a voltage of V_0 at the output. The wave moving toward the shorted switch is reflected with an inverted polarity. The source resistance is effectively an open causing the wave moving toward it to be totally reflected. Both of these reflected waves follow on the tail of their respective original “load-going” wave. Their energy is then dissipated during the second transit time, completing the formation of an output pulse that has an amplitude of V_0 . In this way, the voltage ideally seen across the load directly scales with the number of Blumleins (N) stacked together, $V_L = NV_0$.

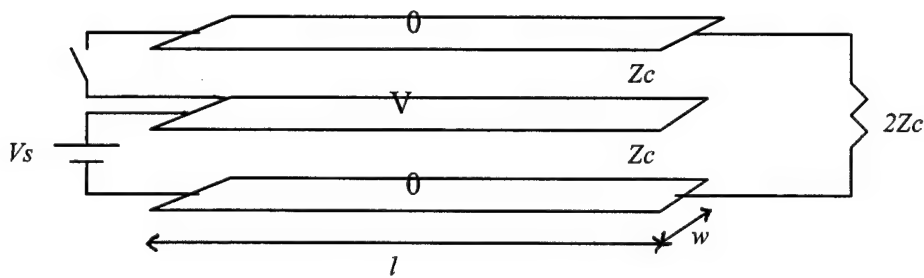


Figure 2. A three dimensional diagram of a single Blumlein as seen from the side. The voltage source is not ideal and contains an infinite resistor to prevent any damage. The voltage waves propagate as described above.

Clearly, the length of the pulse is directly related to the length of the Blumlein. Shorter Blumleins can be operated at a higher repetition rate because it takes less time for the pulses to form. Therefore, any fringing electric fields that might be present during pulse propagation will have a more pronounced effect on the output. This is especially true if the Blumlein is immersed in a medium that is different than the dielectric between the plates. For this case, the wave being propagated within the Blumlein will move at a speed which is different than that of the wave driven by the fringing fields. Thus, this aspect, as well as the transmission line geometry described above, must be taken into account when developing a model of a stacked Blumlein pulsed power device.

Modeling Considerations

The Blumlein can be dealt with in a variety of fashions. According to Humphries, the Blumlein is the distributed element equivalent of the LC generator⁴. Others, such as J. P. O'Loughlin, have viewed this structure as a network of resistances⁵. Treating the Blumlein as a waveguide, and thus considering the electromagnetic wave perspective requires the implementation of the method of moments or conformal transformation. For this work, the moment method is used to determine the distribution of charge, the capacitance, and the impedance of the Blumlein. Combining this with the transmission line equations will then yield the amount of voltage seen at the load, enabling one to define an efficiency.

The treatment of multiconductor transmission-line networks has been well established by Carl

Baum and others through conformal transformation techniques. In a series of papers, the propagation of electromagnetic waves along an N-wire transmission line network⁶, the field distribution and scalar potentials of the TEM mode in symmetrical two-parallel-plate transmission lines⁷, and the impedance and field distributions for parallel plate transmission line simulators⁸ were all studied. Although none of the geometries investigated were exactly like a system of stacked Blumleins, it is fair to say that at least some distortion of the electric field in the transmission line structures was shown to exist, the most marked of which was at the edge of the conducting plates.

Similar results are observed when the method of moments is applied to a parallel plate capacitor, an example that is common in many electrical engineering text books^{9,10}. To some extent, a Blumlein is like two capacitors and can therefore be analyzed with the three dimensional equation⁹

$$\Phi_i = \int_0^{2\pi} d\phi \int_0^{(\Delta S_i/\pi)^{0.5}} \frac{\rho_{si} dr}{4\pi\epsilon} + \sum_{j \neq i}^M \frac{\rho_{sj} \Delta S_j}{4\pi\epsilon |\vec{r}_i - \vec{r}_j|}$$

where Φ_i is the potential at the center of the i th element due to all other elements. Consider a stack of N Blumleins with a plate separation d , length l , and width w . If each plate of the Blumlein is divided into m equal elements, there are a total of $M = 3Nm$ elements for the structure, and, consequently, M equations with M unknown charge densities. Each element has a uniform charge density ρ_{si} and an area of ΔS_i . This distributed charge is treated as a point charge at the center of the element. The total charge on the device is zero. Each element also has a defined potential which is uniform for the entire plate. Therefore, by calculating the distance between elements, $r_i - r_j$, the charge density of each element can be determined and used to find the total charge on one plate, as well as the capacitance matrix of the stacked Blumlein.

An easier approach involves the two dimensional version of the above equation. With this method, a single cross sectional slice of the Blumlein, depicted in Fig. 3, can be analyzed and the results integrated over the entire Blumlein length. This research uses the following equation

$$\Phi_i = -\frac{\rho_{si}}{\pi\epsilon} \int_0^{\Delta w_i/2} \ell n x dx - \sum_{j \neq i}^M \frac{\rho_{sj} \Delta w_j \ell n |\vec{r}_i - \vec{r}_j|}{2\pi\epsilon}.$$

The first term in the equation represents the potential of the i th element due to itself. The second term

reflects the influence of all of the other elements. In this case, Δw_i is the length of each element. Because this variable is constant for all elements, $\Delta w_i = \Delta w_j = \Delta w$. All other variables remain as previously defined. As with the three dimensional treatment, there are M equations with M unknown charge densities. However, per-unit-length matrices are obtained, as opposed to the matrices for the entire device which are generated by the three dimensional case. Solving this system of equations for the charge-per-element matrix (q) was accomplished using MATLAB. Two matrices, one for the elastance per element (ψ), or inverse capacitance, and another for the potential per element (v), were generated with this package.

$$[\psi][q] = [v]$$

This required the input of the width of the conducting plates of the Blumleins, their horizontal separation, the dielectric constant of the material between the plates, the number of Blumleins, and the number of elements per plate. Calculating the charge per element is further facilitated by taking into account the symmetries of the system. The combined total charge of the bottom and top plates of each Blumlein is equal to but opposite of that on the middle plate. Additionally, each plate displays a mirror symmetry when a line is dropped perpendicularly at the center. In other words, the element at one edge of the plate has the same characteristics as the one at the opposite edge.

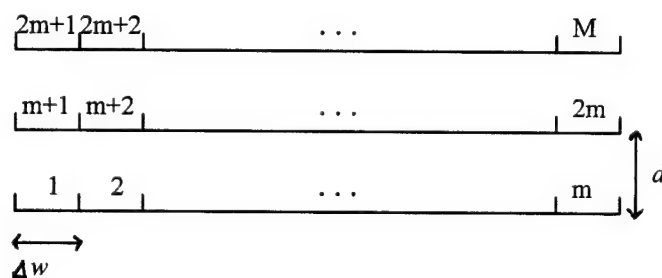


Figure 3. Diagram of the cross section of a single Blumlein used in the method of moments calculation

Although the charge on each element is useful in determining the existence of fringing electric fields, the elastance-per-element matrix is really more important. This matrix is related to the matrix of geometric factors by

$$\frac{1}{\epsilon} [f_g] = [\psi].$$

Therefore, by obtaining f_g , the capacitance (c) and inductance (l) matrices can be generated in order to describe wave propagation for the Blumleins.

$$[l] = \mu [f_g]$$

$$[c] = \epsilon [f_g]^{-1}$$

Once all of the per-element matrices have been computed, their per-plate counterparts can be determined by summing over all of the elements comprising each conducting plate. The transmission line equations in matrix form will then be used to calculate the amount of the initial charging voltage delivered to the output.

Results

Thus far, studies indicate that fringing does, indeed, exist. This should not come as a surprise as the effect is well established for microstrips, parallel plate capacitors, and wires. Other methods of analysis have also verified the phenomenon. In a stack of Blumleins, this is evidenced by the appearance of an increased charge at the edges of the conducting plates. For example, consider a stack of two Blumleins having a plate width of 2.54 cm and a separation of 0.635 cm which is filled with a dielectric having $\epsilon_r = 2.45$. Viewing a cross sectional slice of this structure that has eight elements per plate gives the following results if the first, third, fourth, and sixth plates are at one volt while the two remaining conductors are at zero volts. The absolute value of the charge per element is plotted on the following page against the element number for each plate.

As Fig. 4 indicates, the concentration of charge is located at the conductor's edge. The electric field lines are therefore more prolific at these points. The effects of this fringing field will impair the efficiency of the stacked Blumlein. For instance, the main pulse will be propagated between the conductors of the Blumlein. Another pulse, however, might be observed traveling outside the Blumlein. If the dielectric between the plates is not the same as the surrounding media, these two electromagnetic waves will reach the end points of the Blumlein at different times. Depending on the application, this may or may not

be desirable. As stated earlier, this phenomenon becomes more pronounced for shorter Blumlein lengths.

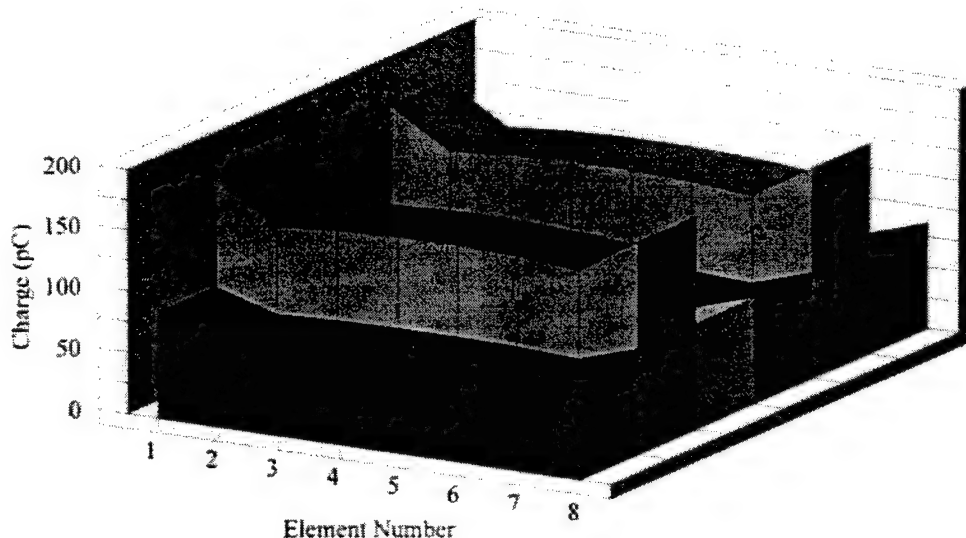


Figure 4. The front curve represents the charge per element of the bottom-most plate. The curve of each successive plate is plotted behind the first one.

Conclusions

Although this analysis is only in the initial stages, it would seem clear that, as the Blumlein is lengthened, the frequency dependent fringing effects should diminish. However, for smaller pulsed power devices relying on shorter Blumleins, the electric field fringing would have a more pronounced impact on the efficiency. This might be evidenced as a pre-pulse observed prior to the larger, main one. Further work is necessary in order to make more definitive conclusions. Research is on-going in an effort to create a more realistic model and test its predictive powers.

Acknowledgments

The author would like to acknowledge the never-ending support of the personnel at Phillips Laboratory, especially: Carl Baum, Bill Prather, Jack Agee, Dave Scholfield, and Dan McGrath.

References

1. I. Smith, Proc. of the 8th IEEE International Pulsed Power Conf. 1991, pp. 15-22.
2. T. Hasama, K. Miyazaki, K. Yamada and T. Sato, IEEE Journal of Quantum Electronics 25, No. 1, Jan. 1989.
3. A. D. Blumlein, U. S. Patent No. 2,465,840 (1948).
4. S. Humphries Jr., Principles of Charged Particle Acceleration, John Wiley & Sons, 1986, pp. 246 - 254.
5. J. P. O'Loughlin, private communications, May 10 and July 27, 1995.
6. C. E. Baum, T. K. Liu, and F. M. Tesche, *On the Analysis of General Multiconductor Transmission-Line Networks*, Interaction Note 350, November 1978.
7. C. E. Baum, D. V. Giri, and R. D. Gonzalez, *Electromagnetic Field, Distribution of the TEM Mode in a Symmetric Two-Parallel-Plate Transmission Line*, Sensor and Simulation Note 219, April 1, 1976.
8. C. E. Baum, *Impedances and Field Distributions for Parallel Plate Transmission Line Simulators*, Sensor and Simulation Note 21, June 6, 1966.
9. S. Ramo, J. R. Whinnery, and T. Van Duzer, Fields and Waves in Communication Electronics, John Wiley & Sons, 1994, pp. 324 - 330.
10. N. N. Rao, Elements of Engineering Electromagnetics, Prentice Hall, 1994, pp. 247 - 253, 368 - 375.

**EXPERIMENTAL VALIDATION OF THREE-DIMENSIONAL
RECONSTRUCTION OF INHOMOGENEITY IMAGES IN TRUBID MEDIA**

**Kelly Lau
Graduate Student
Joint Program in Biomedical Engineering**

**The University of Texas at Arlington
P.O. Box 19138
Arlington, TX 76019**

**Final Report for:
Graduate Student Research Program
Kirtland AFB
Phillips Laboratory**

**Sponsored by:
Air Force Office of Scientific Research
Bolling Air Force Base, Washington, DC**

And

Phillips Laboratory

August 1997

EXPERIMENTAL VALIDATION OF THREE-DIMENSIONAL RECONSTRUCTION OF INHOMOGENEITY IMAGES IN TURBID MEDIA

Kelly Lau
Graduate Student
Joint Program in Biomedical Engineering
The University of Texas at Arlington and
The University of Texas Southwestern Medical Center at Dallas

Abstract

Near infrared radiation for imaging tumors in tissue has been recently explored and investigated. In particular, to validate a novel FFT imaging reconstruction algorithm, we have performed experiments on tissue phantoms using a frequency-domain photon migration system. The system includes an amplitude-modulated laser diode, two radio frequency (RF) signal generators, an avalanche photo detector, and a lock-in amplifier. The tissue phantoms were made with inhomogeneities imbedded and were then scanned with the system at various RF frequencies. The data from the amplitude and phase measurements were analyzed using the FFT reconstruction algorithm. The reconstructed data show clear validation of the FFT algorithm and afford to localize inhomogeneities hidden in turbid media in three dimensions. In addition, based on the results, we present preliminary analysis on optimization of experimental parameters to obtain good-quality, reconstructed images with best experimental efficiency.

EXPERIMENTAL VALIDATION OF THREE-DIMENSIONAL RECONSTRUCTION OF INHOMOGENEITY IMAGES IN TURBID MEDIA

Kelly Lau

1. Introduction

In the last few years, numerous research efforts and technology developments have been made towards using near infrared (NIR) radiation for human tissue quantification and imaging. Three forms of light used in the field include short-pulsed light in time-domain (TD), intensity-modulated light in frequency-domain(FD), and a continuous wave form (CW). Among them, the frequency-domain system has its advantages over the other two: a FD system can acquire data almost in real time in an order of ms, much faster than a TD system, which utilizes a single photon counting method and requires much longer data acquisition time (in multi seconds). In addition, with the help of diffusion theory, the FD system allows us to extract the optical properties of tissues/organs under study and to image inhomogeneities hidden in tissues/organs. In comparison, CW method is in lack of quantification unless close-distanced (2-5 mm) measurements are performed.

The light source used for a FD system is intensity modulated at a radio frequency (RF) ranging from several MHz up to GHz at the wavelength range from 650 nm to 900 nm. In principle, NIR light illuminating tissues become very much scattered about 1 mm after the light travels in tissue. In the FD case, the intensity-modulated light travelling in tissue will form diffuse photon density waves (DPDW's), and the amplitude and phase of DPDW's carry information on the optical properties of the tissue. By extracting amplitude, phase, or optical properties of thick tissue, we can reconstruct tissue images that show inhomogeneities imbedded inside the thick tissue. This provides a new methodology for tumor imaging in medical applications.

Over last few years, common geometries used for imaging studies are 1) source(s)-detector pairs scanning horizontally or 2) circularly.¹ In both cases, mechanical movement is required, and it provides only two-dimensional images. Recently, Matson et al proposed a new approach to three-dimensional tumor localization in turbid media with the use of FD measurements in a single plane.² The theoretical basis of this novel reconstruction algorithm stems from Fourier Optics: applying Fast Fourier Transform (FFT) to the diffusion equation that DPDW's obey, and then extending the solution of Fourier Optics to DPDW's. This FFT reconstruction algorithm has several advantages, such as, 1) the light source does not need to move mechanically, 2) it has a potential to avoid mechanical movement, which has been shown to produce significant errors in imaging reconstruction. The theory has yet to be verified by experiments, although it was supported by computer simulations at one RF frequency of 1 GHz with selected scanning parameters.

The goal of this summer research project is to experimentally validate and optimize this three-dimensional reconstruction algorithm to image inhomogeneities in turbid media. In this report, we will first introduce the theoretical foundation for the FFT reconstruction algorithm, followed by a brief description on experimental setups, materials and methods. Then we will show experimental results and reconstructed images, and then investigate the correlation among experimental parameters that affect the quality of the reconstructed images. Furthermore, computer simulations are performed to confirm the findings that a larger scanning area is more crucial than smaller scanning pixels to obtain a higher resolution image. Finally, we will draw conclusions from this study and indicate future work.

2. Theoretical Background

Based on Fourier Optics³, we define the following relations:

$$A_z(f_x, f_y) = \iint U(x, y, z) e^{-i2\pi(f_x x + f_y y)} dx dy, \quad (1)$$

$$U(x, y, z) = \iint A_z(f_x, f_y) e^{i2\pi(f_x x + f_y y)} df_x df_y, \quad (2)$$

where $U(x, y, z)$ is the complex field of a monochromatic wave across the plane at z , and A_z is a two-dimensional Fourier transform of the function $U(x, y, z)$. It can be shown that a free-space solution to the source-free Helmholtz equation exists in the form of spatial frequency spectrum across a plane parallel to the xy plane but at a distance z from it.³

In addition, it has been proved⁴ that the diffusion equation adequately represents photon propagation in tissue, and the source-free diffusion equation in FD can be written as

$$\nabla^2 U(x, y, z) + k^2 U(x, y, z) = 0, \quad (3)$$

where $U(x, y, z)$ is the spatial distribution of a DPDW in a scattering medium, and $k^2 = (-v\mu_a + i\omega)/D = 3\mu_s'(-\mu_a + i\omega/v)$, v is the speed of light travelling in tissue, ω is the modulation frequency of the light multiplied by 2π , and μ_a and μ_s' are absorption and reduced scattering coefficients of the scattering medium, respectively.

Now inserting the inverse Fourier transform definition, eq. (2), into the diffusion equation, eq. (3), results in:

$$\frac{d^2}{dz^2} A_z(f_x, f_y) + \left[k^2 - (2\pi f_x)^2 - (2\pi f_y)^2 \right] A_z(f_x, f_y) = 0. \quad (4)$$

In analogy to the solution obtained in Fourier Optics for regular plane waves, we can find a solution to eq. (4) using the Fourier transform definition:

$$A_{z_1}(f_x, f_y) = A_{z_0}(f_x, f_y) e^{i\Delta z \sqrt{k^2 - (2\pi f_x)^2 - (2\pi f_y)^2}}, \quad (5)$$

where $\Delta z = z_0 - z_1$, is the distance between the detection plane at z_0 and the reconstruction plane z_1 . Furthermore, we can define a transfer function, $H_{\Delta z}(f_x, f_y)$, describing how a DPDW propagates in a homogeneous medium,

$$H_{\Delta z}(f_x, f_y) = \frac{A_{z_1}(f_x, f_y)}{A_{z_0}(f_x, f_y)} = \exp \left\{ i \Delta z \sqrt{\left(\frac{-v\mu_a + i\omega}{D} \right)^2 - (2\pi f_x)^2 - (2\pi f_y)^2} \right\}. \quad (6)$$

It is worthwhile to notice several important points:

- 1) in using diffusion theory, we neglect boundary effects and assume the medium to be homogeneous with spherical inhomogeneities;
- 2) in applying Fourier Optics to obtain equation (5), we extend the wave vector, k , from a real number to a complex number to include scattering effects, as the diffusion equation does;
- 3) eq. (6) describes the change in the Fourier transform of the photon density wave as it propagates, and thus eq. (6) can be used to invert the propagation and to reconstruct the photon density wave behind the detection plane.

3. Necessity of Experiments

The primary goal of this summer research project is to experimentally validate the FFT reconstruction algorithm, as introduced above. Taking experiments is necessary because

- 1) experiments permit studying boundary effects on the reconstructed images by using finite sizes of tissue phantoms;
- 2) we can study instrument detectability and sensitivity in locating hidden objects with different sizes and optical properties;
- 3) we can optimize scan parameters by performing experiments with various scan dimensions, pixel sizes, and modulation frequencies;
- 4) measurement on homogeneous samples provide feasibility of obtaining correct background information for the reconstruction and demonstrate the importance of such information.

4. Experimental Setup

As shown in Figure 1, the electronic components of our FD system include two RF signal generators, (Rhode & Schwarz, SMY01) ranging from 9 kHz to 1.04 GHz, two 50% power splitters (Mini-Circuits, ZFSC-2-1), two RF amplifiers (Mini-Circuits, ZFL-1000H), a NIR laser diode (LaserMax Inc, LSX-3500) modulatable up to 100 MHz at 780 nm and 680 nm with laser powers of 3 mW (at 116 mA) at 9 mW, an Avalanche Photo Diode (APD) (Hamamatsu, C5331), two frequency mixers (Mini-Circuits, ZLW-2), two low pass filters with the corner frequency at 1 MHz (Mini-Circuits, SLP-1.9), a lock-in amplifier (Stanford Research Systems, SR850), and a computer-controlled, two-dimensional positioning stage (Aerotech, Inc. ATS100).

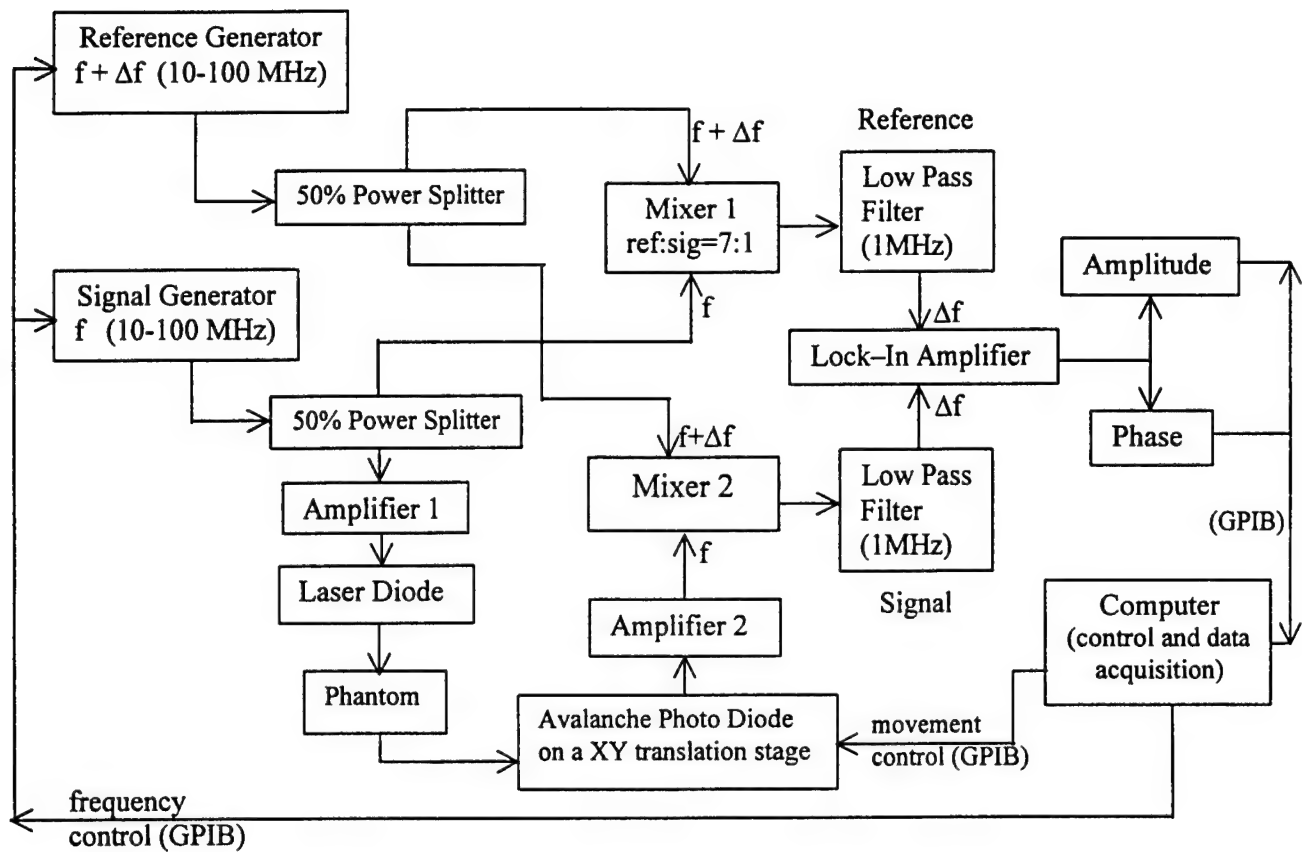


Figure 1. Experimental Setup of a FD system

The frequencies of the two signal generators were chosen from 10 to 100 MHz with an offset $\Delta f=25$ kHz for the reference signal with respect to the measurement signal in order to achieve a heterodyne system. Both RF signals for the reference at $f+\Delta f$ and for the measurement signal at f were 50% power split, and a branch from each the two RF signal generator was mixed by Mixer 1 to generate a reference signal for a lock-in amplifier. The output levels of the two signal generators were set up with a ratio of 7 to 1 between the reference and measurement signals to optimize the mixing efficiency. The second branch of the measurement signal at f was amplified to gain enough power to modulate the intensity of a NIR laser diode at 780 nm. Then the intensity-modulated, manufacture-collimated laser light illuminated a tissue phantom and then was detected by a movable APD to convert the optical signal to electrical signal. A second amplifier amplified the output of APD before the electrical signal was mixed with the second branch of the reference signal at $f+\Delta f$ using Mixer 2. The output frequencies of Mixer 1 and Mixer 2 consisted of $2f+\Delta f$, $f+\Delta f$, f , Δf , and higher harmonic components. By utilizing two low pass filters with a corner frequency of 1 MHz, only the signal with frequency of Δf at 25 kHz passes to the lock-in amplifier. The corresponding readings for amplitude and phase were recorded

automatically by a computer; in turn, feedback from the computer controlled the sensitivity and time constant settings for the lock-in amplifier based on the readings. In addition, through a GPIB interface, the computer set the RF frequencies for the two signal generators and controlled a XY positioning stage, which held the APD for 2-dimensional imaging scans.

5. Materials and Methods

Tissue phantoms were made out of plastic resin that hardens in molds by adding catalyst. The resin is combined with TiO_2 powder for scattering property and sometimes with NIR dye for absorption property.⁵ The optical properties of homogeneous phantoms were determined using the slope algorithm⁶ in transmission geometry. Since the algorithm requires the information on the homogeneous background medium that contains an object/objects, multiple samples were made as a set at the same time to ensure that the samples of the set have the same background optical properties. In general, a set of phantoms included a homogeneous sample, and two others with different objects implanted inside. The phantom sizes were typically 14cm x 14cm x 5cm, and absorption and scattering coefficients of background media were within a range of 0.01 to 0.1 cm^{-1} and 3 to 17 cm^{-1} , respectively. The objects used as inhomogeneities were plastic black, white, and clear beads with various diameters and shapes, as shown and listed in Figure 2.

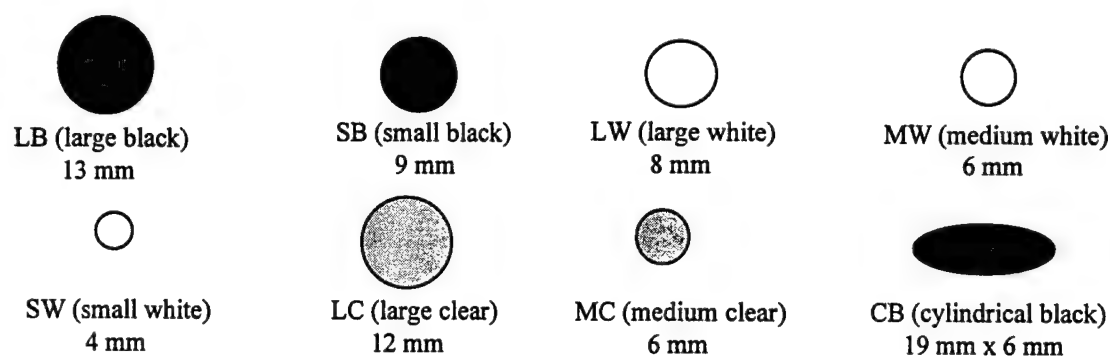
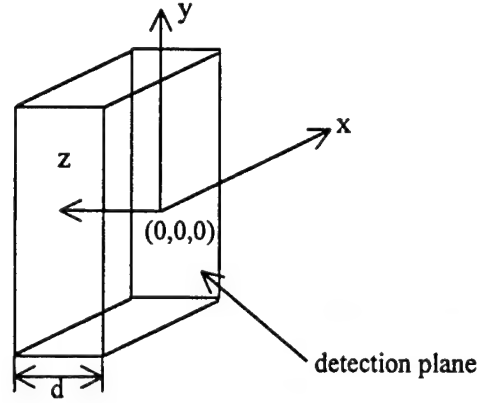


Figure 2. Beads used as tumor objects imbedded in tissue phantoms

We will use a XYZ coordinate system, shown in Figure 3, in this report to refer to the positions of hidden objects in the phantoms. The XY plane is in parallel with the detection plane, the origin is at the center of the detection plane, and the Z axis is pointing from the detection plane into the phantom. Normally, a bead was placed at the center of a phantom with a coordinate of (0, 0, $d/2$ cm), where d is the thickness of the phantom. For multiple hidden tumors, two beads (the same or different kinds) were placed at (0, -2 cm, $-d/2$ cm) and (0, 2 cm, $-d/2$ cm) inside of a phantom. In making inhomogeneous phantoms, we positioned the object(s) on top of a semi-dried, background material which has been cast earlier, and then added equal amount of ready-to-cast resin on top of the first part to complete the

phantom. In this way, we implanted the objects inside the phantoms with good 3-dimensional coordinate references, and X-ray measurements have confirmed the positions of imbedded objects.

Figure 3. the xyz coordinate system used to label locations of hidden objects inside a phantom.



All of the scans used for this report were performed on areas of 8 cm x 8 cm having 64x64, 32x32, or 16x16 pixels with pixel spacing of 0.125 cm, 0.25 cm, and 0.5 cm, respectively. The modulation frequencies were scanned from 10 MHz to 100 MHz in various steps in actual experiments, but all the data shown in this report were taken mainly at 20 or 40 MHz. An average measurement time was about 2.5 hours for a 32x32 scan with two modulation frequencies (20 and 40 MHz). The experiments were performed in transmission geometry with the light source fixed at one side of the sample and the movable detector located on the other side of the sample. The software package Interactive Data Language (IDL) was used to process the measured data and to perform the reconstruction algorithm. In addition, the PMI⁷ simulation code was used to predict and confirm the experimental data.

Because the transfer function contains an exponential decay term, the reconstructed DPDW's are not stable, containing ringing patterns. A better understanding for this artifact is under investigation. However, at present stage, to stabilize the reconstructed data or eliminate ringing patterns, we utilized a low-pass filter (pillbox) to cut off high spatial frequency components. Specifically, the cutoff frequency was ranged from only a few pixels, such as 1-4, in the spatial frequency domain. We multiplied the Fourier spectra by this cutoff filter before inverse Fourier transforming the spatial frequency spectra to reconstruct the DPDW's. For convenience, in the rest of the report, we will use "filter" as a short notation to represent the pixel number in Fourier domain of cutoff spatial frequencies.

After the amplitude, A , and phase, θ , were measured as a function of positions in a XY plane at $z=z_0$, we followed the procedures given below to reconstruct three-dimensional images:

- 1) based on A and θ , calculate complex photon density waves $U_h(x,y,z_0)$ and $U_{inh}(x,y,z_0)$, respectively, for both homogeneous sample and the sample containing objects;
- 2) subtract the homogeneous wave from the inhomogeneous wave, $U(x,y,z_0)=U_{inh}(x,y,z_0)-U_h(x,y,z_0)$;

- 3) FFT $U(x,y,z_0)$ to obtain its Fourier transform $A(f_x, f_y, z_0)$;
- 4) multiply $A(f_x, f_y, z_0)$ by the transfer function to execute the reconstruction process at z_1 ;
- 5) multiply $A(f_x, f_y, z_1)$ by a low-pass filter with a selected filter number (cutoff pixels);
- 6) inverse FFT $A(f_x, f_y, z_1)$ to the spatial domain for the reconstructed image at z_1 ;
- 7) repeat steps 4) to 6) for different values of z_1 to back propagate the reconstruction;
- 8) determine the x, y coordinates of the hidden object at the detection plane, and then plot amplitude versus z to localize the tumor in Z direction.

6. Experimental Results and Image Reconstructions

Figure 4 shows an example of amplitude images of DPDW's measured at the detection plane using a 680 nm laser scanned with 32x32 pixels on a 8 cm x 8 cm area of a phantom containing one black object. The phantom was 4.7 cm thick, and the black bead had a diameter of 9 mm imbedded at (0, 0, 2.3 cm). The illumination spot on the phantom was located at (-1.5 cm, 0, 2.3 cm), 1.5 cm off-centered in x axis with respect to the center of the phantom. The modulation frequency used for this set of measurements was 20 MHz, and the filter used for the reconstruction was 2. The absorption and reduced scattering coefficients of the background medium were 0.14 ± 0.06 and $3.1 \pm 1.4 \text{ cm}^{-1}$, respectively, which were determined using a homogeneous sample. Three amplitude plots of the complex DPDW's in Figure 4 are obtained at the detection plane for a homogeneous field [4(a)] measured from the homogeneous sample, perturbed field [4(b)] from the inhomogeneous sample, and the deviation between the two fields [4(c)], i.e., perturbed field (pfield) - homogeneous field (hfield). Notice that in obtaining the image of 4(c), we first subtracted the two complex fields (pfield-hfield), which were calculated from amplitude and phase measurements of the two samples, and then plotted the amplitude of the subtracted field.

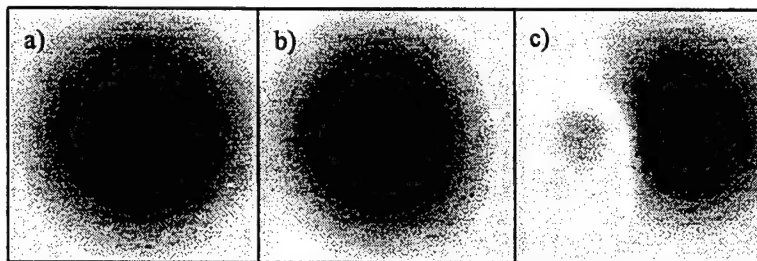


Figure 4. Amplitude images of the DPDW's measured at the detection plane from a phantom with one hidden high-absorbing object, scanned at 20 MHz with an array size of 32 x 32. a) homogeneous field=hfield, b) perturbed field=pfield, c) pfield hfield.

Figure 5 uses the same set of data as those for Figure 4. In the case of Figure 5, the FFT reconstruction algorithm was utilized to obtain the images at different depths behind the detection plane. The filter used here was 2. Let's first look at Figures 5(c) to 5(e), which are amplitude images at the

detection plane, 1.25 cm, and 2.5 cm behind the detection plane, respectively. The center of the actual black object is 2.3 cm behind the detection surface and 1.5 cm off from the center of the scanned area in X direction. These three images clearly and consistently show the location of the center of a hidden inhomogeneity in the XY plane at different depths, indicating that the object is a few centimeters deep behind the detection plane. For more quantitative localization of the object in Z direction, we need to have a XZ/YZ image or a plot in Z direction at the selected x and y coordinates of the detected object determined from the previous XY images. Figures 5(a) and 5(b) are cross-section images at XZ and YZ planes passing through the center of the scanned area. The top of Figure 5(a) corresponds to the detection plane along x axis, and the bottom represents the illumination plane. In this case, this XZ plane goes through the center of the object horizontally at $y=0$, and one can see that the imaged object is 1.4 cm off from the center in x direction. A plot of amplitude versus Z at the corresponding x coordinate provides the location of the object in Z direction (not shown). Same principle applies to Figure 5(b), in which case the YZ plane is at $x=0$, 1.5 cm apart from the plane passing through the center of the object. Because of this, this image does not give accurate location of the object in Z direction.

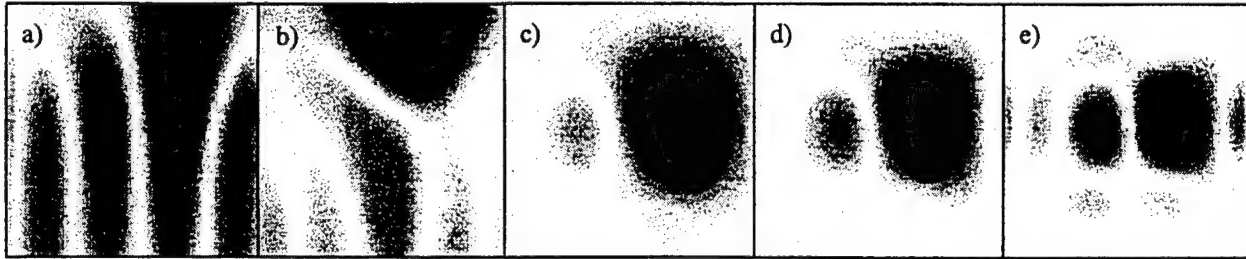


Figure 5. Reconstructed images for a phantom with one object, scanned at 20 MHz with an array size of 32×32 . a) x-z plane: the plane through the center of the measured volume horizontally, b) y-z plane: the plane through the center of the measured volume vertically, c) x-y plane: the detection plane, d) x-y plane: 1.25 cm behind the detection plane, e) x-y plane: plane near the object's center, 2.5 cm behind the detection plane.

Figure 6 is obtained from another set of two phantoms, one of which is homogeneous and the other having two high-absorbing objects with diameters of 9 mm. With the use of a 780 nm laser modulated at 20 MHz, the absorption and reduced scattering coefficients of the background medium are found to be 0.015 ± 0.001 cm and 15.1 ± 0.3 cm, respectively. The thickness of the inhomogeneous phantom is 4.2 cm. The two objects were imbedded inside the phantom with a separation of 4 cm apart at $(0, -2$ cm, 2.1 cm) and $(0, 2$ cm, 2.1 cm). The phantom was set 0.5 cm off centered with respect to the laser and the scanning plane along x axis. Similarly to Figure 5, Figures 6(a) and 6(b) are amplitude images measured from the homogeneous and inhomogeneous phantoms, and subtraction of the two complex fields of the two samples gives Figure 6(c). These three images are obtained at the detection

plane and show clearly two hidden objects after the simple subtraction. Furthermore, if the FFT reconstruction algorithm is applied, we can obtain the reconstructed amplitude images of DPDW's at different depths behind the detection plane. Figures 7(c) to 7(f) show such amplitude images reconstructed at the detection plane, 1 cm, and 2 cm behind the detection plane, respectively. All three images indicate consistently and unambiguously two hidden objects at about (0.5 cm, 2cm) and (0.5 cm, -2 cm) in the XY plane at different depths. As the reconstructed plane goes deeper and closer to the center of the hidden objects, the resolution for the imaged objects becomes better. In this case, a YZ image, shown in Figure 7(b), supports the findings from the XY images, and it also provides locations of the two objects in depth, which occur at the peaks of the two dark, cylindrical spots. Since the image plane for Figure 7(a) is in between the two objects, not passing through either center of the hidden objects, this XZ image does not give us very useful information in locating objects.

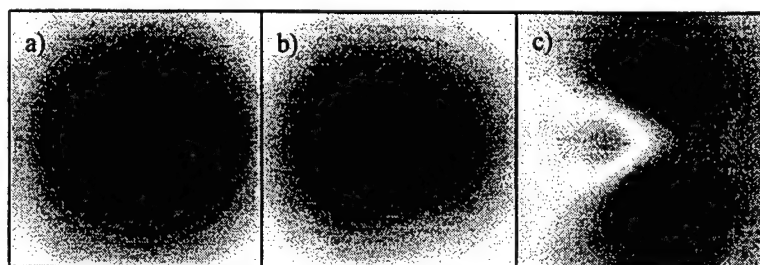


Figure 6. Amplitude images of the DPDW's measured from a phantom with two high-absorbing objects, scanned at 20 MHz with an array size of 32 x 32. a) hfield, b) pfield, and c) pfield-hfield.

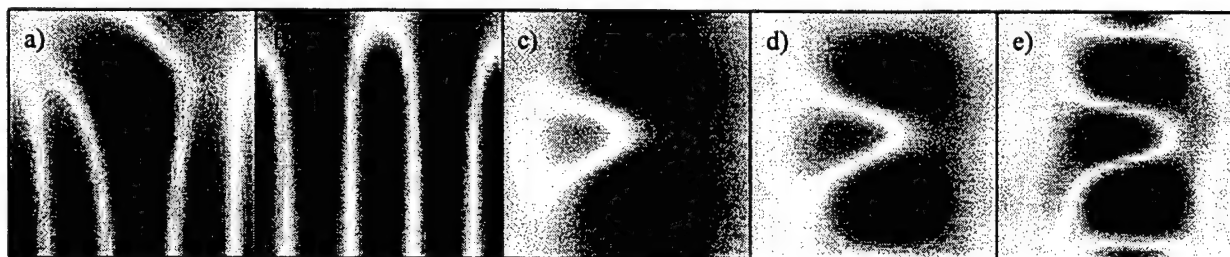
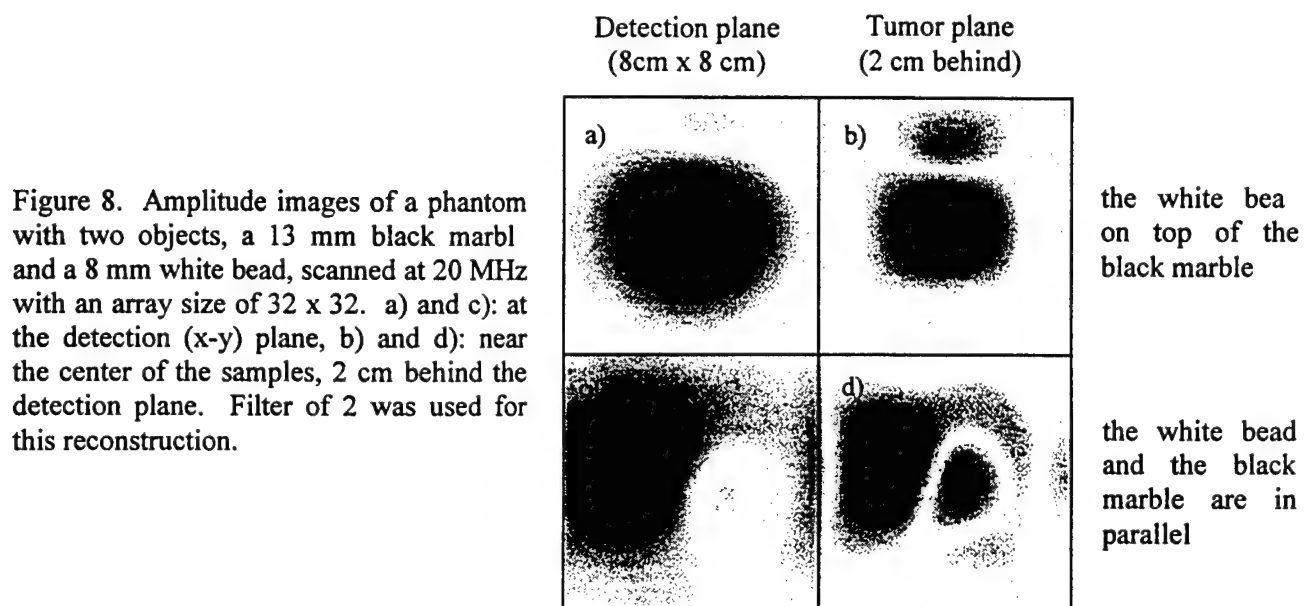


Figure 7. Reconstructed images for a phantom with two objects, scanned at 20 MHz with an array size of 32 x 32 for a scan area of 8 cm x 8cm with Filter 2 used for the reconstruction. a) x-z plane: the plane through the center of the measured volume horizontally, b) y-z plane: the plane through the center of the measured volume vertically, c) x-y plane: at the detection plane, d) x-y plane: 1 cm behind the detection plane, and e) x-y plane: plane near the object's center, 2 cm behind the detection plane.

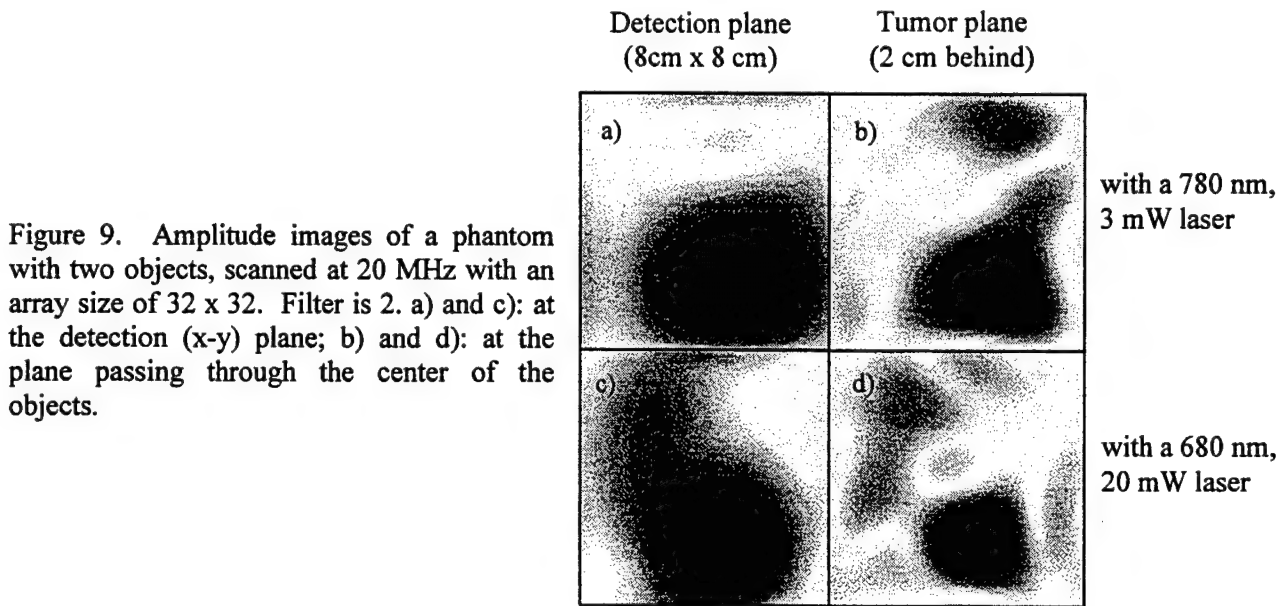
Notice that there are multiple bright, ringing patterns/loops in Figure 7(b); they are artifacts due to Fourier transform. Higher filters used in the Fourier domain for the reconstruction algorithm give more ringing patterns. This limits the bandwidth of the spatial frequency components in the reconstruction and

thus limits the spatial resolution of the reconstructed images. If higher spatial frequency components are included, we have to be careful to differentiate the real hidden objects from FFT reconstruction artifacts. In the next section, we will discuss how to select filter numbers, or cutoff spatial frequencies, to optimize the reconstructed images. Further studies and understanding of the cause of ringing patterns are underway.

The phantom used to obtain Figure 8 contains two objects, one black marble having 13 mm diameter and one white bead of 8 mm diameter. They were implanted at the middle of a 4.5 cm thick phantom in Z direction and about 2.5 cm apart vertically (or horizontally) symmetric to the center of the phantom. Similarly, 32x32 pixels were chosen to scan a 8cm x 8cm area with a modulation frequency of 20 MHz. The absorption and reduced scattering coefficients of the background are $0.017 \pm 0.001 \text{ cm}^{-1}$ and $15.9 \pm 0.6 \text{ cm}^{-1}$, respectively. Figures 8(a) and 8(b) are amplitude plots, respectively, at the detection plane and 2 cm behind the detection plane near the centers of the objects. It is seen that at the detection plane, the image for the white object does not appear very well, whereas the image for the black object is very obvious and clear. The reconstructed image on the XY plane near the centers of the objects (Figure 8(b)), however, displays two clear imaging spots with different magnitudes. The big, dark spot is corresponding to the black marble, and the small, light spot stems from the white bead. We can easily obtain the separation distance of 2.7 cm between the spots from Figure 8(b). To confirm the result, we turned the phantom 90° around the Z axis (the axis perpendicular to the detection plane) and rescanned the phantom. The reconstructed images for this case are shown in Figures 8(c) and 8(d), and the results are very consistent with those observed in Figures 8(a) and 8(b).



In order to know how different wavelengths and powers of the laser affect the quality of the reconstructed images, we performed two measurements on the same phantom using a 780 nm, 3 mW and a 680 nm, 9 mW laser diode. In this case, the phantom contained two objects, one 12 mm black marble and 12 mm clear bead. These two objects were imbedded in the middle of a 5 cm thick phantom, and other parameters were the same as those used for Figure 8. The background medium has absorption and reduced scattering coefficients of $0.016 \pm 0.00 \text{ cm}^{-1}$ and $10.0 \pm 0.7 \text{ cm}^{-1}$ at 780 nm, and $0.015 \pm 0.001 \text{ cm}^{-1}$ and $13.7 \pm 0.3 \text{ cm}^{-1}$ at 680 nm. With a 3 mW laser at 780 nm, we reconstructed amplitude images of the phantom, shown in Figures 9(a) and 9(b), at the detection plane and at the plane passing the centers of the objects, 2.5 cm behind the detection plane. It is seen that the clear bead does not give a very distinguished, resolvable feature in either case. Furthermore, after we switched to a higher (9 mW) power laser at 680 nm, the reconstructed images (Figures 9(c) and 9(d)) look similar to those with the 780 nm laser, except that the 680 nm, higher power laser gives a little better spatial resolution than the other case. This may be because a higher power laser gives a better signal-to-noise ratio. But overall, there is no significant difference between these two lasers in imaging large-mismatched objects in our phantoms.



To study the relationship between the quality of the reconstructed images and pixel spacing, we also performed a series of scans on the same phantom with array sizes of 64 x 64, 32 x 32, and 16 x 16 having pixel spacing of 0.125 cm/pixel, 0.25 cm/pixel, and 0.5 cm/pixel, respectively. In this case, the phantom was 4.4 cm thick and contained a 8 mm black and a 9 mm white bead. They were located at the middle depth of the sample and about 4 cm apart along Y axis with the white bead on top of the black bead. Figure 10 presents a set of reconstructed amplitude images at both the detection plane and at the

plane near the centers of the objects, 2 cm below the detection plane. The filter used here was 1, and the laser was at 780 nm. Figure 10 shows clearly that there is not much difference in image quality among the reconstructed images using either smaller (0.125 cm/pixel) or larger (0.5 cm/pixel) pixel spacing.

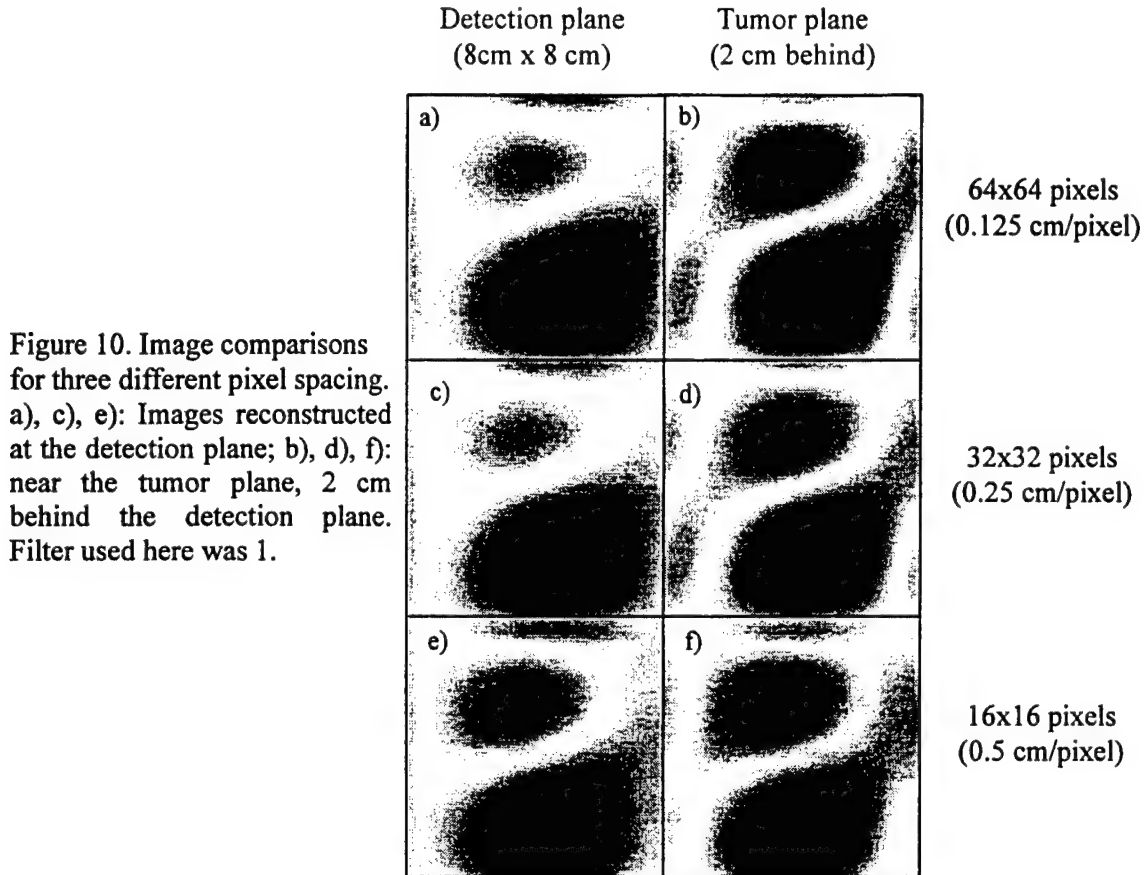


Figure 10. Image comparisons for three different pixel spacing. a), c), e): Images reconstructed at the detection plane; b), d), f): near the tumor plane, 2 cm behind the detection plane. Filter used here was 1.

To obtain the object location in Z direction, we first determine the x and y coordinates of the detected object(s) based on XY images, such as those shown in Figure 10, and then plot the amplitude versus Z to obtain the peak position. The z coordinate at the peak of the amplitude will be the location of the hidden object in Z direction. To show this strategy, we plot a z plot in Figure 11(a) based on Figure 10(d) at $X_{\text{pixel}}=20$, $Y_{\text{pixel}}=6$, which are the pixel coordinates of the observed, dark spot for the hidden black bead. In this case, the pixel step in Z direction is the same as that used in X and Y directions, i.e., 0.25 cm/pixel. Figure 11(a) displays a peak at pixel number=8 behind the detection plane, implying that this peak is at $8 \times 0.25 \text{ cm}=2 \text{ cm}$ behind the detection plane. Similarly, Figure 11(b) plots the amplitude versus Z pixels at $X_{\text{pixel}}=20$, $Y_{\text{pixel}}=22$, for the other observed spot resulting from the hidden white bead. This figure shows a dip at $Z_{\text{pixel}}=8$ behind the detection plane, giving the consistent location of the hidden

object in Z direction. A dip, rather than a peak, in amplitude might stem from a possible fact that the absorption of the white bead is lower than the background material.

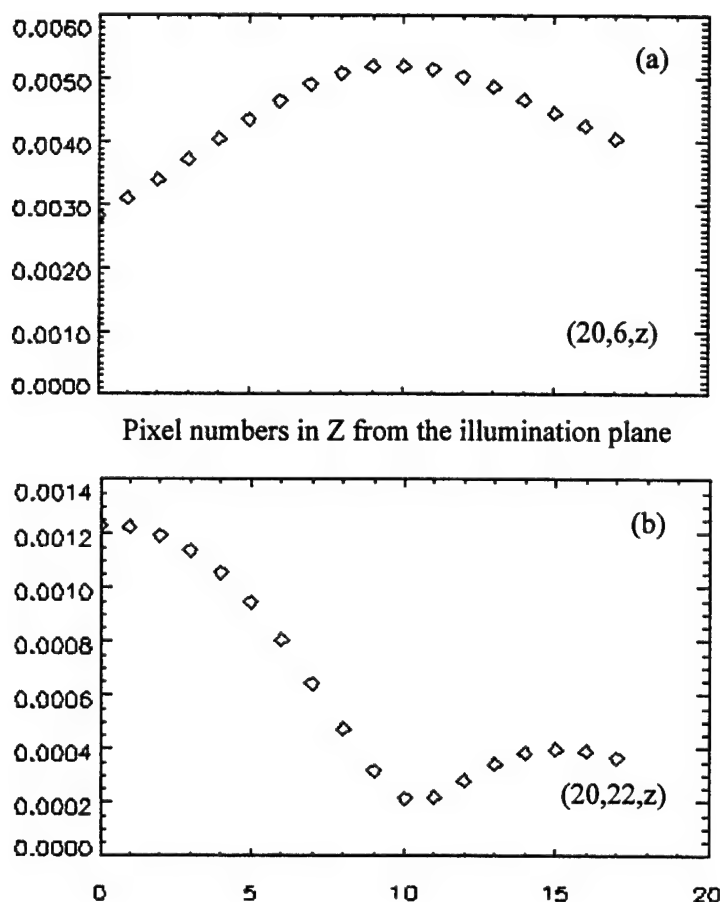


Figure 11. Z plots along the lines perpendicular to the detection plane and containing the black bead (a) and white bead (b). The pixel spacing in Z direction is 0.25 cm/pixel, corresponding to that shown in Figures 10(c) and 10(d). The filter used here was 2.

To confirm the object location in depth obtained from Figure 11, we plot two Z plots for the data with 16 x 16 array sizes, as shown in Figures 10(e) and 10(f), at the corresponding x and y coordinates of the two implanted objects. These two Z plots are given in Figures 12(a) and 12(b), respectively, for the black and white bead. In this case, the pixel spacing in Z is 0.5 cm/pixel. One can see that a peak and a dip appear at Z pixel number=4 behind the detection plane, i.e., 4 x 0.5 cm = 2 cm behind the detection plane. Thus, the object location in Z direction given in figure 11 is in good agreement with that in figure 11.

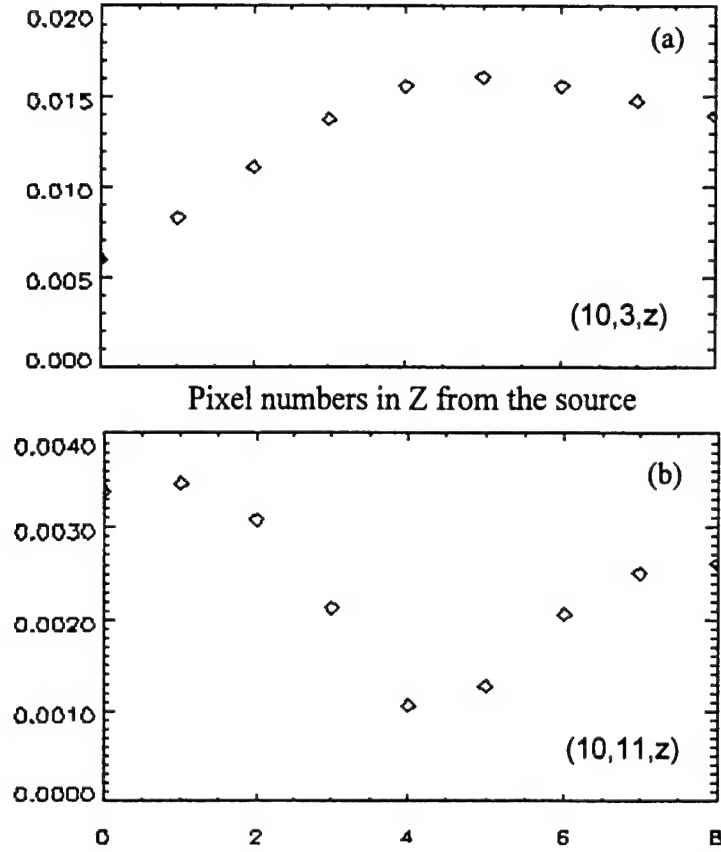


Figure 12. Z plots along the lines perpendicular to the detection plane and containing the black bead (a) and white bead (b). The pixel size in Z direction is 0.5 cm/pixel, corresponding to that shown in Figures 9(e) and 9(f). The filter used here was 2.

7. Data Analysis

Parameters used to scan and reconstruct images are as follows: 1) scanning dimensions/areas, such as 8x8 or 4x4 cm², 2) pixel spacing, such as 0.125, 0.25, or 0.5 cm/pixel, 3) modulation frequencies at 20, 40, or 100 MHz, and 4) filters numbers or cutoff spatial frequencies. What is the relationship among those parameters, and how do they affect the resolution of the reconstructed images? The answer to these questions may be helpful to optimize the scanning and reconstruction parameters for good-quality reconstructed images with best efficiency.

When a FFT of a 2-dimensional spatial domain function is performed, the number of pixels (or elements) in the spatial frequency domain is equal to the same number of pixels in the spatial domain. The 2-d spatial frequencies, f_x and f_y , will be multiple increments of Δf_x and Δf_y . Thus, we can rewrite the transfer function (TF) as follows:

$$H_z(f_x, f_y) = \frac{A_z(f_x, f_y)}{A_0(f_x, f_y)} = \exp \left\{ i\Delta z \sqrt{\left(\frac{-v\mu_a + i\omega}{D} \right) - (2\pi f_x)^2 - (2\pi f_y)^2} \right\}$$

$$= \exp \left\{ -\Delta z \sqrt{\left(\frac{\nu\mu_a}{D}\right) + (2\pi n\Delta f_x)^2 + (2\pi n\Delta f_y)^2} - i\frac{\omega}{D} \right\}, \quad (7)$$

where Δz is the distance from the detection plane to the reconstructed plane behind the detection plane, and Δz is a positive number. n is an integer, ranging from 0 to n_{\max} , where n_{\max} is equal to one half of the number of pixels in a row in the spatial domain. In the reconstruction algorithm, n corresponds to the filter number for the cutoff spatial frequency. It is known that the increments in the 2-d spatial frequency domain, Δf_x and Δf_y , are related to the dimension of the spatial domain as:

$$\Delta f_x = \frac{1}{L_x} = \frac{1}{\text{dimension}(x)}, \Delta f_y = \frac{1}{L_y} = \frac{1}{\text{dimension}(y)}. \quad (8)$$

Therefore, the TF becomes

$$H_z(f_x, f_y) = \exp \left\{ -\Delta z B \left[\cos\left(\frac{\theta}{2}\right) + i \sin\left(\frac{\theta}{2}\right) \right] \right\} = e^{-\Delta z B \cos(\frac{\theta}{2})} e^{i\Delta z B \sin(\frac{\theta}{2})}, \quad (9)$$

where B is a real number and
$$B = \left\{ \left[3\mu_a\mu_s' + \left(\frac{2\pi n}{L_x}\right)^2 + \left(\frac{2\pi n}{L_y}\right)^2 \right]^2 + \left(\frac{\omega}{D}\right)^2 \right\}^{\frac{1}{4}}, \quad (10)$$

$$\theta = \tan^{-1} \left[\frac{\omega/D}{3\mu_a\mu_s' + \left(\frac{2\pi n}{L_x}\right)^2 + \left(\frac{2\pi n}{L_y}\right)^2} \right]. \quad (11)$$

Eqs. (9) to (11) show quantitative dependence of the TF on the spatial dimension, L_x and L_y , modulation frequency, ω , and cutoff pixels, n , for spatial frequencies. It is seen from eq. (9) that the TF, H_z , has an decaying amplitude of $e^{-\Delta z B \cos(\frac{\theta}{2})}$ with a phasor of $e^{i\Delta z B \sin(\frac{\theta}{2})}$. For a given phantom or tissue with fixed values of absorption and reduced scattering coefficients, μ_a and μ_s' having typical values of 0.1 and 10 cm^{-1} , B and θ , and thus H_z , are functions of ω and n , if the scan dimensions, L_x and L_y , are selected. Figure 13 demonstrates that $\theta/2$ is relatively small with a range of modulation frequencies less than 100 MHz. This means that the transfer function is approximately a pure attenuation function with the phasor equal to 1 when the modulation frequencies are within 100 MHz. Using the same parameters as those for

Figure 13, we plot the amplitude of $e^{-\Delta z B \cos(\frac{\theta}{2})}$ with $\theta=0$, as shown in Figure 14. It is seen that at lower modulation frequencies, such as 20 MHz, the amplitude of the transfer function decays much faster than that at higher modulation frequencies, such as 1 GHz. This plot also shows that to obtain the same

magnitude of the normalized amplitude of TF, the number of pixels for Δf would be much smaller at 20 MHz than that at 1GHz. This makes the cutoff filter in the spatial frequency domain to be more limited at lower modulation frequencies than at higher modulation frequencies, i.e., only to be 1 or 2 pixels at 20 MHz but to be up to 5 more pixels at 1GHz. In addition, based on eq. (10), the cutoff filters can be equivalently improved by increasing the scanning dimensions, L_x and L_y .

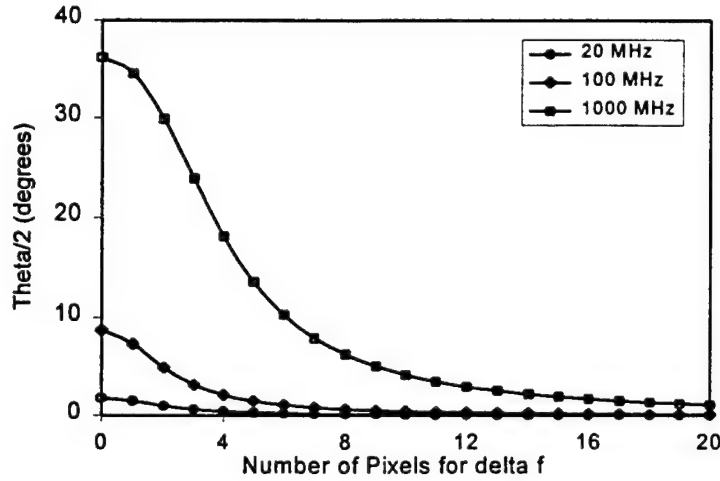


Figure 13. Dependence of $\theta/2$ in degrees on the number of pixels for Δf in the spatial frequency domain. The parameters used for this plot are: $\mu_a=0.1 \text{ cm}^{-1}$, $\mu_s'=10 \text{ cm}^{-1}$, $L_x=L_y=8 \text{ cm}$.

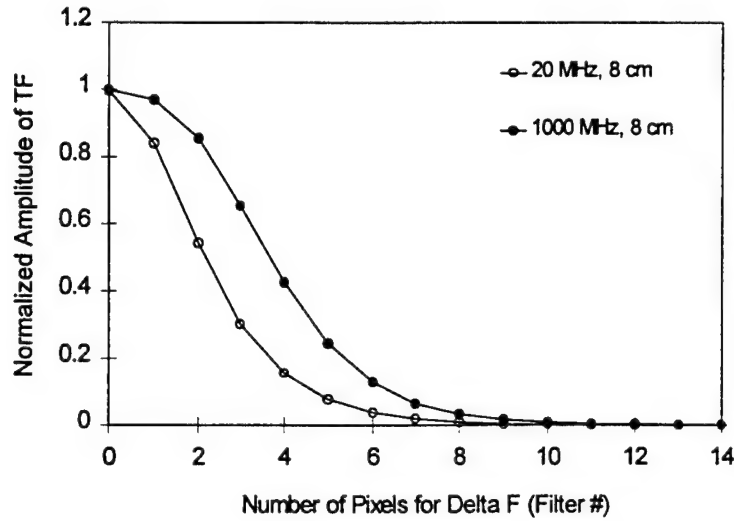


Figure 14. Dependence of normalized amplitude of transfer function on the number of pixels for Δf in the spatial frequency domain. The parameters used for this plot are: $\mu_a=0.1 \text{ cm}^{-1}$, $\mu_s'=10 \text{ cm}^{-1}$, $L_x=L_y=8 \text{ cm}$.

Thus, to improve the resolution of the reconstructed images, we can use higher modulation frequencies or increase the sizes (dimensions) of the detection plane. Decrease in pixel spacing would not be a crucial factor at this point, as long as the sampling frequency (number of pixels per unit length) is larger than the spatial frequency of the imbedded object, i.e., $1/(2 \cdot \text{diameter of the object})$, according to Nyquist's law.

To confirm the findings mentioned above, we have also conducted theoretical simulations using similar parameters. The results are very consistent with the experimental data.

In the case of biomedical imaging, let us discuss two extreme cases as follows: the first case is where the medium is highly absorbing in comparison to the modulation frequency. For example, at 20 MHz, we have μ_a (typically $0.1\sim 0.3\text{ cm}^{-1}$) $\gg \omega/v$ ($=0.006\text{ cm}^{-1}$ for 20 MHz signal), and the TF becomes a purely exponential decay function. We can approximately use the following relationship to optimize the parameters for the cutoff filter and the scanning dimension, n , L_x and L_y .

$$(2\pi n/L_x)^2 + (2\pi n/L_y)^2 = 3\mu_a \mu_s \sim 3\text{ cm}^{-2}, \text{ or } n/L_x \sim 0.2\text{ cm}^{-1}.$$

In the second case, where the modulation frequency is comparable to or higher than the absorption factor of the medium, we will have μ_a (typically $0.04\sim 0.1\text{ cm}^{-1}$) $\ll \omega/v$ ($=0.3\text{ cm}^{-1}$ for 1 GHz signal). The TF has an exponential decay term and phase shift. In this case, we will use the following relationship to estimate the parameters for the cutoff filter and the scanning dimension, n , L_x and L_y .

$$(2\pi n\Delta f_x)^2 + (2\pi n\Delta f_y)^2 = 3\mu_s \omega \sim 3\pi\text{ cm}^{-2}, \text{ or } n\Delta f_x \sim 0.6\text{ cm}^{-1}.$$

8. Conclusions and Future Work

What we have learned from this summer research project is as follows:

- 1) the FFT reconstruction algorithm works in imaging and positioning inhomogeneities 3-dimensionally with good accuracy;
- 2) background information is necessary and important for accurate reconstruction;
- 3) At present stage, for high sensitivity, the imbedded object should be off-centered with respect to the light source and the detection plane. Further studies are underway to improve the reconstruction algorithm in order to eliminate this requirement.
- 4) large scanning dimension/area is more important than small scanning pixel size to achieve better resolution;
- 5) high modulation frequencies ($>500\text{ MHz}$) may be helpful to achieve better resolution; low modulation frequencies can provide adequate information for tumor screening;
- 6) this summer project has demonstrated that the experimental set-up works and the results generated from it are in good agreement with the theoretical simulations. Inhomogeneities can be detected and located in three-dimensions. However, we are not able to characterize the optical properties of the inhomogeneities at this point. This remains for further study.

Our future work includes:

- 1) make phantoms containing objects which are small, purely absorptive, perturbations from the background medium;
- 2) take measurements on the new phantoms;

- 3) complete a diffraction tomographic model for quantitative reconstruction of optical property imaging;
- 4) apply the diffraction tomographic model to the data taken from the new phantoms for μ_a , μ_s image reconstruction;
- 5) extend the modulation frequencies to KHz range, and explore the possibility at using CCD cameras for image capture;
- 6) extend the system to clinical tests.

9. Acknowledgement

The authors are grateful to Dr. Chuck Matson for providing adequate laboratory equipment and the bulk of the reconstruction programs, as well as for his theoretical insight and useful discussions. In addition, the authors also wish to thank Grant Denton and Scott Newey for all of their helpful technical support. Without all of them, this research project would not have been possible.

10. References

- ¹ M. A. O'Leary, D. A. Boas, B. Chance, and A. G. Yodh, "Simultaneous Scattering and Absorption Images of Heterogeneous Media Using Diffusive Waves within the Rytov Approximation," SPIE, **2389**, p.328-339 (1995).
Brain W. Pogue, Michael S. Patterson, and Tom J. Farrell, "Forward and Inverse Calculations for 3-D Frequency-Domain Diffuse Optical Tomography," SPIE, **2389**, p.328-339 (1995).
- ² C. L. Matson, N. Clark, L. McMackin, and J. S. Fender, "Three-dimensional tumor localization in thick tissue with the use of diffuse photon-density waves," Appl. Opt. **36**, 214-220 (1997).
- ³ Joseph W. Goodman, Introduction to Fourier Optics, (San Francisco, McGraw-Hill Book Company, 1968).
- ⁴ M. S. Patterson, B. Chance, and B. C. Wilson, "Time resolved reflectance and transmittance for the non-invasive measurement of tissue optical properties," Appl. Opt. **28**, 2331-2336 (1989).
- ⁵ M. Firbank, M. Hiraoka, and D. T. Delpy, "Development of a stable and reproducible tissue equivalent phantom for use in infrared spectroscopy and imaging," SPIE, **1888**, 264-274 (1993).
- ⁶ J. B. Fishkin and E. Gratton, "Propagation of photon-density waves in strongly scattering media containing an absorbing semi-infinite plane bounded by a straight edge," J. Opt. Soc. Am. A **10**, 127-140 (1993).
- ⁷ See the PMI (Photon Migration Imaging) Code Home Page: <http://www.osa.org/homes/BIOOPTIC/Resource/softwar.htm>

A QUASI-PARTICLE ANALYSIS OF AMPLITUDE SCINTILLATION

Ruthie D. Lyle
Graduate Student
Department of Electrical Engineering

Polytechnic University
Route 110
Farmingdale, NY 11735

Final Report for:
Graduate Student Research Program
Phillips Laboratory

Sponsored by:
Air Force Office of Scientific Research
Bolling Air Force Base, DC

and

Phillips Laboratory

August 1997

A QUASI-PARTICLE ANALYSIS OF AMPLITUDE SCINTILLATION

Ruthie D. Lyle
Graduate Student
Department of Electrical Engineering
Polytechnic University

ABSTRACT

A quasi-particle approach is applied to study amplitude scintillation of a transionospheric signal associated with bottomside sinusoidal (BSS) irregularities in the equatorial F region of the ionosphere. The power spectrum of a three second sample of high-resolution density perturbation data obtained in situ, by the low orbiting Atmosphere-E (AE-E) Satellite (orbit 22700, 12/11/79) during its passage through BSS irregularities, is modeled analytically by a superposition of three functions, which define the scatterer of the quasi particles. Numerical results are presented, and their physical significance discussed.

A QUASI-PARTICLE ANALYSIS OF AMPLITUDE SCINTILLATION

Ruthie D. Lyle

1 Introduction

An extraterrestrial signal, solar emissions or geostationary satellite signal, experiences a distortion in phase and amplitude as a result of transversely crossing a drifting inhomogeneous ionosphere, diffraction of the emerging wavefront during free space propagation enhances the distortion. The resultant amplitude and phase fluctuations observed at a ground based receiver are denominated, ionospheric scintillation. Scintillation varies with signal frequency, season, time of day, and global location.

Consequently, investigation of the scintillation phenomenon has been a powerful method of remote sensing the morphology of the ionosphere. Initial interest in this phenomenon was sparked, in the mid 1940's, by unexplained irregular amplitude fluctuations observed in signals received from the radio star, Cygnus A. A series of deductive experiments surmised that the effect was produced locally in the ionosphere, conclusive results followed with the introduction of ionospheric sounding experiments [7].

Observation of beacon satellite signals revealed two classes of scintillation occurrence, weak and strong. Weak scintillation occurring when the irregularity region is thin, or the fluctuation in electron density along the path of propagation is small, such that only the phase of the emerging signal is perturbed. Conversely strong scintillation occurring when the fluctuation in electron density is large, and/or the irregularity layer is thick, causing both the phase and amplitude to be perturbed significantly. Most theories exclusively address weak or strong scattering regimes from a stochastic approach, where statistical characteristics are used to describe the randomness of the ionospheric perturbations. The Phase screen and Rytov theories [12] are examples of weak scintillation models, while the Parabolic Equation Method (PEM), addresses strong scintillation [5].

The Quasi-particle theory has been used to analyze the effect of ionospheric irregularities on a transionospheric signal from both a stochastic [11] and a deterministic [6] approach.

Similarly, the theory uses the wave equation as a starting point, as done in other theories. However, making use of the concept of wave particle duality, the wave is viewed as a distribution of particles in the (\vec{r}, \vec{k}) phase space via a Wigner distribution function. Scattering of the signal by the irregularities is equivalent to collision of quasi particles with objects in the medium leading to the evolution of the quasi-particle distribution. Multiple scattering is an intrinsic feature of the derivation, and thus the theory is applicable for strong scintillation.

In this work the Quasi-Particle Theory, based on a deterministic approach is applied to study the effect of Bottomside Sinusoid (BSS) Irregularities on a 250MHz transionospheric signal originating from the LES - 8 geostationary satellite. A brief introduction of this approach is presented in the Formulation section of this report. A rigorous introduction can be found in the paper by Marcuvitz [8].

1.1 The Ionosphere and BSS Irregularities

Ionospheric sounding experiments show that the background electron density, N_o , has a 'bell-like' profile with respect to altitude [9]. It is deduced from theoretical interpretations based on the index of refraction. The index of refraction neglecting electron-ion collisions and the geomagnetic field is given by

$$n(\vec{r}) = \sqrt{1 - \frac{\omega_{po}^2(\vec{r})}{\omega^2}} \quad (1)$$

The value of the index varies between zero and unity depending on plasma frequency, ω_{po} , and the transionospheric signal frequency, ω . If the transionospheric signal frequency equals the plasma frequency, $\omega = \omega_{po}(\vec{r})$, at a particular altitude, then $n(\vec{r}) = 0$. Subsequently, the group velocity of the wave is zero, and thus, the wave is reflected. This interpretation is the basis of the ionospheric sounding experiments. Similarly, investigation of scintillation occurrence is accompanied by a rudimentary understanding of experimental observations and the theoretical basis describing wave propagation in an inhomogeneous ionosphere.

In this case, the effect of fluctuations in the electron density on transionospheric signals is considered. Unpredictable fluctuation of the electron density, ΔN , about the background density, N_o , results in a corresponding fluctuation in the index of refraction, Δn , and consequently a fluctuation in the amplitude and phase of the transionospheric signal. The

perturbed index of refraction, due to the presence of density fluctuations, is given by

$$\Delta n(\vec{r}) \cong -\frac{\Delta \omega_p^2(\vec{r})}{2\omega^2} = -\frac{\Delta N e^2}{2\omega^2 m \epsilon_0} \quad (2)$$

where $\omega^2 \gg \omega_{po}^2$ is assumed and $\Delta \omega_p^2 = \omega_p^2 - \omega_{po}^2 = \Delta N e^2 / \epsilon_0 m$. Although $\Delta n(\vec{r})$ is inversely proportional to ω^2 , and in general is very small, it can still have a significant effect on a transionospheric signal depending on the length of the propagation path.

The extent of the effect can be estimated by considering the phase perturbation of the transionospheric signal due to the density fluctuations along a straight line path. Assuming that the density fluctuations exist in a finite layer of thickness L , with propagation in the x direction, the perturbed phase of the signal for $x > L$ is given by

$$\Delta \phi(y) = \int_0^L \frac{\Delta \omega_p^2}{2\omega^2} dx \quad (3)$$

where the effect of the irregularities add spatial variations through the ΔN . The amount of phase distortion is proportional to the variation of electron density along the ray path, and inversely proportional to the signal frequency. The effect can become significant for deterministic fluctuation (e.g. BSS) because of the additional y variation.

Experimental observations, in situ and remote, indicate that the electron density in the ionosphere can be highly complex and irregular [12]. Currently, low orbiting satellites conduct high-resolution in situ measurements of the relative density fluctuations along known satellite paths (e.g. [10]). These measurements detect irregularities in the night time for up to 300 minutes within a narrow belt approximately ± 12 degrees from the dip equator in the bottomside of the equatorial F region of the ionosphere. The irregularities extend for at least 7000km in the E-W direction and are characterized by 'quasi-sinusoidal' electron density fluctuation, thus, termed Bottomside Sinusoidal (BSS) irregularities.

2 Formulation

The wave characteristics including its amplitude and phase can be described by a joint distribution function of the position vector, \vec{r} , and the wavevector, \vec{k} , known as the Wigner distribution function which is defined to be

$$F(\vec{r}, \vec{k}, t) = \pi^{-2} \int d\vec{r}' \exp(2i\vec{k} \cdot \vec{r}') \psi^*(\vec{r} + \vec{r}', t) \psi(\vec{r} - \vec{r}', t) \quad (4)$$

where ψ is the phasor of the wave field component, and the integration is over all space where the field exists. The quasi-particle spatial density and spectral density can be obtained from the Wigner distribution function by the two relations $|\psi(\vec{r}, t)|^2 = \int F(\vec{r}, \vec{k}, t) d\vec{k}$ and $|G(\vec{k}, t)|^2 = \int F(\vec{r}, \vec{k}, t) d\vec{r}$ respectively.

Considering a modeled single-mode type wave equation expressed as

$$i \frac{2\omega \partial \psi}{c^2 \partial t} = -[\nabla^2 + k_o^2(\epsilon_1(\vec{r}) + 1)]\psi \quad (5)$$

where $\epsilon_1(\vec{r}) = \epsilon(\vec{r}) - \epsilon_{oo} = \epsilon_{1r}(\vec{r}) + i\epsilon_{1i}(\vec{r})$ is the perturbed dielectric function due to the presence of the density irregularities, $\epsilon(\vec{r}) = 1 - \frac{\omega_p^2}{\omega(\omega - i\nu)}$ and $\epsilon_{oo} = 1 - \frac{\omega_{po}^2}{\omega(\omega - i\nu)}$ are the total and the perturbed dielectric function of the ionospheric plasma, and ν is the electron-ion collision frequency, the corresponding transport equation of the Wigner distribution function for the stationary irregularities is derived to be [6]:

$$\vec{k} \cdot \nabla F = -\frac{k_o^2}{\pi^2} \int d\vec{k}' F(\vec{r}, \vec{k}') \int d\vec{s} (\epsilon_{1r}(\vec{r} - \vec{s}) \sin[2(\vec{k} - \vec{k}') \cdot \vec{s}] + \epsilon_{1i}(\vec{r} - \vec{s}) \cos[2(\vec{k} - \vec{k}') \cdot \vec{s}]) \quad (6)$$

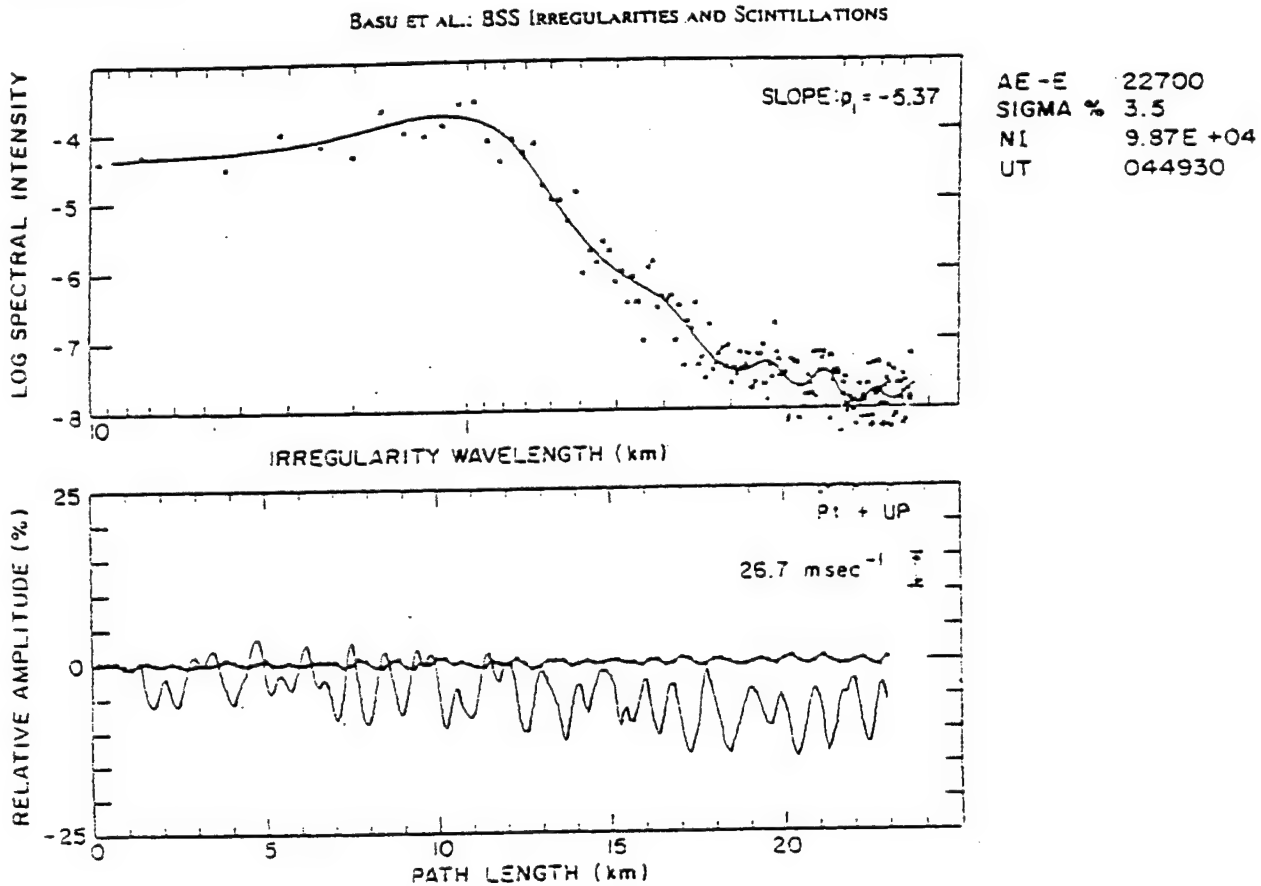
In calculating the scintillation index, $S_4 = \sqrt{\frac{\langle \rho^2 \rangle - \langle \rho \rangle^2}{\langle \rho \rangle^2}}$, only the intensity distribution $\rho = |\psi(\vec{r}, t)|^2$ of the wave is needed, where the average is performed over a spatial period of the dominant BSS irregularity scale length. The zeroth and first moments of the Wigner distribution function are the quasi-particles' number density and current density, which are defined respectively as $\rho = \int d\vec{k} F(\vec{r}, \vec{k})$ and $\vec{J} = \int d\vec{k} \vec{k} F(\vec{r}, \vec{k}) = \vec{k}_o \rho + \vec{J}_1$. The second and third moments of the WDF are $\underline{\underline{s}} = \int d\vec{k} \vec{k} \vec{k} F(\vec{r}, \vec{k}) = \vec{k}_o \vec{k}_o \rho + \vec{k}_o \vec{J}_1 + \vec{J}_1 \vec{k}_o + \underline{\underline{s}}_1$, and $\underline{\underline{u}} = \int d\vec{k} \vec{k} \vec{k} \vec{k} F(\vec{r}, \vec{k}) = \vec{k}_o \vec{k}_o \vec{k}_o \rho + \vec{k}_o \vec{k}_o \vec{J}_1 + \vec{k}_o \vec{J}_1 \vec{k}_o + \vec{k}_o \underline{\underline{s}}_1 + \vec{J}_1 \vec{k}_o \vec{k}_o + \vec{k}_o \hat{x}[\hat{x} \hat{x} S_1 + \hat{x} \hat{y} S_3] + \vec{k}_o \hat{y}[\hat{x} \hat{x} S_3 + \hat{x} \hat{y} S_2] + \underline{\underline{s}}_1 \vec{k}_o + \underline{\underline{u}}_1$. The transport equation (6) leads to a hierarchy of moment equations in the \vec{r} space. Truncating the system of equations to the third moment results to

$$\begin{aligned} k_o \frac{\partial}{\partial x} \rho + \nabla \cdot \vec{J}_1 &= 0 \\ k_o \frac{\partial}{\partial x} \vec{J}_1 + \nabla \cdot \underline{\underline{s}}_1 &= \frac{k_o^2}{2} \rho \nabla \epsilon_{1r} \end{aligned}$$

$$\begin{aligned}
k_o \frac{\partial}{\partial x} \underline{s}_1 + \nabla \cdot \underline{u}_1 &= k_o^2 \tilde{J}_1 \nabla \epsilon_{1r} \\
k_o \frac{\partial}{\partial x} \underline{u}_1 &= 3 \frac{k_o^2}{2} [\underline{s}_1 \nabla \epsilon_{1r} - \frac{\rho}{12} \nabla \nabla \nabla \epsilon_{1r}]
\end{aligned} \tag{7}$$

2.1 BSS Density Model

The power spectrum of a three second sample of high-resolution BSS data obtained in situ by the low orbiting AE-E Satellite is shown in Fig. 1. The irregularity spectral maximum occurs near one kilometer scale length and decreases for scale lengths longer than one kilometer [2].



The bottom panel shows the fluctuations of ion density (solid curve) from the RPA during a 3-s interval starting at 0449:30 UT on December 11, 1979, and the pitch or vertical drift (curve with solid circles) from the ion drift meter. The top panel shows the FFT (crosses) and maximum entropy method (solid line) spectrum of ion density fluctuations. The percent irregularity amplitude (sigma), the background ion density (NI), and the power law index (slope) of the roll-off portion of the spectrum are indicated on the diagram. The satellite altitude was 440 km.

Fig. 1.

The modeled irregularity spectrum, shown in Fig. 2, captures the BSS irregularities' characteristics specifying the perturbed dielectric function $\epsilon_1(\vec{r})$. The modeling procedure began with the superposition of the following three functions

$$\frac{\Delta N(k)}{N_o} = C_1[u(k) - u(k - k_2)] + C_2 \exp\left(\frac{-(k - k_2)^2}{2\Delta^2}\right) + C_1 \exp(-\gamma(k - k_2))u(k - k_2) \quad (8)$$

where $u(k)$ is the unit step function, $k_2 = \frac{2\pi}{\lambda_2}$ and $\lambda_2 = 1km$ is the dominate irregularity wavelength. C_1 , C_2 , Δ , and γ were chosen such that the power spectrum, $20 \log |\frac{\Delta N(k)}{N_o}|$, closely matched the observed irregularity spectrum in Fig. 1. An one dimensional inverse Fourier Transform, $\frac{\Delta N(k)}{N_o} \leftrightarrow \frac{\Delta N(\xi)}{N_o}$ was applied to Eqn. 8. The expression for the BSS irregularity in configuration space was then obtained to be

$$\frac{\Delta N(\xi)}{N_o} = \frac{C_1}{\pi} \frac{\sin(k_2 \xi)}{\xi} + \frac{2\Delta C_2}{\sqrt{2\pi}} \exp\left(\frac{-(\Delta \xi)^2}{2}\right) \cos(k_2 \xi) + \frac{C_1}{\pi} \frac{(\gamma \cos(k_2 \xi) - \xi \sin(k_2 \xi))}{\gamma^2 + \xi^2} \quad (9)$$

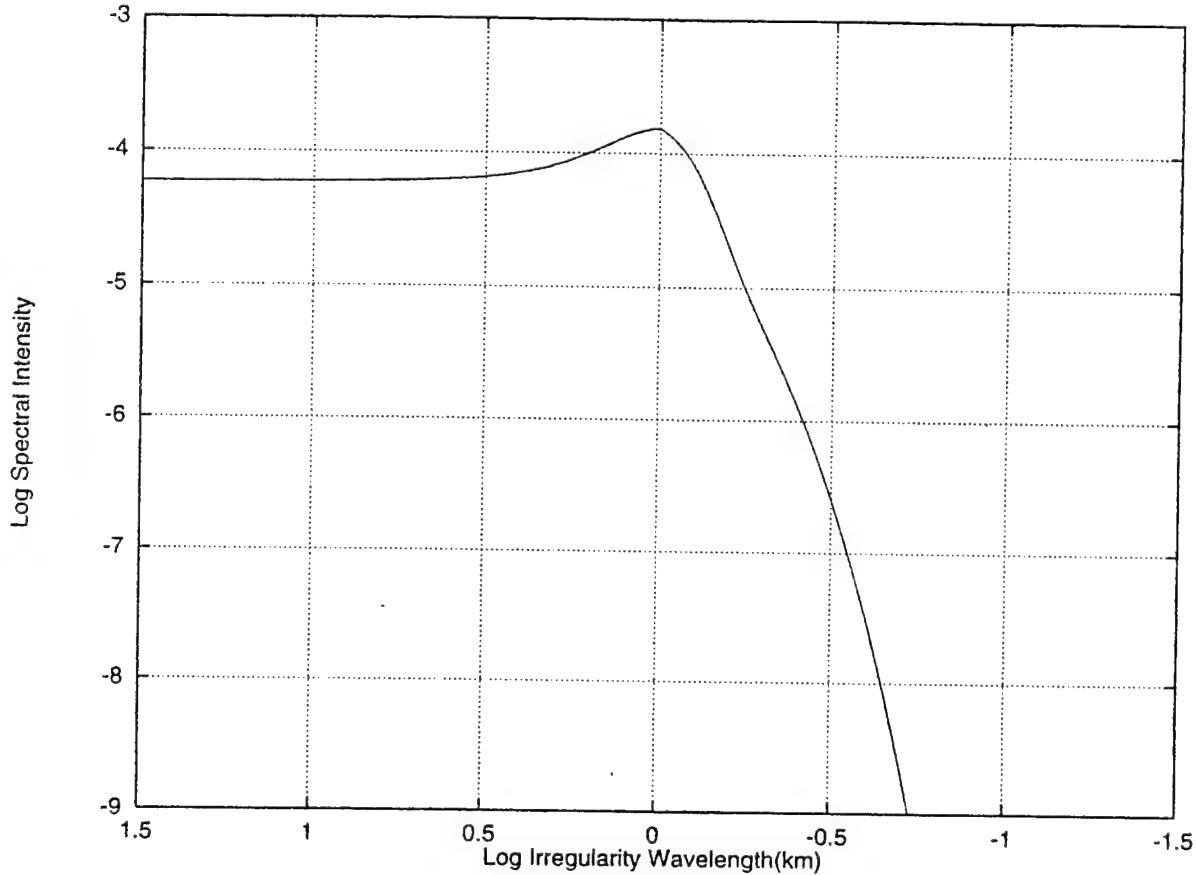


Fig. 2 Model of the Irregularity Spectrum

2.2 Schematic

A beacon satellite signal enters the BSS irregularity layer at an angle as shown in Fig. 3.

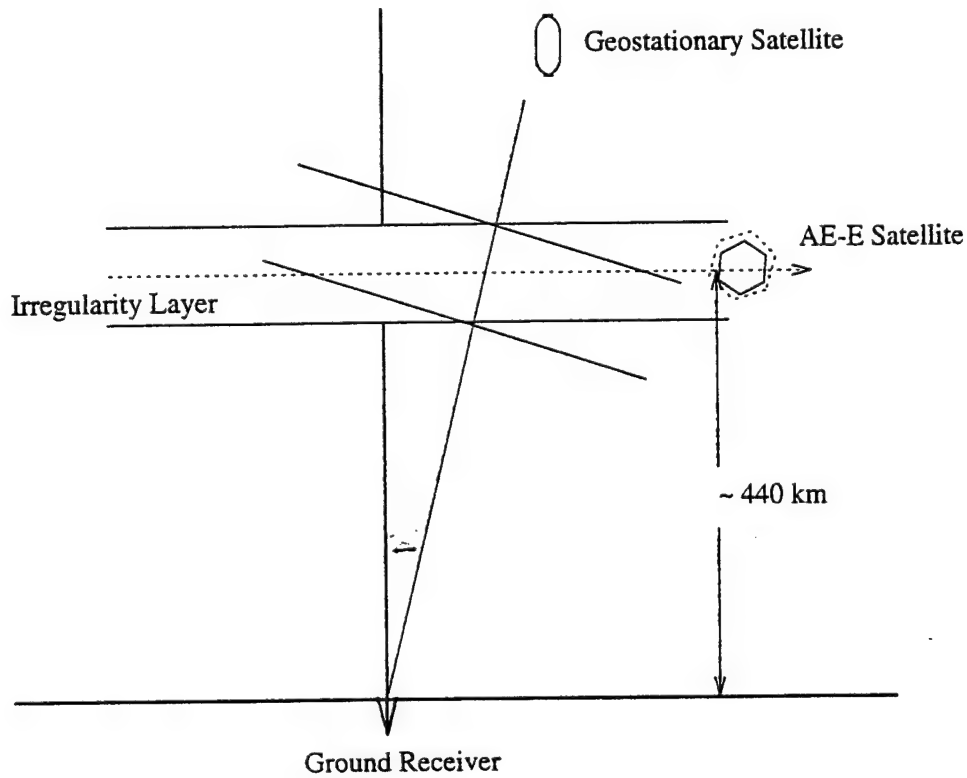


Fig. 3.

Generalizing Eqn. 9 into two dimensions, the density perturbation becomes

$$\frac{\Delta N(x, y)}{N_o} = P_\ell(x - \ell) \frac{\beta}{k_2 + \alpha + \frac{1}{\gamma}} \left[\frac{\sin \eta}{y \cos \theta} + \alpha \exp \frac{-(\Delta y \cos \theta)^2}{2} \cos \eta + \frac{\gamma \cos \eta - y \cos \theta \sin \eta}{\gamma^2 + (y \cos \theta)^2} \right] \quad (10)$$

where α is a shaping parameter related to C_1 , C_2 , Δ , and γ , $\eta = k_2 \cos \theta (y + x \tan \theta)$, $\beta = \frac{\Delta N}{N_o}$ the percentage of density fluctuation, $P_\ell(x - \ell) = 1$ for $0 \leq x \leq \ell$ and 0 otherwise. We consider the wave scattering within a two dimensional layer of BSS irregularities as shown in Fig. 4, where the layer is assumed to extend to infinity in the transverse direction and have a finite extent along the direction of propagation.

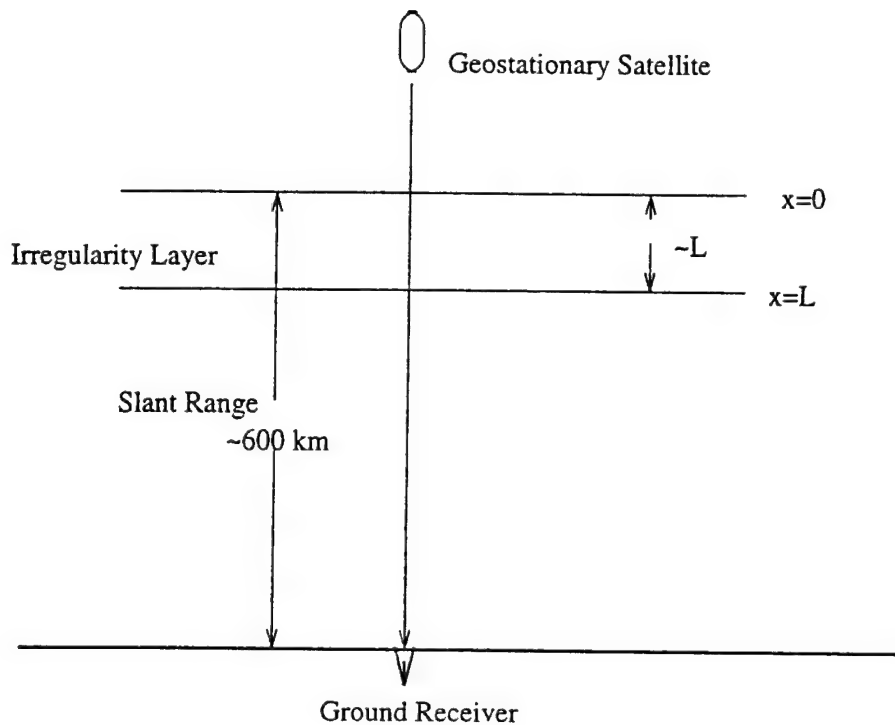


Fig. 4 Incoming plane wave scattered by a two dimensional irregularity layer with thickness L .

3 Numerical Analysis

Experimental observations were used to validate the applicability of the model to predict the scintillation index, S_4 , for various ionospheric conditions. Presented in Fig. 5 is the dependence of S_4 on the percentage of density fluctuation, β . S_4 increases with an increase in β as expected. Presented in Fig. 6 is the dependence of S_4 on propagation distance for three different scale lengths, $\lambda_2 = 1.0, 1.5$, and 2.0 km . $S_4 \approx .25$ at $x \approx 600 \text{ km}$ for $\lambda_2 = 1.0 \text{ km}$. The experimentally measured spectrum, shown in Fig. 1 has a maximum value near one kilometer scale length, indicating that this scale length is the dominant contributor to the observed scintillation. Presented in Fig. 7 is the dependence of S_4 on propagation distance for three beacon satellite frequencies 250, 350 and 450 MHz. S_4 decreases with an increase in signal frequency in agreement with theoretical predictions and experimental observations. Presented in Fig. 9 is the dependence of S_4 on the angle of incidence. It is

shown that the value of S_4 decreases, as the angle is increased. This may be a result of an increase in the scale length transverse to the direction of propagation. The curve for $\theta = 45^\circ$ presented in Fig. 8 shows that $S_4 = .29$ at $x \approx 600km$. This value agrees well with that of a 250MHz LES-8 geostationary satellite signal received at Huancayo, $S_4 = 0.31$ at $x = 588km$, measured in the presence of the BSS irregularities shown in Fig. 1 [2].

Propagation of beacon satellite signals through BSS irregularities in the equatorial F region of the ionosphere has been studied by the quasi particle approach, which intrinsically handles multiple scattering. The diffraction effect which was neglected in the previous work [6] is contained in this study, by including up to the third moment equation. The modeled density irregularities, including essential features of the experimentally measured power spectrum, makes the numerical simulation comparable to experimental conditions, consequently, the numerical results of S_4 agrees well with the measured S_4 .

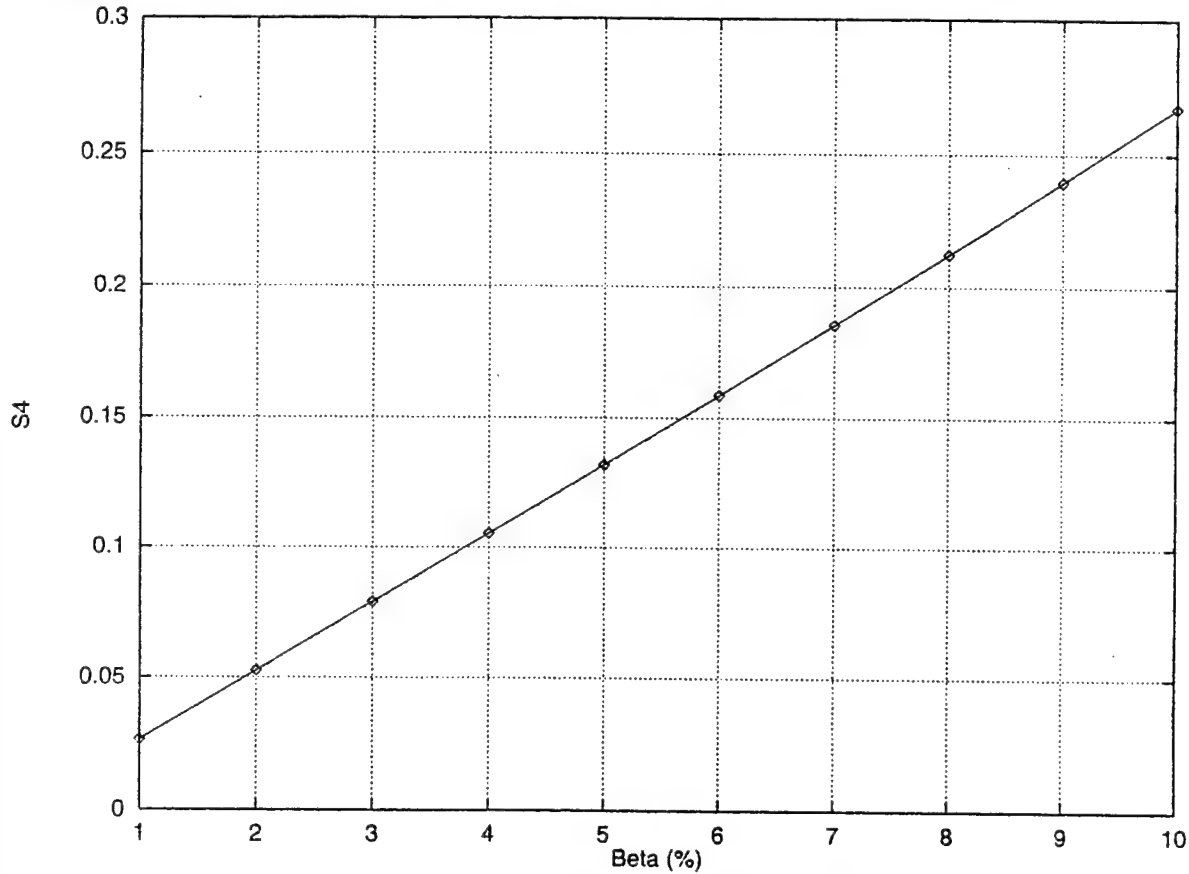


Fig. 5 S_4 verses β at $x = 600km$ for $\lambda_2 = 1.5km$, $L = 50 km$, $N_o = 1 \times 10^{11} m^{-3}$, $\theta = 45^\circ$, and signal frequency = 250MHz.

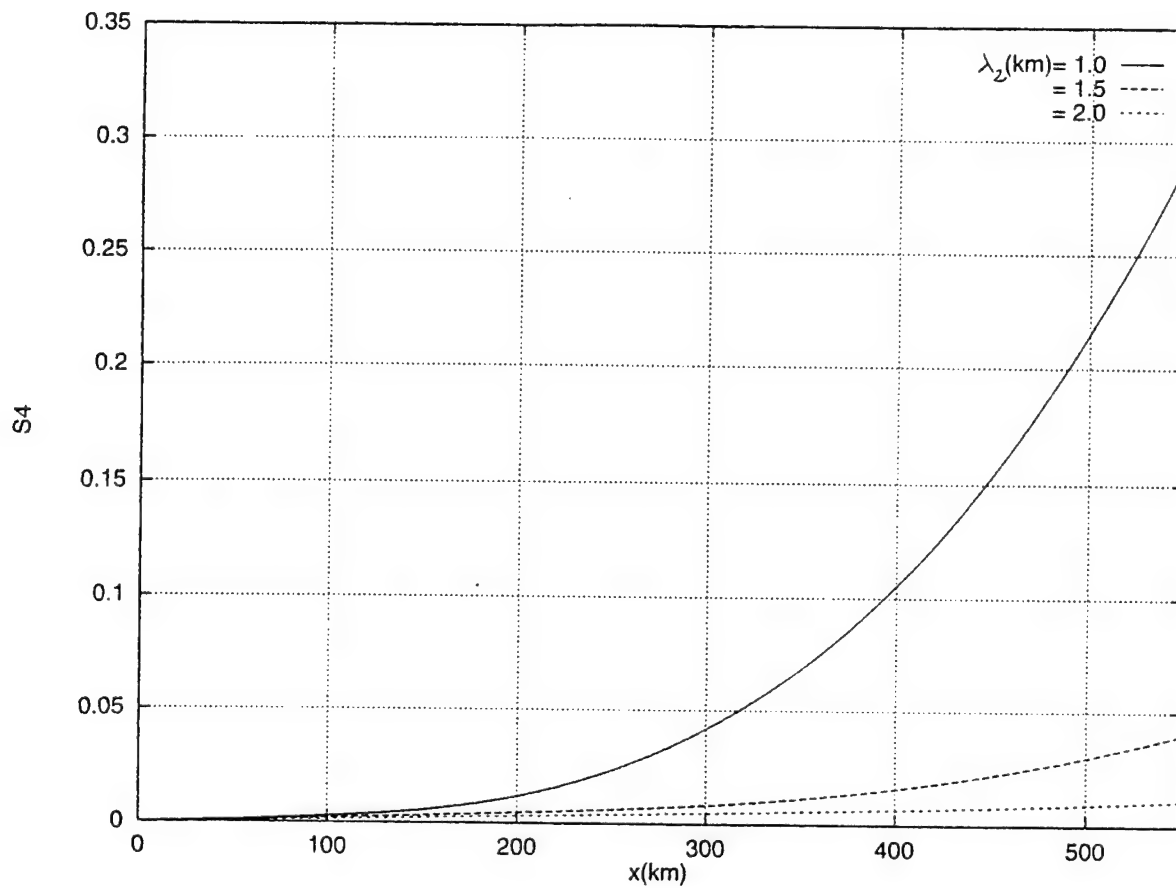


Fig. 6 S_4 verses propagation distance for $\beta = 2\%$, $L = 50$ km, $N_o = 1 \times 10^{11} m^{-3}$, $\theta = 45^\circ$, signal frequency = 250MHz, and $\lambda_2 = 1, 1.5$, and 2 km.

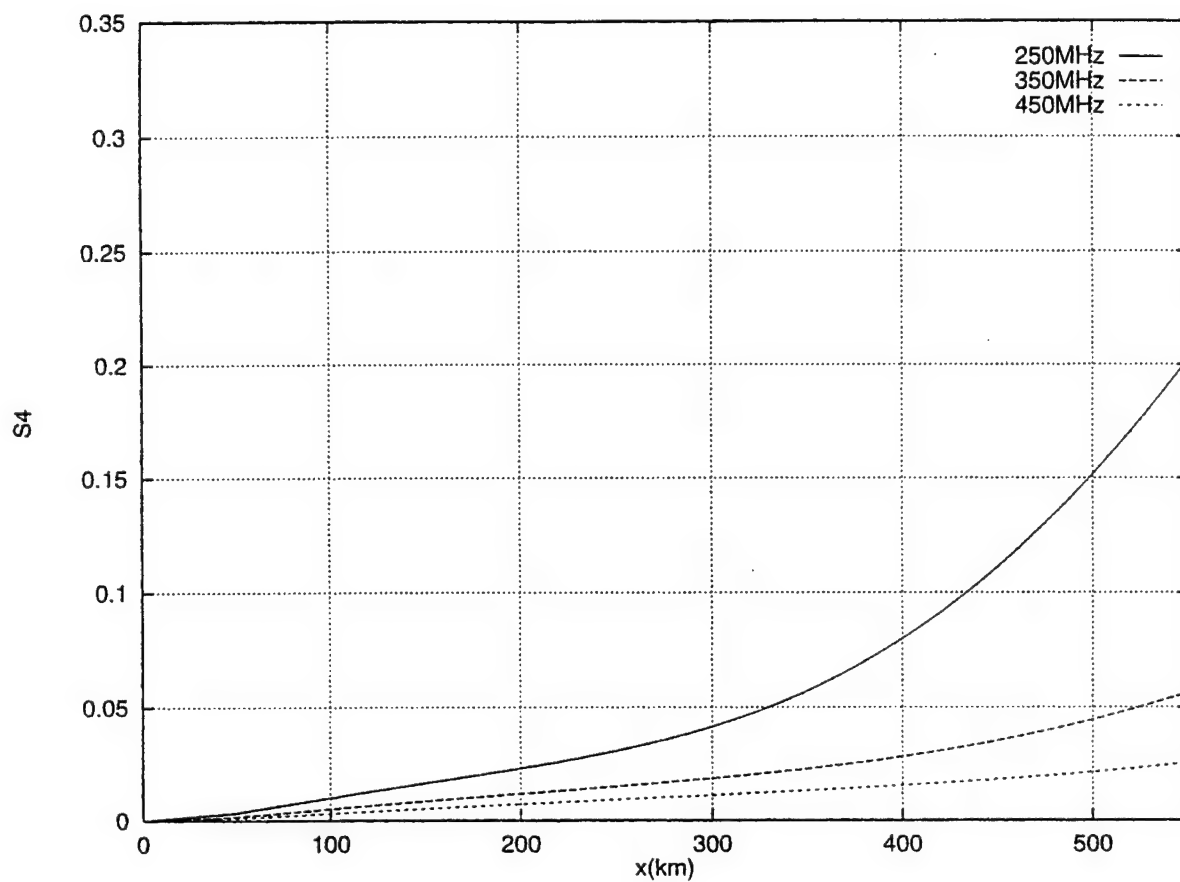


Fig. 7 S_4 versus propagation distance for $\beta = 10\%$, $\lambda_2 = 1.5 \text{ km}$, $L = 50 \text{ km}$, $N_o = 1 \times 10^{11} \text{ m}^{-3}$, $\theta = 45^\circ$, and signal frequency = 250, 350, and 450 MHz.

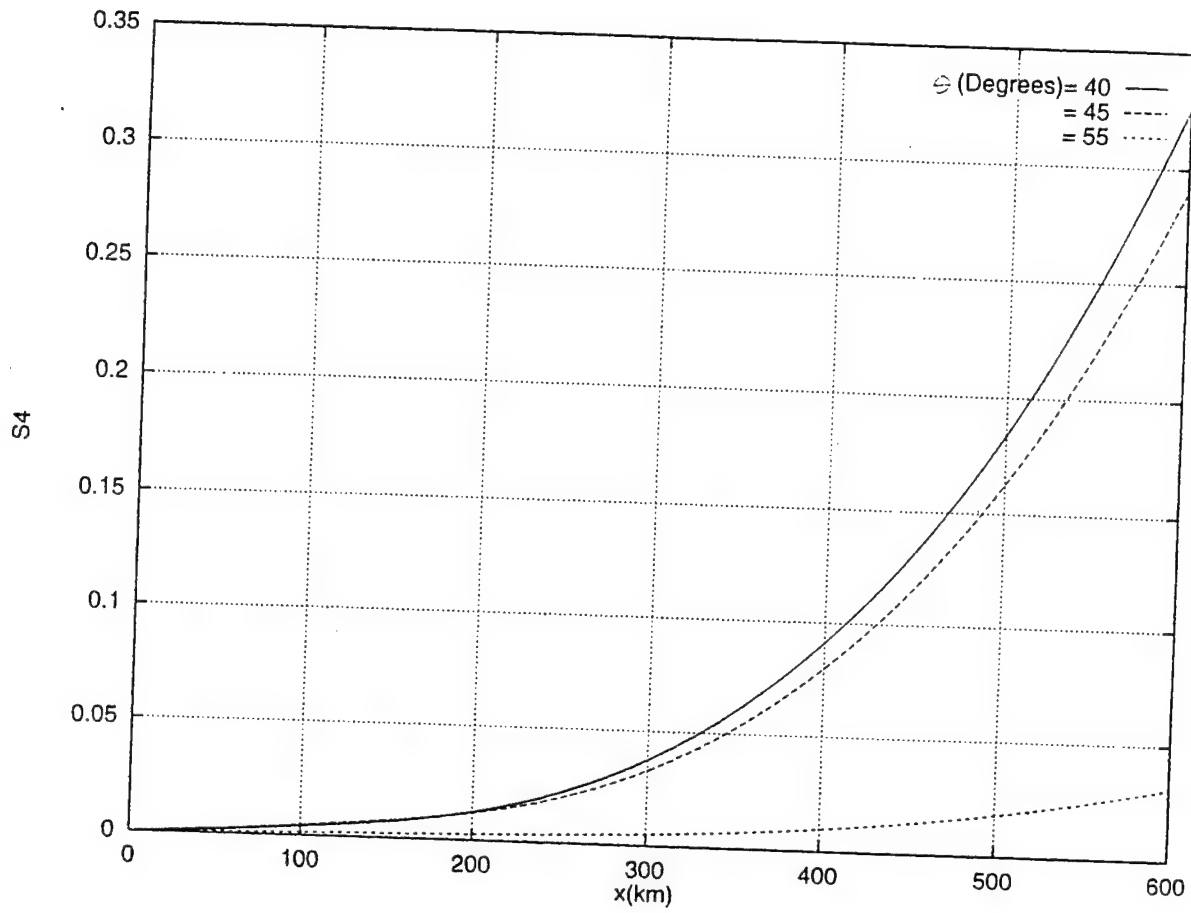


Fig. 8 S_4 verses propagation distance for $\beta = 3.5\%$, $\lambda_2 = 1.2\text{km}$, $L = 50\text{ km}$, $N_o = 1 \times 10^{11} \text{m}^{-3}$, signal frequency = 250 MHz, and $\theta = 40^\circ, 45^\circ$ and 55° .

Acknowledgments

The author is extremely thankful to her thesis advisor, Professor S. P. Kuo, for his guidance and commitment to excellence. The author extends sincere thanks to the entire Ionospheric Effects Division of Phillips Laboratory, Hanscom AFB. She is especially grateful to: Dr. Basu, Dr. Groves and Dr. Weber for useful discussions; to Dr. Valladares for providing experimental data; and to Dr. Bullet for lending computer expertise. The author is also grateful to Dr. Joe Huang of Lucent Technologies, and Professor D. Smith of the University of South Carolina for many useful discussions.

This work is supported by the AFOSR.

References

- [1] Basu, S., Eileen MacKenzie, Su. Basu, E. Costa, P. Fougere, H. C. Carlson, Jr., H. E. Whitney, 250 MHz/GHz Scintillation Parameters in the Equatorial, Polar, and Auroral Environments, *IEEE Journal on selected areas in Communications*, SAC-5(2), 102-115, 1987
- [2] Basu, S., Su. Basu, C. E. Valladares, A. Dasgupta, and H. E. Whitney, Scintillations Associated with Bottomside Sinusoidal Irregularities in the Equatorial F region, *J. Geophys. Res.*, 91(A1), 270-276, 1986.
- [3] Bremmer, H., General remarks concerning theories dealing with scattering and diffraction in random media, *Radio Sci.*, 8(6), 511-534, 1983.
- [4] Briggs, B. H., Ionospheric Irregularities and Radio Scintillations, *Contemp Phys.*, 16(5), 469-488, 1975.
- [5] Crane, R. K., Ionospheric Scintillation, *Proc. IEEE*, 65(2), 180-199, 1977.
- [6] Ho, A., S. P. Kuo, and M. C. Lee, Analysis of Electromagnetic Wave Scattering by Ionospheric Irregularities, *Radio Sci.*, 29(5), 1179-1186, 1994.
- [7] Jursa, A., "Handbook of Geophysics and the Space Environment", USAF, ch. 10, 1985
- [8] Marcuvitz, N., Quasi-particle view of wave propagation, *Proc. IEEE*, 68(11), 1380-1395, 1980.
- [9] Rishbeth, H., Physics and Chemistry of the Ionosphere, *Contemp. Phys.*, 14(3), 229-249, 1973.
- [10] Valladares, C. E., W. B. Hanson, J. P. McClure, and B. L. Cragin, Bottomside Sinusoidal Irregularities in the Equatorial F Region, *J. Geophys. Res.*, 88(A10), 8025-8042, 1983.
- [11] Wu, D. M., and N. Marcuvitz, Ionospheric scintillations, *Radio Sci.*, 18(4), 589-607, 1983.
- [12] Yeh, K., and C. Liu, Radio Wave Scintillations in the Ionosphere, *Proc. IEEE*, 70(4), 324-359, 1982.

**RESEARCH ON PLASMA DIAGNOSTICS FOR
VERSATILE TOROIDAL FACILITY:
GRIDDED ENERGY ANALYZERS**

**Shaun Meredith
Research Assistant
Department of Nuclear Engineering**

**Massachusetts Institute of Technology
77 Massachusetts Avenue
Cambridge, MA 02139**

**Final Report for:
Graduate Student Research Program
Phillips Laboratory**

**Sponsored by:
Air Force Office of Scientific Research
Bolling Air Force Base, DC**

and

Phillips Laboratory

September 1997

**RESEARCH ON PLASMA DIAGNOSTICS FOR
VERSATILE TOROIDAL FACILITY:
GRIDDED ENERGY ANALYZERS**

**Shaun Meredith
Research Assistant
Department of Nuclear Engineering
Massachusetts Institute of Technology**

Abstract

Gridded Energy Analyzers (GEA) are useful diagnostic tools for determining plasma ion energy distributions and ion temperature. The Versatile Toroidal Facility (VTF) at MIT's Plasma Science and Fusion Center provides a laboratory environment for studying ionospheric plasmas. Research was done on the theory behind Gridded Energy Analyzers and their applicability for use in the Versatile Toroidal Facility. A design and method for constructing a miniaturized GEA for VTF was developed and documented.

RESEARCH ON PLASMA DIAGNOSTICS FOR VERSATILE TOROIDAL FACILITY: GRIDDED ENERGY ANALYZERS

Shaun Meredith

Introduction

In 1989 Professor Min-Chang Lee and Ronald Parker proposed that a large plasma experiment be constructed at MIT's Plasma Science and Fusion Center, to simulate the ionospheric plasma conditions in a laboratory experiment. The Versatile Toroidal Facility as it became known was built starting in the summer of 1989. The device had a very slim budget and much of the construction was made possible through the donation of materials from discontinued fusion projects. The construction was completed by over twenty five students and VTF produced its first plasma in 1991. Since then several diagnostics have been installed and removed as the plasma was characterized further. Such instruments have included Langmuir probes, potential probes, dipole antennas, loop antennas, and a gridded energy analyzer. It is the latter of these devices which I have sought to improve upon.

The device itself is a toroidal plasma device with a major radius of 0.9 m and a minor radius of 0.3 m in which ionospheric plasma interactions can be studied. A basic list of parameters for VTF can be found detailed below.

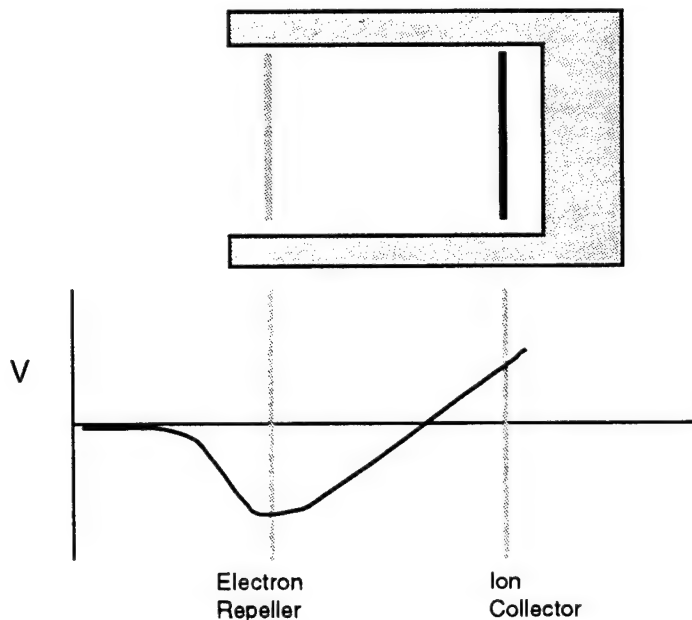
Major Radius	0.9 m
Minor Radius	0.3 m
Toroidal Field	1800 G
Vertical Field	20 G
Electron Density	10^{10} - 10^{12} cm ⁻³
Bulk Electron Temperature	10 eV

Currently, VTF has a diagnostic suite consisting of a potential probe, Langmuir probe, dipole antenna, and a loop antenna. A gridded energy analyzer was used as a diagnostic as recently as 1989 and it is this probe that I chose to concentrate my research efforts on. In order to understand how the project has

advanced, first some Langmuir Probe theory will be discussed followed by application of that theory to gridded energy analyzers. Finally, the discussion will address the shortcomings of the 1989 GEA and how the new probes design and manufacturing will differ.

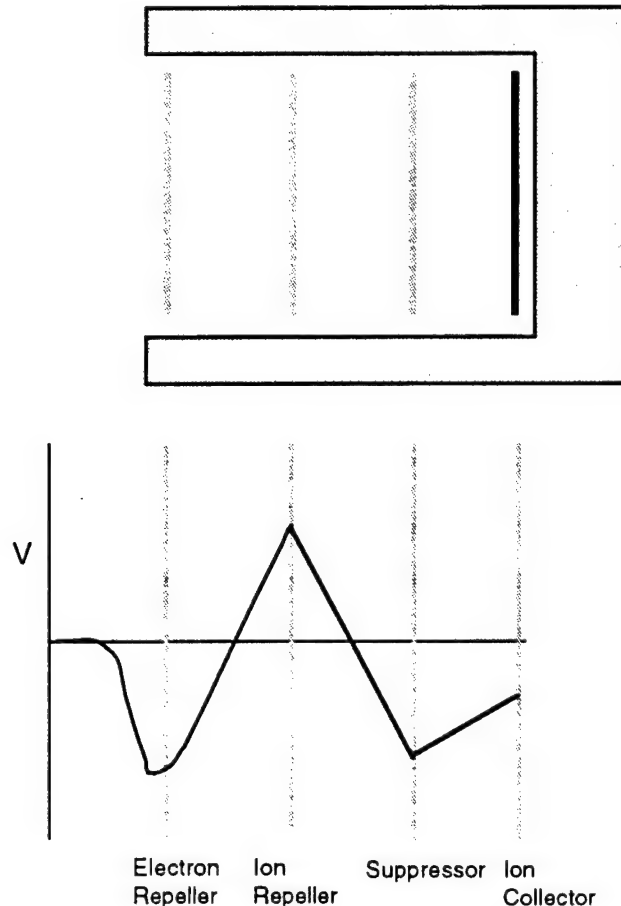
Theory

A detailed explanation of Langmuir probe theory is provided in Appendix A. As can be seen from Appendix A, when $T_i < T_e$ the Langmuir probe current is rather insensitive to ion temperature. That is where a more sophisticated analyzer can be of use. The Langmuir probe cannot easily obtain ion distribution measurements due to the large electron saturation current it draws when at a positive potential.



A solution to this dilemma is to use a gridded energy analyzer. A simple representation is shown in the previous diagram. The plasma is allowed to approach the collector only after passing through a grid. This grid is biased strongly negative to repel all the electrons. Then the collector voltage is varied so that only ions with energy greater than eV_c will be collected. This allows the logarithmic slope of the collected current to give the ion temperature.

The drawback of using a single grid is seen when we take into account secondary electron emissions from ions impinging on the grid. This problem can be accounted for by using the setup shown below.



In this gridded energy analyzer (which is the simplified diagram of the approach chosen to use in VTF), the first grid repels the electrons in the bulk of the plasma. The second grid is varied to allow ions of different energies to pass through to the collector and the third grid is biased negative again to repel secondary electrons. Finally, the collector is given a small negative bias to ensure good ion collection.

Another problem with gridded energy analyzers is the limitation caused by space-charges. When the plasma enters the analyzer additional charges are placed between the grids causing changes in the potential. This can be a problem if the charge builds up between two grids to be greater or smaller than the lesser of the

two grid potentials. If this happens then the result will be a lowering of the current of the species in question.

We can see that this worst case scenario can occur between the ion and electron repellers when the bulk of the ions have just enough energy to reach the ion repeller. This occurs when the potential has zero slope at the ion repeller which we can see in Appendix A is equivalent to the sheath solution when $V_s=0$. Thus we get an approximate result of

$$\frac{x}{\lambda_D} = \frac{2}{3} \left[\frac{2}{\exp(-1)} \right]^{\frac{1}{4}} \left(\frac{eV}{T_e} \right)^{\frac{3}{4}} = 1.02 \left(\frac{eV}{T_e} \right)^{\frac{3}{4}}$$

Therefore we can see for our plasma parameters, the distance between grids must be less than ~0.4 mm. This will be very difficult to manufacture.

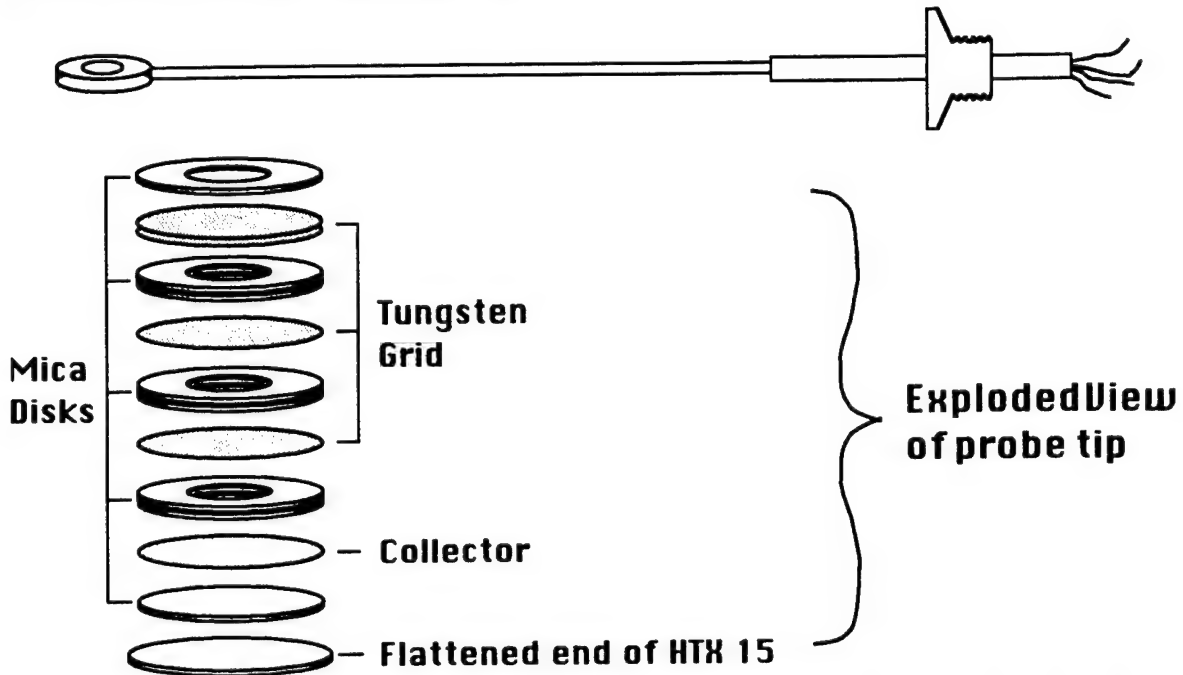
The GEA circa 1989 allotted for the space charge limit by placing a aperture before the probe to effectively reduce the density in the probe which increased the minimum spacing. This creates an unknown error in the plasma in the manifestation of total effective collection area. In addition, the previous probe perturbed the plasma in the respect that its dimensions were approximately 2.5 cm across in a 3 cm diameter plasma.

It is these limits that the new design has addressed. The probe is designed to be a non perturbing probe by reducing the characteristic size of the probe tip to approximately 5 mm. The space charge limitation is being addressed by placing thin mica sheets between the grids which should result in a spacing of .4 mm. Should this prove to be insufficient, a modified probe with a initial entrance grid of lower transparency will be used to increase the relative debye length.

Construction Technique

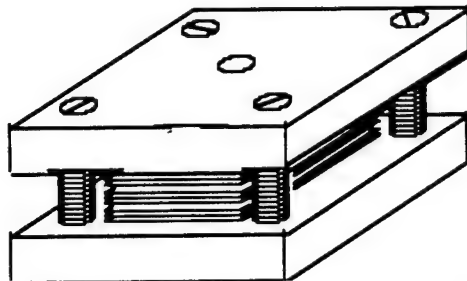
As the probe is much smaller than its predecessor extreme caution must be taken during the construction process. Many of the parts are small and delicate. In addition, many surfaces are nearly inaccessible for cleaning once the probe is

constructed. Since they will be exposed to vacuum it is necessary that great care be taken to maintain a high degree of cleanliness throughout the construction. Below is an exploded diagram of the probe tip.



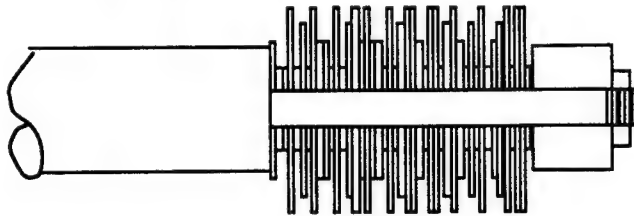
Manufacturing will be explained by addressing each part and then addressing the overall assembly.

The mica washers are extremely delicate and tend to crack during the machining process. For this reason it is recommended that three times the number of washers needed should be machined.

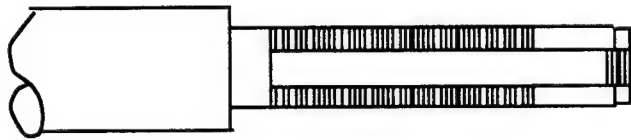


First, machine two brass plates approximately 1/4" thick with tapped holes at each corner for screwing them together. Using mica sheets of 0.4 mm thickness sandwich three times the number of mica sheets needed between two brass plates and clamp the plates together with screws at the corners. Drill a small hole through

the stack in the middle and then progressively use a larger bit until a diameter of 0.23 cm is reached. Next machine a mandrel like that shown below with an outer diameter equal to the inner diameter of the mica.



Before Turning

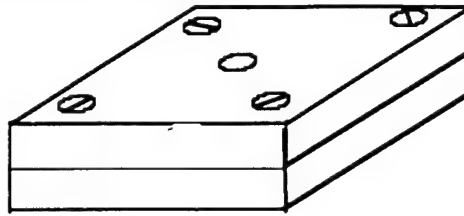


After Turning

Do not thread the rod where the mica will rest. This will cause the mica to fracture easily on the lathe. Clamp the mica down on the mandrel with a nut and then spin the mica disks down to an outer diameter of 0.43 cm on a lathe. This completes the mica washers.

Next, a tungsten mesh of 250 lines per inch and a line thickness of 0.001 inch is cut to provide the gridding. This mesh material was chosen to produce a grid capable of withstanding the high temperatures of the plasma. The grid also provides a 94% transparency to the plasma which minimizes secondary electron emissions. Using the same brass plates as before, clamp them together and drill the center hole out to 0.37 cm diameter. Then clamp the grid material between the brass plates one sheet at a time. This will prevent tearing of the material as it is cut to size. Grind the back end of the same drill bit that was used to widen the center hole so that it leaves a sharp edge all the way around. Keep the end of the bit flat so as not to deform the grid material during the cutting. Finally, use the drill bit as a punch and cut four meshes. More may need to be made for quality assurance purposes. Two meshes should be placed together slightly offset from one

another to make an entry grid with a lower effective transparency.

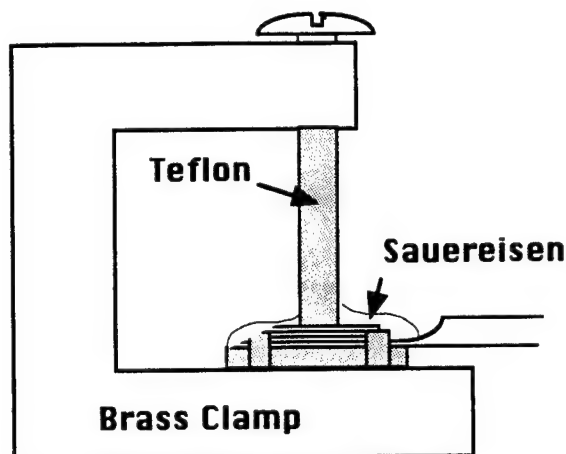


To connect the grids to the circuit, platinum wire of 0.005 inch diameter was chosen. The wire has high conductivity and also deforms easily for sufficient connection to the tungsten mesh as will be seen in the next few steps. Cut a length of wire that can go through about 8-10 inches of the four bore ceramic tubing discussed below. Loop the wire around the same drill bit used to punch out the mesh so that it has just enough material to form a single loop. Next, place the end of the loop and a section of tungsten mesh between two stainless steel blocks and clamp in a vise. This will flatten the platinum wire and press the mesh into the edges providing a semi-permanent bond.

Now the individual parts are constructed and the probe head is ready for final assembly.

To house the back of the probe use a "small parts" HTX 15 stainless steel hypodermic syringe cut open on one end and flattened to provide a disc shaped paddle of 0.46 cm in diameter as shown below. Four bore ceramic tubing is then cut to a desired length for the probe tip and placed inside the bore of the hypodermic syringe. The end of the four bore ceramic should just be even with the "paddle" on the syringe. The four bore ceramic is available from McDanel Refractory and has an outside diameter of 0.047 cm. As for the collector of the probe any conductive material should work nicely. Remember to cut one last mica disk of 0.46 cm diameter. This disk will not have a center hole.

Build a teflon and brass holder like the one pictured on the next page. The teflon material is used because the Sauereisen cement will not adhere to it during



the curing process. Make sure when building the clamping assembly that the central clamp post comes down evenly and aligned with the aperture of the probe tip. Three or four teflon posts can be used to position the probe head. Assemble the probe head by first placing the "small parts" HTX 15 hypodermic on the clamping assembly. Next, place a mica disk without a central hole and then the collector with a platinum loop. Following the exploded diagram place the components of the probe head down on the clamping mechanism in the correct order. Make sure that the four bore ceramic is included in the assembly. The ceramic should butt against the disk assembly and contain four platinum wires, one in each bore. Turn the central post down until the probe materials are held firmly in place. Carefully place Sauereisen Insa-lute Paste No. 7 around the edges of the probe head. Gently cut the teflon posts away from the probe and spread paste everywhere. Make sure that the paste extends a little over the end of the four bore ceramic. Once the paste is dry remove the probe from the clamping assembly and coat the back side.

Conclusion

The construction of the miniature gridded energy analyzer is currently in progress. The techniques presented here are working well and the scheduled completion of the probe is the first week in November, 1997. At that time the probe will be used to examine both electron and ion distributions in the VTF machine.

This should provide new insight into the interactions of particles and waves within the VTF plasmas. With this diagnostic functioning the researchers at VTF are anticipating looking further into using laboratory results to correlate with experiments conducted at the Arecibo Observatory in Puerto Rico. In addition, this documentation will aid in the maintenance of the probe and possibly the construction of more probes for other research devices.

Appendix A: Langmuir Probe Theory

The following assumptions are made for the analysis below:

- probe dimensions are large compared to the Debye length (VTF's Debye Length is about 0.1 mm and the probe tip will be about 0.5 cm)
- probe dimensions are small relative to the mean free path (VTF's mean free path is on the order of 1 m)
- in the ion saturation region the dimensions are much smaller than the Larmor radius of the ions. (VTF's ion Larmor radius is approximately 4 mm)

A metal probe inserted in a plasma will draw a current that depends on the applied potential, the plasma temperature, density, species, and the plasma reference potential. Careful interpretation of the results is required because the presence of the probe can alter local plasma conditions. Measurement of the I-V characteristic of the probe will yield electron temperature, T_e , electron density, n_e , floating potential, V_f , and plasma reference potential, V_p . Below is the theory that enables the interpretation of the results.

The current leaving a probe of surface area, A , is

$$I = -Ae (n_i v_i - n_e v_e)$$

where

n_i = ion density

n_e = electron density

v_i = ion velocity towards the probe

v_e = electron velocity towards the probe

For a Maxwellian distribution (using a one dimensional approach),

$$\sigma_e(x) = -e \int_{-v_0}^{\infty} f_e dv$$

$$J_e = -e \int_{-v_0}^{\infty} v f_e dv$$

where

σ_e = electron charge density

x = distance from the probe

J_e = current density

$$v_o = \sqrt{\frac{2e}{m_e} (\phi - \phi_o)}$$

ϕ = potential in sheath region near the probe

ϕ_o = potential of probe with respect to the bulk plasma

$$f_e = n_o \left(\frac{m_e}{2\pi T_e} \right)^{\frac{1}{2}} \text{Exp} \left(\frac{-m_e v^2}{2 T_e} + \frac{e\phi}{T_e} \right)$$

n_o = density far from probe

$$\sigma_e(x) = -en_o \left(\frac{m_e}{2\pi T_e} \right)^{\frac{1}{2}} \text{Exp} \left(\frac{e\phi}{T_e} \right) \int_{-v_o}^{\infty} \text{Exp} \left(\frac{-m_e v^2}{2 T_e} \right) dv$$

$$\sigma_e(x) = -en_o \text{Exp} \left(\frac{e\phi}{T_e} \right) \quad \text{since } e\phi \gg T_e$$

$$J_e(x) = -en_o \left(\frac{m_e}{2\pi T_e} \right)^{\frac{1}{2}} \text{Exp} \left(\frac{e\phi}{T_e} \right) \int_{-v_o}^{\infty} v \text{Exp} \left(\frac{-m_e v^2}{2 T_e} \right) dv$$

Since J_e is constant, choose x in the bulk plasma where $\phi=0$.

$$J_e = -en_o \left(\frac{T_e}{2\pi m_e} \right)^{\frac{1}{2}} \text{Exp} \left(\frac{e\phi}{T_e} \right)$$

Next we divide space into two regions, Region I where the Ions are accelerated to sonic velocity in quasineutral space and Region II or the sheath region where Poisson's equation must be solved.

Each Ion enters the sheath region at velocity v_i . Then, conservation of energy yields

$$\frac{1}{2} m_i v_i^2 + e\phi = e\phi_s + \frac{1}{2} m_i v_s^2$$

But the ions started deep in the plasma with no energy so the left hand side is set to zero leaving

$$v_i = \sqrt{-\frac{2e\phi}{m_i}}$$

Now

$$\sigma_i = \frac{J_i}{v_i} = \frac{J_i}{\sqrt{-\frac{2e\phi}{m_i}}}$$

Solving Poisson's equation:

$$\frac{d^2 \phi}{dx^2} = \frac{-1}{\epsilon_0} (\sigma_i - \sigma_e) = \frac{-1}{\epsilon_0} \left(\frac{J_i}{\sqrt{-\frac{2e\phi}{m_i}}} - en_o \text{Exp}\left(\frac{e\phi}{T_e}\right) \right)$$

It can be shown that to match regions I and II, ions must enter the sheath at the acoustic velocity (see Chen, 1984)

$$v_s = \sqrt{\frac{T_e}{m_i}}$$

then,

$$\phi_s = -\frac{m_i v_s^2}{2e} = \frac{-m_i}{2e} \frac{T_e}{m_i} = \frac{-T_e}{2e}$$

Since $n_e \sim n_i$ at the boundary,

$$\begin{aligned} \frac{J_i}{\sqrt{-\frac{2e\phi_s}{m_i}}} &= en_o \text{Exp}\left(\frac{e\phi_s}{T_e}\right) \\ J_i &= en_o \sqrt{-\frac{2e}{m_i} \left(\frac{-T_e}{2e}\right)} \text{Exp}\left(\frac{e}{T_e} \left(\frac{-T_e}{2e}\right)\right) \end{aligned}$$

$$J_i = en_o \sqrt{\frac{T_e}{m_i}} e^{-\frac{1}{2}} \sim 0.61 en_o \left(\frac{T_e}{m_i}\right)^{\frac{1}{2}}$$

Then the current is calculated as

$$I = -A (J_i + J_e) = A en_o \left(\left(\frac{T_e}{2\pi m_e}\right)^{\frac{1}{2}} \text{Exp}\left(\frac{e\phi}{T_e}\right) - 0.61 \left(\frac{T_e}{m_i}\right)^{\frac{1}{2}} \right)$$

(A more accurate numerical solution yields a coefficient of 0.54 instead of 0.61. From here on out we will use the more accurate coefficient.)

If we let V_p = plasma potential with respect to the chamber and realizing for an open circuit $V = V_f$ and $I=0$, we get,

$$V_f = V_p + \frac{T_e}{2e} \left(\text{Ln} \frac{m_e}{m_i} + 0.61 \right) \quad \text{Eqn (1)}$$

If we make ϕ_o sufficiently negative that the electron contribution is negligible and we run out of ions in the area, we get a limit on the current called the ion saturation current, I_{si} .

$$I_{si} = -Aen_o(0.54) \left(\frac{T_e}{m_i} \right)^{\frac{1}{2}} \quad \text{Eqn (2)}$$

We can obtain T_e by taking the derivative dI/dV

$$\begin{aligned} \frac{dI}{dV} &= Aen_o \left(\frac{T_e}{2\pi m_e} \right)^{\frac{1}{2}} \frac{e}{T_e} \text{Exp}\left(\frac{e\phi}{T_e}\right) \\ \Rightarrow T_e &= \frac{e(I - I_{si})}{\frac{dI}{dV}} \quad \text{Eqn (3)} \end{aligned}$$

So, The following procedure can then be used:

- measure the I-V characteristic
- from the slope at an arbitrary point get T_e using (3)
- from I_{si} and T_e get n_o from (2)
- from the zero crossing the floating potential, V_f , can be determined
- Using (1) get V_p using V_f and T_e

We can check the values of n_o obtained by recognizing that when $V = V_p$, the probe does not disturb the plasma. Then J_e correspond to the flux of electrons with half a Maxwellian distribution.

$$\begin{aligned} J_e &= -en_o \left(\frac{T_e}{2\pi m_e} \right)^{\frac{1}{2}} \\ I_{si} &= -AJ_e = Aen_o \left(\frac{T_e}{2\pi m_e} \right)^{\frac{1}{2}} \end{aligned}$$

We can approximate the electron saturation current as the value of I corresponding to voltage, V_p .

References

D. N. Arion and R. F. Ellis, Rev. Sci. Instrum. **53**, 1032 (1982).

R. Jones, Rev. Sci. Instrum. **49**, 21 (1976).

I. H. Hutchinson, *Principles of Plasma Diagnostics*, Cambridge University Press, Cambridge, 1987.

F. Chen, *Introduction to Plasma Physics and Controlled Fusion*, Plenum Press, 1984.

D. T. Moriarty, *Laboratory Studies of Ionospheric Plasma Processes with the Versatile Toroidal Facility*, MIT Nuclear Engineering Department Doctoral Thesis, 1996.

Massachusetts Institute of Technology, *Plasma Laboratory 22.69 Class Notes*, (Spring 1997).

**A Study of Atmospheric Perturbations
On a Suborbital Space Plane
Skipping Trajectory**

**Eric J. Paulson
Graduate Student
Department of Aerospace Engineering Sciences
University of Colorado-Boulder**

**Final report for:
Summer Graduate Research Program
Phillips Laboratory**

**Sponsored by:
Air Force Office of Scientific Research
Bolling Air Force Base, DC**

and

**Phillips Laboratory
Propulsion Directorate
Edwards Air Force Base, CA**

August, 1997

**A Study of Atmospheric Perturbations
On a Suborbital Space Plane
Skipping Trajectory**

**Eric J. Paulson
Graduate Student
Department of Aerospace Engineering Sciences
University of Colorado-Boulder**

Abstract

A study was conducted to investigate the possibility of a suborbital global reach military space plane, using the Gram-95 atmospheric model integrated with the trajectory analysis code POST 3D. The ability to perturb the atmosphere through GRAM-95 provided a look at the possible problem areas with regards to this specific mission design. Items pointed out include heat rates, total heat, diurnal variations, and dynamic pressures.

A Study of Atmospheric Perturbations On a Suborbital Space Plane Skipping Trajectory

Introduction

Professor David Stapleton of the University of Central Oklahoma and myself, in connection with the Propulsion Analysis Branch conducted a study, supported by the Air Force Office of Scientific Research (AFOSR), at Phillips Laboratory, Edwards AFB. We modified a trajectory analysis and optimization code (Program to Optimize Simulated Trajectories-POST), and a modern atmospheric model (NASA-Marshall Space Flight Center's GRAM-95), to perform trajectory Monte Carlo simulations. The purpose was to investigate the perturbations a dynamic atmosphere makes to a proposed mission design, such as the suborbital-skipping trajectory investigated here.

By using a skipping trajectory, you enable an extended range for a reentry vehicle. This allows delivery of a substantial payload to a near-orbital separation point, where a small upper stage boosts the payload to its final orbit, while the launch vehicle continues around the globe. This enables a vehicle launched from a CONUS location to return to its original launch site, or a CONUS dispersed site.

The model vehicle used for the study was the Boeing Reusable AeroSpace Vehicle (RASV) single stage to orbit (SSTO) concept. RASV is a sled launched HTHL (horizontal takeoff, horizontal landing) vehicle using two SSME derived engines with extendible two-position nozzles for propulsion. The two-position nozzles increase the nozzle's efficiency through the flight regime, and for this case could possibly be further optimized for the suborbital trajectory. A cutaway illustration of the vehicle is shown in figure 10-1.

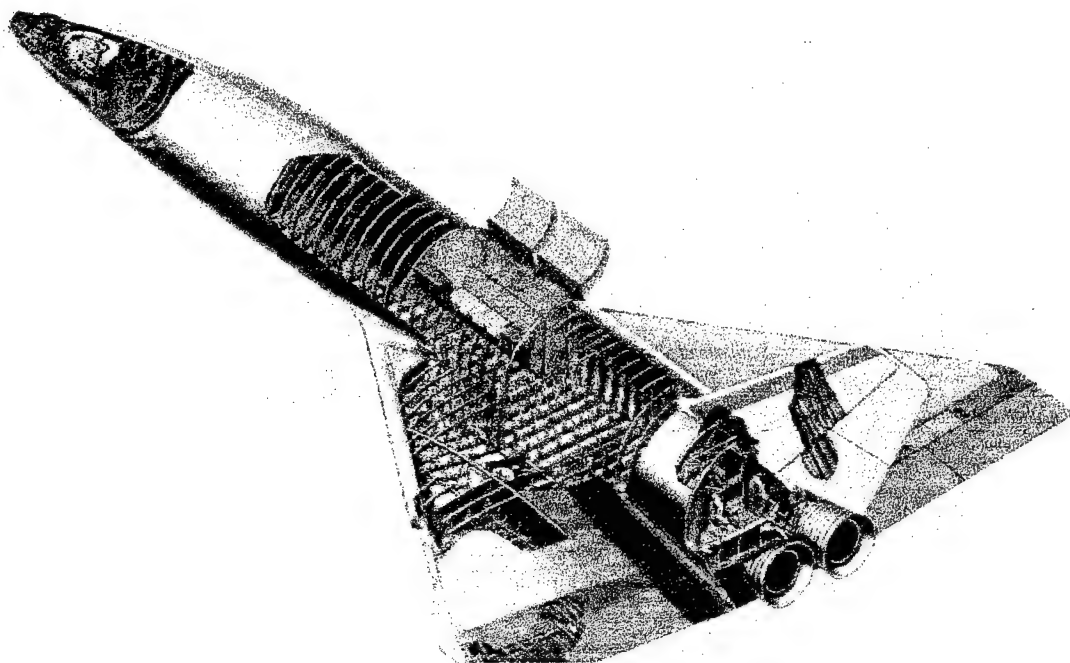


Figure 10-1 (Boeing)

The vehicle model flight controls were optimized in POST 3D to maximize payload to the suborbital delivery target. The model simulated a polar route to the south, returning with its entire payload, as a worst case scenario. The launch and targeted landing site was Edwards AFB. During initial optimization the POST program used the 1962 U. S. Standard model atmosphere, which returns density as an exponential function of altitude.

The controls that optimized the payload weight were then input as the flight controls of a second POST RASV model, using the GRAM-95 model atmosphere called as a subroutine. A series of 20 runs with varying atmospheres for each of four separate months were run: January, March, July, & October. The original 80 runs by Dr. Stapleton were run for a GMT of 1:00 AM. The perturbed atmosphere caused variations to the original baseline RASV trajectory. The resulting changed flight paths are detailed in Dr. Stapleton's paper in the 1997 Summer Research AFOSR report, Chapter 29. In all cases the final position was short of the targeted landing site, by varying amounts. An example trajectory is shown in figures 10-2 and 10-3.

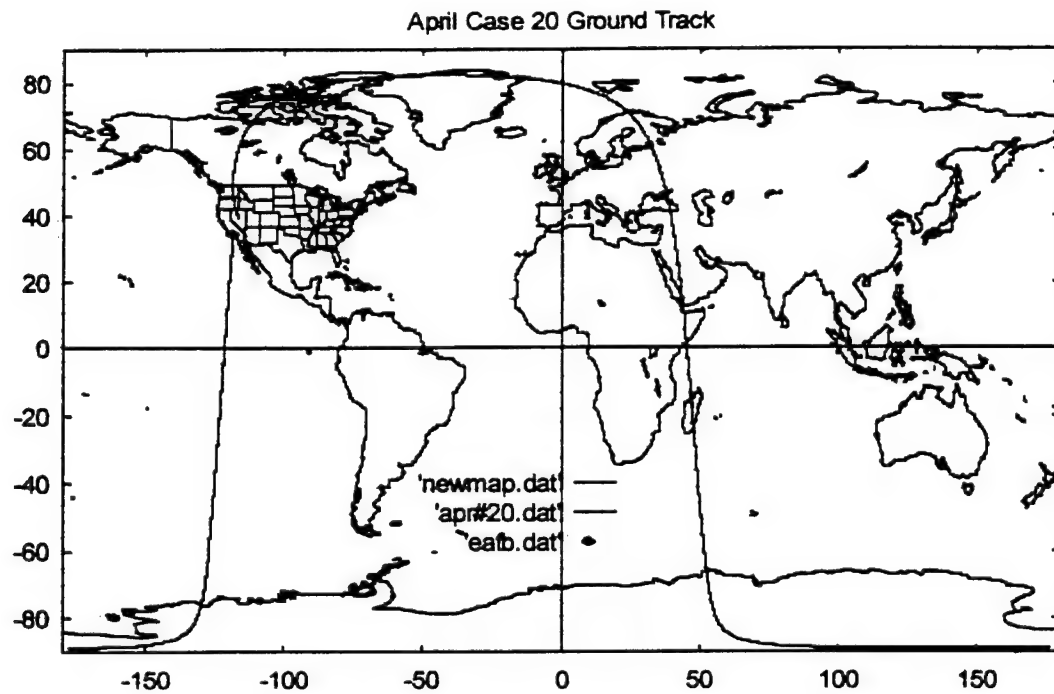


Figure 10-2

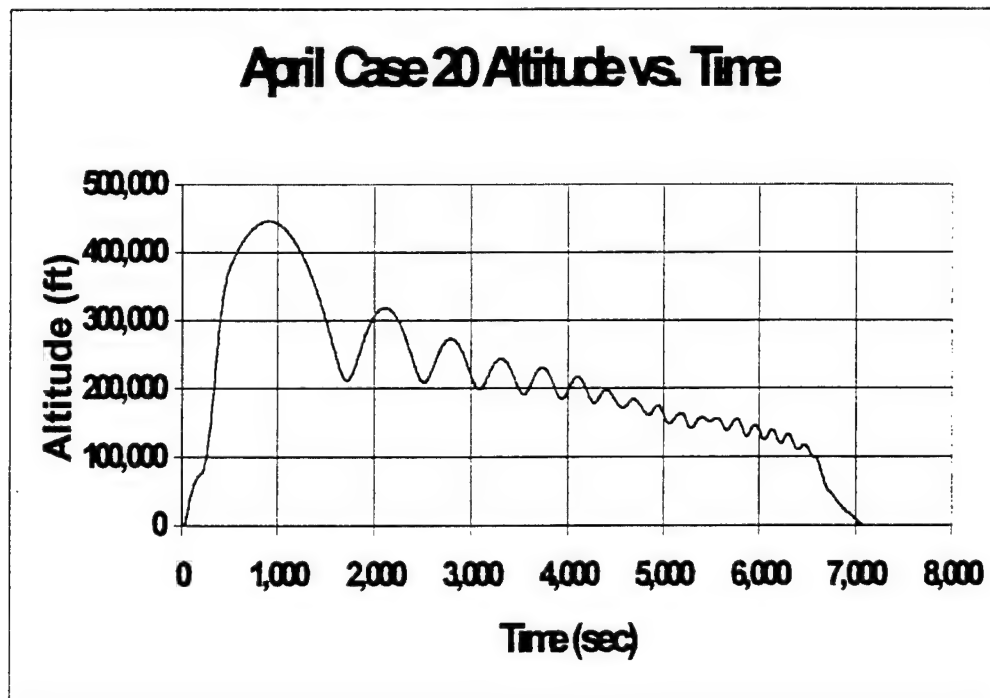


Figure 10-3

Tools

We started with POST 3D Version 5.1, modified for the PC. The FORTRAN code was modified to take advantage of modern computer processor abilities, such as multiply-add units. In other cases we unrolled do loops, and reduced subroutine calls. At the completion of the POST modifications, the CPU time required for an ATLAS launch-to-GTO test case was reduced from 400 seconds to 216 seconds on a 120 MHz Pentium laptop. This allows for significant timesavings in a batch job such as a Monte Carlo simulation.

Dr. Stapleton modified the POST subroutines that called the atmosphere models built into POST. The change code instead calls GRAM-95 as a subroutine during equation-of-motion calculations for atmospheric density, to calculate drag, atmospheric heating, lift, etc. This results in a slower POST run, due to the more elaborate GRAM atmosphere model, but one that takes into account wind, latitude, seasons, and other atmospheric perturbations.

NASA/MSFC's GRAM-95 was originally written for workstations, and plans are to integrate GRAM and POST for workstations at Phillips Lab's Propulsion Analysis Branch. Since the modified POST code does take longer to run, a high end PC or workstation is advisable to run the program. The Monte Carlo runs referred to in this study were, in most cases, performed on a 200 MHz PC with 16MB of RAM in DOS mode, which is the minimum amount of RAM required. A CD-ROM drive with Global Upper Air Climatic Atlas CD data (GUACA Version 1.0-see Ruth, et al., 1993) was also required for the ~ 42MB of data required by the GRAM 95 lower atmosphere (less than 27 km) routine.

Maximum Altitude Variation

The most striking result of the data from the 80 model runs, was the wide variation in the peak altitude after launch. The original optimized simulation had several targets that had to be met at engine burnout. They were:

- 1) *inertial flight path angle = zero degrees, within 0.001 degrees*
- 2) *altitude = 340,495 ft, within 100 ft*
- 3) *relative velocity = 25,814 ft/s, within 10 ft/s.*

In addition, the vehicle had to return to EAFB.

A second model was run using the GRAM-95 atmospheric model, fixing aerodynamic controls to the optimized values from the first simulation. The resulting peak altitudes in the 80 simulations varied from 366,600 ft to over 665,000 ft. The low and high of the 80 trajectories are displayed in figure 10-4 below.

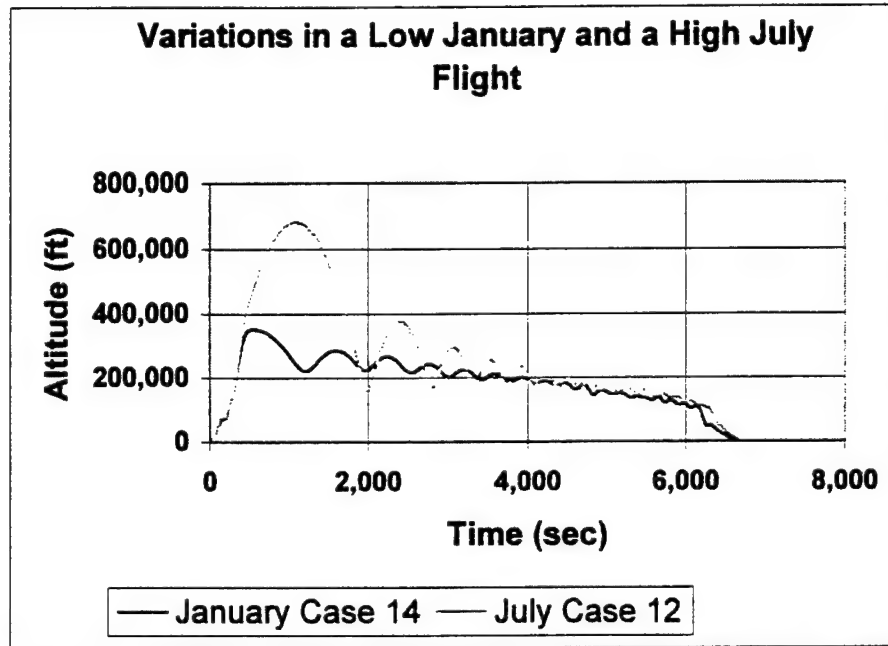


Figure 10-4

Heating

A related consequence of the altitude sensitivity, was the variation in heating rate that occurred in the troughs of the altitude excursions during skipping. The aeroheating calculations were calculated by POST using the Chapman equation for stagnation convection heating.

$$\frac{dQ}{dt} = \frac{17600}{\sqrt{R_N}} \cdot \sqrt{\frac{\rho}{\rho_{SL}}} \cdot \left(\frac{V_A}{26000} \right)^{3.15}$$

Where R_N = spherical nose radius, ρ_{SL} = atmospheric density at sea level, and V_A = vehicle velocity relative to the atmosphere

As you can see from figure 10-5, the peak heating rate varied from 400-200 BTU/ft²/sec.

The total heating varied between 600,000 and 490,000 BTU/ft². A more precise heating model allowing for Boeing's RASV design and radiation to the atmosphere during skipping peaks would be a valuable point of study for a skipping trajectory mission design. The limitations of TPS (thermal protection systems) obviously would be a design driver for this type of mission design.

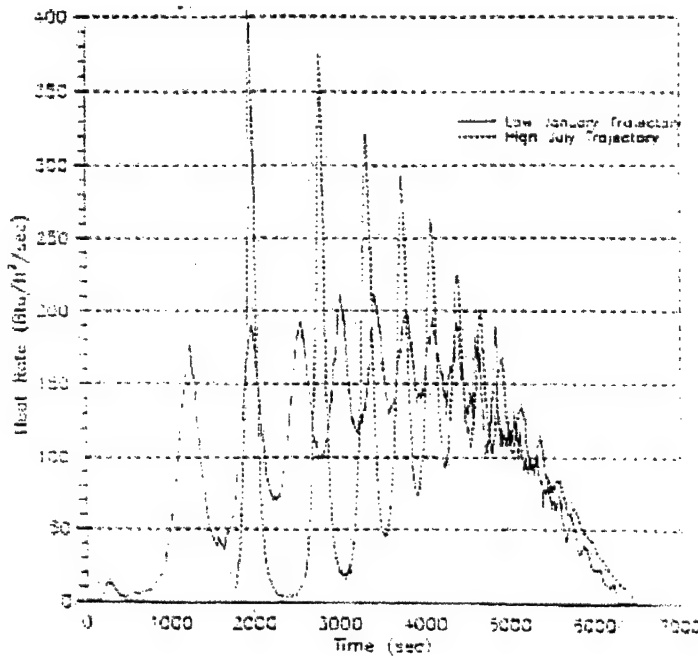


Figure 10-5: Heat Rates for a High January and a Low July Trajectory

Diurnal Perturbations

The GRAM-95 model takes into account diurnal variations in the atmosphere through the use of data for the Jacchia model, for altitudes above 90 km (295,300 ft). The trajectories in general spent very little time in this region, so the effect on the trajectories was small. Figure 10-6 shows the difference due to diurnal effects in a January case launched at 1 AM and 1 PM for comparison. The variation in final position compared to the 1 AM launch was 0.07 degrees east, and 0.23 degrees south, overall about 20 miles closer to the target landing site.

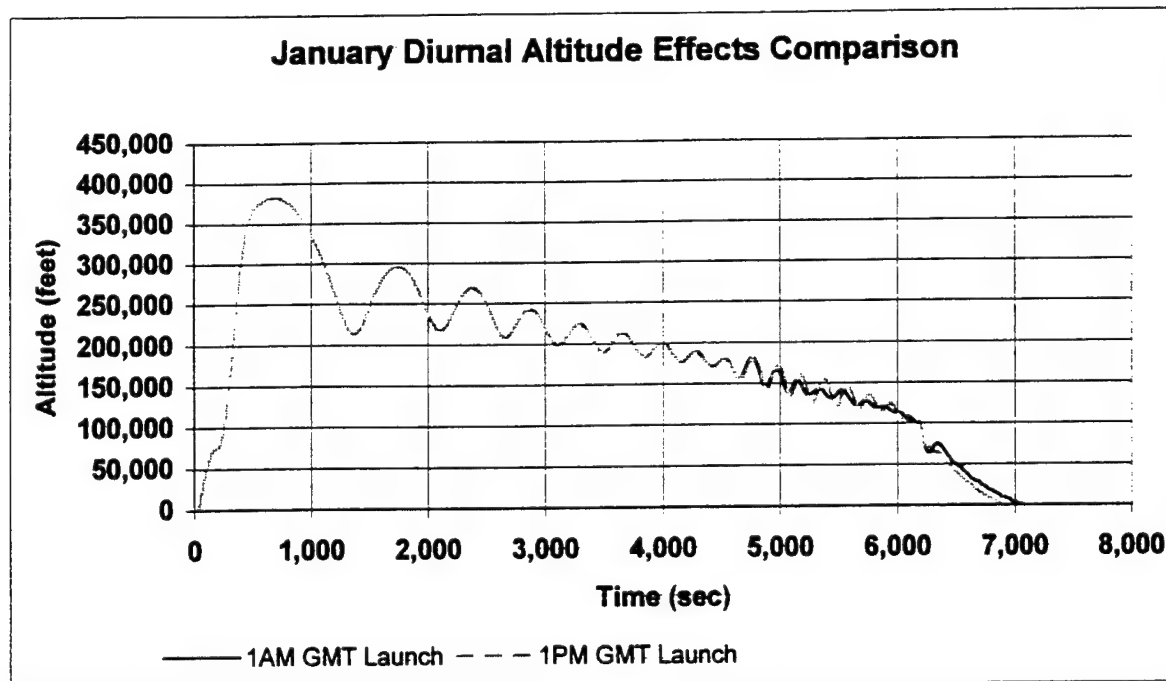


Figure 10-6

Dynamic pressures

An example of the dynamic pressures experienced during these flight trajectories simulations is shown in figure 10-7. A maximum dynamic pressure limitation for the structure may be a limitation on allowed trajectories. This would become a constraint for a more in depth trajectory analysis. Also of interest for controllability are the low dynamic pressures for the first several altitude peaks.

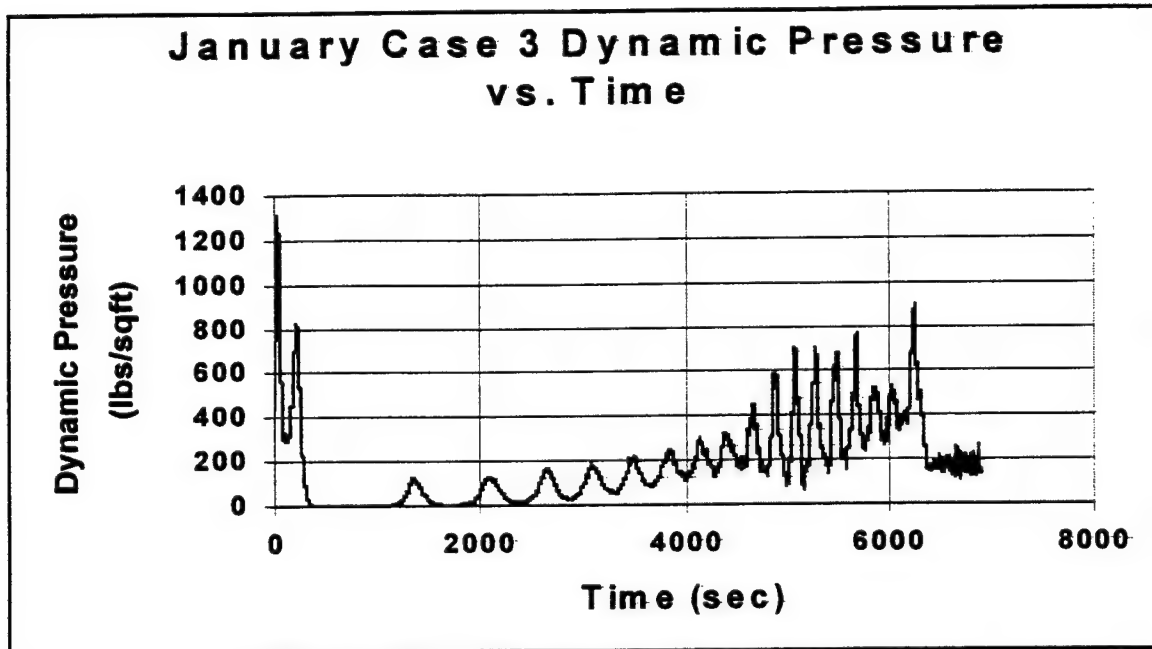


Figure 10-7

Altitude Drops during Takeoff

A trend manifested in some of the case runs, including a majority of the July runs, was an altitude loss 20-30 seconds after liftoff, when the vehicle is essentially a plane dependent on wing-generated lift for ascent. This vehicle design has a thrust-to-weight ratio of less than one at takeoff. With variations in atmospheric density, and an angle of attack at liftoff from the sled of 12 degrees in our RASV POST model, the lift generated, in some cases, was less than adequate to maintain climbing flight. In 18/20 July simulations, an altitude drop of 50-100 feet was seen, including one run that achieved a negative flight altitude for several seconds.

Upon further research into the RASV design, a takeoff angle of attack of 15 degrees was cited in later documents. The cases have not been rerun at the 15-degree AOA. This problem illustrates the sensitivity of a horizontal takeoff vehicle to atmospheric perturbations.

Summary

The data resulting from the simulations performed seem to indicate that a suborbital-skipping trajectory is a possible solution to a payload delivery system. The vehicle modeled here was not optimized for this type of trajectory, and there are other issues not addressed by this study. A few of which include wing/structural loading during the troughs of the skips, the possibility of vehicle structure radiating to the atmosphere during the peaks of the skips, and even the physiological effects, in a piloted vehicle, of a two-hour rollercoaster-like ride. Further study could include the potential of synergistic orbit changes during the skips to increase the effective groundtrack width of the vehicle, and the performances of different body types (i.e. winged body vs. lifting body) with regards to this type of trajectory.

References

Brauer, G. L., et al., (1989): *Program to Optimize Simulated Trajectories (POST)*, VOL. I & II, Martin Marietta Corp., Denver CO.

Justus, C. G., et al., (1995): *NASA/MSFC Global Reference Atmospheric Model-1995 Ver. (GRAM-95)*, NASA Technical Memorandum 4715, NASA Marshall Flight Center.

Ruth, D.B., et al. (1993): *Global Upper Air Climatic Atlas (GUACA)*, U.S. Navy – Dept. of Commerce, Naval Oceanography Command Detachment Asheville National Climatic Data Center

Stapleton, David P., (1997): *Atmospheric Effects Upon Sub-orbital Boost Glide Spaceplane Trajectories*, 1997 AFOSR Summer Research Program Final Report.

**A NEW TECHNIQUE USED TO DETERMINE THE TIME EVOLUTION OF
THE FREQUENCY IN HETERODYNE SYSTEMS**

**Christopher W. Peters
Graduate Student
Department of Nuclear Engineering**

**University of Michigan
Department of Nuclear Engineering and Radiological Sciences
Ann Arbor, MI 48109-2104**

**Final Report for:
Graduate Student Research Program
Kirtland AFB
Phillips Laboratory**

**Sponsored by:
Air Force Office of Scientific Research
Bolling Air Force Base, Washington, DC**

And

Phillips Laboratory

August 1997

A NEW TECHNIQUE USED TO DETERMINE THE TIME EVOLUTION OF THE FREQUENCY IN HETERODYNE SYSTEMS

Christopher W. Peters
Graduate Student
Department of Nuclear Engineering and Radiological Sciences
University of Michigan

Abstract

Determining the time rate of change of frequency from heterodyne signals is difficult. Many methods have been attempted in solving this problem. Both the zero point and least squares method result in gross overestimation or underestimation of the frequency when the frequency is changing with time. This causes improper determination of competing modes and frequency chirping in waveguides. The method described in this report utilizes the model of sinusoids. Results show this model is more accurate than the zero point and least squares method. The Interactive Data Language (IDL)² by Research Systems, Inc. is used for the programming so the analysis can be immediately executed upon obtaining the data.

Methodology to Solving Problem

Heterodynes used for microwave detection measure voltage as a function of time. The signal from the heterodyne is relatively smooth and will generally have oscillatory properties. Assume the heterodyne signal is of the form

$$V = V_0 \sin(\omega t) \quad (1)$$

Where

V =Voltage

V_0 =Amplitude of the signal

ω =frequency (rads/sec), which can change with time

Taking the derivative with respect to time gives,

$$\frac{dV}{dt} = V_0 \cos(\omega t) \frac{d\omega t}{dt} \quad (2)$$

But

$$V_0 \cos(\omega t) = \sqrt{V_0^2 - V^2} \quad (3)$$

Therefore

$$\frac{d\omega t}{dt} = \frac{dV}{dt} \frac{1}{\sqrt{V_0^2 - V^2}} \quad (4)$$

Both of the terms on the RHS of the last equation can be positive or negative. The result can be expressed as the absolute value of both terms. Hence,

$$\frac{d\omega t}{dt} = \left| \frac{dV}{dt} \frac{1}{\sqrt{V_0^2 - V^2}} \right| \quad (5)$$

Integration of Eq. (5) yields

$$\omega = \frac{\int_0^t \left| \frac{dV}{dt} \frac{1}{\sqrt{V_0^2 - V^2}} \right| dt}{t} \quad (6)$$

The information obtained directly from a heterodyne is the voltage and amplitude. The derivative of voltage with respect to time can be calculated using a numerical method technique.

PROCESSING OF THE SIGNAL

The data from a heterodyne is discrete. Therefore, important data may not be present. This section discusses the various methods used to manipulate the data obtained from the heterodyne.

Calculation of zero points

Because the data is discrete, it is possible for the voltage to switch from a positive value to a negative value (or vice versa) without resulting in a zero value. Interpolation between the two data points is necessary. Linear interpolation is sufficient if the time interval between data points is small and the assumption that the signal is a linear function between the data points.

Calculation of minimums and maximums

The calculation of frequency requires knowledge of the minimums and maximums of each signal. Consider a sinusoidal function with two points, 1 and 2, which have a positive and negative slope. There must be a minimum or a maximum, point 3, present between these points if the data is smooth and continuous. Taking the slopes at points 1 and 2, the result is two equations with two unknowns, of which the position of the maximum and minimum can be solved simultaneously.

Normalization of data

The signal may not have the same absolute value at each minimum and maximum. The frequency of the signal is not dependent on amplitude, therefore no problems should occur if the data is normalized between zeroes. This allows for easier calculation of frequency. Thus, V_0 will always have a value of one.

Cubic splining of data

The resolution of the heterodyne has a direct effect on the calculation of frequency. If the resolution is poor, then the sampling rate is insufficient at higher frequencies. Calculation of frequency is more accurate with heterodynes having higher sampling rates. To compensate for the resolution, a cubic spline interpolation of the data is used.

RESULTS

Five different simulations in frequency variation were used to test the validity of the method used. Figures 1 through 5 represent the various tests. For each figure, three graphs are presented. The top graph represents the input signal created by the computer. The middle graph displays the cubic spline fit of the data in the top graph. The bottom graph presents the calculated and expected frequency. The solid line indicates the calculated frequencies, while the dotted line indicates the expected frequencies.

The tests conducted were:

1. Constant Frequency - a constant frequency of 100 MHz was chosen due to the relatively high frequency over a time span of 250 ns. Testing the simulation for high frequency allows for determining when the program fails due to poor sampling. Figure 1 displays the signal created, the cubic spline fit, and the frequency calculation. The equation used to generate the data was

$$V = \sin(2\pi ft) \quad (7)$$

where f is the frequency and t is time. The generated data behaved as expected. The frequency calculation revealed a deviation from the expected value at early times. This deviation is due to the integration technique and the simulated resolution. IDL uses a five point Newton-Cotes¹ technique for tabulated integration. The resolution of the data was 2.5 ns.

2. Linearly Increasing Frequency- an input signal with a frequency varying from 50 MHz to 120 MHz in 250 ns. Figure 2 displays the signal, spline, and calculations. The equation used to generate the signal was

$$V = \sin(2\pi(50 \times 10^6 + 4 \times 10^{14} t)t) \quad (8)$$

The generated data did not behave as expected. Due to poor data generation, the values of the voltage between 170 ns and 210 ns were irregular. Increased sampling improved the results. This deviation from the expected results is observed in the bottom graph of Figure 2. Note that the deviations occur at 170-210 ns.

3. Linearly decreasing signal- a signal with a frequency varying linearly from 150 MHz to 50 MHz in 250 ns. Figure 3 displays the simulated signal, cubic spline, and frequency calculation. The equation used to generate the data was

$$V = \sin(2\pi(150 \times 10^6 - 4 \times 10^{14} t)t) \quad (9)$$

The data generated did not behave as expected. The reason is the same as the linearly increasing signal.

4. Linearly decreasing, leveling off, then linearly increasing frequency- a signal in which the frequency linearly decreased from 100 MHz to 50 MHz in 100 ns, remained constant at 50 MHz for the next 100 ns, and then linearly increased to 100 MHz in the remaining 100 ns. Figure 4 represents the information for the simulation. The equations used to construct the data was

$$V = \sin(2\pi t(100 \times 10^6 - 5 \times 10^{14} t)), 0 \leq t \leq 100 \text{ ns} \quad (10)$$

$$V = \sin(2\pi t(50 \times 10^6)), 100 \text{ ns} \leq t \leq 200 \text{ ns} \quad (11)$$

$$V = \sin(2\pi t(50 \times 10^6 + 5 \times 10^{14} t)), 200 \text{ ns} \leq t \leq 300 \text{ ns} \quad (12)$$

The data behaved as expected, with the exception at 100 ns. A discontinuity at 100 ns was observed in the frequency calculation. Properly created data (smooth sinusoidal) corrects the error.

5. Test of digitizer resolution-Figures 1-3 were simulations in which the simulated data was generated with the assumption that the digitizer has a resolution of 2.5 ns. However, data resolution can make a difference. Finer resolution can yield better integration results. Figure 5 displays a signal linearly increasing from 50 MHz to 150 MHz over a time span of 250 ns. The resolution for this simulation is 1 ns. The equation used to generate the data is the same as the previous simulation in which the frequency was linearly increasing (test 2). Observation of the generated data revealed a signal in which the values were expected. Frequency calculations indicate finer resolution allows for better calculation. There was an unexpected trend in the frequency calculation. A shift in the starting point was noticed. Interpolated values from the spline method prevented the value of the first data point from being zero. Setting the initial data point value to zero after interpolation corrected the result.

Real Data Evaluation

Data from the Magnetically Insulated Line Oscillator (MILO) was analyzed. Figure 6 displays the signal from the heterodyne. Proper analysis requires that non-oscillatory parts of the signal be removed. The time frame must also be shifted such that the starting time is zero. The data before and after the oscillations is removed to prevent gross overestimation of frequency due to noise. Another reason the data after the oscillations is removed is that the method would predict a frequency inversely proportional to time even without the existence of noise. Figure 7 displays the modified data and results. The frequency was erratic at the beginning of the signal, then smoothly oscillated. The erratic behavior can be attributed to the

MILO behavior itself and not to the method. Comparison between methods of frequency calculations is represented by the bottom graph in Figure 8. Calculation by zero crossing is represented by small dashes. Calculation by linear least squares fitting is represented by large dashes. The solid line represents the frequency calculation by integration. Neither method gives an accurate estimation for linearly changing frequencies. The zero crossing method, when using a signal in which the frequency increased linearly, always resulted in the slope of frequency versus time to be twice the expected frequency.

Conclusion

Many insights were gained from utilizing this method. The method works better than previously used methods. However, there are limitations. Data analysis requires the evaluation of frequency to start at the first time the voltage is zero. Calculation of frequency prior to the first zero cannot happen, as the maximum value of the half-sine wave is not known. Prior data is important, though, as it helps in calculating the derivatives properly. Discontinuities in the data cause the calculations to be erratic. Fortunately, heterodyne signals are usually continuous and smooth. Poor resolution can cause deviations in calculations. Unfortunately, the only method used to correct this problem is having equipment with better resolution. Noise can contribute to improper calculations, but smoothing should help correct this.

Acknowledgments

The author would like to thank Doctors T.A. Spencer, K.J. Hendricks, J.W. Luginsland, M.J. Arman, M. Haworth, and L. Bowers for guidance and insight. Support from the Air Force Office of Scientific Research and Research and Development Laboratory is gratefully acknowledged.

References

- 1) W. H. Press, B. P. Flannery, S. A. Teukolsky, and W. T. Vetterling, *Numerical Recipes: The Art of Scientific Computing*, Cambridge University Press, New York, 1987.
- 2) Research Systems, Inc., *IDL User's Guide*, Boulder, 1995.

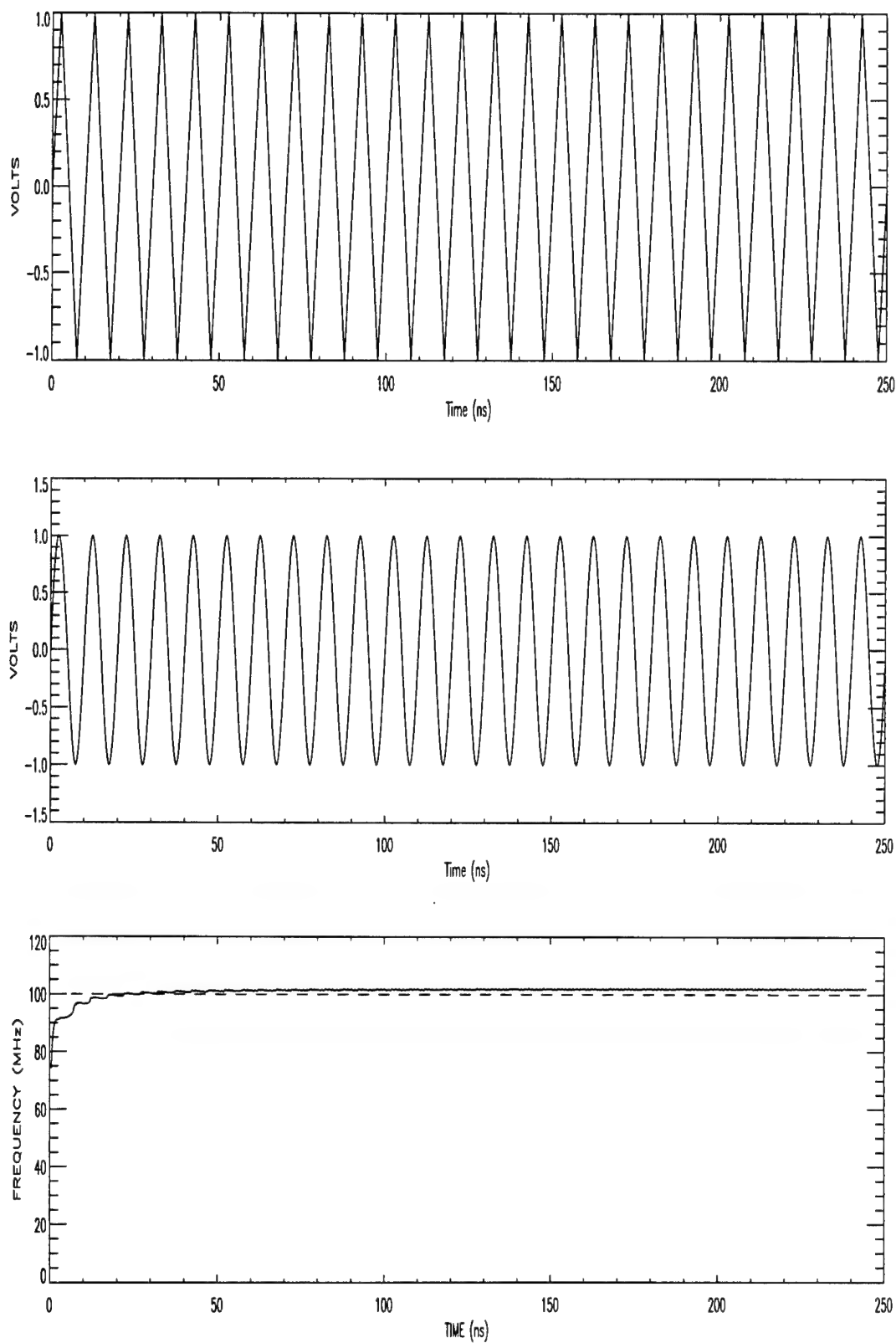


Figure 1 Signal and calculations for a constant frequency of 100 MHz. The top graph is the generated data. The middle graph is the cubic spline of the data. The bottom graph is the frequency calculation. The solid line is the calculated frequency, while the dashed line is the expected frequency.

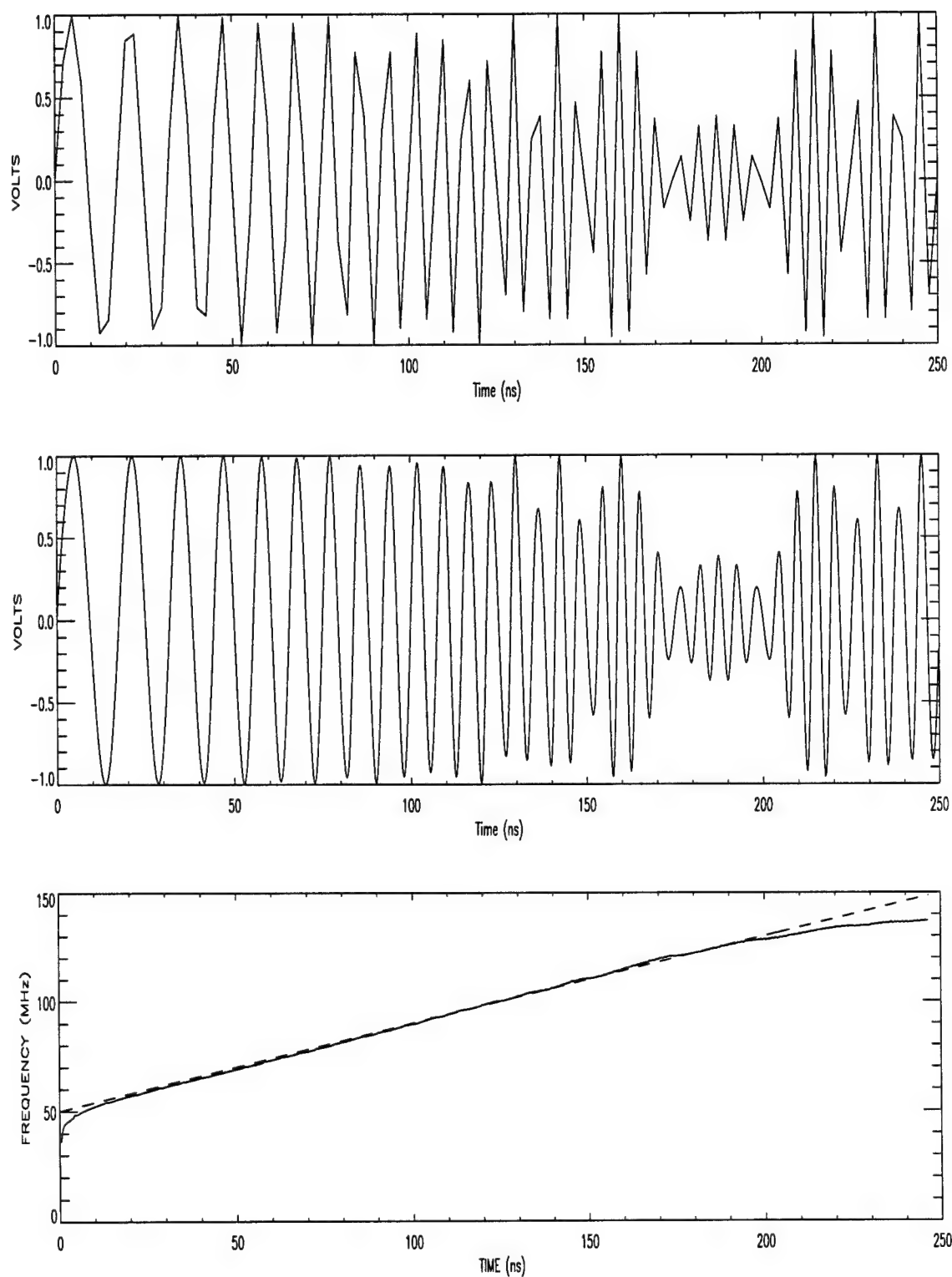


Figure 2 Signal and calculations for a linearly increasing frequency (50 MHz-150 MHz) in 250 ns. The top graph is the generated data. The middle graph is the cubic spline of the data. The bottom graph is the frequency calculation. The solid line is the calculated frequency, while the dashed line is the expected frequency. Note the deviation due to improper data generation.

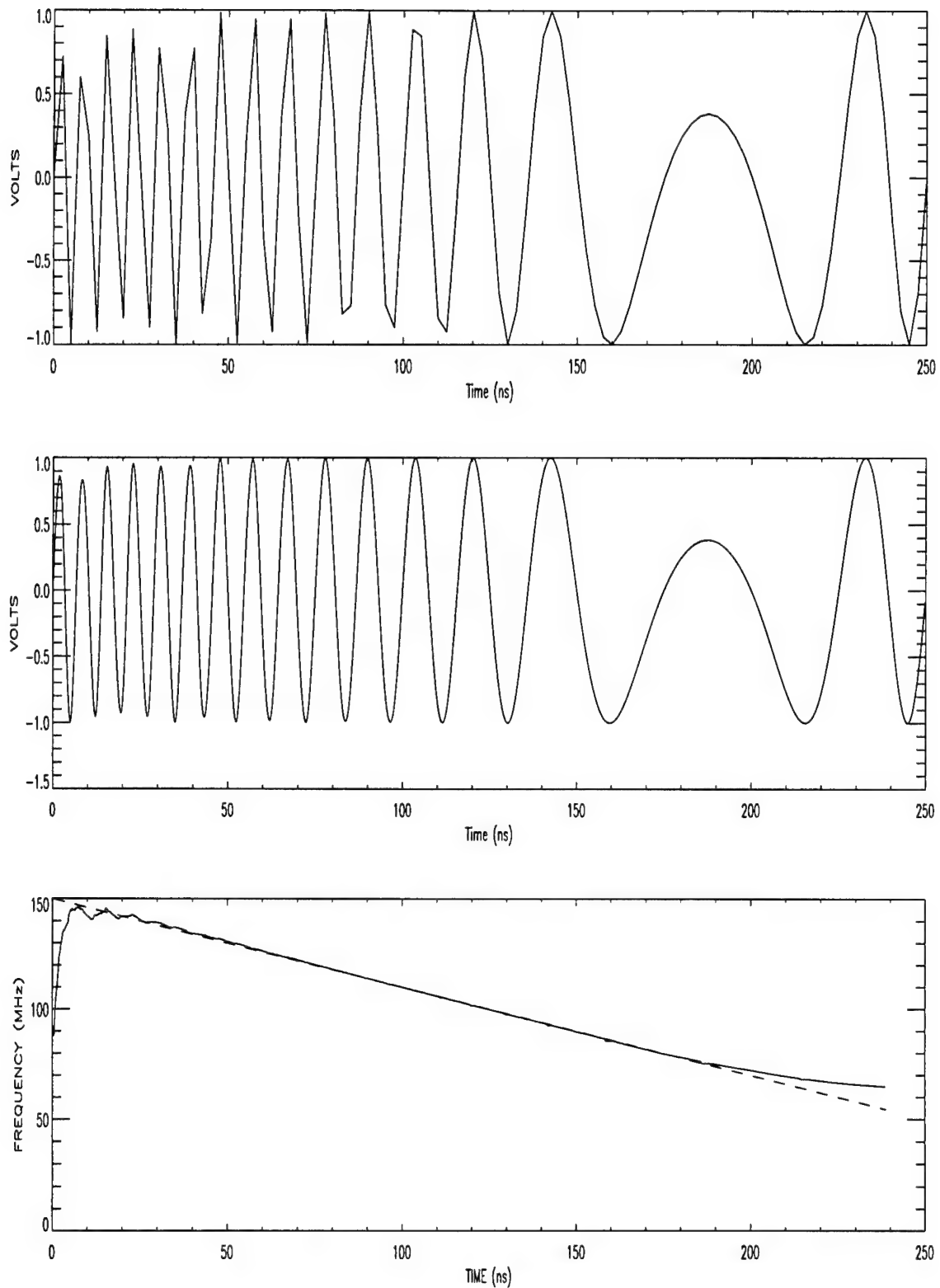


Figure 3 Signal and calculations for a linearly decreasing frequency (150 MHz-50 MHz) in 250 ns. The top graph is the generated data. The middle graph is the cubic spline of the data. The bottom graph is the frequency calculation. The solid line is the calculated frequency, while the dashed line is the expected frequency. Note the deviation due to improper data generation.

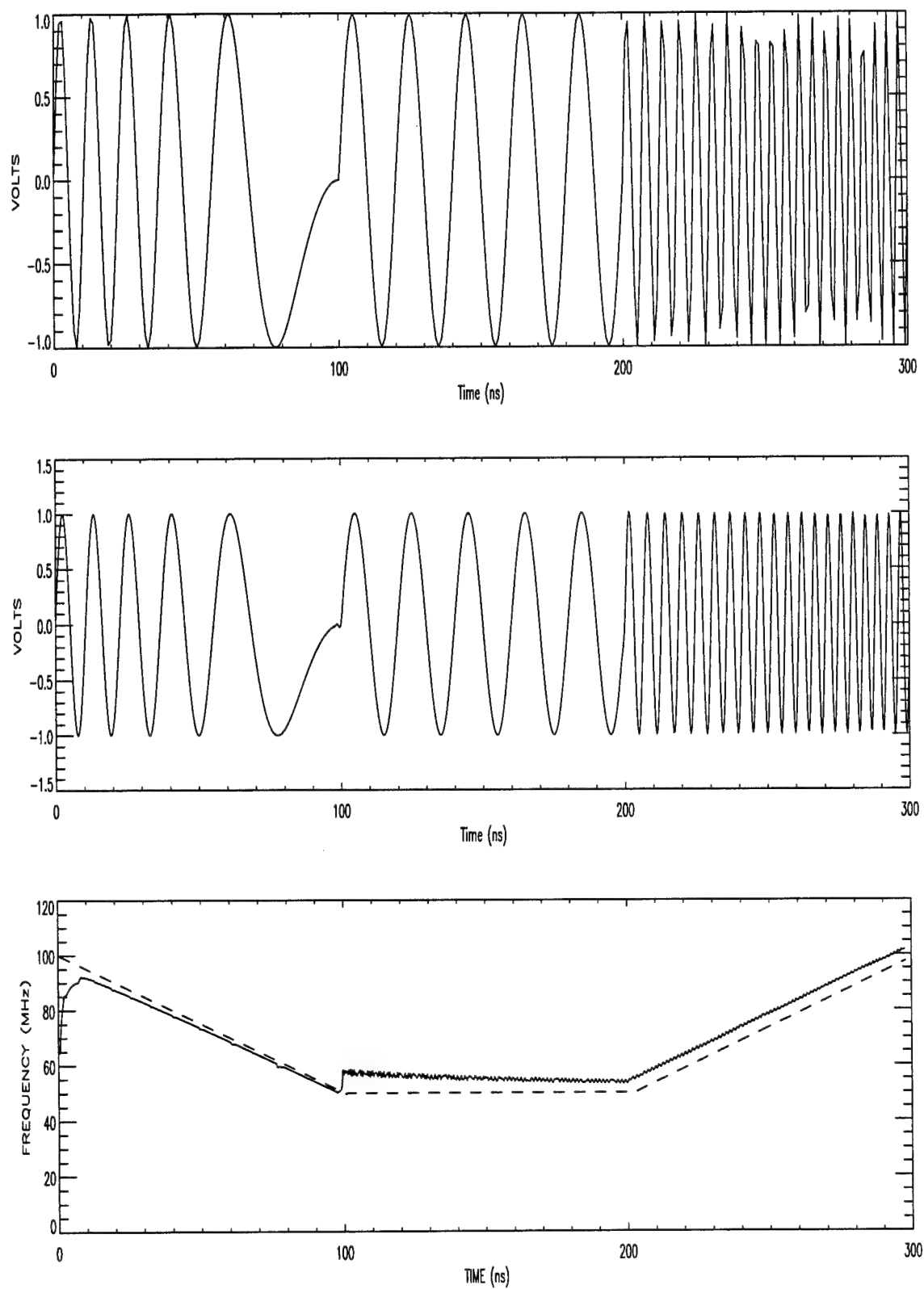


Figure 4 Signal and calculations for a signal decreasing, leveling, and then increasing in 250 ns. The top graph is the generated data. The middle graph is the cubic spline of the data. The bottom graph is the frequency calculation. The solid line represents the calculated frequency, while the dashed line represents the expected frequency. Note the deviation due to improper data generation at 100 ns.

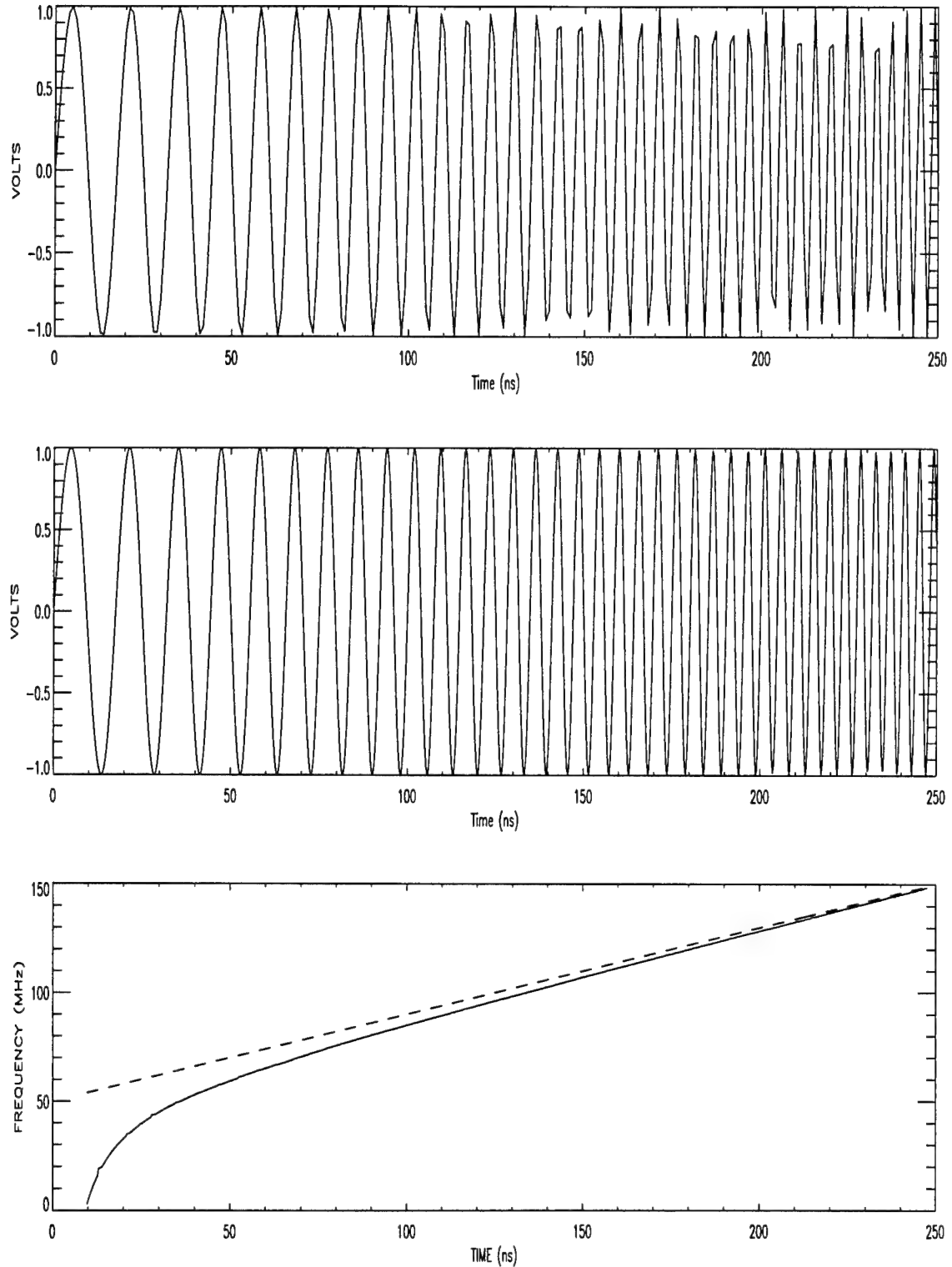


Figure 5 Results for a linearly increasing frequency (50 MHz-150 MHz) in 250 ns with a resolution of 1 ns. The top graph is the generated data. The middle graph is the cubic spline of the data. The bottom graph is the frequency calculation. The solid line represents the calculated frequency, while the dashed line represents the expected frequency. Note the deviation due to the cubic spline technique.

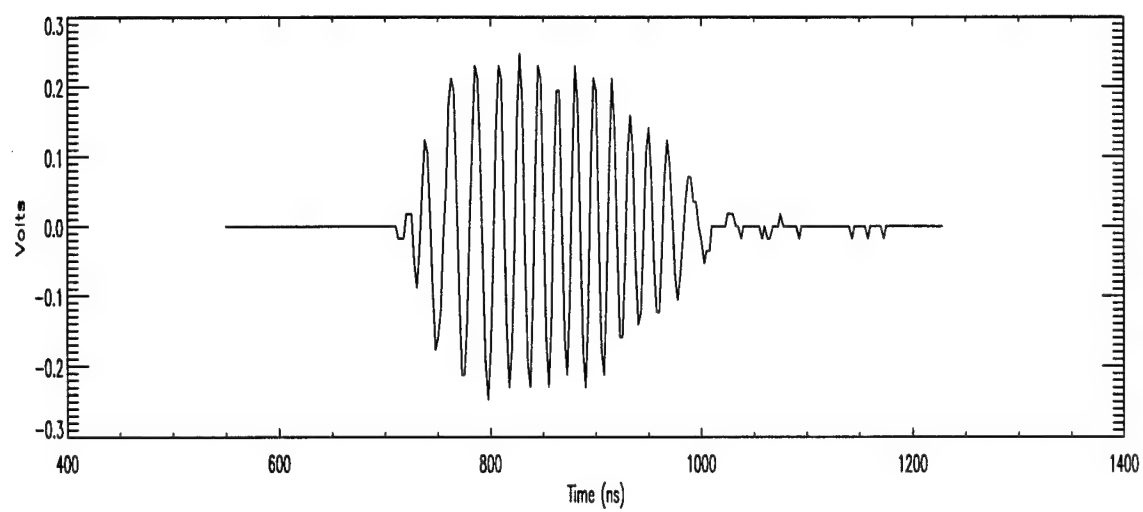


Figure 6 Heterodyne signal from the MILO.

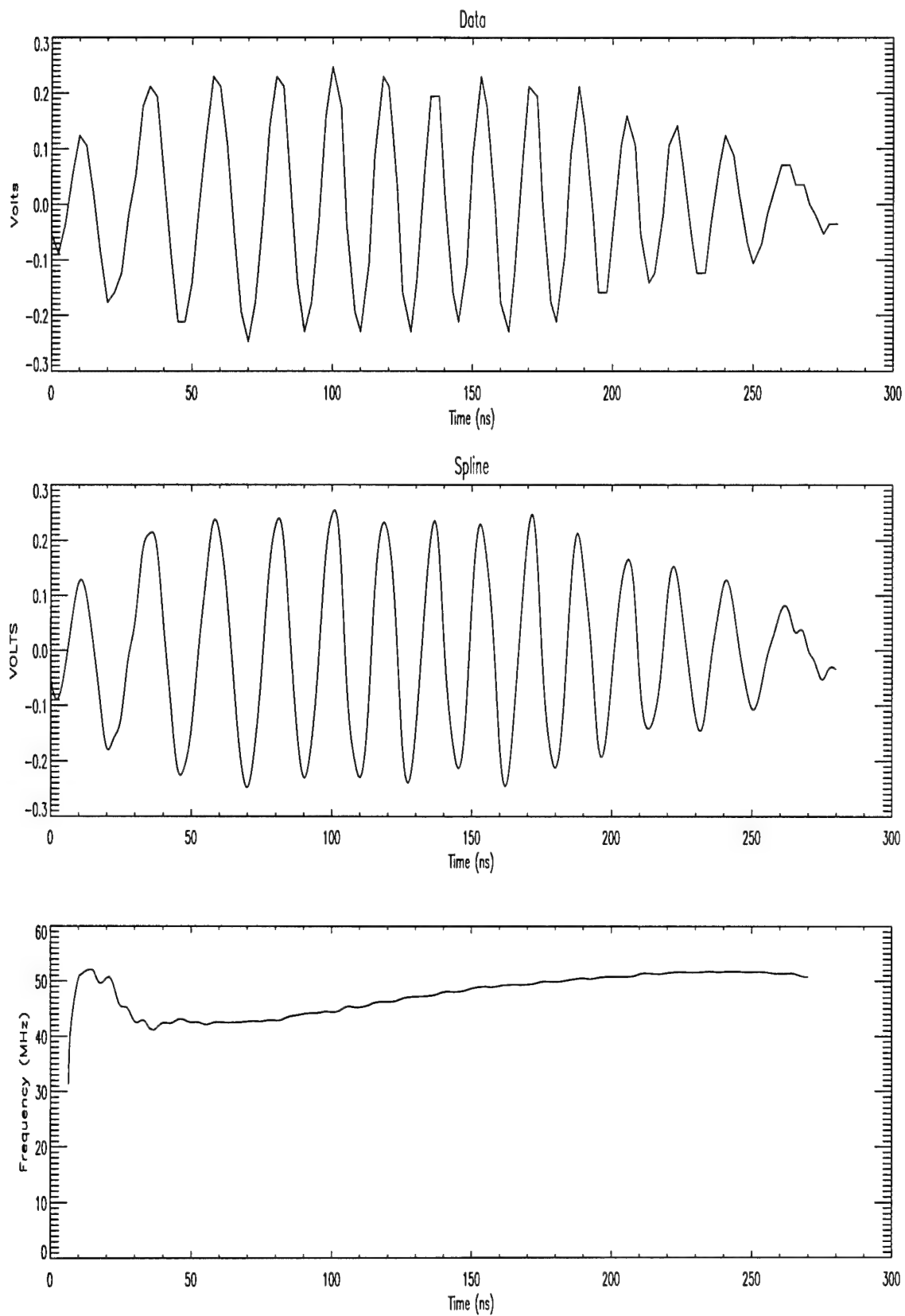


Figure 7 Signal and results from the clipped signal of Figure 6. The top graph is the generated data. The middle graph is the cubic spline of the data. The bottom graph is the frequency calculation.

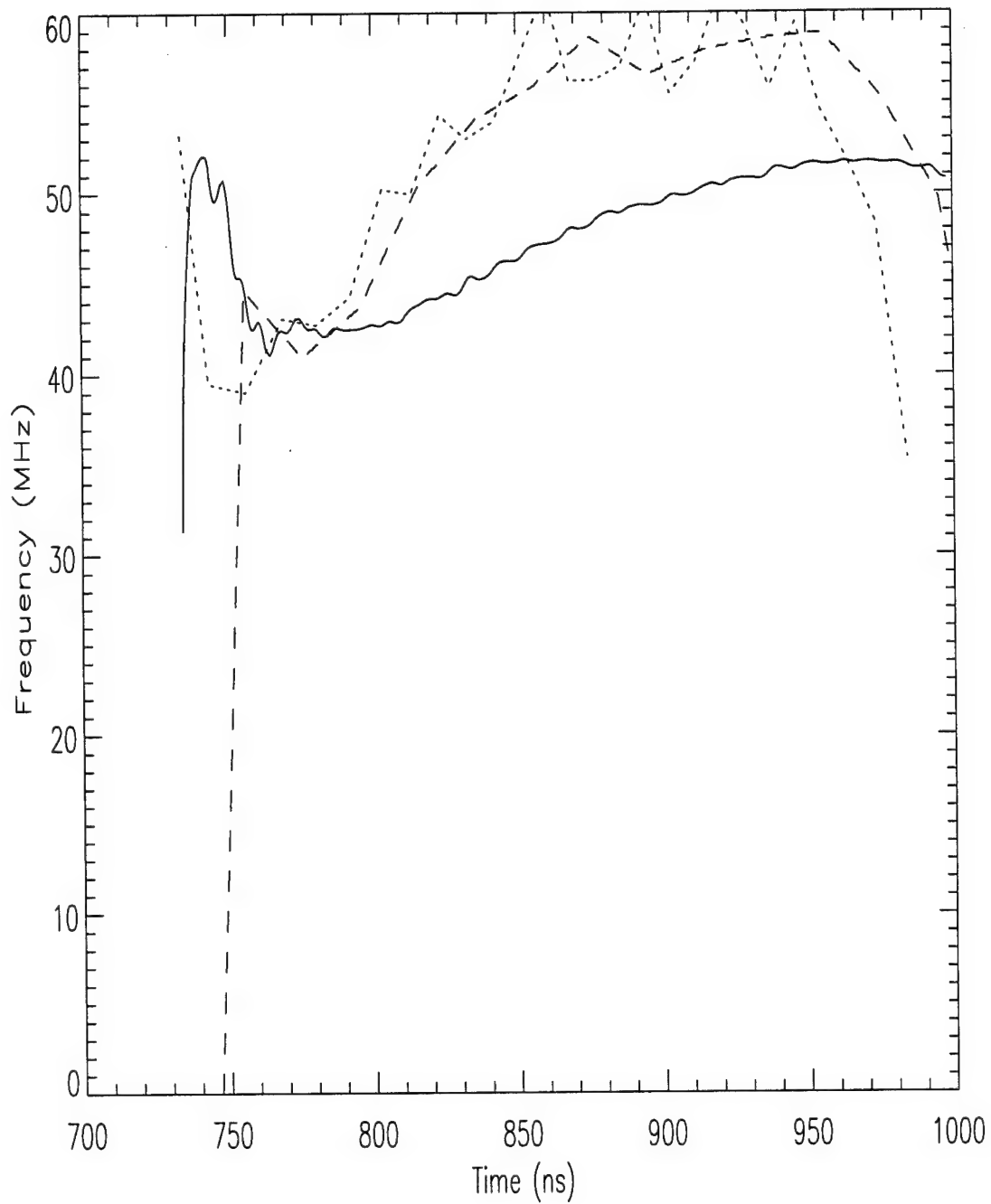


Figure 8 Graph of different methods used to analyze the data from Figure 6. The solid line is the method discussed in this paper. The line with large dashes is calculation by linear least squares fitting. The line with small dashes is calculation by zero crossing.

Appendix A

Program Created

The program below was created to calculate frequency as a function of time. A cubic spline interpolation of the signal is conducted first. Calculation and insertion of zeroes was next. Minimums and maximums were inserted after evaluation of the derivative of the signal. Normalization between zeroes is the next step. Recomputing the derivatives was conducted immediately after normalization. Prevention of division by zeroes is needed. Voltages with an absolute value between 0.01 and 0.99 is used. Finally, the frequency was calculated by integration.

```
; THIS PROGRAM CALCULATES FREQUENCY AS A FUNCTION OF TIME
;
; WRITTEN JULY 1997
; BY CHRISTOPHER W. PETERS
;
; VARIABLE DEFINITION
;
; MAXARRAY-DETERMINES THE MAXIMUM NUMBER OF VALUES IN AN ARRAY
; TI=VARIABLE USED TO READ IN TIMES
; PO=VARIABLE USED TO READ IN VOLTAGES
; COUNT=NUMBER OF DATA POINTS AVAILABLE
; X=ARRAY OF TIMES THAT ARE READ FROM A FILE
; Y=ARRAY OF VOLTAGES THAT ARE READ FROM A FILE
; DT=TIME DIFFERENCE FROM FIRST TO LAST DATA POINTS
; NPTS=NUMBER OF POINTS TO INTERPOLATE FROM CUBIC SPLINE
; TEMPX=TEMPORARY STORAGE ARRAY FOR GENERATED TIMES
; TEMPY=TEMPORARY STORAGE ARRAY FOR GENERATED VOLTAGES
; TIME=ARRAY OF TIMES USED FOR CALCULATIONS
; VOLT=ARRAY OF VOLTAGES USED FOR CALCULATIONS
; ADD=COUNTER USED TO ADD DATA TO EXISTING DATA
; SLOPE=SLOPE BETWEEN TWO DATA POINTS
; DPDT=ARRAY OF THE DERIVATIVE OF VOLTAGE WITH RESPECT TO TIME
; ZCROSS=NUMBER OF TIMES THE SIGNAL CROSSES ZERO VOLTAGE
; TZERO=ARRAY OF THE TIMES WHERE THE SIGNAL CROSSES ZERO VOLTAGE
; PEAK=MAXIMUM AMPLITUDE BETWEEN ZERO CROSSINGS
; NVOL=ARRAY OF NORMALIZED VOLTAGES
; RRANGE=COUNTER USED TO KEEP TRACK OF MODIFIED DATA
; TTIME=ARRAY OF TIME FOR MODIFIED DATA
; TNVOL=ARRAY OF NORMALIZED VOLTAGES FOR MODIFIED DATA
; TK=ARRAY OF THE VALUES OF THE RHS OF EQUATION
; FREQ=ARRAY OF CALCULATED FREQUENCIES
```

PRO FREQ

```
MAXARRAY=8000
Y=DBLARR(MAXARRAY)
X=DBLARR(MAXARRAY)
TIME=DBLARR(MAXARRAY)
VOLT=DBLARR(MAXARRAY)
TEMPT=DBLARR(MAXARRAY)
TEMPV=DBLARR(MAXARRAY)
DPDT=DBLARR(MAXARRAY)
TZERO=DBLARR(MAXARRAY)
TTIME=DBLARR(MAXARRAY)
TNVOL=DBLARR(MAXARRAY)
```

```

TK=DBLARR(MAXARRAY)
NVOL=DBLARR(MAXARRAY)
FREQ=DBLARR(MAXARRAY)
EXPECT=DBLARR(MAXARRAY)
CFREQ=DBLARR(MAXARRAY)
TI=0.D
PO=0.D

; READ IN DATA

OPENR,DATA,'C:\CHRIS\hetdata\162-1.txt',/GET_LUN
COUNT=0
WHILE NOT EOF(DATA) DO BEGIN
  COUNT=COUNT+1
  READF,DATA,TI,PO
  X(COUNT)=DOUBLE(TI)
  Y(COUNT)=DOUBLE(PO)
ENDWHILE

!P.MULTI=[0,1,3]
WINDOW,0,TITLE='Data, Spline Fit, and Frequency Calculations',XSIZE=500,YSIZE=500
PLOT,X(1:count)/1d-9,y(1:count),XTITLE='Time (ns)',YTITLE='Volts',TITLE='Data'

; NOW NEED TO CUBIC SPLINE THIS DATA

DT=X(COUNT)-X(1)
NPTS=1500
TEMPX=DINDGEN(NPTS)*DT/NPTS+X(1)
TEMPY=SPLINE(X(1:COUNT),Y(1:COUNT),TEMPX,.0000)
TIME(1:NPTS)=TEMPX(0:NPTS-1)
VOLT(1:NPTS)=TEMPY(0:NPTS-1)
PLOT,TIME(1:npts)/1d-9,volt(1:NPTS),TITLE='Spline',XTITLE='Time (ns)',YTITLE='VOLTS'
OPLOT,X(1:count)/1d-9,Y(1:count)
COUNT=NPTS

;ADD ZEROES IN DATA
ADD=0
FOR I=1,COUNT DO BEGIN
  A=VOLT(I)*VOLT(I+1)
  IF (A LT 0.0) THEN BEGIN
    SLOPE=(VOLT(I+1)-VOLT(I))/(TIME(I+1)-TIME(I))
    ADD=ADD+1
    VOLT(COUNT+ADD)=0.0D
    TIME(COUNT+ADD)=TIME(I)-VOLT(I)/SLOPE
  ENDIF
ENDFOR

COUNT=COUNT+ADD

; SORT THE DATA

FOR I=1,COUNT DO BEGIN
  FOR J=1,COUNT DO BEGIN
    A=TIME(I) LT TIME(J)
    IF A THEN BEGIN
      TI=TIME(I)

```

```

        VO=VOLT(I)
        VOLT(I)=VOLT(J)
        TIME(I)=TIME(J)
        VOLT(J)=VO
        TIME(J)=TI
    ENDIF
ENDFOR
ENDFOR

; PLACE MINS AND MAXS IN DATA

DPDT(1:COUNT)=DERIV(TIME(1:COUNT),VOLT(1:COUNT))
ADD=0
FOR I=1,COUNT-1 DO BEGIN
    A=DPDT(I)*DPDT(I+1)
    IF (A LT 0.0) THEN BEGIN
        ADD=ADD+1
        RSLOPE=DPDT(I)/DPDT(I+1)
        VOLT(COUNT+ADD)=DPDT(I)*(TIME(I+1)-TIME(I))+VOLT(I)
        VOLT(COUNT+ADD)=VOLT(COUNT+ADD)-RSLOPE*VOLT(I+1)
        VOLT(COUNT+ADD)=VOLT(COUNT+ADD)/(1.-RSLOPE)
        TIME(COUNT+ADD)=(VOLT(COUNT+ADD)-VOLT(I+1))/DPDT(I+1)+TIME(I+1)
    ENDIF
ENDFOR

COUNT=COUNT+ADD

; SORT THE DATA

FOR I=1,COUNT DO BEGIN
    FOR J=1,COUNT DO BEGIN
        A=TIME(I) LT TIME(J)
        IF A THEN BEGIN
            TI=TIME(I)
            VO=VOLT(I)
            VOLT(I)=VOLT(J)
            TIME(I)=TIME(J)
            VOLT(J)=VO
            TIME(J)=TI
        ENDIF
    ENDFOR
ENDFOR

; RECOMPUTE DERIVATIVES

DPDT(1:COUNT)=DERIV(TIME(1:COUNT),VOLT(1:COUNT))

;FIND ZERO CROSSINGS

ZCROSS=0

FOR I=1,COUNT DO BEGIN
    IF (VOLT(I) EQ 0.0) THEN BEGIN
        ZCROSS=ZCROSS+1
        TZERO(ZCROSS)=TIME(I)
    
```

```

ENDIF
ENDFOR

; CONDUCT NORMALIZATION OF DATA

FOR I=1,ZCROSS-1 DO BEGIN
  FOR J=1,COUNT DO BEGIN
    IF (TIME(J) EQ TZERO(I)) THEN A=J
    IF (TIME(J) EQ TZERO(I+1)) THEN B=J
  ENDFOR
  PEAK=MAX(ABS(VOLT(A:B-1)))
  NVOL(A:B-1)=VOLT(A:B-1)/PEAK
ENDFOR

COUNT=B

;CONDUCT INTEGRATION

DPDT(1:COUNT)=DERIV(TIME(1:COUNT),NVOL(1:COUNT))

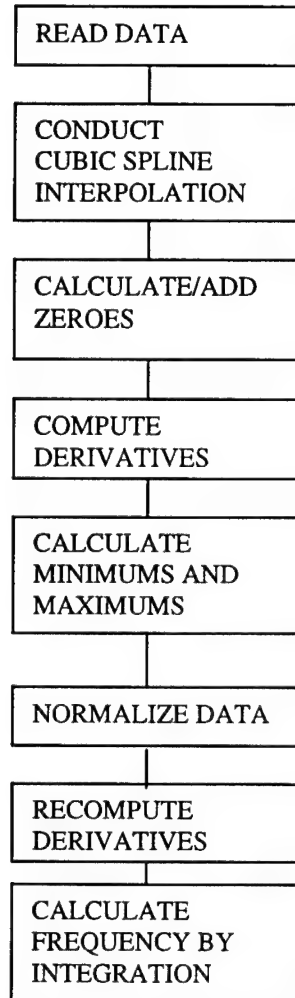
RRANGE=0

FOR I=1,COUNT DO BEGIN
  Q=ABS(NVOL(I)) LT 0.999 AND TIME(I) GE TZERO(1) AND TIME(I) LE TZERO(ZCROSS)
  IF (Q) THEN BEGIN
    RRANGE=RRANGE+1
    TTIME(RRANGE)=TIME(I)
    TNVOL(RRANGE)=NVOL(I)
    TK(RRANGE)=ABS(DPDT(I)/(1.-NVOL(I)^2.)^0.5)
  ENDIF
ENDFOR
MARK=TZERO(1)
FOR I=1,ZCROSS-1 DO BEGIN
  CFREQ(I)=(1./(TZERO(I+1)-TZERO(I)))/2.d6
ENDFOR
TTIME(1:RRANGE)=TTIME(1:RRANGE)-MARK
OPENW,NUNIT,'C:\CHRIS\results\162-1.out',/GET_LUN
FOR I=2,RRANGE DO BEGIN
  FREQ(I)=INT_TABULATED(TTIME(1:I),TK(1:I))/(TTIME(I)*2.*!PI)
  PRINTF,NUNIT,(TTIME(I)+MARK)/1D-9,FREQ(I)/1D6
ENDFOR
TTIME(2:RRANGE)=TTIME(2:RRANGE)/1D-9+MARK/1D-9
FREQ(2:RRANGE)=FREQ(2:RRANGE)/1D6
CLOSE,NUNIT
FREE_LUN,NUNIT
PLOT,TTIME(2:rrange)+MARK,FREQ(2:rrange),XTITLE='Time (ns)',YTITLE='Frequency (MHz)'

END

```

Appendix B
FLOWCHART OF PROGRAM



**DUCTED WHISTLER WAVES AND EM EMISSIONS IN THE LABORATORY
AND THE IONOSPHERE**

**Michael J. Rowlands
Master's of Engineering 1998
Department of Electrical Engineering and Computer Science**

**Massachusetts Institute of Technology
77 Massachusetts Avenue
Cambridge, MA 02139**

**Final Report for:
Graduate Student Research Program
Versatile Toroidal Facility and Phillips Laboratory**

**Sponsored by:
Air Force Office of Scientific Research
Bolling Air Force Base, DC**

and

Phillips Laboratory

September 1997

WHISTLER WAVE CUTOFF AND EM EMISSIONS IN THE LABORATORY AND THE IONOSPHERE

Michael J. Rowlands

Abstract

Electromagnetic waves, propagating parallel to the magnetic field in a magnetized plasma, are detected in the Versatile Toroidal Facility, (VTF), up to the electron cyclotron frequency. Since plasmas in VTF are formed from either electron beams or microwaves, the plasma densities are in the shape of a single crest. Ionospheric theory predicts that these electromagnetic waves, called whistler waves, can only be ducted up to half the cyclotron frequency in a crest. This discrepancy between theory and experiment was investigated and an adapted theory was developed for VTF conditions. Electromagnetic emissions and wave-particle interactions in the magnetosphere were also analyzed.

List of Figures

1	(a) Schematic outlining the electron beam and ECRH plasma generation methods and (b) magnetic field, density and fractional density fluctuations as a function of radius in a typical beam plasma	7
2	Power vs. Frequency for top, no microwave, plasma density $7 \times 10^{15}/m^3$, and bottom, with microwave, plasma density $1.5 \times 10^{16}/m^3$	15
3	Whistler Wave Cutoff Frequency vs. Radius for a single beam shot . .	16
4	Whistler Wave Cutoff Frequency vs. Radius for a two beam shot	17
5	Side views of two dimensional contours of beam plasmas	18
6	High frequency spectrum of whistler waves	19

WHISTLER WAVE CUTOFF AND EM EMISSIONS IN THE LABORATORY AND THE IONOSPHERE

Michael J. Rowlands

Introduction

In the ionosphere, electromagnetic waves can be generated by Cerenkov radiation; high speed electrons which slow down and give off electromagnetic radiation. Some sources of this radiation are lightning and wave-particle interactions with electrons in the magnetosphere's plasma sheet. These electromagnetic waves propagate in plasma. The magnetized plasma is a dispersive medium and has an anisotropic dielectric constant. This anisotropy causes electromagnetic waves to be ducted along the earth's magnetic field in areas of enhanced or depleted ionization. Helliwell's theoretical analysis showed that in plasma density crests, electromagnetic waves are only ducted up to half the cyclotron frequency, while in troughs, they can be ducted up to the cyclotron frequency. At VTF, electromagnetic waves traveling along the toroidal magnetic field are detected at three-quarters of the cyclotron frequency and sometimes up to the cyclotron frequency. However, the electron beams form a plasma density that is enhanced along the magnetic field, creating a crest. Experiments were used to investigate the theory and to explain whistler wave cutoff in VTF.

The Versatile Toroidal Facility (VTF) in the Plasma Science and Fusion Center at MIT is supervised by Prof. Min-Chang Lee. The VTF is a medium-size torus which can simulate some plasma processes found in the earth's ionosphere. The project investigated is whistler wave cutoff. Whistler waves are electromagnetic waves propagating along the magnetic field in a magnetized plasma. In the upper ionosphere, whistler waves travel along the earth's magnetic field, in ducts of enhanced plasma density. In VTF there is a similar geometry. The highest density plasma is in the center of the chamber, while at the walls, the density goes to zero. Therefore, the plasma density profile is a single crest in which whistler waves can be ducted. In the ionosphere, these whistler waves are induced by lightning, in VTF, they are excited by electron beams which simulate such lightning inside the vacuum chamber. Ducting

along the earth's magnetic field only occurs up to half the electron cyclotron frequency, and agrees with existing theory. However, in VTF, under certain conditions, whistler waves are detected up the electron cyclotron frequency. This project's goal was to describe, explain and understand this discrepancy. To do so, a loop probe has been built and rebuilt, a theory to analyze whistler wave propagation in a plasma has been written, and experiments at VTF have been run. This report will describe the VTF laboratory cell, explain the loop probe diagnostic, and show the theoretical analysis and experimental data.

The Vacuum Chamber

The VTF vacuum chamber is a torus of rectangular cross section. It has a major radius and height of approximately 1 m with a minor radius of 60 cm. The total volume of the chamber is therefore around 6 cubic meters. A pumping apparatus involving a turbo pump, valves and various safety mechanisms, keeps the vacuum at a base pressure on the order of 10^{-7} torr. Toroidal field coils are wrapped around the chamber poloidally. There are 18 such coils, each with 4 turns, so 72 turns of copper coils produce the toroidal magnetic field. Three phase 240V current is converted to DC current via two six phase power converters. The TF current is usually at 6 kiloamps producing a magnetic field toroidally in the chamber which is inversely proportional to radius. At the radius of highest plasma density, its magnitude is about 0.08 Tesla. A constant, vertical magnetic field is created using Helmholtz coils around the top and bottom of the chamber. About a thousand amps of vertical field current pass through these coils to produce a 0.001 Tesla magnetic field oriented vertically. These two magnetic fields, toroidal and vertical, add to make a helical magnetic field inside the chamber.

Plasma Sources

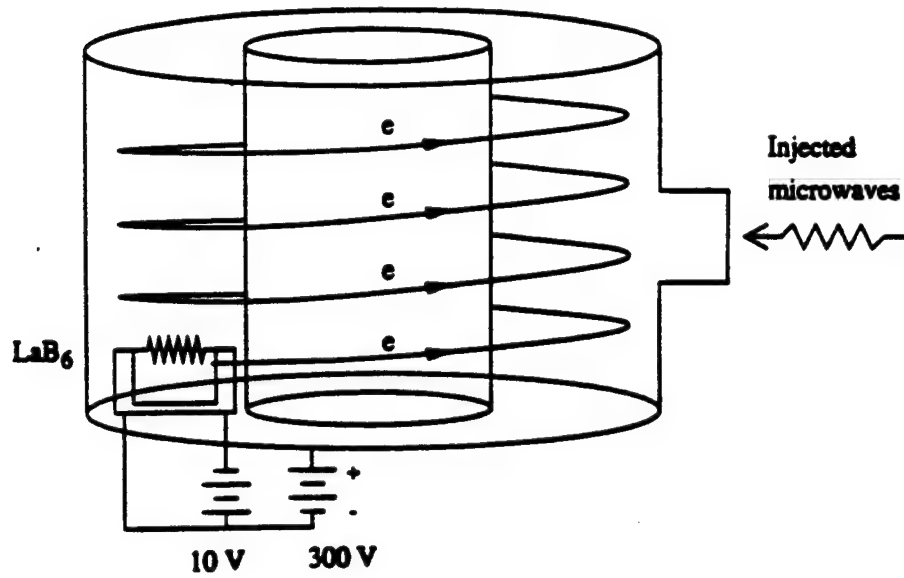
In order to form a plasma in the vacuum chamber, a gas must be leaked into the chamber and some mechanism to ionize the gas must be employed. Currently, VTF uses two ways to produce plasma: microwave ECRH (electron cyclotron resonance heating) and using electron beams. These mechanisms can be run either individually or simultaneously. The microwave plasmas are formed when a 2.45 gigahertz microwave

source is powered by a 3 kilowatt power supply while microwaves are injected radially into the machine. Hydrogen or Argon gas is leaked into the vacuum chamber and the toroidal field magnets are turned on, producing the .08 Tesla field. When the frequency of injected microwaves and those of the electron cyclotron frequency match, the gas ionizes and a plasma forms. Hydrogen is used most often because it produces a singly charged plasma, facilitating more accurate analysis of the data and simplifying subsequent calculations. Plasma densities for ECRH plasmas are near 10^{17} ions/ m^3 . Thermionic electrons emitted from LaB_6 filaments, traveling along the helical magnetic field, form electron beams. By applying a current for 60 seconds, the filaments are heated to 1600 degrees Celsius, then they're biased at -360 Volts. The negative voltage repels and accelerates electrons from the filaments. As the electrons move along the field, they ionize the hydrogen and produce a plasma in the electron beam. Densities for beam plasmas are near 10^{18} ions/ m^3 . Figure 1, shows the chamber with its unique helical magnetic field and the two plasma sources.

Diagnostic Devices

At present, three probes are inserted into the plasma chamber itself: the loop probe, the dipole probe and the radial probe. There are also measurements made on the various power supplies used to run the machine. The loop probe measures a changing magnetic field radially in the chamber. The probe tip can be moved to different radii during different shots. The dipole probe measures the difference in electric field between the tips of its two wires. The radial probe is motorized to allow movement during a shot. It can measure both plasma density and temperature. Power supply consists of voltage and current measurements made at specific points in the supply. All data is digitized by modules in a CAMAC crate inside the laboratory cell. The digitized information is sent by fiber optic cable to the data viewing and storing computer in the control room. The operation of the machine is controlled by another computer. The user inputs the run times of the instruments in the cell and the magnitude of certain outputs, for example toroidal field coil current. This information is sent to a Programmable Logic Controller (PLC) in the cell. The PLC controls the power supplies in two ways. First, by coordinating the fiber optic transmitters and

(a)



(b)

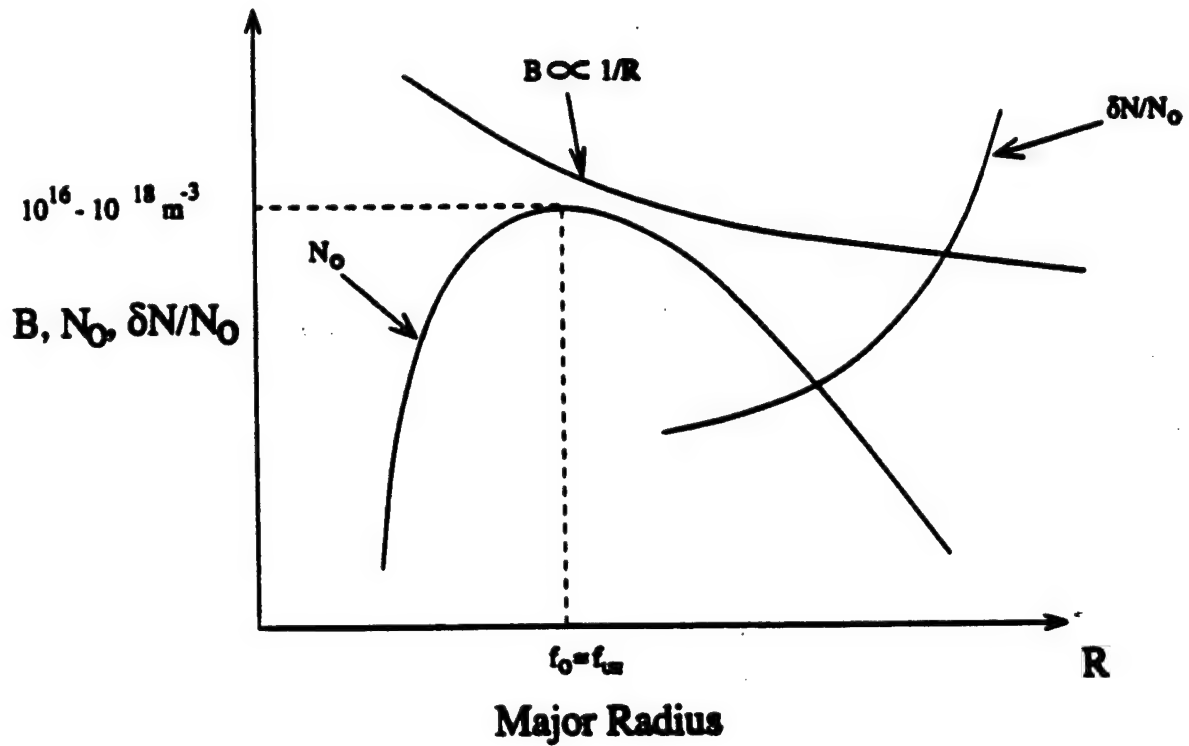


Figure 1: (a) Schematic outlining the electron beam and ECRH plasma generation methods and (b) magnetic field, density and fractional density fluctuations as a function of radius in a typical beam plasma

receivers which in turn control the power supplies's firing circuits. Secondly, it controls relays which run all the power supplies.

The Project

The focus of this project was to accurately model and simulate electromagnetic waves propagating in a plasma parallel to the magnetic field (a.k.a. whistler waves) including exploration of whistler wave cutoff frequency for different parameters in the vacuum chamber. An adapted theory is needed to explain the experimental results under VTF conditions. There were two main parts to this project: using a loop probe to measure whistler wave frequency, and adapting electromagnetic wave ray-tracing theory and scanning plasma density to measure the density contour of the plasma.

The Loop Probe

In order to measure electromagnetic waves in the plasma, a loop probe was inserted into the plasma. The loops were oriented so their normal was perpendicular to the toroidal field. When a whistler wave caused a change in the the magnetic field through the loops, a voltage was induced across the loops. This voltage was fed into a spectrum analyzer which measures the frequencies of the voltage fluctuations and therefore the frequencies of the whistler waves. Due to the toroidal configuration of the magnetic coils around the VTF chamber, the strength of the magnetic field was inversely proportional to radius. Thus, the electron cyclotron frequency decreases with increasing radius. The loop probe measured the whistler wave cutoff throughout the radius of the machine. These data gives insight as to the dependence of whistler wave cutoff frequency on background magnetic field and plasma density. Using the two types of plasma, microwave and beam, experiments were run with the loop probe. The data confirmed results from previous loop probe experiments and from measurements made with other probes. These data was also compared to results from ionospheric experiments, existing theory and adapted theory. Existing theory from Robert Helliwell (1965 and references therein) shows that in the ionosphere, along the earth's magnetic field lines, lightning-induced whistler waves can only be ducted up to half the electron cyclotron frequency. For anisotropic media, such as a plasma, the ray

path, or direction that wave energy flows, is often different than wave normal path, or k-vector path. The theory, using Appleton's equation for index of refraction in an anisotropic media, and a Snell's law construction for ray path, describes how waves, for frequencies above half the electron cyclotron frequency, either escape the duct or their ray path becomes perpendicular to their wave normal direction. In either case, the wave is not ducted.

Data Analysis

Theoretical ducting analysis was done to determine if whistler waves can be ducted well above half the cyclotron frequency in VTF. This has not been demonstrated. Under no conditions can electromagnetic waves, in a magnetized plasma, be ducted above half the cyclotron frequency. The dispersion relation used for the ray tracing is shown below, with μ being the index of refraction.

In VTF experiments, whistler wave cutoff frequencies have not matched the half-cyclotron frequency cutoffs of ionospheric theory and experiments. Therefore, starting with Appleton's dispersion relation, an adapted theory has been developed. Appleton's equation follows where μ is the index of refraction:

$$\mu^2 = 1 - \frac{X}{1 - iZ - \frac{\sin^2 \theta}{2\Lambda^2(1-X-iZ)} - \frac{1}{1-X-iZ} \left[\frac{\sin^4 \theta}{4\Lambda^4} + \frac{\cos^2 \theta}{\Lambda^2} (1-X-iZ)^2 \right]^{\frac{1}{2}}}$$

ω_o = whistler wave frequency

ω_{ce} = electron cyclotron frequency

ω_{pe} = plasma frequency

θ = angle between wave normal and magnetic field

ν = collision frequency

$$\Lambda = \frac{\omega_o}{\omega_{ce}}$$

$$X = \frac{\omega_{pe}^2}{\omega_{ce}^2}$$

$$Z = \frac{\nu}{\omega_o}$$

Given that the collision frequency is small compared to the whistler wave frequency:

$$\omega \gg \nu, Z \rightarrow 0$$

then simplifying, the expression for the square of the index of refraction becomes:

$$\mu^2 = 1 + \frac{\Lambda^2 X (1 - X)}{\Lambda^2 X - \Lambda^2 + \frac{\sin^2 \theta}{2} + \left[\frac{\sin^4 \theta}{4} + \Lambda^2 \cos^2 \theta (1 - X)^2 \right]^{\frac{1}{2}}}$$

The angle α between the ray path and the k-vector of a whistler wave is needed because it gives the direction of energy flow with respect to wave front direction. When α reaches 90° , the electromagnetic wave no longer propagates in the anisotropic medium because no component of the wave's energy is in the direction that the wave fronts are traveling. The expression relating α to the index of refraction is:

$$\tan \alpha = \frac{1}{\mu} \frac{d\mu}{d\theta}$$

Rationalizing μ to simplify the calculations:

$$\mu^2 = 1 + \frac{A}{B}$$

$$A = \Lambda^2 X (1 - X)$$

$$B = \Lambda^2 X - X + \frac{\sin^2 \theta}{2} + \left[\frac{\sin^4 \theta}{4} + \Lambda^2 \cos^2 \theta (1 - X)^2 \right]^{\frac{1}{2}}$$

Differentiating using A and B and plugging into the expression for $\tan \alpha$ yields:

$$\frac{1}{\mu} \frac{d\mu}{d\theta} = \frac{1}{2} \sqrt{\frac{1}{1 + \frac{A}{B}}} \left(1 + \frac{A}{B} \right)^{-\frac{1}{2}} \frac{d}{d\theta} \left(\frac{A}{B} \right) = \frac{1}{2} \left(\frac{1}{1 + \frac{A}{B}} \right) \frac{d}{d\theta} \left(\frac{A}{B} \right)$$

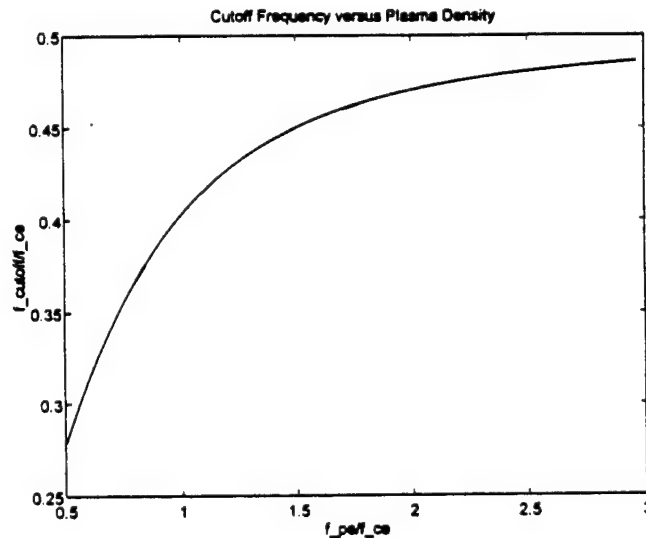
$$\frac{d}{d\theta} \left(\frac{A}{B} \right) = \frac{\left(B \frac{dA}{d\theta} - A \frac{dB}{d\theta} \right)}{B^2} = \frac{-A \frac{dB}{d\theta}}{B^2}$$

Substituting back in for A and B in terms of λ and X gives:

$$\frac{dB}{d\theta} = \sin \theta \cos \theta + \frac{1}{2} \left[\frac{\sin^4 \theta}{4} + \Lambda^2 \cos^2 \theta (1 - X)^2 \right]^{\frac{-1}{2}} \left(\sin^3 \theta \cos \theta - \Lambda^2 (1 - X)^2 \cos \theta \sin \theta \right)$$

$$\tan \alpha = \frac{1}{2} \frac{-\Lambda^2 X (1 - X) \left[\sin \theta \cos \theta + \frac{1}{2} \left[\frac{\sin^4 \theta}{4} + \Lambda^2 \cos^2 \theta (1 - X)^2 \right]^{\frac{-1}{2}} \left(\sin^3 \theta \cos \theta - \Lambda^2 (1 - X)^2 \cos \theta \sin \theta \right) \right]}{\left(\Lambda^2 X - X + \frac{\sin^2 \theta}{2} + \left[\frac{\sin^4 \theta}{4} + \Lambda^2 \cos^2 \theta (1 - X)^2 \right]^{\frac{1}{2}} + \Lambda^2 X (1 - X) \right) \Lambda^2 X - X + \frac{\sin^2 \theta}{2} + \left[\frac{\sin^4 \theta}{4} + \Lambda^2 \cos^2 \theta (1 - X)^2 \right]^{\frac{1}{2}}}$$

With the adapted expressions for α and μ , ray-tracing can be done by using a Snell's law construction and modeling each point in a given plasma density as a slab of dielectric media. The simulation will draw out the path that energy travels for an electromagnetic wave at a certain frequency. The ray-tracing technique is the one described in Helliwell's textbook and *Propagation Characteristics of Whistlers Trapped in Field-Aligned Columns of Enhanced Ionization* by R.L. Smith (1961). With this analysis, cutoff frequency is defined as the highest frequency that a wave's k-vector is in the same direction as its ray path. Plotting $\theta - \alpha$ vs. θ and finding Λ where the graph is tangent to $\theta - \alpha = 0$ at $\theta = 0$ yields cutoff frequency. Below is a graph of this Λ vs. $\frac{f_{pe}}{f_{ce}}$.



Wave-particle Interactions in the Magnetosphere

In addition to laboratory experiments, some ionospheric plasma theory was studied. During geomagnetic storms, a steady rain of electrons precipitate into the atmosphere at high latitudes. These particles enter the loss cone at about 100 kilometers above the earth's surface. It is theorized that waves in the equatorial regions interact with the trapped electrons so that the electrons gain enough velocity along the earth's magnetic field to escape, and enter the loss cone. The earth's dipole magnetic field is like a magnetic mirror which confines moving charged particles to the equatorial regions of the magnetic field lines. When a particle travels along a field line toward high latitudes, the earth's magnetic field lines converge. The resulting force causes the particle to "bounce" back along the field line toward the equator. The force on a particle is related to the angle, of its velocity, with respect to magnetic field. Therefore, there is a loss cone within which the particle has enough parallel velocity to escape the trapping mechanism and precipitate into the ionosphere. The loss cone is the maximum angle, with respect to the field line, that the particle can travel and still escape. If the angle were zero, the particle would experience no bouncing force and would therefore go directly down the field line. There are waves in the equatorial regions, specifically whistler waves and electron Bernstein waves, that can interact with trapped electrons. These interactions can transfer energy to the electrons, increase their parallel velocity, and knock them into the loss cone. Electrostatic waves propagating across B_o at harmonics of the cyclotron frequency are known as Bernstein waves. Using the hot plasma dielectric tensor and Poisson's equation, $\nabla \cdot \epsilon \cdot E = 0$, then assuming $E_1 = -\nabla \phi_1$ and $\phi_1 = \phi_1 e^{k \cdot r - \omega t}$, and doing significant algebra, the dispersion relation of electron Bernstein waves is found.

$$1 = \sum_s \frac{k_D^2}{k_\perp} e^{-b} \sum_{n=1}^{\infty} I_n(b) \frac{2n^2 \omega_c^2}{\omega^2 - n^2 \omega_c^2}$$

$$b = \frac{k_x^2 v_{thermal}^2}{2\omega_c^2}$$

$$k_D^2 = \frac{2\omega_p^2}{v_{thermal}^2}$$

In the magnetosphere and ionosphere, electron Bernstein waves are typically at harmonics like 3/2 and 5/2 of the cyclotron frequency. Bernstein waves can resonantly interact with equatorially trapped electrons and transfer energy, sometimes causing these electrons to precipitate into higher latitudes.

Interactions between plasma sheet electrons and electromagnetic waves are non-linear and complex. Plasmaspheric hiss affects the local electron velocity distribution which, in turn, affects whistler wave generation. This background hiss is basically noise from electrons in the plasma sheet at various temperatures. In a certain frequency range, the hiss grows and forms coherent waves. The coherent waves interact with electrons and generate whistler waves at various frequencies. Electromagnetic whistler waves resonate with the electron cyclotron frequency of trapped electrons due to the Doppler effect. The resonance condition is given by $\omega - n\omega_{ce} - k_{||}v_{||} = 0$, where n is the harmonic number. [Villalón and Burke] The harmonic number can be any integer. The parallel direction for k-vector and velocity is along the geomagnetic field. When energy is transferred to electrons, from background plasmaspheric hiss, it causes a step-like change in the electron velocity distribution function at the boundary between resonant and non-resonant particles. Linear interactions between electromagnetic waves and these step-like distribution functions give rise to electromagnetic wave packets, or wavelets. Wavelets grow and their electric fields increase, trapping electrons and creating a plateau in the electron distribution function. The trapped electrons generate resonant currents which either return energy to electromagnetic plasma sheet hiss, or trigger chorus emissions. Chorus emissions are whistler waves whose frequency spread is related to the bandwidth of the wavelets which help generate it. This chorus of whistler waves can propagate at large angles to the geomagnetic field and interact with electrons. When the aforementioned resonance condition is met, the relative phase between the wave electric field and the electrons's cyclotron motion remains stationary during their interaction. This resonant interaction can either increase or decrease the perpendicular velocity of the electrons. Since there are more electrons with pitch angles near 90 degrees than at zero degrees, there is diffusion of electrons into smaller pitch angles and therefore into the loss cone. Electrons

in the loss cone precipitate into the atmosphere at an altitude near 100 kilometers. Kinetic energy from the perpendicular velocity of electrons is transferred to the waves from the electron distribution. The waves then scatter more electrons and grow even larger. This cycle repeats until the loss cone fills, and the process reaches saturation.

Results, Conclusions and Plans for the Future

The loop probe has acquired data in several experiments. Theoretical analysis has determined that the data seen is not from whistler wave ducting in a crest of magnetized plasma density. Experimentally, it has been observed that the exact whistler wave cutoff frequency is not directly related to density. (see Figure 2) It did appear to be directly related to the toroidal magnetic field magnitude from shot to shot. (see Figures 3 and 4) The cutoff frequency changed often, depending on electron beam current and number of beams firing. However, on a particular day, cutoff frequency was approximately the same percentage of cyclotron frequency regardless of the loop probe radius. A two dimensional density scan of the plasma was done and showed that one beam plasma had distinct, periodic “rungs” of higher density plasma, while a two beam plasma was more uniform vertically. (see Figure 5) The mechanism which caused the discrepancy between day-to-day cutoff frequency and ionospheric studies is not yet fully understood, but two dimensional plasma density results indicate a relation to the density contour of the plasma. In addition, data shows that electromagnetic waves can be ducted up to the cyclotron frequency. (Figure 6) Additionally, wavelengths of whistler waves in VTF are in the tens of centimeters range, while the ducts are about 15 cm wide. Since wavelength is not bigger than the duct size, a waveguide dispersion effect could occur. Damped waves could propagate outside the duct and find a new duct before they completely decay. Therefore, whistler waves in VTF could be ducted in the trough of density between electron beams. The electron beams form rungs in a helical shape because they follow the contour of the magnetic field in the vacuum chamber. The trough is imperfect because density does not increase in all directions; however, waves that escape the trough may find another trough within which to be ducted, before they totally decay. So, the experimental data could be

explained by wave ducting in a trough with waveguide dispersion. This work will be continued for a master's thesis.

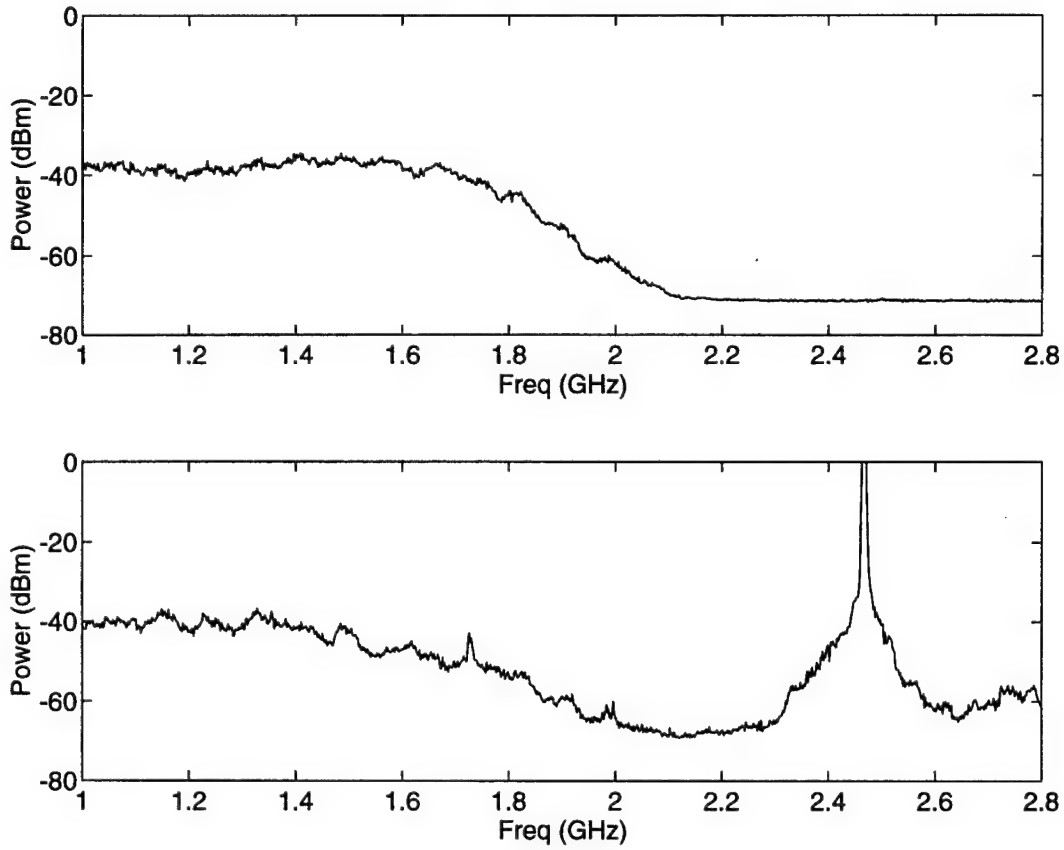


Figure 2: Power vs. Frequency for top, no microwave, plasma density $7 \times 10^{15}/m^3$, and bottom, with microwave, plasma density $1.5 \times 10^{16}/m^3$

Toroidal field magnitude has $1/r$ dependence. The plot shows that cutoff frequency increases with decreasing magnetic field. Magnetic field is about .08 tesla at a radius of 100cm so the cyclotron frequency is 2.24 GHz. Cutoff frequency is about 1.95 GHz so it's at .87 of the cyclotron frequency.

1 Beam Plasma

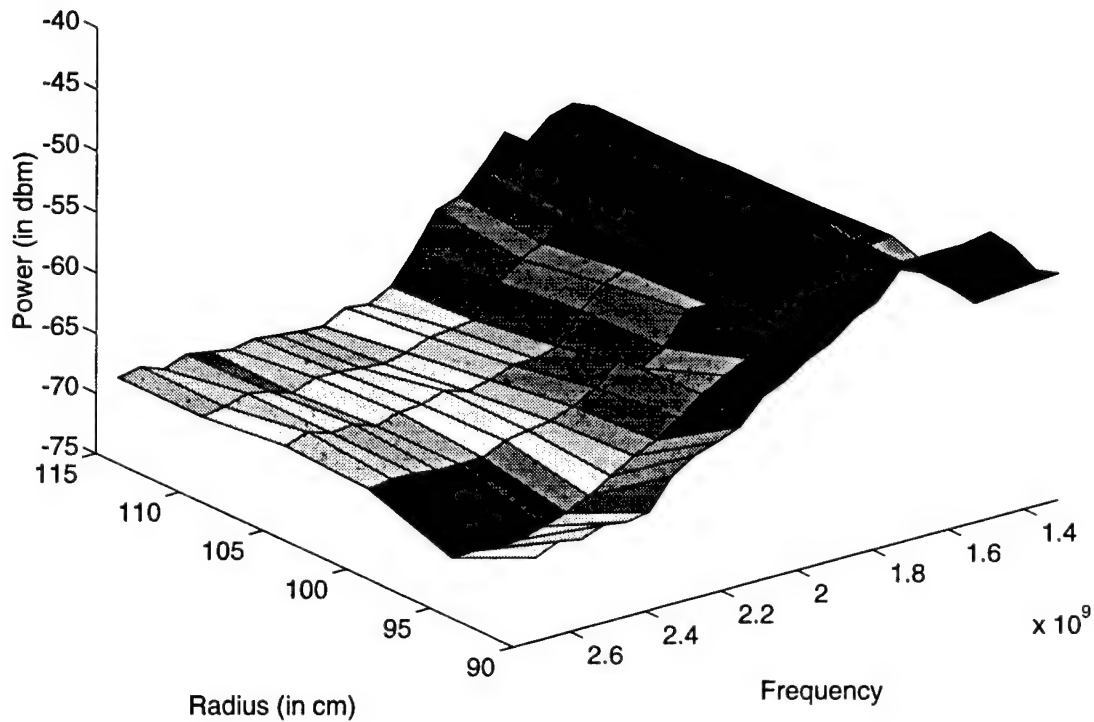


Figure 3: Whistler Wave Cutoff Frequency vs. Radius for a single beam shot

Toroidal field magnitude has $1/r$ dependence. Again, the plot shows that cutoff frequency increases with decreasing magnetic field. Magnetic field is about .08 tesla at a radius of 100 cm so the cyclotron frequency is 2.24 GHz. Cutoff frequency is about 2.25 GHz so it's at the cyclotron frequency.

2 Beam Plasma

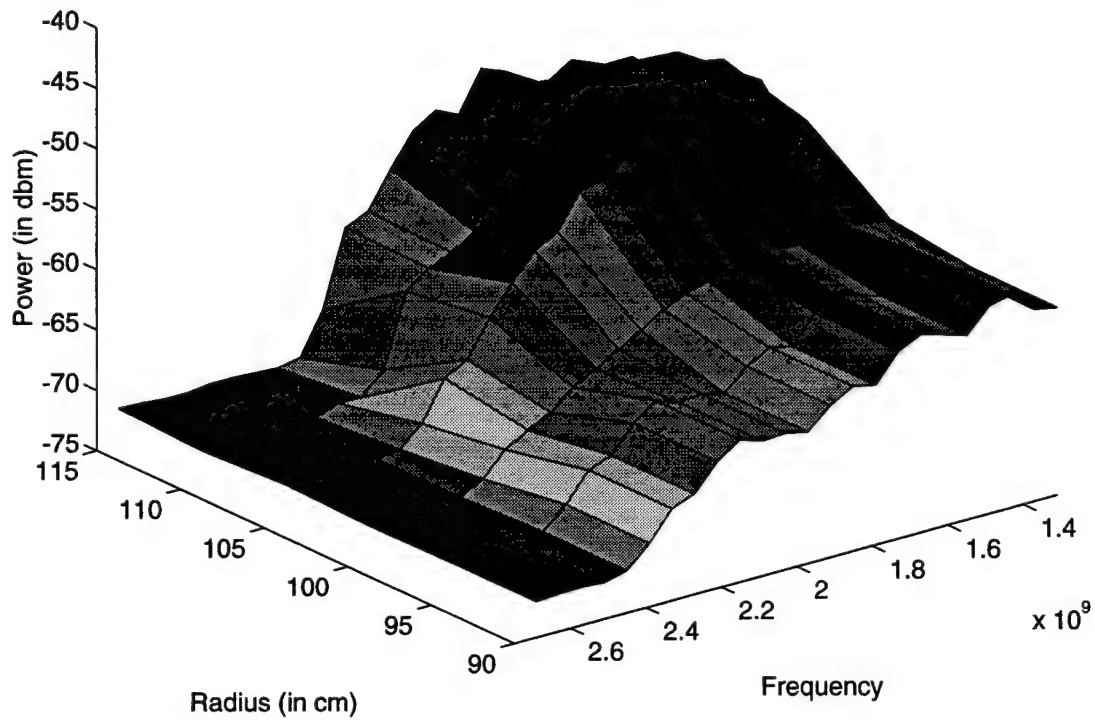


Figure 4: Whistler Wave Cutoff Frequency vs. Radius for a two beam shot

Top shows one beam contour, bottom shows two beam. From lowest density to highest, the shades go from lightest to darkest, respectively.

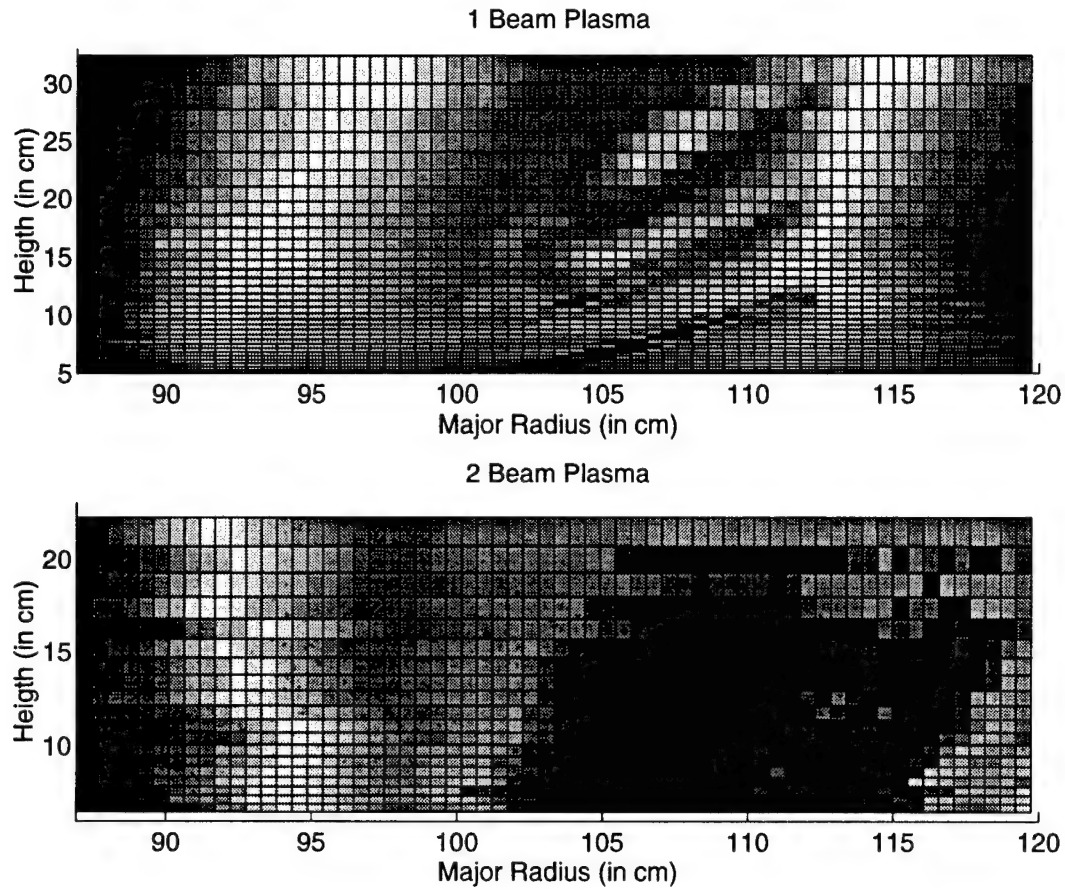


Figure 5: Side views of two dimensional contours of beam plasmas

Magnetic field was .1 Tesla at the probe tip when this spectrum was taken. Therefore cyclotron frequency was 2.78 GHz and waves were detected up to the cyclotron frequency.

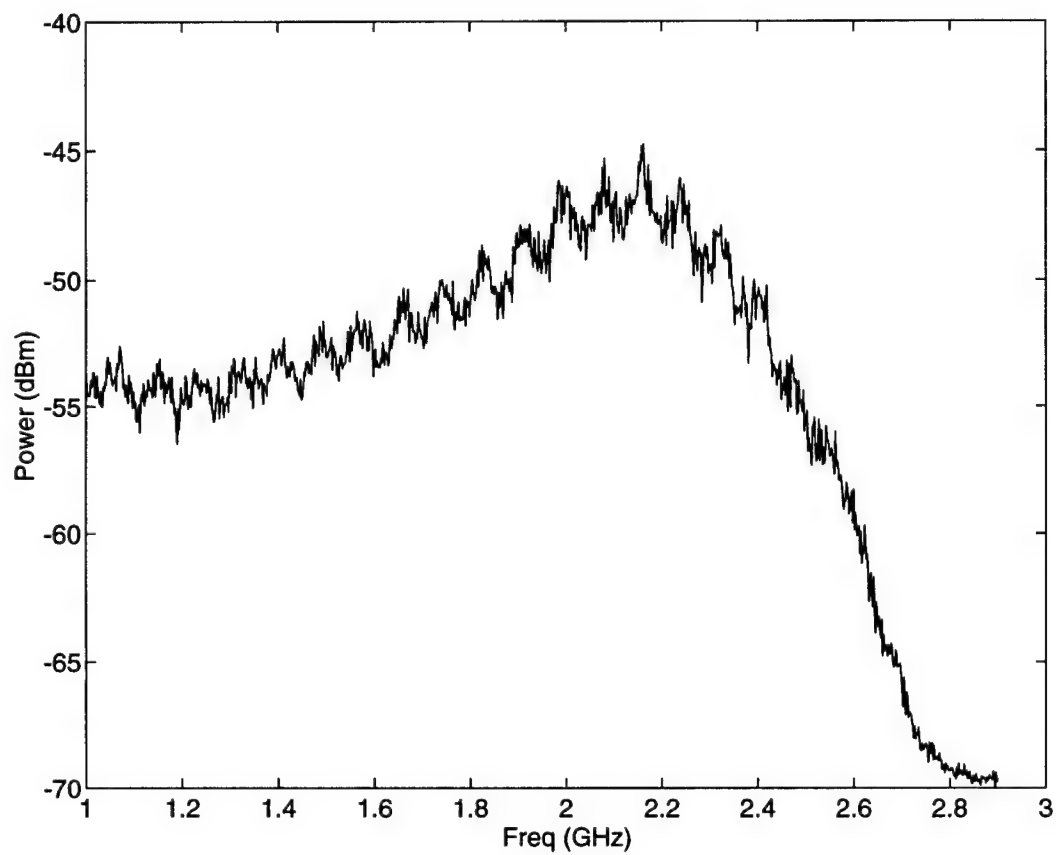


Figure 6: High frequency spectrum of whistler waves

References

[Helliwell, 1965] Helliwell, Robert, A., *Whistlers and Related Ionospheric Phenomena*, Stanford University Press, Stanford, CA, 1965.

[Smith, 1961] Smith, R.L., Propagation Characteristics of Whistlers Trapped in Field-Aligned Columns of Enhanced Ionization, *Journal of Geophysical Research*, Vol. 66, Page 3699, 1961.

[Villalón and Burke] Villalón, Elena, and Burke, William, J., *Theory of Quasi-monochromatic Whistler Wave Generation in the Inner Plasma Sheath*

**A PRELIMINARY STUDY OF THE EFFECTS OF PROCESS CONDITIONS ON
CURVATURE IN GRAPHITE/EPOXY PULTRUDED RODS**

**Lorena L. Sanchez
Research Assistant**

**University of New Mexico
Department of Civil Engineering
Albuquerque, NM 87131-1351**

**Final Report for:
Graduate Student Research Program**

**Sponsored by:
Air Force Office of Scientific Research
Bolling Air Force Base, Washington DC**

and

**Phillips Laboratory
Kirtland Air Force Base, Albuquerque, NM**

August 1997

A PRELIMINARY STUDY ON THE EFFECTS OF PROCESS CONDITIONS ON
CURVATURE IN GRAPHITE/EPOXY PULTRUDED RODS

Lorena L. Sanchez
Research Assistant
Department of Civil Engineering
University of New Mexico

ABSTRACT

Pultrusion is a cost-effective and highly mechanized process for manufacturing advanced fiber reinforced plastics (FRP) composites. Studying advanced pultruded composites is relevant for the manufacture of lightweight structural components for the 'Precision Deployable Space Structures' program of the Air Force. Space based radars currently being pursued by NASA and the Air Force will require long (up to 200ft) supporting structures in order to accommodate the larger optics which will be utilized to increase resolution and obtain more precise images. A critical requirement for these supporting structures is to maintain part straightness; therefore, investigation of process conditions during pultrusion was conducted to determine the contributing variables effecting curvature.

A PRELIMINARY STUDY ON THE EFFECTS OF PROCESS CONDITIONS ON
CURVATURE IN GRAPHITE/EPOXY PULTRUDED RODS

Lorena L. Sanchez

1.0 Introduction

Pultrusion is a cost-effective and environmentally benign process for manufacturing advanced fiber/matrix (carbon/epoxy, E-glass/polyester) composites. It is a continuous process which enables a high productivity rate for continuous cross-sectional shapes of any desired length. Applications of pultruded composites include a very broad spectrum, from the sporting industry to space applications.

Studying advanced pultruded composites is relevant for the manufacture of lightweight structural components for the 'Precision Deployable Space Structures' program of the Air Force. Space based radars currently being pursued by NASA and the Air Force will require long (up to 200ft) supporting structures with minimal thermal deflections during service of approximately 150°F changes in temperature during orbit. An ongoing project which is being pursued by NASA in a collaborative effort with the Defense Mapping Agency of the U.S. Department of Defense is the Shuttle Radar Topography Mission (SRTM). It is a planned 11-day mission to be flown in May 2000 which will map 80 percent of the Earth's surface with an accuracy of better than 53 feet.

The topographic images will be collected using three-dimensional measurements, and will cover regions which are home to about 95 percent of the world's population. In order to collect these images, a mast of almost 200 feet will be constructed. The members of this mast will be composed of 5/8 inch diameter graphite/epoxy pultruded rods, and must meet the requirements provided by NASA. These requirements include maintaining a straightness of 0.01 inch per 27 or 29 inches in length, possess a minimum tensile modulus of 24E06psi, a coefficient of thermal expansion (CTE) between -0.2 to -0.32 ppm/°F, contain a reasonable surface finish, and be free of internal cracking.

It is the intent of this paper to primarily focus on the requirement of maintaining part straightness by analyzing the process variables which are suspect to cause curvature, namely die temperature, fiber volume, and pull force. A brief description of the pultrusion process will also be presented in order to better comprehend the process.

2.0 Pultrusion Process

The pultrusion process consists of pulling continuous rovings of fiber through a resin bath or impregnator then into preforming fixtures where the section is partially shaped and excess resin and/or air are removed. The part then proceeds into a heated forming and curing die where the section is cured continuously. A schematic diagram of the pultrusion process is shown below in Figure 1.

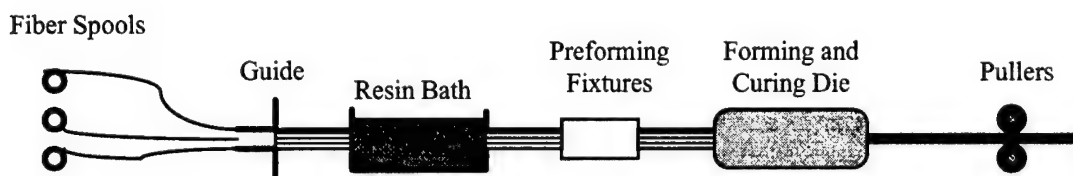


Figure 1

3.0 Process Variables

The quality of pultruded fiber/matrix composites depends on several process variables such as die temperature, curing rate, resin wet-out, pull force, pull speed and fiber volume. A variation in these process variables may result in significant differences in physical and mechanical properties of the end product.

The pull force is not a controllable process variable, as is the die temperature and percent fiber volume. However, the pull force can be indirectly controlled by changing another process variable. The simplest method for accomplishing this is to increase the percent fiber volume. As the fiber volume is increased, the pull force correspondingly increases to make up for the additional number of tows which are added to the process. The pull force may also change with a change in die temperature, but is more difficult to control since a significant amount of time is required for the die temperature to stabilize.

To determine the effects of increasing the fiber volume and varying the die temperature, experimental ¼" diameter graphite/epoxy rods were produced with a variation in die temperature in the first run, and with a variation in fiber volume in the second. Each of these variables effected both the pull force and the curvature, and an analysis was performed to determine if ultimately, a direct correlation between pull force and curvature could be established. Several specimens from each of these conditions were taken, and the curvature was physically measured.

4.0 Accounting for Curvature

To measure the curvature, a string was held taught at the two ends of the specimen, and the difference in height at the center was measured using a dial gauge (see Figure 2). The following formula was used to calculate the curvature:

$$\phi = \frac{2h}{(c^2/4) + h^2} \quad (1)$$

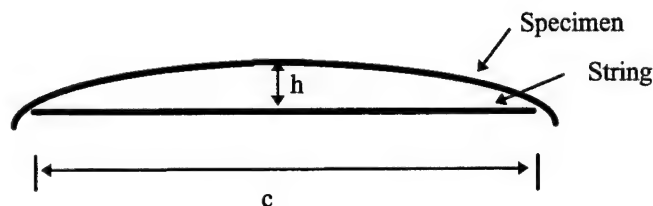


Figure 2

The results of this experiment are tabulated in the following section.

4.1 Pull Force vs. Curvature

A significant curvature was detected in the ¼" diameter graphite/epoxy rods from both the fiber volume variation and the die temperature variation. It was found that the curvature increased linearly with an increase in fiber volume, which leads to the assumption that the curvature increases with an increase in pull force since the pull force and fiber volume are directly related. However, no correlation could be established between a variation in temperature with curvature. This is an implication that the temperature of

the die may not be a significant factor in the curvature. An analysis on the effects of die temperature on curvature are discussed in section 4.3.

Tables 1 and 2 list the process conditions with the corresponding measured curvature, radius of curvature, and average pull force:

1/4" Diameter Rods Processed with a Temperature Variation

Initial Temp.	Rod #
340 (°F)	5-20
290 (°F)	24,26
240 (°F)	28-30

1/4" Diameter Rods Processed with a Fiber Volume Variation

# of Tows	% Fiber Volume	Rod #
41	0.63	3-4
42	0.65	6-7
43	0.66	11-12
44	0.68	16-20

Rod #	Avg. Pull Force (lb)	Curvature (in ⁻¹)	Radius of Curvature (ft)
3	275.76	0.00059488	140.08
6	240.53	0.00060737	137.20
7	535.26	0.00046586	178.88
19	525.52	0.00039655	210.14
20	537.35	0.00038731	215.16
26	592.86	0.00048856	170.57
28	954.05	0.0006439	129.42
29	920.47	0.00066359	125.58

Table 1

Rod #	Avg. Pull Force (lb)	Curvature (in ⁻¹)	Radius of Curvature (ft)
4	320	0.00040414	206.20
7	370	0.00047968	173.73
12	420	0.00056241	148.17
17	480	0.0006496	128.28

Table 2

The results of this experiment indicate that the pull force ultimately effects the curvature when the pull force is linearly increased, as in the fiber volume variation. However, since it is improbable that the pull force could act alone to change the curvature, another variable was taken into consideration. It was noticed that the pullers were misaligned during the process, and was therefore suspected that this misalignment was the ultimate cause of the curvature. This would explain that an increase in pull force (by increasing the fiber volume) would result in an increase in curvature.

4.2 Misalignment in Pullers

An analysis was performed to determine the effects of a misalignment of the pullers on the curvature. The actual misalignment of the pullers was not measured during the course of pultruding the experimental $\frac{1}{4}$ " diameter rods, therefore, hypothetical numbers were used. It was assumed that the pullers were misaligned by 0.01", and the average pull force was 400lbs. A simplified analogy of the process was utilized for calculations. A clamped-end mechanism was assumed in place of the die, therefore yielding a maximum moment at the die (see Figure 4).

Actual mechanism:

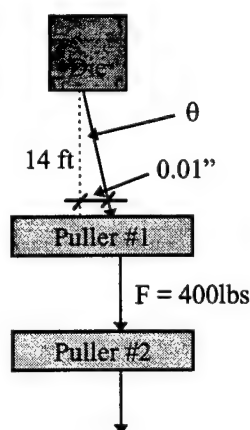


Figure 3

Assumed mechanism:

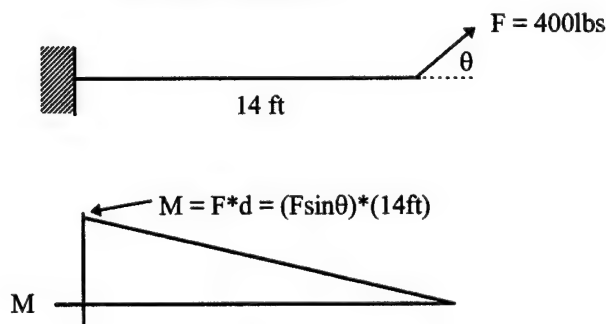


Figure 4

To calculate the moment due to a misalignment of 0.01" in the pullers, θ must first be known. From basic trigonometry, θ is simply:

$$\theta = \tan^{-1}(0.01/168) = 3.41\text{E-}03$$

The applied moment, M , then is:

$$\begin{aligned} M &= (400\text{lbs}) * (\sin(3.41\text{E-}03)) * (168\text{in}) \\ &= 4 \text{ in-lb} \end{aligned}$$

From the concepts of bending stress, the following relationship was used to determine the curvature as a function of the moment.

$$\frac{M}{I} = \frac{\sigma}{y} = \frac{E}{R} \quad (2)$$

Where: I = moment of inertia, σ = bending stress, y = distance from neutral axis to outer most fiber = radius, R = radius of curvature = $1/\phi$, and ϕ = curvature.

From the previous relationships, the curvature as a function of the moment is:

$$\phi = \frac{M}{EI} \quad (3)$$

Using the calculated applied moment of 4in-lb, a Young's Modulus of 24E06psi, and a moment of inertia of 1.92E-04in⁴, the curvature is:

$$\begin{aligned} \phi &= \frac{4\text{in-lb}}{(24\text{E}06\text{psi})(1.92\text{E}-04\text{in}^4)} \\ &= 8.68\text{E}-04 \text{ in}^{-1} \end{aligned}$$

This curvature is significantly higher than the calculated curvature of the ¼" diameter graphite/epoxy pultruded rods. This indicates that a slight misalignment of the pullers definitely effects the curvature of the pultruded rods. Further investigation will be conducted to determine the curvature from a known misalignment in the pullers.

4.3 Thermal Effects

The temperature of the die is a three-zone controlled electrical resistance heating unit with each zone having resistance heating cartridges. Zone 1 is where the material enters the die at a relatively lower temperature. A water-cooling system at the inlet is provided in order to prevent premature hardening of the resin as it enters the die.

Zone 2, known as the gel zone, is the area where the resin changes from a viscous liquid into a non-flowing sticky liquid, then into a rubber-like texture. This is the area in which the peak exotherm of the resin is achieved, which is often higher than the die temperature itself. This peak temperature causes the pressure to increase substantially, which is desired for curing. Curing under pressure results in a glossy part surface by holding the product tightly to the surface of the die during gelation (Hunter, 1988). As the resin cures to a hard solid, it partakes in a volumetric shrinkage allowing the pressure force inside the die to decay,

therefore allowing the product to release from the surface of the die. Minor sliding frictional forces between the cured material and the die are a resultant of the cured part releasing from the surface of the die. The remainder of the die is Zone 3, which acts to draw heat from the cured composite thereby reducing thermal shock to the product upon exiting the die (Sumerak, 1984). It is sometimes desirable, especially for thicker sections, to reduce the temperature in Zone 3, therefore lowering the product temperature prior to exiting the die in order to prevent thermal shock which may result in internal cracking.

4.3.1 Die Temperature Characterization

A die temperature characterization was conducted to determine if temperature effects curvature. A temperature profile of the die itself without fiber or resin was conducted in order to determine if there was a temperature variation across the die. The same die which was used to produce the ¼" diameter rods was used to conduct this experiment. It was suspected that the thermocouples on the pultrusion machine, the Pulstar® 1600, was incorrectly reading the actual temperature of the die.

The die was placed inside a chase, and thermocouple wires were fed through on the four corners between the die and the chase in order to obtain a temperature profile along the length of the die. A constant temperature setting of 380°, 380°, 380° was used, and the entrance cooler was turned on to agree with standard operating conditions.

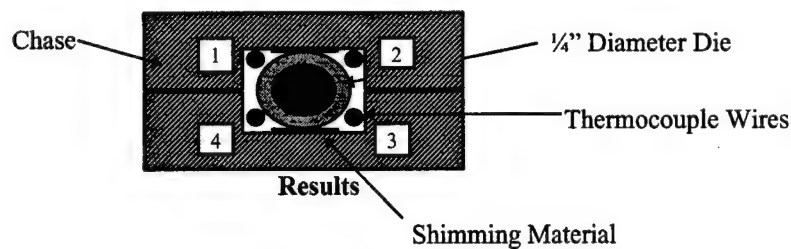


Figure 5

Length into Die (in.)	Temperature (°F)				
	1	2	3	4	Inside Die
0	169.5	178.5	195.5	187.5	191
6	387.5	392	400.5	383.5	387.5
12	401.5	404	418.5	417.5	415
18	397.5	391.5	415.5	414.5	402
24	372	373.5	373.5	394	371.5
30	326	320.5	325.5	328	323.5
36	113.5	115	123	120.5	120.5

Table 3

The profile of the die displayed significant differences in actual temperature as compared to the set temperature. This is due to the fact that the internal thermocouple of the Pulstar® 1600 is not located at the die, therefore does not accurately read the temperature of the die itself. The results also indicate approximately a 20°F temperature difference from the top of the die to the bottom (see Table 3 above), which may be the cause of the curvature of the ¼” diameter rods. The following section analyzes this possibility.

4.3.2 Theoretical Values of Curvature due to Variation in Temperature

Basic equations characterizing the strain as a function of temperature and curvature were utilized to determine if a variation in temperature of 20°F across the die had a significant effect on the curvature. The strain due to a temperature change is the change in temperature, δt , multiplied by the coefficient of thermal expansion, α :

$$\varepsilon = (\alpha) * (\delta t) \quad (4)$$

The curvature was then calculated from the following relationship:

$$\varepsilon = (\phi) * (r) \quad (5)$$

Where: ε = strain, ϕ = curvature, and $r = y$ = distance from neutral axis to outer most fiber = radius.

The previous relationship was derived from the concepts of bending stress (refer to equation (2) in section 4.1). The coefficient of thermal expansion of the carbon/epoxy composite is $0.6\text{E-}06 \text{ in/in}^\circ\text{F}$, therefore the strain is:

$$\varepsilon = (0.6\text{E-}06 \text{ in/in}^\circ\text{F}) * (20^\circ\text{F}) = 1.2\text{E-}05 \text{ in/in}$$

And the corresponding curvature is:

$$\phi = \frac{1.25\text{E-}05 \text{ in/in}}{0.125 \text{ in}} = 9.6\text{E-}05 \text{ in}^{-1}$$

This curvature due to a 20°F thermal gradient across the die is not significant when compared to the curvature due to misalignment of the pull shoes and a correspondingly increase in pull force, as was discussed in section 4.1.

4.4 Microscopic Analysis

One common concern in composite materials is that one area of the part may be more resin-rich than at another area. This would cause the more resin-rich area to cure faster, therefore will shrink sooner than the area with less resin, thereby causing the part to curve in the direction of the more resin-rich area.

In order to determine if the cause of curvature may be due to a resin-rich area, a microscopic analysis was conducted using a Scanning Electron Microscope (SEM). It was found that the fibers and the resin were evenly distributed throughout the part, therefore concluding that the curvature was not effected by an uneven distribution of resin. The following pictures are of one of the $\frac{1}{4}$ " diameter pultruded rods, taken with a Scanning Electron Microscope at 1,000x magnification. Photo 1 is taken at the center of the specimen, and Photo 2 is taken at the edge. The round objects shown are the individual carbon fibers and the dark areas are the resin. Each individual carbon fiber is approximately 7 microns in diameter. For comparison, a human hair averages 50 microns.

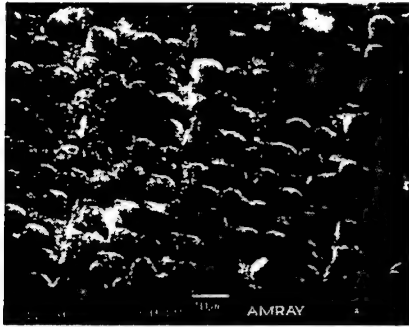


Photo 1

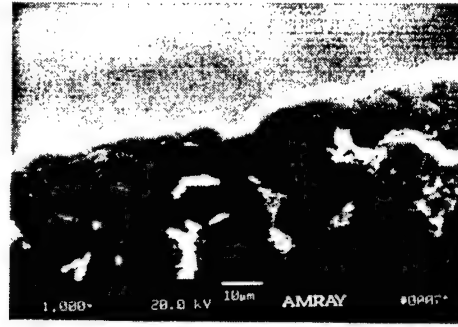


Photo 2

5.0 Conclusions

Based on these experiments, the results suggested that the main contribution to curvature is from the misalignment of the pullers. It was found that an increase in fiber volume caused an increase in pull force, which ultimately resulted in an increase in curvature. From this, it can be deduced that pull force and curvature are directly related. However, a direct correlation between pull force and curvature could not be established due to a variation in temperature. A thermal analysis was conducted to determine if temperature was a significant factor in curvature. It was found that a temperature variation of 20°F across the die was not significant when compared to the curvature due to misalignment of the pull shoes, therefore implying that a temperature variation was not a significant factor in curvature. These results are only preliminary, and further experiments need to be conducted in order to confirm these results.

6.0 Future Plans

Further experiments with ¼" diameter graphite/epoxy rods will be conducted to verify that a temperature variation across the die does not effect the curvature, and that pull force and curvature are directly related through a known misalignment of the pullers. To ensure the remaining NASA requirements are met, experiments on the Young's Modulus and the coefficient of thermal expansion will be conducted.

REFERENCES

Hunter, G. A. (1988). "Pultruding Epoxy Resin." *Proceedings of the SPI/CI 43rd Annual Conference*.

Sumerak, Joe and Martin, Jeff (1984). "Pultrusion Process Variables and their Effect Upon Manufacturing Capability." *Proceedings of the 39th Annual SPI Conference*.

NASA Press Release Archive, "Future Topographic Radar Shuttle Mission Will Map 80 Percent of Earth." NASA HQ Public Affairs Office, July 15, 1996.
<http://www.calix.com/nasamail/msg00079.html>

**A STUDY OF ALTERNATE PROPELLANTS
FOR PULSED PLASMA THRUSTERS**

**John H. Schilling
Research Assistant
Department of Aerospace Engineering**

**University of Southern California
University Park
Los Angeles, CA 90089-1191**

**Final Report for:
Graduate Student Research Program
Phillips Laboratory**

**Sponsored by:
Air Force Office of Scientific Research
Bolling Air Force Base, DC**

and

**USAF Phillips Laboratory
Edwards Air Force Base, CA**

September, 1997

A STUDY OF ALTERNATE PROPELLANTS FOR PULSED PLASMA THRUSTERS

John H. Schilling

Introduction

The USAF Electric Propulsion Laboratory is currently developing several types of pulsed plasma thrusters for stationkeeping and attitude control purposes on future satellites. Such thrusters have the potential for dramatically reduced propellant consumption, but current designs are plagued by inefficiencies which render them only marginally superior to existing chemical rockets. One major source of propellant inefficiency is believed to be post-discharge vaporization and sputtering due to radiation emitted by the plasma discharge and deposited some depth into the teflon propellant.

In order to reduce such losses, several alternate propellants with increased absorptivity were proposed. These propellants were tested under operational conditions using a laboratory test model PPT, and the propellant consumption carefully monitored. Reductions of 50% or more in propellant consumption were observed with the new high-absorptivity propellants, but all such propellants tested proved to have electrical or chemical properties incompatible with the reliable long-term operation of current pulsed plasma thruster designs. A new PPT design capable of exploiting the improved performance of these propellants is therefore under development.

Discussion

The operational lifetime of most modern satellites is limited not by the reliability or longevity of its various components or systems, but by the supply of propellant for the spacecraft's attitude control and/or stationkeeping thrusters. When this propellant is exhausted, the satellite inevitably drifts from its assigned orbit, loses orientation, and is no longer able to carry out its mission. It then becomes necessary to replace an otherwise fully functional satellite at a cost of tens or hundreds of millions of dollars. Obviously, some means of extending the propellant-limited lifetime of spacecraft is urgently needed.

One such method is the use of electric propulsion. By using electric energy to accelerate a propellant by electrostatic, electromagnetic, or electrothermal effects, much higher exhaust velocities can be achieved than with chemical rockets, leading to correspondingly lower propellant consumption and longer spacecraft life. Electric propulsion systems are inherently low in thrust, precluding their use in launch vehicles, but are entirely adequate for stationkeeping duties.

The Pulsed Plasma Thruster is one of the more promising near-term electric propulsion systems. A PPT consists simply of a solid propellant bar (usually teflon) mounted between two electrodes, a capacitive discharge circuit, and a spark trigger. When the capacitor is discharged, an arc forms along the surface of the propellant bar and ablates a small amount of propellant. This propellant is ionized by the

discharge, and then accelerated by the Lorentz force interaction between the plasma current and the current in the electrodes. Exhaust velocities of up to 40,000 meters per second, corresponding to a specific impulse of roughly 4,000 seconds, can be achieved. This high efficiency, coupled with the lack of moving parts or volatile or otherwise dangerous propellants, make the PPT ideal for stationkeeping and attitude control applications in satellites.

Unfortunately, existing PPT designs are plagued by extremely low propellant utilization efficiencies. Only about 20% of the propellant consumed, is ionized and accelerated as a plasma. The remaining 80% is emitted in the form of low-velocity neutral vapor and particulates, producing no significant contribution to the thrust of the system. This is clearly unacceptable for a propulsion system whose primary goal is to reduce propellant consumption.

At present, the loss mechanisms involved are not clearly understood, but excessive heating of the propellant seems to play a major role. Radiation emitted from the arc discharge is deposited in the propellant bar, causing substantial heating that may lead to surface vaporization and sputtering. This problem is compounded by the fact that the propellant of choice, polytetrafluoroethylene (teflon), is partially transparent to the wavelengths of interest, leading to absorption as deep as 50 microns from the propellant face. This in turn leads to a much greater degree of vaporization than would otherwise be the case.

One possible route of improvement would be to alter the propellant properties so as to reduce this premature vaporization. Since a certain amount of propellant must be ablated to form the plasma arc necessary for thruster operation, tailoring the absorptive properties of the propellant so that the bulk of the incident radiation is deposited in the desired ablation region would likely reduce losses due to unwanted late-term vaporization and sputtering.

This can be accomplished either by incorporating additives to the PTFE propellant, or by using a fundamentally new propellant. As PTFE is ideally suited for the application in many respects, and most of the current experience with PPT thrusters is with PTFE propellant, additives seem preferable. Two additives in particular were chosen for closer study. Carbon, either amorphous or as graphite, offers greatly increased absorptivity in the visible and near-UV spectrum, and molybdenum disulphide in the far UV and soft X-ray region, at fairly small concentrations.

Methodology

The USAF Electric Propulsion Laboratory currently uses the XPPT-1 pulsed plasma thruster for most test purposes. This is a design intended to be functionally identical to the flight-rated LES-8/9 PPT for which extensive operational data is available, but with greater accessibility for diagnostic instrumentation. An XPPT-1 was made available for use in this study, and its performance verified with a series of tests with ordinary PTFE propellant at normal operating conditions.

Three alternate propellant compositions were tested in this program. PTFE with 5% carbon added, PTFE with 5% graphite, and PTFE with 5% molybdenum disulfide. The carbon and graphite were expected to provide increased absorption of visible and near-UV light, the MoS₂ of far UV and soft X-ray radiation. In all cases the propellant was manufactured by mixing PTFE powder of 20 micron grain size with the appropriate additive in the same form, pressing to shape, and sintering. Standard PTFE propellant bars have traditionally been manufactured in this fashion, minus any additives, so the propellant microstructure should remain unchanged - a potentially important consideration, as some of the propellant loss is speculated to come from the ejection of entire, incompletely bonded, propellant grains during or immediately after the discharge.

All tests were conducted using a 20 microfarad capacitor charged to 1,414 volts to provide 20 joules of energy for the main discharge. The discharge was triggered at a rate of 1 pulse per second by a 1,800 volt pulse to one of the two spark plugs in the PPT cathode, alternating the spark plug used at every discharge to promote uniform ablation of the propellant surface. This conforms to most previous PPT performance tests, allowing the data collected to be directly compared with previous work. While both the LES-8/9 and XPPT-1 thrusters have two complete discharge assemblies with provisions for two propellant bars, only one was used in this test series due to a shortage of spark plugs suitable for triggering the PPT. This is not expected to alter the results, as the two discharge assemblies operate independently and at different times, and so presumably do not affect one another. All tests were conducted in a 6' vacuum chamber maintained at a pressure of 10^{-4} torr or less to simulate the space environment.

As the objective was to reduce propellant losses by minimizing late-term vaporization, the primary measurement of interest was propellant consumption. Propellant bars were weighed three times on a quartz microbalance both before and after the test, and the weight difference divided by the number of discharges gave the propellant consumption. A precision thrust stand was available in the lab, but due to competing demands and difficulty of use, initial evaluation of alternate propellants was made on the basis of measured consumption only - any particularly promising propellant could then have thrust and consumption measured concurrently to determine propellant specific impulse.

Each test required a minimum of five thousand pulses in a single operational period, to obtain accurate data on steady-state propellant consumption. It has been observed that the first thousand pulses of a test session show anomalously low propellant consumption, presumably due to thermal effects. During operation, the bulk temperature of the propellant bar increases by roughly 50 C, which may significantly increase late-term vaporization. It is also believed that propellant consumption may be anomalously high during the first few tens of thousands of shots on a new propellant bar, as the flat propellant face is eroded to the shape preferred by the arc discharge. As no more than twenty thousand pulses can be made during a single day's operation, up to a week of testing is required to accurately evaluate the propellant consumption for any proposed propellant.

Results

The following table gives a summary of the successful test series performed using the baseline and modified propellants:

Propellant:	Initial Mass:	Final Mass:	# Discharges:	Propellant Usage:
PTFE	101.8662g	101.3918g	18,657	25.4 μg / discharge
PTFE	101.2094g	100.9968g	7,378	28.8 μg / discharge
PTFE	100.9639g	100.9226g	2,137	19.3 μg / discharge
5% MoS ₂	102.5529g	102.2716g	29,737	10.1 μg / discharge
5% MoS ₂	102.2746g	102.0592g	26,782	8.0 μg / discharge
5% MoS ₂	102.0627g	101.8394g	22,752	9.8 μg / discharge
5% Carbon	101.0569g	101.9939g	7,267	8.6 μg / discharge

As can be seen, both the MoS₂ and amorphous carbon additives resulted in a significant decrease in propellant consumption, on the order of 50%.

Unfortunately, reliable operation of the thruster using either of the carbonaceous propellant additives turned out to be generally infeasible. In both cases, the conductivity of the propellant was too high to allow the creation of an arc discharge across the surface, the capacitor instead preferring to discharge through the bulk of the propellant bar. After repeated attempts and with careful positioning of the propellant bar with respect to the electrodes, one successful test run of reasonable length was completed using the amorphous carbon propellant, with the results indicated. This suggests that a redesigned thruster with no electrical path through the solid propellant bar could exploit the improved performance of carbonaceous propellants. Preliminary design work on such a thruster has commenced at the Electric Propulsion Laboratory, and tests are expected sometime in 1998.

Molybdenum disulphide showed a smaller but still significant improvement in propellant erosion. It also had the advantage of being an insulator, and thus usable as a propellant additive in existing thruster designs. However, extremely atypical erosion was observed with this propellant. Under normal circumstances, the PTFE propellant is eroded over time into a smooth but slightly concave profile on the exposed face. The propellant with MoS₂ additive showed deep grooves carved into the propellant face, apparently coinciding with very narrow arc discharges originating at the two spark plugs in the anode and traversing the propellant face in a repeatable fashion. In addition, a rough, black deposit was observed on the face and edges of the propellant bar, particularly concentrated at the electrode surfaces and along the heavily eroded arc paths.

Observation of the deposit via optical and electron microscope were inconclusive, as was an attempt to obtain the elemental composition by electron backscatter analysis. We suspect, but cannot prove, that the deposit is metallic molybdenum produced by the breakdown of MoS₂ in the arc discharge, left behind by the acceleration process due to its high molecular weight, and redeposited on the surface. This seems to lead to increased conductivity along the arc path, encouraging subsequent discharges along the same path and producing the irregular erosion patterns observed.

Conclusions

The concept of using alternate propellants to reduce the depth or radiant energy deposition, and thus of propellant consumption, was verified. Both the use of carbonaceous propellant additives to increase absorption of longer wavelengths and high-Z materials like MoS₂ for increased absorptivity at longer wavelengths, led to measurable reductions in propellant consumption. Unfortunately, the material properties of those particular propellants rendered them unsuitable for use in current thruster designs. The high conductivity of the carbonaceous propellants led to unreliable operation of the discharge circuit, and the breakdown and redeposition of the MoS₂ in the plasma discharge caused anomalous propellant erosion.

These results suggest avenues for continued research. With minor design changes, plasma thrusters should be able to operate with conductive propellants. This would allow more extensive testing, and possibly operational use, of the extremely promising carbonaceous propellant additives. It could also facilitate use of MoS₂, in that local deposition of conductive material from the discharge may not tend to draw future discharges to the same path and produce nonuniform erosion if the propellant as a whole is already conductive.

Barring the successful operation of a conductive-propellant thruster, it would still be imperative to continue searching for propellant additives with increased absorptivity but without the operational disadvantages observed with carbon and molybdenum disulfide. The demonstrated 50% reduction in propellant consumption points to an extreme inefficiency which should not be tolerated in an operational system.

INVESTIGATION OF AN EXPLOSIVELY FORMED FUSE USING MACH2

Kenny F. Stephens II
Doctoral Candidate
Department of Physics

University of North Texas
Denton TX 76203

Final Report for:
Summer Graduate Research Program
Phillips Laboratory

Sponsored by:
Air Force Office of Scientific Research
Bolling Air Force Base, DC

and

Phillips Laboratory

August 1997

INVESTIGATION OF AN EXPLOSIVELY FORMED FUSE USING MACH2

Kenny F. Stephens II
Doctoral Candidate
Department of Physics
University of North Texas

Abstract

A particular type of opening switch, known as an explosively formed fuse, capable of transferring megajoules of electrical energy within a few microseconds is simulated using the magneto-hydrodynamic code, MACH2. In the simulations, an electrical current is made to flow in a thin foil that surrounds the explosive material. The explosion causes the foil to effectively lengthen and thin, thereby increasing its resistance. Preliminary calculations; with a time-independent current of 1 kA were performed. The results indicate the necessary considerations for thoroughly modeling such a device. Aspects such as hydrodynamics, magnetic flux compression, and resistive diffusion are discussed.

INVESTIGATION OF AN EXPLOSIVELY FORMED FUSE USING MACH2

Kenny F. Stephens II

I. Introduction

Devices capable of providing several mega-joules of electrical energy within a few microseconds are of current interest for driving high-impedance loads with large voltages. Low voltage capacitor banks and magnetic-flux compression generators are frequently used for this role. However, their energy-delivery time scales typically exceed preferred experimental time scales. Thus, there is a need for systems capable of filling this void.

In 1975, A. I. Pavlovskii [1] proposed an explosively-driven opening switch potentially capable of satisfying these requirements. His idea involved detonating a high explosive (HE) near a current-carrying conductor. The ensuing shock wave would deform the conductor in such a way as to increase its resistance. In Pavlovskii's experiment, the switch resistance increased from 1 m Ω to 200 m Ω within 0.5 μ s; the peak switching voltage was 300 kV.

This paper investigates the properties of an opening switch configuration, known as an explosively-formed fuse (EFF), devised at Los Alamos National Laboratory (LANL). Using the magneto-hydrodynamic program, MACH2 (Multi-block Arbitrary Coordinate Hydrodynamics 2D), developed at Phillips Laboratory, several aspects of such a device are considered.

II. MACH2

MACH2 [4-5] is a finite-difference code that solves the time-dependent, single-fluid, multi-temperature MHD equations. Computing on a mesh composed of arbitrarily shaped hexahedral cells, the problem geometry is constructed out of multiple blocks (logically rectangular collections of cells), using an Arbitrary Lagrangian-Eulerian (ALE), multi-grid scheme. The geometry can be either planar or axially-symmetric. The code calculates all three components of the velocity and magnetic vector fields. For this reason, it is usually referred to as a 2-1/2 dimensional code. The finite differences are determined using a finite volume technique, along with second order accurate Van Leer convection and flux-conserving, constrained transport for magnetic advection.

MACH2 solves the fluid momentum equation,

$$\rho D_t \mathbf{u} = -\nabla P + \mathbf{J} \times \mathbf{B},$$

INVESTIGATION OF AN EXPLOSIVELY FORMED FUSE USING MACH2

Kenny F. Stephens II

the continuity equation,

$$D_t \rho + \rho \nabla \cdot \mathbf{u} = 0,$$

and energy equation,

$$\rho D_t \varepsilon = -P \nabla \cdot \mathbf{u} + \nabla \cdot (\kappa \nabla T),$$

for a fluid of mass density, ρ , and velocity, \mathbf{u} , in a magnetic field, \mathbf{B} ; $D_t = \partial_t + \mathbf{u} \cdot \nabla$ is the convective derivative. The time evolution of the magnetic field is governed by the magnetic induction equation,

$$\partial_t \mathbf{B} = -\nabla \times \mathbf{E}.$$

The electric field is determined from a generalized Ohm's law,

$$\mathbf{E} = \eta \mathbf{J} - \mathbf{u} \times \mathbf{B} + \frac{1}{en} (\mathbf{J} \times \mathbf{B} - \nabla P)$$

And closing out the system of equations is an equation of state, $P = P(\rho, T)$, for which several models are available.

Energy changes are determined from changes in the temperature according to $d\varepsilon = c_v(T) dT_0$. And to assist in the modeling of shocks, the code includes compressional viscosity.

Boundary conditions are imposed on the mass density, various transport coefficients, the specific energies, and the components of the magnetic and velocity fields.

III. EFF Model

The EFF configuration considered in this report is shown in Figure 1. It is an axially symmetric system. The inner-most material is a HE characterized by an explosive specific internal energy of 5.543 MJ/kg and modeled by a Grüneisen equation of state. The next material is the aluminum active switch conductor. This is the primary path for the interrupted current. A tabular equation of state, SESAME, developed at LANL, is employed for the aluminum. Next is the extrusion die: a periodic sequence of annular regions of teflon, separated by gaps of air. It is this construction that deforms the switch conductor. Once the explosive shock wave begins pressing the aluminum against the die, the conductor is stretched across the teflon, increasing its length and decreasing its cross-section. The final material is an outer backing of teflon that provides the base for the teflon annuli.

INVESTIGATION OF AN EXPLOSIVELY FORMED FUSE USING MACH2

Kenny F. Stephens II

The electrical diffusivity, defined as η/μ_0 for a material of resistivity η , of the aluminum was determined from the SESAME tables. At the initial temperature of 0.0270 eV, this value is 0.0226 m²/s and corresponds to a resistivity of 2.85 $\mu\Omega\cdot\text{cm}$. For all other materials, a fixed value of 10 m²/s was chosen. Also, an external circuit is placed along the outer radius of the backing teflon.

IV. Simulation of the EFF

To develop an intuition of the EFF, a constant 1 kA current was employed on the geometry detailed in Figure 1. This simple case allows for easy assurance that MACH2 was calculating the correct voltage across the EFF. This section discusses the primary aspect of this diagnostic.

A. Hydrodynamics

Hydrodynamics plays a fundamental role in the operating principles of the EFF. Detonation of the HE produces a high pressure shock wave that forces the active switch against the extrusion die. From this, the conductor stretches into very thin cross-sections. From elementary physics, the resistance of a material with resistivity, η , is given by

$$R = \eta \frac{L}{A},$$

where L is the length and A the cross-sectional area of the material. Thus, the stretching and thinning of the conductor is primary to increase the overall resistance of the EFF.

Figure 2 shows a sequence of mass density plots generated by MACH2 during a typical run. At $t = 0$, the HE is axially detonated. After 2.5 μs , the explosive shock wave reaches the aluminum, shown in the first frame. The dashed rectangle indicates the region displayed in the following six frames, sequenced at 1 μs . As is clearly seen, the Al is forced into the air gaps while the teflon fingers are more slowly compressed. Thus the extrusion die does indeed deform the conductor as desired.

B. Resistive Diffusion, Resistance and Voltage

MACH2 calculates the voltage according to the elementary relation between electric field and electric potential, i.e.,

$$V = \int \mathbf{E} \cdot d\mathbf{l}.$$

INVESTIGATION OF AN EXPLOSIVELY FORMED FUSE USING MACH2

Kenny F. Stephens II

The integration path is taken along the circuit boundary, and as mentioned above, the electric field is determined from Ohm's law.

To obtain a numerical value by hand, it was necessary to determine the resistance for each material in the direction of the circuit. Using the electrical diffusivity values cited above and considering the EFF to be equivalent to a three parallel resistor circuit, the expected total resistance is $3.040 \mu\Omega$. However, it took some clever manipulations to obtain an agreeable voltage from MACH2.

For MACH2 to calculate the above voltage, the time required for the magnetic field to diffuse through the teflon/air and into the switch was needed. To find this resistive diffusion time, a magnetic diffusion equation was required. Using the simple form of Ohm's law, $E = \eta J$, along with Faraday's and Ampere's laws, the magnetic diffusion equation is

$$\partial_t B = \frac{\eta}{\mu_o} \nabla^2 B,$$

for η constant. To obtain an approximate expression for the time required for the field to diffuse a distance L , a dimensional analysis shows that

$$\delta t \approx \frac{\mu_o L^2}{\eta}.$$

Thus, for the separation of 2.6 cm between the circuit path and the active switch conductor, the diffusion time through the teflon/air combination is $67.6 \mu s$. Thus time steps small compared to this value had to be taken.

To further simplify the load on MACH2 to completely diffuse the magnetic field through the insulators, a new magnetic field option was added to the code. The code already provided numerous current configurations, but we added one that bears considerable importance to the present problem. This is the field due to a current carrying annulus:

$$B_\theta = \frac{\mu_o J}{2\pi r} (r^2 - r_o^2),$$

where r_o^2 is the inner radius and J the constant, axial current density in the annulus.

INVESTIGATION OF AN EXPLOSIVELY FORMED FUSE USING MACH2

Kenny F. Stephens II

The voltage MACH2 calculated by resistive diffusion, before the explosion, was 3.0 mV. Figure 3 shows the voltage during the entire computational run. The expected result is a large voltage rise as the Al is increasingly deformed, as explained above. However, the plot clearly shows no such rise. Instead, there is a significant drop, even a change in polarity. There are two explanations for this. First, in order to lay the external circuit along the outer teflon boundary, a boundary condition of insulator had to be imposed. Thus, magnetic flux is lost through the circuit boundary. Ideally, that boundary would be a conductor and the flux would be compressed. The second reason for the change in polarity can be seen by considering the formula,

$$V = IR - I \frac{dL}{dt}.$$

If the inductive changes increase before the resistance begins to rise, the voltage can clearly become negative. This can be verified by estimating the inductive drop. For an annular inductor of fixed height, h ,

$$\frac{dL}{dt} = \frac{\mu_0}{2\pi} \frac{h}{r} \frac{dr}{dt}.$$

Thus, for a cylinder of height 1.5 cm and nominal radius 3 cm, moving at 4 mm/ μ s,

$$I \frac{dL}{dt} = 0.4V,$$

for a current of 1 kA. This is consistent with the voltage drop of ~ 0.35 V as indicated in Figure 3. As for the rise in voltage at $t = 8.5$ μ s shown in Figure 3, it is unclear whether the resistive effect is beginning to dominate the inductive effect. Recall that after 8 μ s, the compression begins interacting with the fixed, external teflon boundary (see Figure 2).

V. Conclusion

MACH2 can effectively calculate the complicated hydrodynamics present in an EFF. The only aspect missing from this calculation deals with the strength of the materials. Although MACH2 does provide such computations, the author was more concerned with the hydrodynamic and electrical properties. As for the voltage across the EFF, a more realistic external current source needs to be considered. The diagnostic current indicated several points which must be considered for such a computation, but is lacking as a proper driving current for an EFF.

INVESTIGATION OF AN EXPLOSIVELY FORMED FUSE USING MACH2

Kenny F. Stephens II

Future considerations for modeling an EFF should include a more realistic driving current model, *i.e.*, a magnetic-flux compression generator. Such information was not available to the author. The adaptive grid feature of MACH2 would benefit this simulation. A moderate value, ~ 5.0 , of the density gradient weighting option seems best suited. The velocity gradient weighting option is not recommended.

Acknowledgment

The author would like to thank Dr. N. F. Roderick, Dr. P. J. Turchi and Dr. M. H. Frese for helpful instruction and guidance. In particular, Dr. R. E. Peterkin, Jr., deserves special thanks for leading me through the intricacies of MHD and MACH2.

Appendix A

This appendix includes the input file for the simulation considered in this report. It was run on the interface-tracker version of MACH2, v9508a.

```
EFF: Mesa model 407a; 1 kA diagnostic current
eff9
! exact annular mag field solution into Al
! run resistive diffusion for 4 ms - then start hydro
! tabular Al diffusivity; 10 m^2/s diffusivity elsewhere
! runs on v9508a with interface tracker
$contrl
  dt = 1.e-6,
  dtmax = 1.e-6,
  twfn = 4.e-3,
  cyl = 1.,
  eoson = .true.,
  tsplit = 0,
! use explosive eos model
  trackon = .true.,
  explon = .false.,
  radiate = .false.,
  ciron = .true.,
  thmldif = .false.,
  artherm = .false.,
  mgmodet = 'converge',
  cntmint = 1.,
  nthrmx = 200,
  tdtol = 1.e-4,
  bdiff = .true.,
  mgmode = 'converge',
  rdtol = 1.e-3,
  rdrelax = 1.5,
  jouhtmlt = 1.,
  hallon = .false.,
! magnetic field here
```

```
  magon = .true.,
  brbzon = .false.,
  hydron = .false.,
  eps = 1.e-3,
  volratm = 0.8,
  courmax = 1.0,
  rmvolm = 0.2,
! artificial viscosity multiplier
  mu = 5.6,
  theb = 1.,
  conserv = 0.,
  conservh = 0.,
  donor = .false.,
  meshon = .false.,
  nsmooth = 4,
  wrelax = 0.25,
  nigen = 0,
  niter = 1,
  eqvol = 1.5,
  zeroghcl = .false.,
! material strength model: see elpname
  strength = .true.,
  multgrd = .true.,
  mglmax = 4,
$end
$output
  intty = 'edits.01',
  dtrst = 1.e-3,
  dtp = 100.e-6,
  plot(0) = 'pfs',
  plot(8) = 'efield',
```

INVESTIGATION OF AN EXPLOSIVELY FORMED FUSE USING MACH2

Kenny F. Stephens II

```

plot(9) = 'vorticity',
plot(10) = 'material',
plot(11) = 'numvis',
plot(12) = 'diffusiv',
plot(13) = 'joulheat',
plot(14) = 'poynting',
intbound = .false.,
clabpict = .false.,
kcon = 12,
contyp = 'linear',
! don't keep axis in the problem
frcl = .false.,
dtslic = 100.e-6,
slice(0) = 'pfs',
lblkslic = 7,
ibdslic = 4,
ijslic = 8,
ncychist = 1,
histenrg = .true.,
$end
$sezphys
tempig = .027036086385,
teflrg = 0.025,
binitg = 'nocurnt',
bzig = 0.,
arsmodlg = 'none',
gdvlg = 0.0,
rofg = 1.e-5,
rofvacg = 1.e-5,
$end
$scurnt
cirttype(1) = 'linear',
currvalu(1,1) = 1.e3, 1.e3,
curtime(1,1) = 0., 1.,
$end
$matmdl
! 6061 aluminum
matnam(1) = 'al-new',
eosmodl(1) = 'tabular',
resmodl(1) = 'tabular',
yield(1) = 9.e8,
elplmodl(1) = 'steinb-g',
elpname(1) = 'al',
rofsiecp(1) = 2.7e3,
! CF2
matnam(2) = 'teflon',
eosmodl(2) = 'tabular',
resmodl(2) = 'constant',
eta0(2) = 1.e1,
yield(2) = 9.e8,
elplmodl(2) = 'steinb-g',
elpname(2) = 'lead',
rofsiecp(2) = 2.152e3,
matnam(3) = 'dryair',
resmodl(3) = 'constant',
eta0(3) = 1.e1,
eosmodl(3) = 'tabular',
yield(3) = 0.,
rofsiecp(3) = 1.1618,
! PBX9501
matnam(4) = 'gel',
resmodl(4) = 'constant',
eta0(4) = 1.e1,
eosmodl(4) = 'grun',
density(4) = 1.84004e3,
gm1(4) = 0.6666667,
gm10(4) = 1.6,
tfusi(4) = 1.e-6,
hfusi(4) = 1.e-2,
tvap(4) = 2.e-6,
hvap(4) = 1.e-2,
tdiss(4) = 3.e-3,
hdiss(4) = 1.e2,
tionize(4) = 8.e6,
hion(4) = 1.e2,
nfe0(4) = 1.e-3,
an(4) = 5.598417,
aw(4) = 10.980013,
rofsiecp(4) = 1.833e3,
explosiv(4) = .true.,
! column initiation at t=0 on far left of blocks 1,4,6,9,11
! detlock (should be detloci) is the block number
detnums = 5,
detlock(4,1) = 1,
detloci(4,1) = 1,
detlocj(4,1) = -1,
detlock(4,2) = 4,
detloci(4,2) = 1,
detlocj(4,2) = -1,
detlock(4,3) = 6,
detloci(4,3) = 1,
detlocj(4,3) = -1,
detlock(4,4) = 9,
detloci(4,4) = 1,
detlocj(4,4) = -1,
detlock(4,5) = 11,
detloci(4,5) = 1,
detlocj(4,5) = -1,
siecrit(4) = 5.e5,
xplsie(4) = 5.543e6,
yield(4) = 0.,
! 7770 m/s reference sound speed
csq0(4) = 60.37e6,
matnam(5) = 'spent',
resmodl(5) = 'constant',
eta0(5) = 1.e1,
eosmodl(5) = 'idealgas',
! gamma=2 for spent fuel -- Fig. 6 in NumerEx Report 94-04
gm1(5) = 1.,
nfe0(5) = 1.e-3,
an(5) = 5.598417,
aw(5) = 10.980013,
rofsiecp(5) = 1.833e3,
nfemodl(5) = 'constant',
nfe0(5) = 1.e-3,
yield(5) = 0.,
$end
$sezgeom

```

INVESTIGATION OF AN EXPLOSIVELY FORMED FUSE USING MACH2

Kenny F. Stephens II

```

nblk = 20,
npnts = 30,
pointx(1) = 0.00,
pointy(1) = 1.50e-2,
pointx(2) = 2.54e-2,
pointy(2) = 1.50e-2,
pointx(3) = 2.615e-2,
pointy(3) = 1.50e-2,
pointx(4) = 3.915e-2,
pointy(4) = 1.50e-2,
pointx(5) = 0.00,
pointy(5) = 1.20e-2,
pointx(6) = 2.54e-2,
pointy(6) = 1.20e-2,
pointx(7) = 2.615e-2,
pointy(7) = 1.20e-2,
pointx(8) = 3.915e-2,
pointy(8) = 1.20e-2,
pointx(9) = 0.00,
pointy(9) = 1.05e-2,
pointx(10) = 2.54e-2,
pointy(10) = 1.05e-2,
pointx(11) = 2.615e-2,
pointy(11) = 1.05e-2,
pointx(12) = 3.915e-2,
pointy(12) = 1.05e-2,
pointx(13) = 0.00,
pointy(13) = 0.45e-2,
pointx(14) = 2.54e-2,
pointy(14) = 0.45e-2,
pointx(15) = 2.615e-2,
pointy(15) = 0.45e-2,
pointx(16) = 3.915e-2,
pointy(16) = 0.45e-2,
pointx(17) = 0.00,
pointy(17) = 0.30e-2,
pointx(18) = 2.54e-2,
pointy(18) = 0.30e-2,
pointx(19) = 2.615e-2,
pointy(19) = 0.30e-2,
pointx(20) = 3.915e-2,
pointy(20) = 0.30e-2,
pointx(21) = 0.00,
pointy(21) = 0.00,
pointx(22) = 2.54e-2,
pointy(22) = 0.00,
pointx(23) = 2.615e-2,
pointy(23) = 0.00,
pointx(24) = 3.915e-2,
pointy(24) = 0.00,
pointx(25) = 4.56e-2,
pointy(25) = 1.50e-2,
pointx(26) = 4.56e-2,
pointy(26) = 1.20e-2,
pointx(27) = 4.56e-2,
pointy(27) = 1.05e-2,
pointx(28) = 4.56e-2,
pointy(28) = 0.45e-2,
pointx(29) = 4.56e-2,
pointy(29) = 0.30e-2,
pointx(30) = 4.56e-2,
pointy(30) = 0.00,
corners(1,1) = 1,2,6,5,
corners(1,2) = 2,3,7,6,
corners(1,3) = 3,4,8,7,
corners(1,4) = 5,6,10,9,
corners(1,5) = 6,7,11,10,
corners(1,6) = 9,10,14,13,
corners(1,7) = 10,11,15,14,
corners(1,8) = 11,12,16,15,
corners(1,9) = 13,14,18,17,
corners(1,10) = 14,15,19,18,
corners(1,11) = 17,18,22,21,
corners(1,12) = 18,19,23,22,
corners(1,13) = 19,20,24,23,
corners(1,14) = 7,8,12,11,
corners(1,15) = 15,16,20,19,
corners(1,16) = 4,25,26,8,
corners(1,17) = 8,26,27,12,
corners(1,18) = 12,27,28,16,
corners(1,19) = 16,28,29,20,
corners(1,20) = 20,29,30,24,
$end
$imnesh
! choose density to give zero pressure
! inner radius of Al annulus
momfld = 2.54e-2,

icells(1) = 24,
jcells(1) = 16,
matnami(1) = 'gel',
roi(1) = 1.833e3,
hydbc(4,1) = 'axis',
magbc(4,1) = 'axis',
thrmhc(4,1) = 'axis',

icells(2) = 8,
jcells(2) = 16,
matnami(2) = 'al-new',
roi(2) = 2.7e3,
binit(2) = 'annulrjy',
bzi(2) = 0.1313935,

icells(3) = 36,
jcells(3) = 16,
matnami(3) = 'dryair',
roi(3) = 1.1618,
binit(3) = 'nocurt',
bzi(3) = 7.874016e-3,

icells(4) = 24,
jcells(4) = 8,
matnami(4) = 'gel',
roi(4) = 1.833e3,
hydbc(4,4) = 'axis',
magbc(4,4) = 'axis',
thrmhc(4,4) = 'axis',

```

INVESTIGATION OF AN EXPLOSIVELY FORMED FUSE USING MACH2

Kenny F. Stephens II

icells(5) = 8,
jcells(5) = 8,
matnami(5) = 'al-new',
roi(5) = 2.7e3,
binit(5) = 'annulrjy',
bzi(5) = 0.1313935,

icells(6) = 24,
jcells(6) = 32,
matnami(6) = 'gel',
roi(6) = 1.833e3,
hydbc(4,6) = 'axis',
magbc(4,6) = 'axis',
thrmbc(4,6) = 'axis',

icells(7) = 8,
jcells(7) = 32,
matnami(7) = 'al-new',
roi(7) = 2.7e3,
binit(7) = 'annulrjy',
bzi(7) = 0.1313935,

icells(8) = 36,
jcells(8) = 32,
matnami(8) = 'dryair',
roi(8) = 1.1618,
binit(8) = 'nocurnt',
bzi(8) = 7.874016e-3,

icells(9) = 24,
jcells(9) = 8,
matnami(9) = 'gel',
roi(9) = 1.833e3,
hydbc(4,9) = 'axis',
magbc(4,9) = 'axis',
thrmbc(4,9) = 'axis',

icells(10) = 8,
jcells(10) = 8,
matnami(10) = 'al-new',
roi(10) = 2.7e3,
binit(10) = 'annulrjy',
bzi(10) = 0.1313935,

icells(11) = 24,
jcells(11) = 16,
matnami(11) = 'gel',
roi(11) = 1.833e3,
hydbc(4,11) = 'axis',
magbc(4,11) = 'axis',
thrmbc(4,11) = 'axis',

icells(12) = 8,
jcells(12) = 16,
matnami(12) = 'al-new',
roi(12) = 2.7e3,
binit(12) = 'annulrjy',
bzi(12) = 7.874016e-3,

icells(13) = 36,
jcells(13) = 16,
matnami(13) = 'dryair',
roi(13) = 1.1618,
binit(13) = 'nocurnt',
bzi(13) = 7.874016e-3,

icells(14) = 36,
jcells(14) = 8,
matnami(14) = 'teflon',
roi(14) = 2.152e3,
tempi(14) = 2.5693e-2,
binit(14) = 'nocurnt',
bzi(14) = 7.874016e-3,

icells(15) = 36,
jcells(15) = 8,
matnami(15) = 'teflon',
roi(15) = 2.152e3,
tempi(15) = 2.5693e-2,
binit(15) = 'nocurnt',
bzi(15) = 7.874016e-3,

icells(16) = 18,
jcells(16) = 16,
matnami(16) = 'teflon',
roi(16) = 2.152e3,
tempi(16) = 2.5693e-2,
magbc(2,16) = 'insulatr',
currcir(2,16) = 1,
binit(16) = 'nocurnt',
bzi(16) = 7.874016e-3,

icells(17) = 18,
jcells(17) = 8,
matnami(17) = 'teflon',
roi(17) = 2.152e3,
tempi(17) = 2.5693e-2,
magbc(2,17) = 'insulatr',
currcir(2,17) = 1,
binit(17) = 'nocurnt',
bzi(17) = 7.874016e-3,

icells(18) = 18,
jcells(18) = 32,
matnami(18) = 'teflon',
roi(18) = 2.152e3,
tempi(18) = 2.5693e-2,
magbc(2,18) = 'insulatr',
currcir(2,18) = 1,
binit(18) = 'nocurnt',
bzi(18) = 7.874016e-3,

icells(19) = 18,
jcells(19) = 8,
matnami(19) = 'teflon',
roi(19) = 2.152e3,
tempi(19) = 2.5693e-2,
magbc(2,19) = 'insulatr',

INVESTIGATION OF AN EXPLOSIVELY FORMED FUSE USING MACH2

Kenny F. Stephens II

```

currir(2,19) = 1,
binit(19) = 'nocurnt',
bzi(19) = 7.874016e-3,

icells(20) = 18,
jcells(20) = 16,
matnami(20) = 'teflon',
roi(20) = 2.152e3,
tempi(20) = 2.5693e-2,
magbc(2,20) = 'insulat',
currir(2,20) = 1,
binit(20) = 'nocurnt',
bzi(20) = 7.874016e-3,
$end

$modtim
ncycmod = 20,
$end
$contrl
dt = 10.e-6,
dtmax = 10.e-6,
mgmode = 'vcycle',
nvycmx = 10,
$end

$modtim
ncycmod = 40,
$end
$contrl
dt = 100.e-6,

dtmax = 100.e-6,
$end

$modtim
ncycmod = 78,
$end
$contrl
t = 0.,
twfn = 10.e-6,
dt = 1.e-9,

explon = .true.,
hydron = .true.,

mglmax = 0,
nvycmx = 3,
$end
$output
intty = 'edits.10',
dtp = 0.25e-6,
dtslic = 0.25e-6,
$end

$modtim
! time explosion reaches A1
tmod = 2.5e-6,
$end
$output
kplrtreg(1) = 0.1,1,0,1,0,1,1,0,1,0,1,1,1,1,1,1,1,1,1,1,
$end

```

Appendix B

An improved resistance plot, see Figure 4, was obtained using the input deck listed in Appendix A (with the following three changes: 1) scrtch(1) = 1.0; 2) strength = .true.; and, 3) elpname(1) = 'al-6061') and v9510a of the code. In this case, the resistance was not computed from Ohm's law, $V = IR$, as above. Rather, it was calculated from the Joule heating rate: $P = I^2 R$ [6]. The "scrtch(1) = 1.0" option instructs the code to compute the Joule heating rate in material number 1, which in this case is the aluminum. As shown, the initial resistance is $1.43 \mu\Omega$, approximately half the expected value of $3 \mu\Omega$. Despite this, the resistance rises nearly a factor of 20 after the shock wave strikes the switch conductor. The drop in resistance at 6 μs lacks explanation at this time, as does the following rise. Furthermore, the strength of materials option was included in this simulation.

INVESTIGATION OF AN EXPLOSIVELY FORMED FUSE USING MACH2

Kenny F. Stephens II

References

- [1] Pavlovskii, A. I., V. A. Vasyukov and A. S. Russkov, "Magnetoinpulsive Generators for Rapid Risetime Megampere Pulses," *Sov. Tech. Phys. Lett.*, vol. 3, No. 177, pp. 320.
- [2] Goforth, J. H., I. R. Lindemuth, S. P. Marsh and R. E. Reinovsky, "Experiments with Explosively Formed Fuse Opening Switches in Higher Efficiency Circuits," in the *Proceedings of the 7th IEEE Pulsed Power Conference*, 1989, pp. 479-482.
- [3] Goforth, J. H., A. H. Williams and S. P. Marsh, "Multi-Megampere Current Interruption from Explosive Deformation of Conductors," in the *Proceedings of the 5th IEEE Pulsed Power Conference*, 1985, pp. 200-203.
- [4] Peterkin, R. E., Jr, and U. Shumlak, "Discovering some of the Physics of Accelerated Magnetized Plasma Rings with the 2 1/2-Dimensional MHD Code, MACH2," in the *Proceedings of the 6th Join EPS-APS International Conference on Physics Computing*, 1994, pp. 121-124.
- [5] Peterkin, R. E., Jr, A. J. Giancola and J. E. Sturtevant, *MACH2: A Reference Manual -- Fifth Edition*, Phillips Laboratory, July 1992.
- [6] Frese, M. H., private communication.

INVESTIGATION OF AN EXPLOSIVELY FORMED FUSE USING MACH2

Kenny F. Stephens II

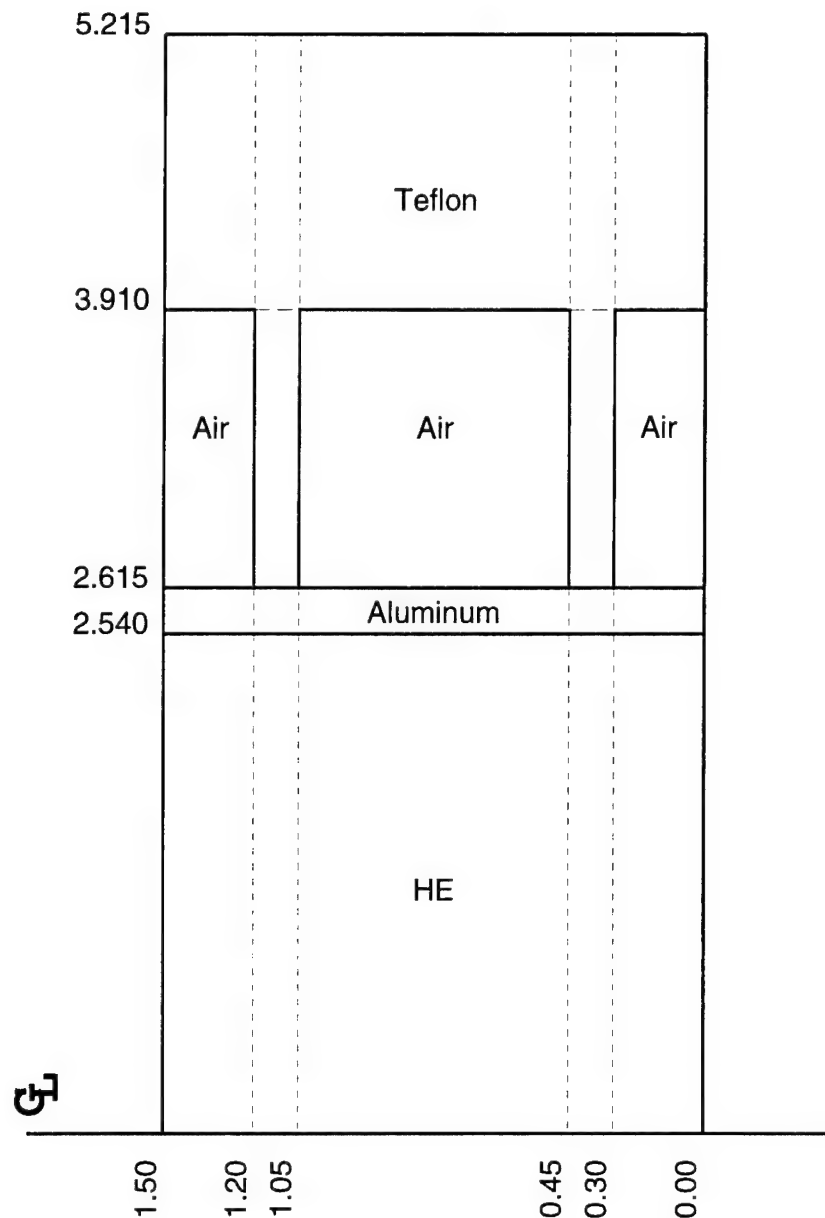


Figure 1. Configuration of EFF model. The HE is line-detonated along the center-line. The circuit is parallel to the center-line and along the outer radius of the teflon. (All dimensions are in cm. Solid lines indicate material boundaries and dashed lines indicate block boundaries within materials.)

INVESTIGATION OF AN EXPLOSIVELY FORMED FUSE USING MACH2

Kenny F. Stephens II

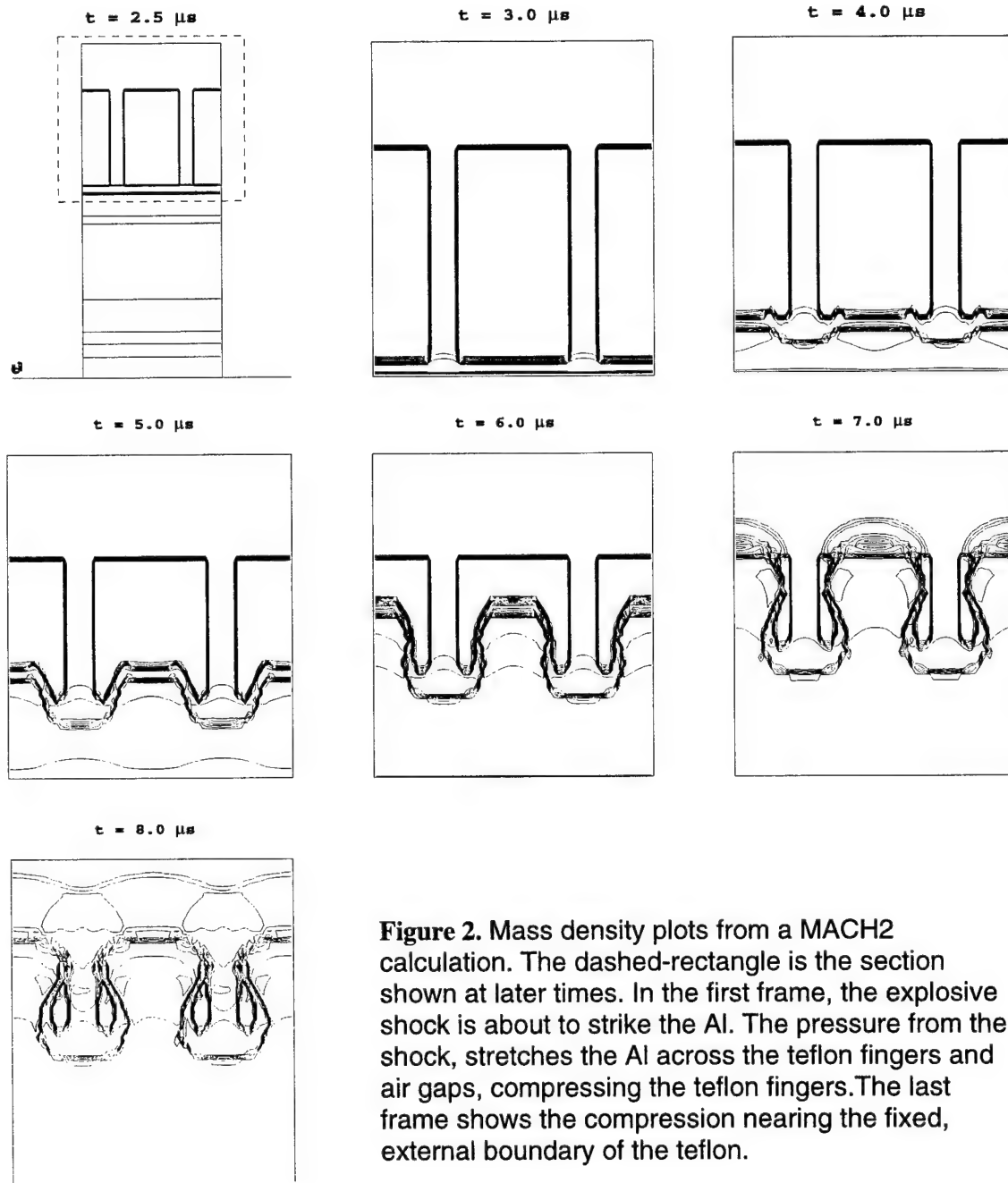


Figure 2. Mass density plots from a MACH2 calculation. The dashed-rectangle is the section shown at later times. In the first frame, the explosive shock is about to strike the Al. The pressure from the shock, stretches the Al across the teflon fingers and air gaps, compressing the teflon fingers. The last frame shows the compression nearing the fixed, external boundary of the teflon.

INVESTIGATION OF AN EXPLOSIVELY FORMED FUSE USING MACH2

Kenny F. Stephens II

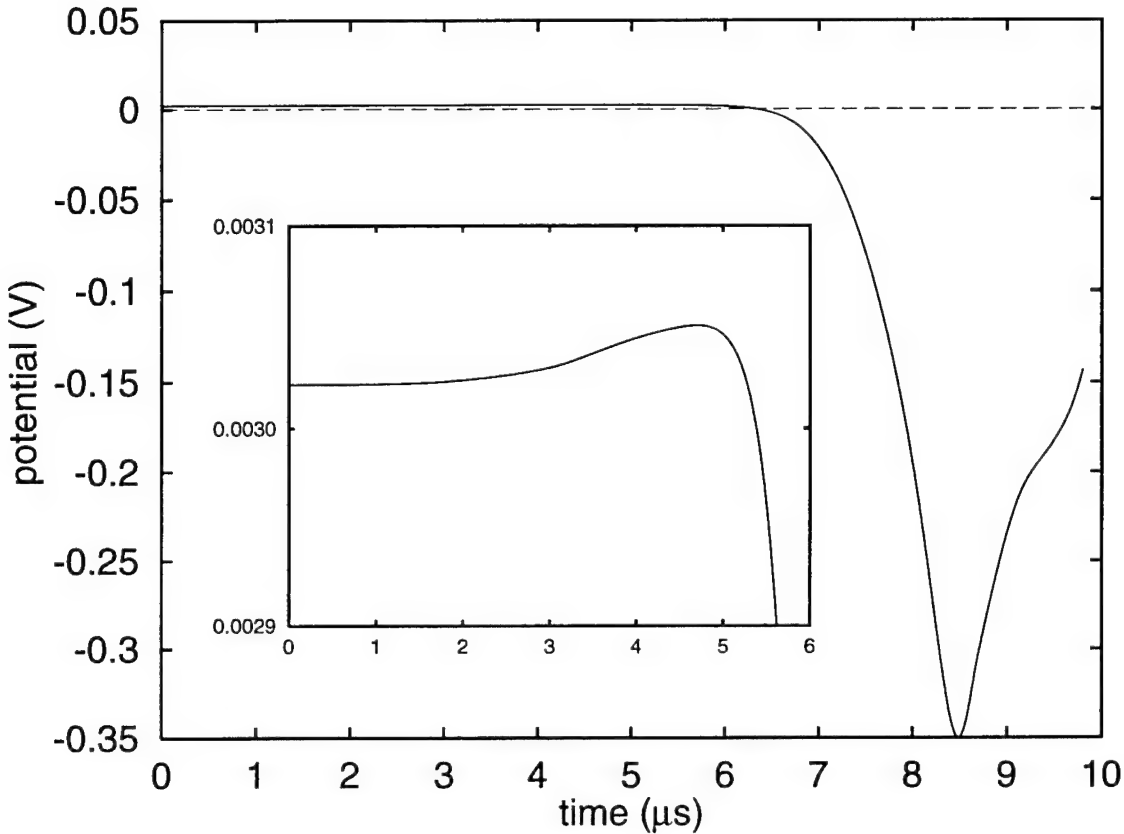


Figure 3. Electric Potential across EFF for diagnostic, 1 kA current. HE is detonated at $t=0$ and explosive shock impinges Al at $t=2.5\mu\text{s}$. At $t=8.5\mu\text{s}$, the Al deforms enough to start compressing the outer teflon against the fixed, external boundary. The potential drop is a consequence of inductive effects dominating resistive effects. The inset is an enlarged view of the time before $6\mu\text{s}$. From this, it is clear that the resistance does begin to rise once the conductor begins deforming. However, this rise is negligible compared to the magnitude of the inductive effects.

INVESTIGATION OF AN EXPLOSIVELY FORMED FUSE USING MACH2

Kenny F. Stephens II

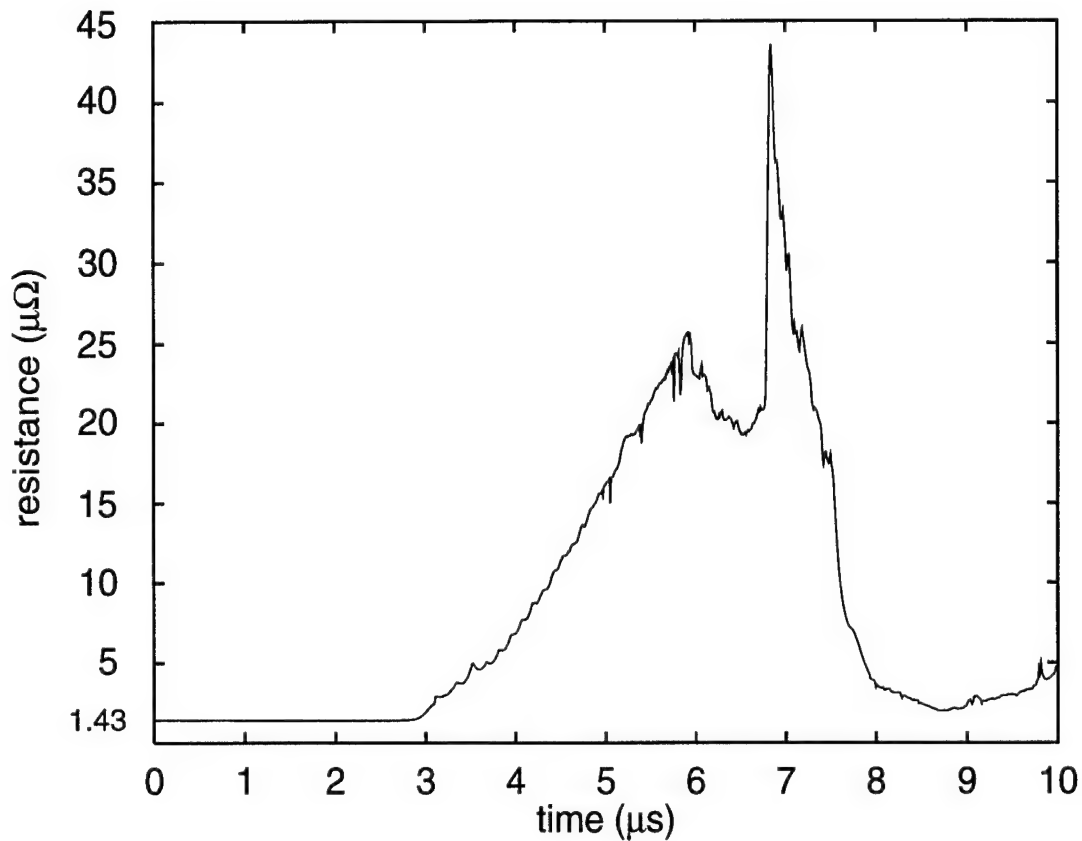


Figure 4. Resistance across EFF. Calculation of resistance using the Joule heating rate instead of Ohm's law. The initial value of 1.43 $\mu\Omega$ is approximately one-half the expected value of 3 $\mu\Omega$. The explosive shock wave strikes the switch condutor at 2.5 μs . The reason for the rise and subsequent fall after 6 μs is presently unclear.

**LOW LATITUDE IONOSPHERIC TEC
MEASURED BY NASA TOPEX**

**Jane A. Vladimer
Master's Degree Candidate
Department of Electrical and Computer Engineering**

**Boston University
8 St. Mary's Street
Boston, MA. 02215**

**Final Report for:
Graduate Student Research Program
Phillips Laboratory**

**Sponsored by:
Air Force Office of Scientific Research
Hanscom Air Force Base, MA.**

and

Phillips Laboratory

August 1997

LOW LATITUDE IONOSPHERIC TEC MEASURED BY NASA TOPEX

Jane A. Vladimer
Master's Degree Candidate
Department of Electrical and Computer Engineering

Abstract

The NASA TOPEX altimeter obtains accurate sea range measurements which require correction for the dispersive ionospheric radar signal delay. The resulting over-ocean dataset is used to demonstrate Total Electron Content (TEC) values at all longitudes. A four year period (September 1992 to April 1996) of TOPEX ionospheric data has been longitudinally binned and averaged. Software was developed and a user document was prepared to facilitate utilization of this extensive dataset. Trends in TEC variability are presented with respect to day-to-day, seasonal and longitudinal dependencies as well as the influence of solar and magnetic activity. Additional applications include verification of ionospheric models and the use of TOPEX data as a supplement to other sources of TEC. For example, vertical measurements of TEC which are determined by the TOPEX altimeter have been compared to GPS slant TEC values that are converted to vertical. These TOPEX / GPS comparisons show disagreement when satellite passes involve measurements within 20° to the south and to the north of the magnetic equator. The Parameterized Ionospheric Model (PIM) results of vertical / *equivalent* vertical TEC comparisons show similar patterns of discrepancy. The slant-to-vertical TEC mapping function was evaluated and modified to illustrate the effects of the ionospheric shell model assumptions.

LOW LATITUDE IONOSPHERIC TEC MEASURED BY NASA TOPEX

Jane A. Vladimer

Introduction

The forecasting of ionospheric Total Electron Content (TEC) is of significant importance to the consistent, precise operation of satellite communications, aircraft and space vehicle positioning and defense surveillance systems. The ionospheric correction that is derived from NASA dual-frequency altimeter measurements provides accurate information pertaining to TEC variability from 0° to 360° longitudes and -66° to 66° latitudes. Several applications of the extensive TOPEX database to ionospheric research are presented. Discussion of the low latitude ionospheric physics precedes the demonstration of TOPEX data with emphasis on the formation and longitudinal structure of the equatorial anomaly. Also, results are shown from a low latitude study* of TOPEX / GPS TEC that was computed from measurements obtained near the magnetic equator. Figure 1 shows TOPEX ten day coverage, seven GPS ground stations and their perspective to the geomagnetic equator.

It is difficult to provide accurate predictions of TEC at low latitude due to the large temporal variations of the ionosphere near the magnetic equator. Large values of TEC are observed within 30° magnetic latitude on each side of the equator from approximately noontime until 2200 hours (local time) as a result of the formation of the electromagnetic phenomenon known as the equatorial anomaly [Appleton, 1946]. These bilateral enhancements are formed by the perpendicular electrodynamic ($E \times B$) uplifting of the F-region plasma in combination with the parallel plasma flow due to non-electromagnetic forces of gravity and pressure gradients. This so-called plasma fountain is illustrated in Figure 2.

The diurnal variation in electric field strength and ionospheric plasma density is believed to be caused by an increase in the thermospheric winds in the F-region which create ion and electron separation. Currents develop and in response, an electrostatic field is generated and interacts with the earth's magnetic field causing vertical plasma drifts [Anderson, 1981; Kelley, 1989]. There is variability in the equatorial anomaly with respect to time of day, season, longitude, solar cycle and other daily geophysical conditions indicated by magnetic and solar indices.

Previously, possible reasons for longitudinal variability of ionospheric TEC at equatorial anomaly latitudes have been presented. [Walker, 1981; Su et al., 1995] Contributing factors include: i) the physical difference between the geographic equator and the geomagnetic equator, ii) variations in magnetic declination and iii) variations in electric and magnetic fields. Effects of neutral winds and lower atmosphere planetary waves are also considered to be influential in the development of the equatorial anomaly.

* Vladimer J. A., Lee, M. C., Doherty, P. H., Decker D. T., Anderson D. N., Comparisons of TOPEX and GPS TEC Measurements at Equatorial Anomaly Latitudes. (Accepted for publication July 1997, Radio Science)

FIGURE 1

TOPEX 10 Day Cycle / Geomagnetic Equator / GPS Stations

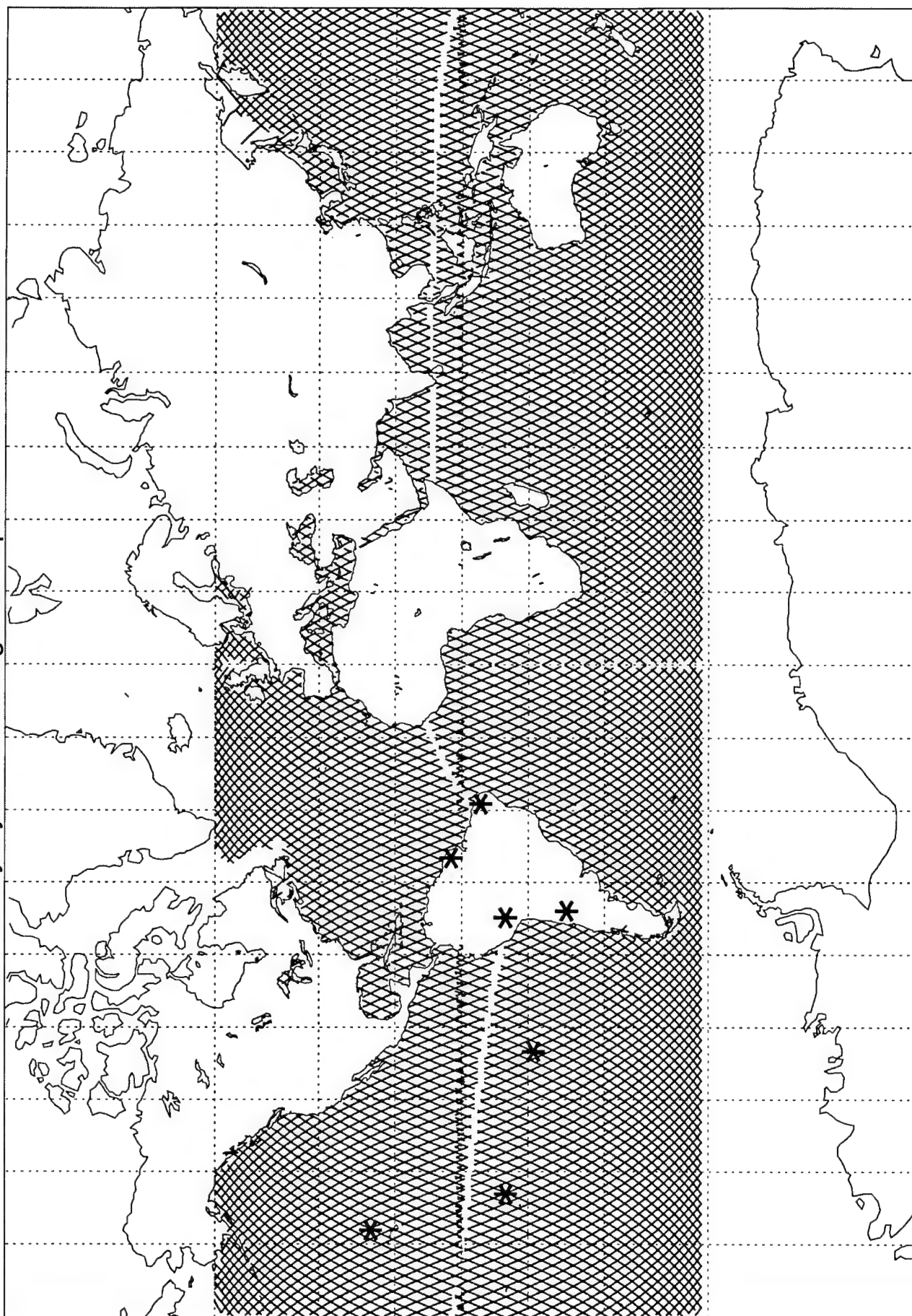
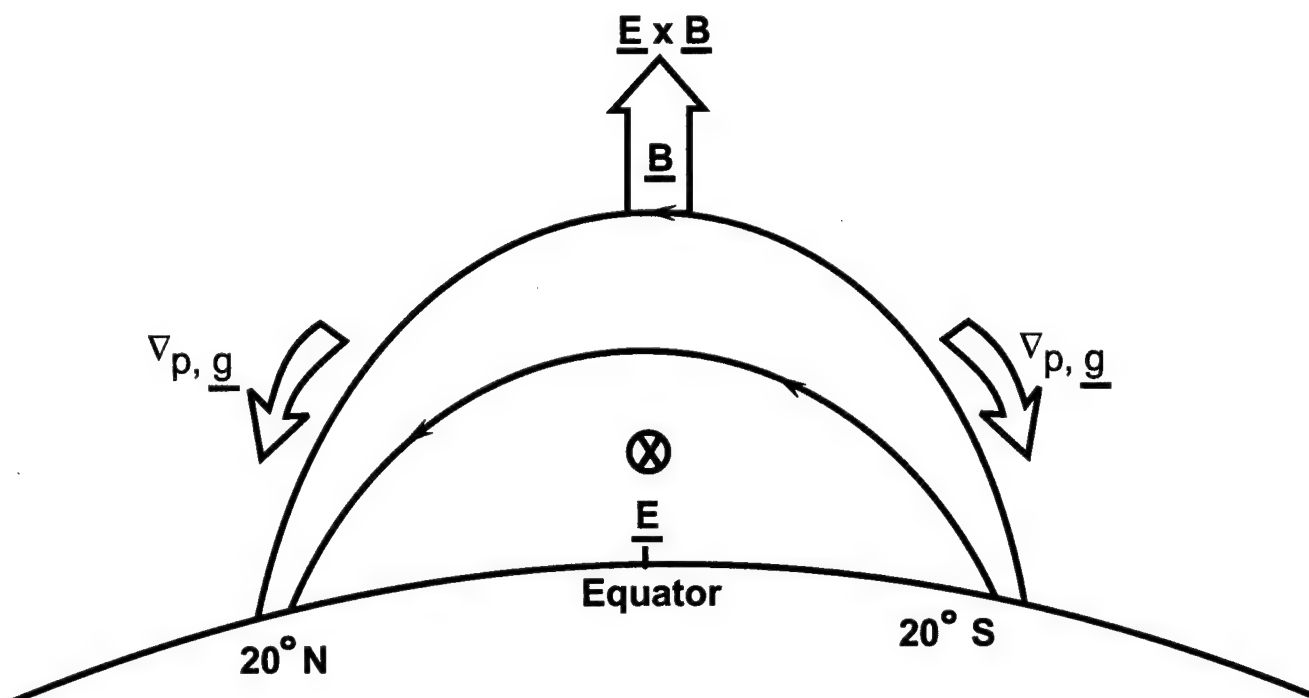


FIGURE 2



TOPEX TEC Measurements

The Topex/Poseidon satellite was launched in 1992 by NASA and CNES* for the study of global ocean dynamics. The satellite has an orbital altitude of 1336 km. (equatorial reference) and an inclination of 66° . One full revolution, which is achieved in 112 minutes, consists of two passes each of which spans 150° of longitude from west to east and 133° of latitude. (An ascending pass spans -66° to 66° latitude; a descending pass spans 66° to -66° latitude.) Consecutive revolutions are offset to the west by approximately 30° . This TOPEX coverage provides the ability to observe TEC variability across the world in one day at 30° intervals at approximately the same local time. There are 127 revolutions (254 passes) in a TOPEX cycle which covers the same surface tracks every ten days. The differential between UT and LT, in combination with the "overlap" required to accomplish ice-free ocean coverage, results in a 2 hour loss of local time for each consecutive ten day cycle. Day-to-day TEC variability can be studied as well using TOPEX data since the satellite's coverage during one day comes within 8° and 12 minutes of the previous day's position and local time. Figure 3 gives an example of TOPEX data which illustrates longitudinal and day-to-day variation in the equatorial anomaly. The top row shows 4 consecutive TOPEX passes on day 41 in the Pacific. The bottom row shows 4 consecutive passes on day 42. Each of the lower passes is approximately 8° offset to the west and 12 minutes earlier (LT) than the upper corresponding passes.

TOPEX orbital speed is 7.2 km. per second and altimeter measurements are obtained at a rate of one per second. The ionospheric correction and vertical TEC is computed from TOPEX dual-frequency range measurements. (5.3 GHz., C band and 13.6 GHz., Ku band). The uncertainty in the TOPEX ionospheric correction has been evaluated to be approximately 0.5cm. [Imel, 1994] Consider the measured range:

$$R_{\text{measured}} = R_{\text{true}} + \Delta R_{\text{ionosphere}} + \Delta R_{\text{other}} \quad (1)$$

where R_{measured} is the R_C or R_{Ku} range measurement, R_{true} is the true range, and ΔR_{other} are the range errors due to other frequency-dependent and non-frequency-dependent sources and $\Delta R_{\text{ionosphere}}$ is the ionospheric range error which is assumed to have the form:

$$b_C / f_{C2} \quad \text{or} \quad b_{Ku} / f_{Ku2} \quad \text{where } b_i \sim 40.3 \text{ TEC} \quad (2)$$

The R_{measured} equations for C and Ku bands provide an expression for the ionospheric correction at Ku band:

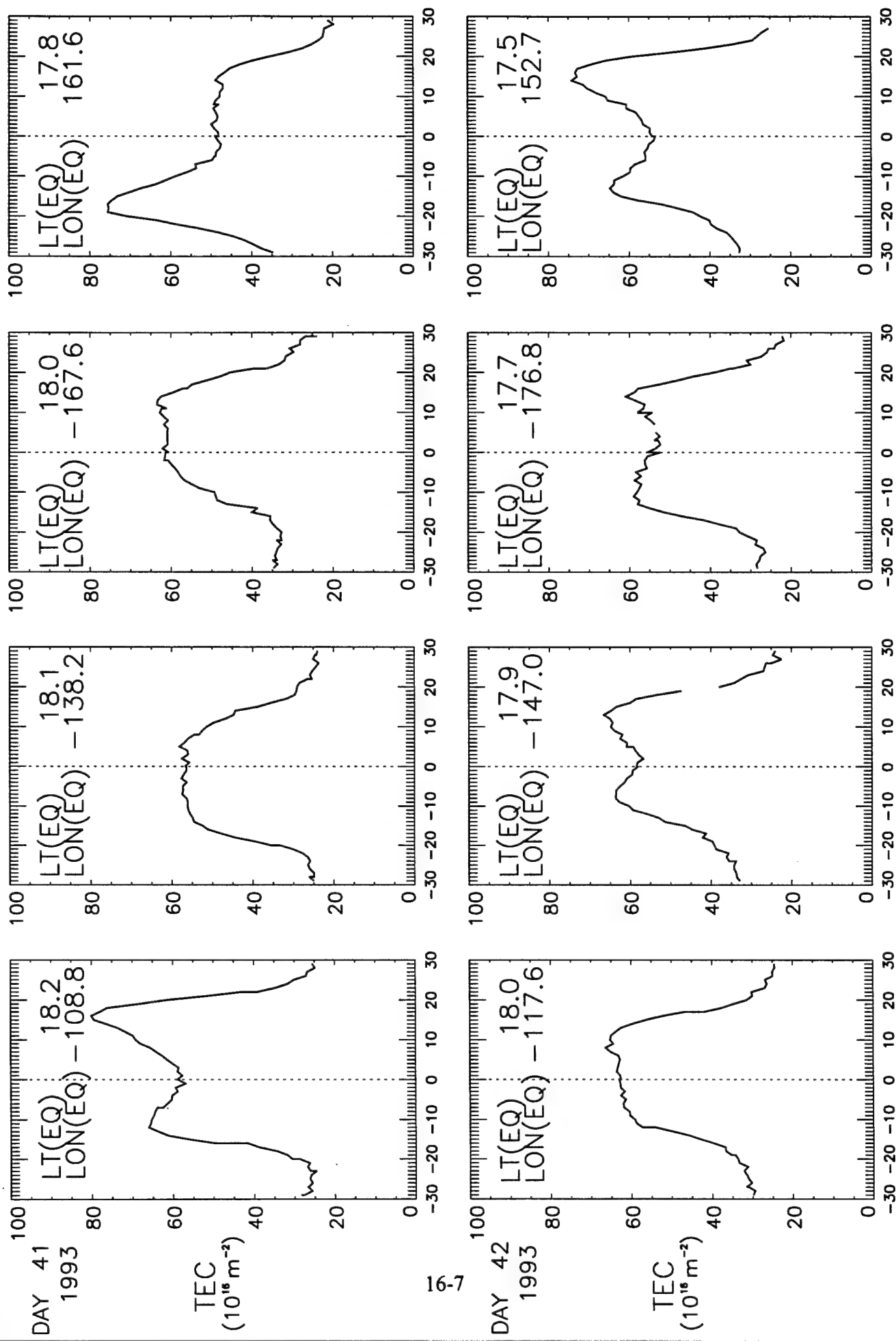
$$\Delta R_{\text{ionosphere}} = [f_{C2} / (f_{Ku2} - f_{C2})] [R_{Ku} - R_C] \quad (3)$$

and vertical TEC is given by:

$$\text{Vertical TEC} = \Delta R_{\text{ionosphere}} [f_{C2} f_{Ku2} / (f_{Ku2} - f_{C2}) 40.3] \quad (4)$$

One TECU (10^{16} el./m.²) corresponds to 12.17 mm. range error at the given TOPEX altimeter frequencies.

FIGURE 3



TOPEX Data

Seasonal variability can be observed at different longitudes at the same local time. An example of two longitudinal bins of TOPEX TEC is shown in Figures 4a and 4b. The scatter plots on the left side of each figure show TEC during equinox 1993 and 1994. Figure 4a shows TEC data at bin #2 (82W - 110W) and Figure 4b shows data at bin #4 (139W - 165W). Both bins illustrate greater TEC variability during the equinox periods than during summer and winter. TEC values in summer are generally smaller than during other seasons which is true for both bins as well. Longitudinal differences are seen in TEC variability and peak values: i) bin #4 shows slightly more TEC variability, ii) winter peak TEC values are larger in bin #4 and iii) bin #2 exhibits higher peak TEC values in summer.

Longitudinal and solar cycle dependencies are illustrated in Figure 5. Each bin represents 30° of longitude and contains 10 TOPEX passes over a period of 10 days and 2 hours of local time. Bin #1 (53W - 81W) shows clear southern anomaly peaks directly to the west of South America (the missing data indicates the presence of land.) Bins #2 - #4 continue to move to the west over the Pacific Ocean ending with bin #5 (166W - 194W). As expected, TEC values decrease as the solar cycle progresses from 1993 to 1996 with the exception of bins #2 and #3 of 1996. This can be explained by an increase in magnetic activity in April, 1996. A noticeable decline in TEC values is seen at bin #3. Although not shown in this report, the bin #3 - bin#4 minimum is also observed in fall equinox (September - October) and in winter (November - February) but not as consistently in summer months (May - August).

Finally, longitudinal structure is investigated by extending the bins to cover all longitudes. The limitation of TOPEX is the missing data over land. South America and Africa are indicated between bins in Figures 6a and 6b. Averages of the southern anomaly peak TEC values during 10 day periods in the spring equinox period of 1993 reveal a consistent pattern. A maximum in TEC is observed near longitude 100E - 120E and a minimum in TEC is seen in the longitude range of 130W - 150W. The maximum trend is observed every day while the minimum trend is observed less consistently. Figure 6a shows periods of time between 1400 - 1600 hours and 1600 - 1800 hours local time during which the configurations are similar. Figure 6b adds earlier (12 - 14) and later (20 - 22) time periods during which the maximum pattern is maintained but the minimum pattern near the Pacific is not observed.

FIGURE 4a

TOPEX/BIN #2: 82W - 109W

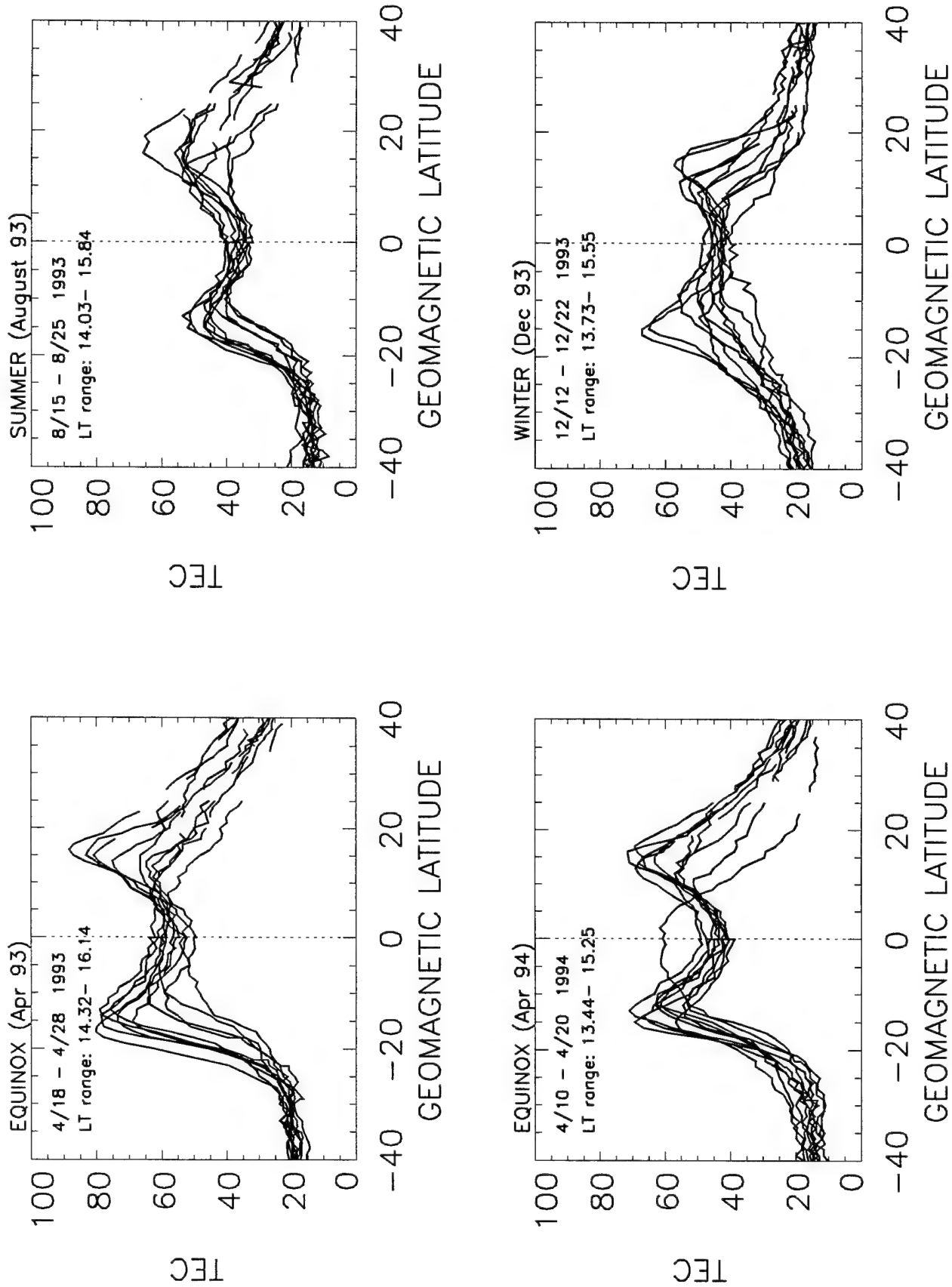
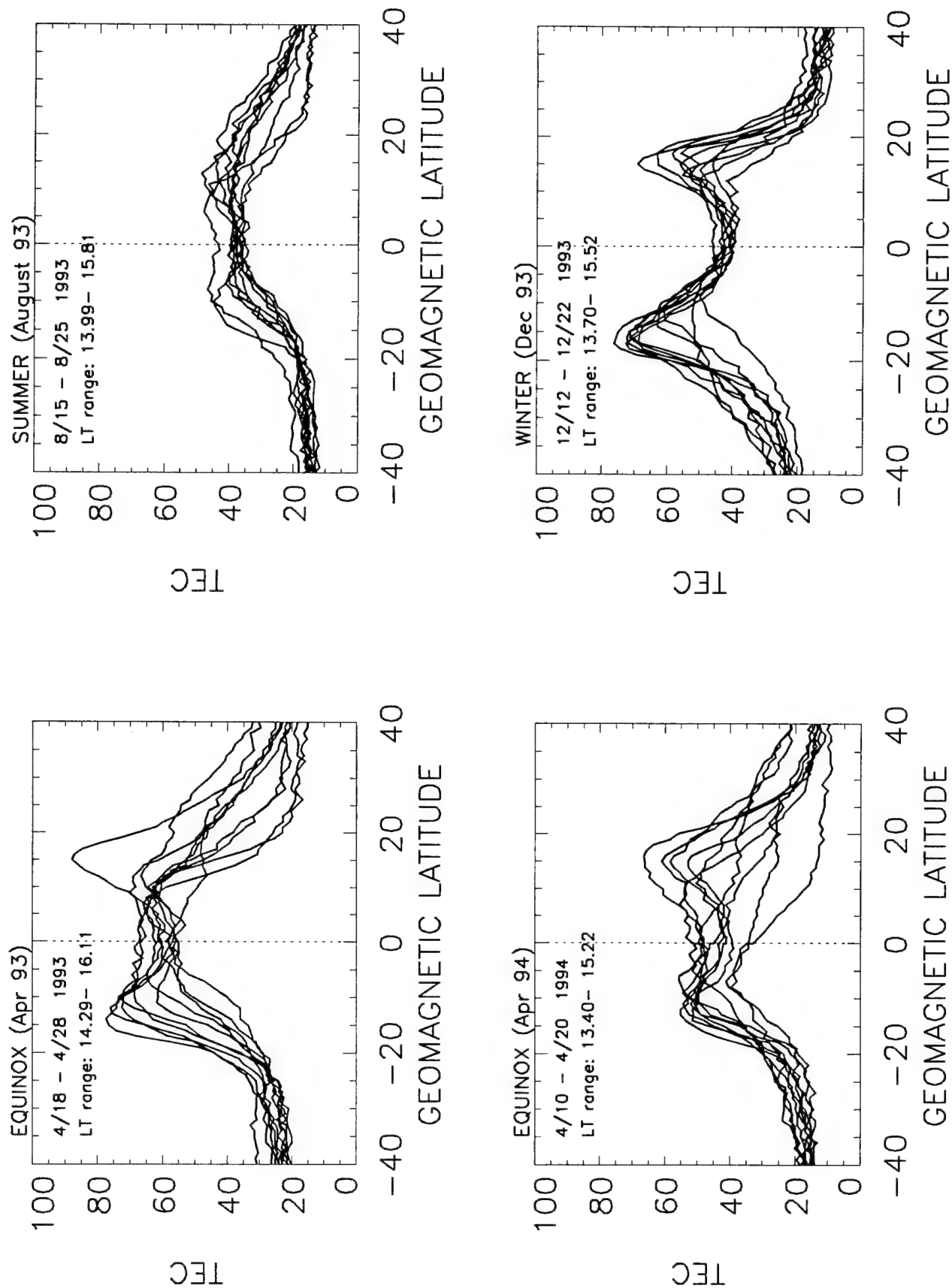


FIGURE 4b

TOPEX/BIN #4: 139W - 165W



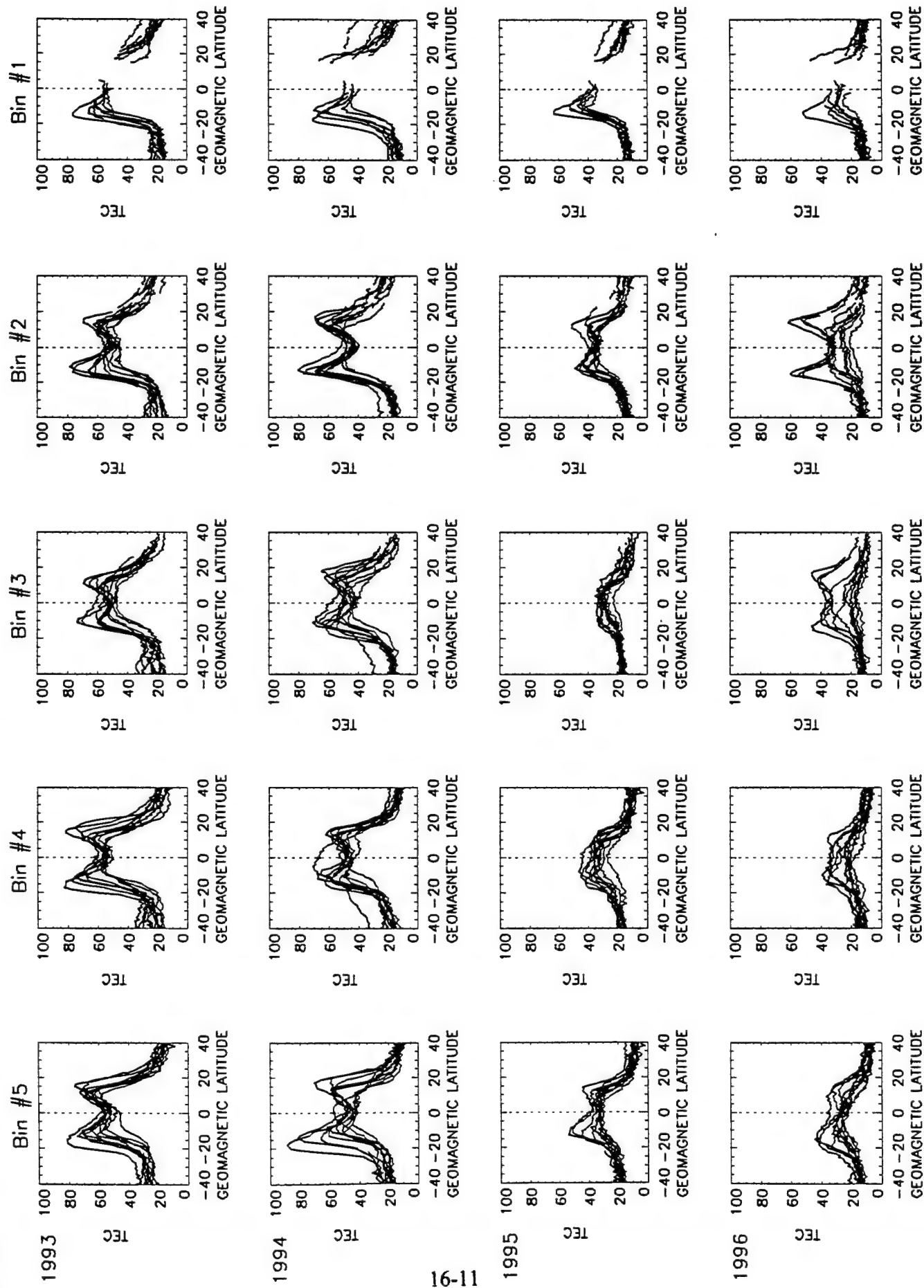


FIGURE 6a

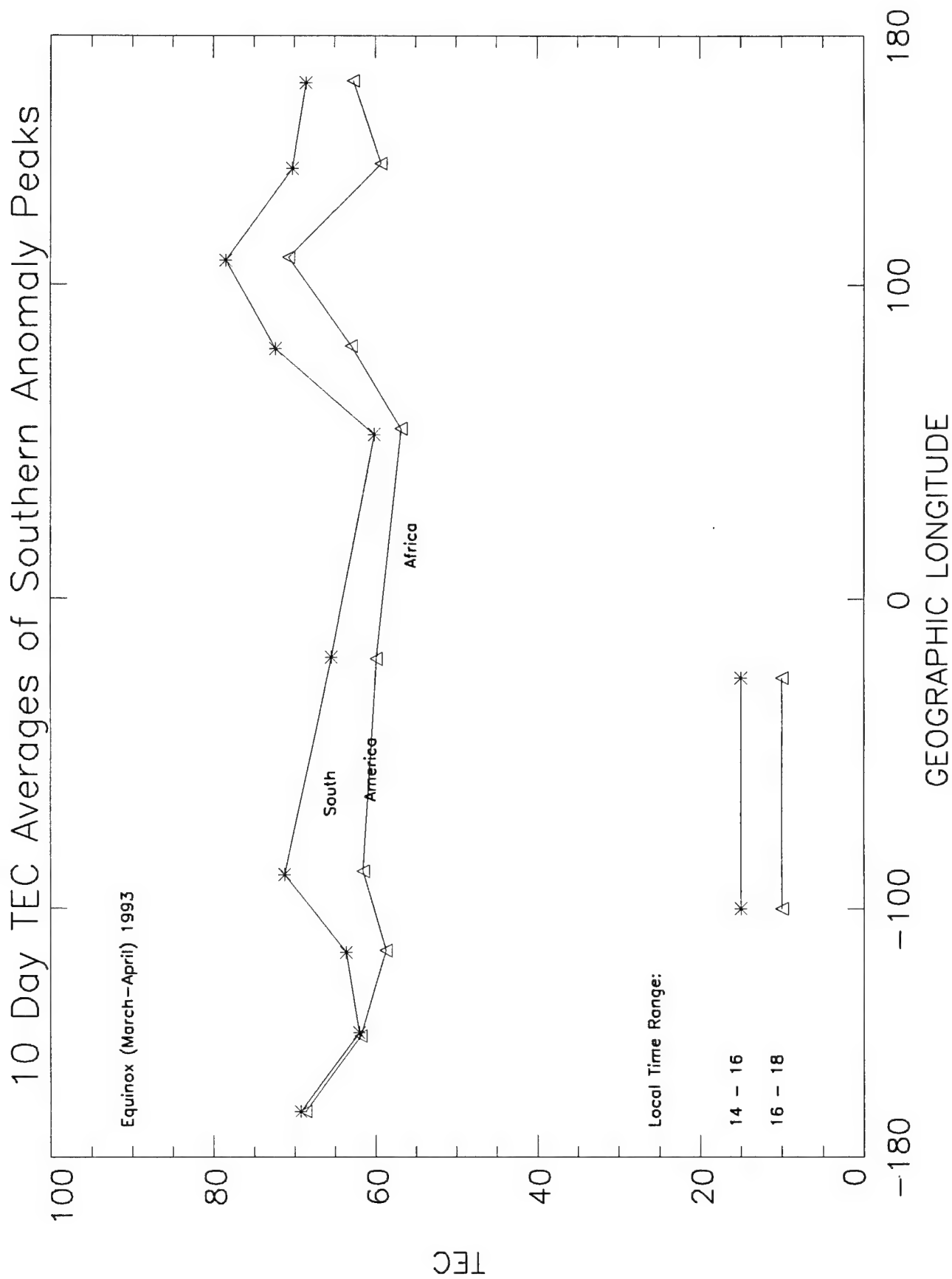
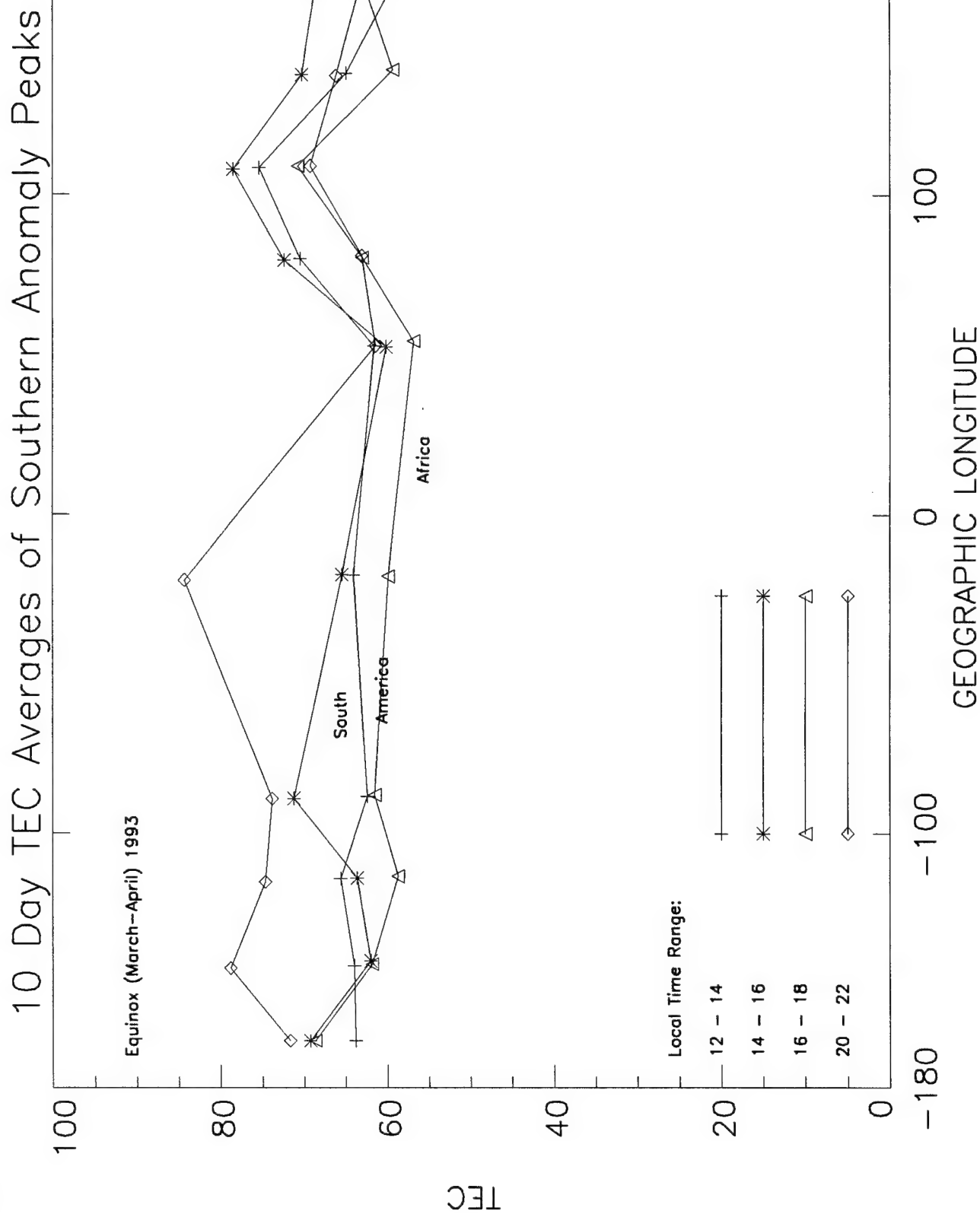


FIGURE 6b



GPS TEC Measurements

Each of the GPS satellites is in a 12-hour circular orbit at an inclination of 55° and an altitude of 20,000 km.. GPS signals which are transmitted at dual-frequency (L_1 , 1575.42 MHz. and L_2 , 1227.60 MHz.), experience a dispersive ionospheric delay. This GPS delay data provides line-of-sight TEC measurements. The measured pseudorange is given by (1) where $\Delta R_{\text{ionosphere}}$ is the ionospheric delay at the frequency, L_1 or L_2 . The measured range is represented by the integral of the refractive index (n) along the path of the signal and the geometric range is the integral of ($n = 1$) along the straight line between satellite and receiver.

Approximations are used to compute the ionospheric delay [Hofmann-Wellenhof et al., 1994]:

1. Higher orders of frequency are ignored when considering the phase and group refractive indices:

$$n_{\text{phase}} = 1 + b^2 / f_i^2 \quad \text{and} \quad n_{\text{group}} = 1 - b^2 / f_i^2 \quad (5)$$

where $b^2 = -40.3 N_e \text{ (Hz}^2 \text{ m}^3\text{)}$ and f_i is the frequency L_1 or L_2 . (TEC equals the integral of the electron density (N_e) along the signal path.)

2. The geometric path (ray bending ignored) is used for the Fermat integrations resulting in:

$$\Delta R_{\text{ionosphere}} = (40.3 / f_i^2) \text{ TEC} \quad (6)$$

where the TEC in this case is the vertical Total Electron Content (elevation = 90°). To determine the slant TEC, a mapping function ($M(E)$) is used to account for elevations that are less than the zenith angle:

$$M(E) = (1 / \cos \phi) = [1 - (R \cos E / R + H)^2]^{-1/2} \quad (7)$$

where R is the radius of the earth and H is an average value of electron density peak positions which is approximated at 400 km.. E is the elevation angle of the line-of-sight measurement and ϕ is the incident angle at the ionospheric shell intersect. Figure 7 shows the ionospheric shell geometry and the relationship between the slant and vertical paths. The ionospheric range delay is then given by

$$\Delta R_{\text{ionosphere}} = (1 / \cos \phi) (40.3 / f_i^2) (\text{Vertical TEC}) \quad (8)$$

and the Total Electron Content along an arbitrary line-of-sight is:

$$\text{Slant TEC} = (1 / \cos \phi) \text{ Vertical TEC} \quad (9)$$

Problems in the application of the TEC mapping function have been acknowledged [Lanyi and Roth, 1988; Wilson et al., 1995] at low elevation (less than 20°) but the observations indicate that disagreement can begin to occur at elevations as high as 50° to 70° . Figure 8 illustrates a comparison between an ascending TOPEX pass and a portion of an ascending GPS pass with shell coverage over the southern crest of the equatorial anomaly. There is good agreement at high elevation (80°) but separation from agreement begins to occur at 53° . The Parameterized Ionospheric Model (PIM) [Daniell et al, 1995] also predicts this configuration of overestimation. The model comparison is shown in Figure 9a.

FIGURE 7

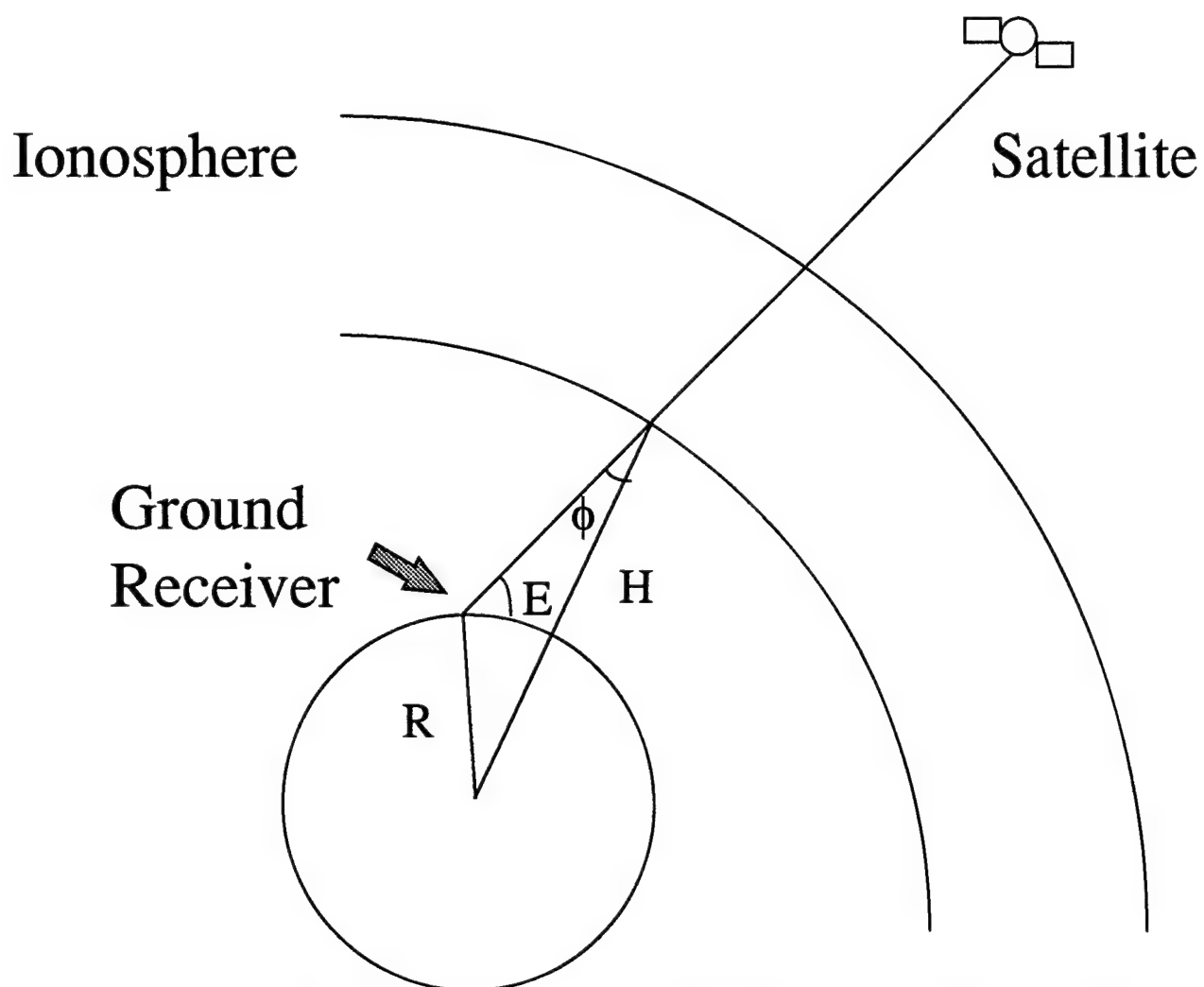


FIGURE 8

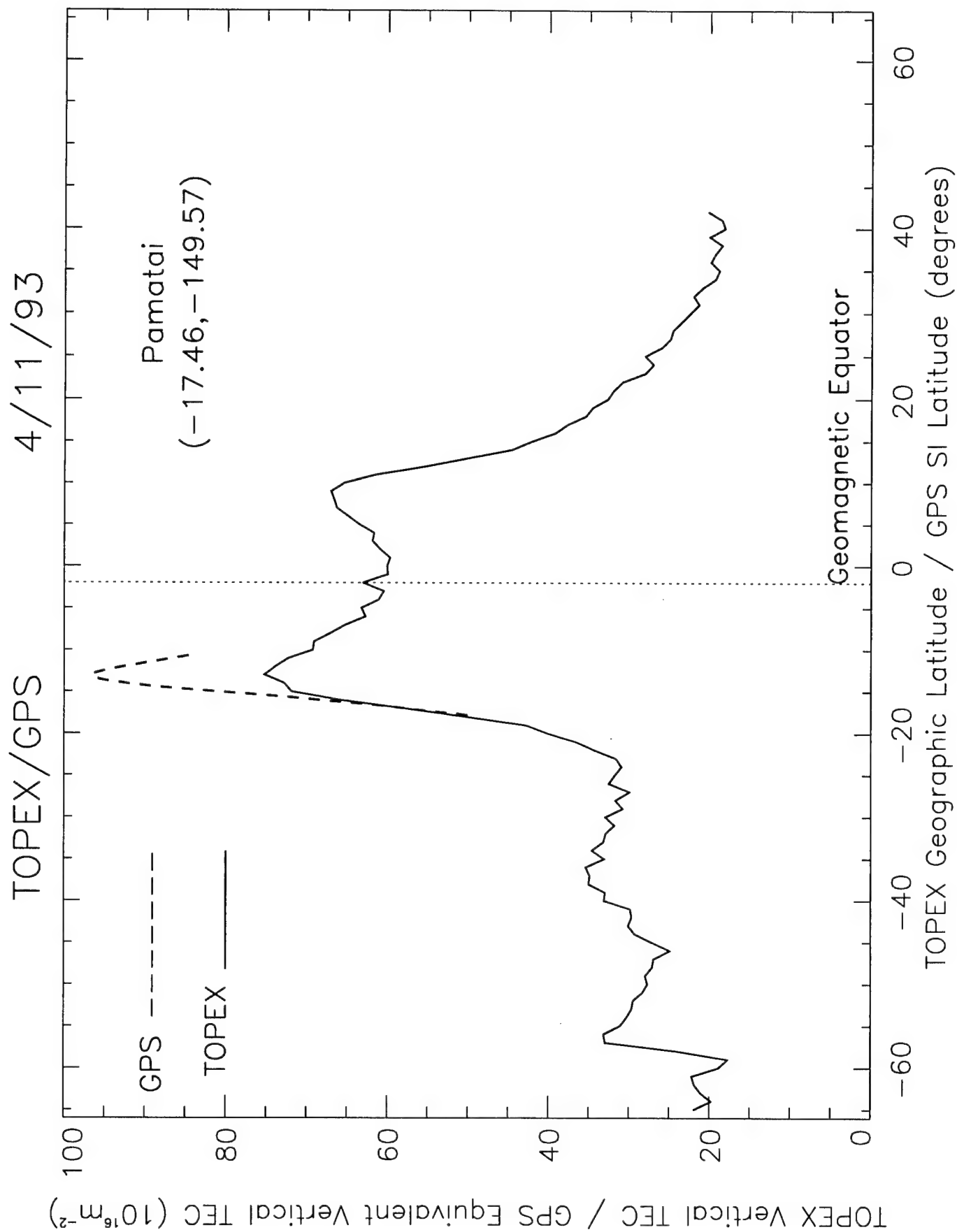


FIGURE 9a

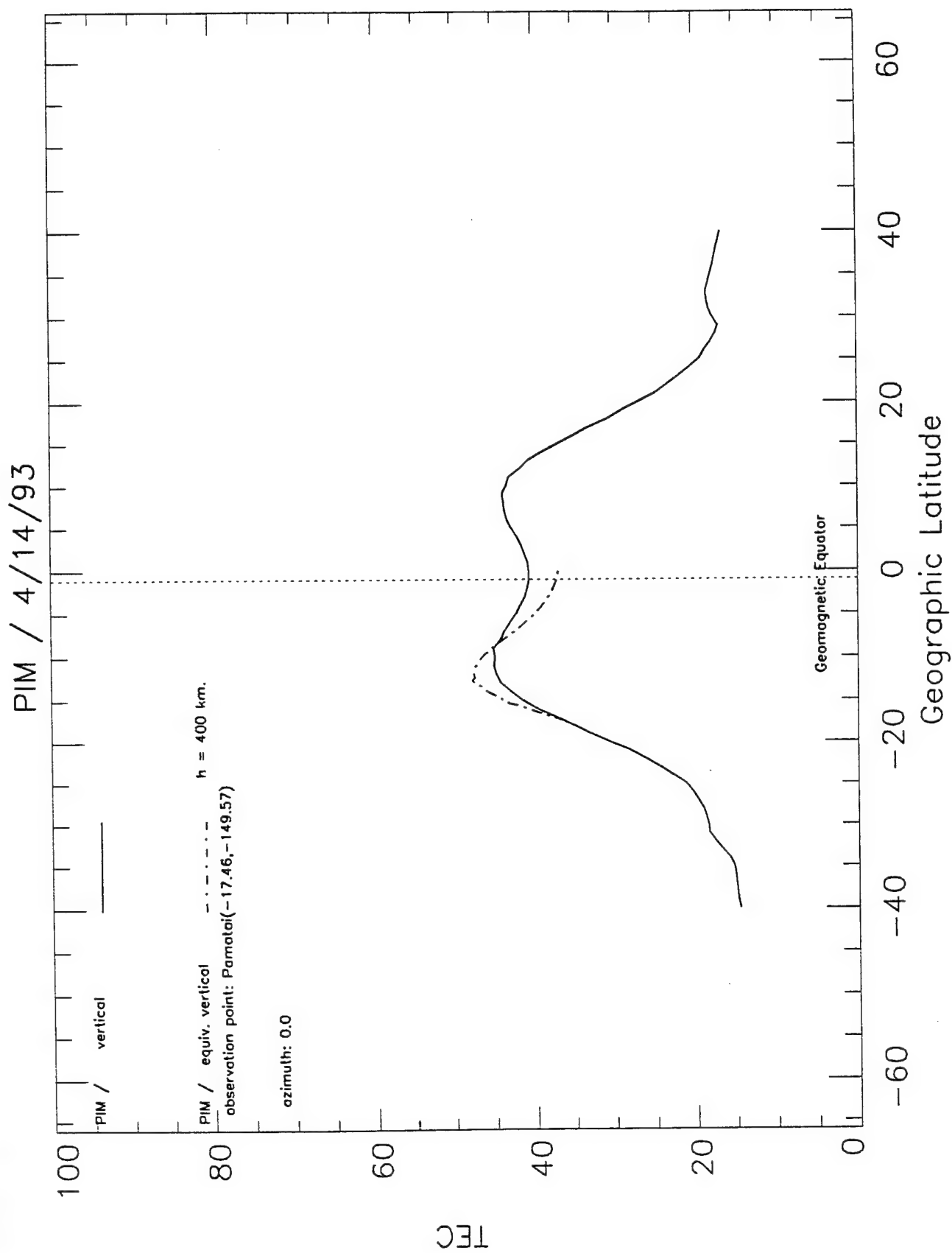
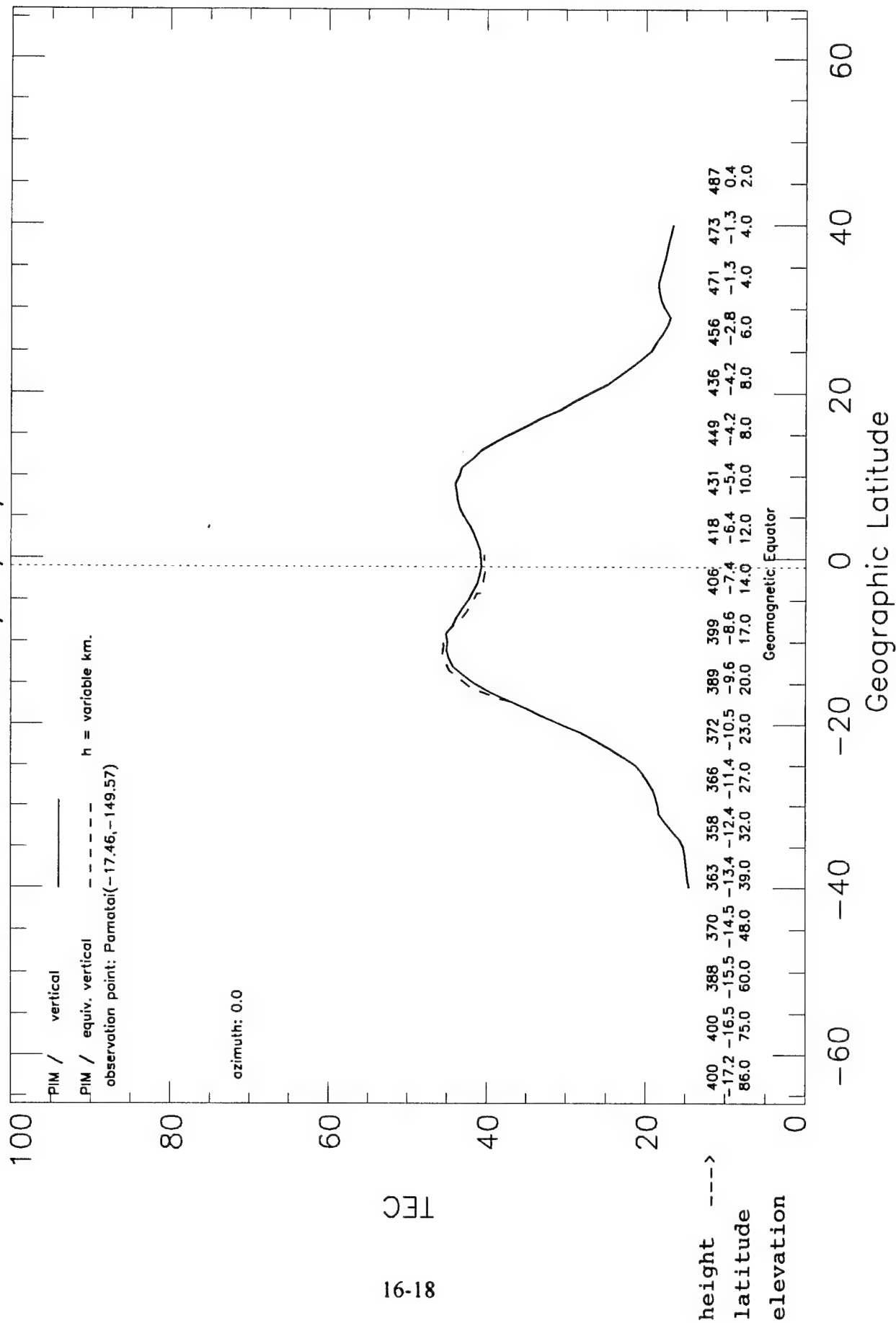


FIGURE 9b

PIM / 4/14/93



The mapping function was manipulated to convert slant (PIM) TEC to vertical values within 0.5 TECU of the "true" vertical (PIM) TEC using a variable shell height (H). The height, latitude and elevation are indicated to the left of the plot in Figure 9b. It is clear that even at high elevation, the constant value of 400km for the shell height is not adequate to avoid slant-to-vertical conversion errors.

Conclusions

The TOPEX satellite provides a world-wide over-ocean dataset that can be used in many ionospheric research applications. Several examples of TOPEX TEC data have been presented. Evaluation of longitudinal structure of the equatorial ionosphere is continuing with TEC averaging of all seasons within each of the available years of data. The goal of further investigation will be to pursue a significant statistical analysis and predictable patterns of behavior of the equatorial anomaly. Consistent configurations of TEC at given longitudinal sectors will contribute to the ability to forecast low latitude TEC variability.

TOPEX data has been utilized in the evaluation of slant-to vertical conversion errors at low latitude. Recent work with the PIM model involves gradual changes in azimuth during slant TEC measurements to determine the dependency of the breakdown of the effectiveness of the mapping algorithm on the line-of-sight of the satellite to the GPS ground station.

References

- Anderson D. N., Modeling the ambient, low latitude F-region ionosphere - a review. J. Atmos. Terr. Phys. 43, 753. 1981
- Appleton E. V., Two anomalies in the ionosphere. Nature 157, 691. 1946
- Daniell R. E., Brown L. D., Anderson D. N., Fox M. W., Doherty P. H., Decker D. T., Sojka J. J. and Schunk R. W., Parameterized Ionospheric Model: A global ionospheric parameterization based on first principles models. Radio Sci. 30, 1499. 1995
- Hofmann-Wellenhof B., Lichtenegger H. and Collins J., "GPS Theory and Practice", third edition, Springer-Verlag Wein, New York. 1994
- Imel D. A., Evaluation of the TOPEX/Poseidon dual-frequency ionospheric correction. J. Geophys. Res. 99,24,895. 1994
- Kelley M. C., "The Earth's Ionosphere", Academic Pres, California. 1989
- Lanyi G. E. and Roth T., A comparison of mapped and measured total ionospheric electron content using global positioning system and beacon satellite observations. Radio Sci. 23, 483. 1988
- Su Y. Z., Bailey G. J. and Balan N., Modelling studies of the longitudinal variations in TEC at equatorial anomaly latitudes. J. Atmos. Terr. Phys., 57, 433. 1995
- Walker G. O., Longitudinal structure of the F-region equatorial anomaly - a review. J. Atmos. Terr. Phys., 43, 763. 1981.
- Wilson B. D., Manucci A. J. and Edwards C. D., Subdaily northern hemisphere maps using an extensive network of GPS receivers. Radio Sci. 30, 639. 1995

**CHARACTERIZATION OF SPATIAL LIGHT MODULATOR FOR
APPLICATION TO REAL - TIME HOLOGRAPHY**

**Michael V. Wood
Graduate Student
Department Of Electrical Engineering**

**The Pennsylvania State University
121 Electrical Engineering East
University Park, PA 16802**

**Final Report For:
Graduate Student Research Program
Phillips Laboratory, Kirtland AFB**

**Sponsored By:
Air Force Office of Scientific Research
Bolling Air Force Base, DC**

And

Phillips Laboratory, Kirtland AFB

August 1997

CHARACTERIZATION OF SPATIAL LIGHT MODULATOR FOR APPLICATION TO REAL - TIME HOLOGRAPHY

Michael V. Wood
Department of Electrical Engineering
The Pennsylvania State University

Abstract

Spatial light modulators are used in a wide variety of applications ranging from optical computing to display. The application that is of interest for this report is that of real-time holography. A system architecture has recently been developed that uses a spatial light modulator as a real-time holographic element in a telescope system to perform adaptive optical correction of primary mirror distortions. This allows a less expensive primary mirror to be used with little or no degradation of the resulting image. The spatial light modulator is the key element to this system. This paper reports the results of an investigation of the Hamamatsu X5641 PAL-SLM parallel aligned nematic liquid crystal spatial light modulator for use as a real-time holographic element in this adaptive optics system.

CHARACTERIZATION OF SPATIAL LIGHT MODULATOR FOR APPLICATION TO REAL - TIME HOLOGRAPHY

Michael V. Wood

Introduction to spatial light modulators

Spatial light modulators are electro-optical devices that change an optical readout beam in space according to a prescribed input. Although in this paper a two- dimensional spatial light modulator (SLM) is used, in general they can modulate in one-, two-, or three-dimensions². There are two main types of SLMs differentiated by the type of input necessary to create the modulation pattern, electrically addressable spatial light modulator (EASLM) and optically addressable spatial light modulator (OASLM). The EASLM has the requirement of external circuitry or a computer to introduce the modulation pattern onto it whereas the OASLM only needs to have an input image to cause modulation. Both of these configurations have their own benefits and drawbacks.

Though other materials can be used, such as photorefractives and some organic structures, most SLMs, including the one investigated here, use a liquid crystal material to accomplish the modulation of the readout beam. The liquid crystal material can either be used to modulate the phase of the readout beam, or, with the use of a polarizer and analyzer, its intensity. This is accomplished by aligning the liquid crystals in a specific structure and then applying an electric field to change the local optical index seen by the readout beam and therefore locally change the phase or intensity according to the input. The way that this spatially varying electric field is applied to the liquid crystal is what determines whether the device is an EASLM or an OASLM.

The EASLM has fingers of a transparent electrodes, called crossbar elements, oriented perpendicular to each other on either side of the liquid crystal. When a voltage is applied on a particular set of crossbar elements an electric field forms between them and the readout beam is affected. The EASLM has a pixilated structure, with only one set of crossbar elements addressable at a time.

The OASLM converts the spatial intensity distribution from an input image into a spatial modulation of either the readout beam's phase or the intensity. Figure 1 shows a schematic of a typical OASLM⁴. The device consists of a layer of photoconductor (a material whose conductivity changes with the application of light), a reflective layer, and liquid crystal sandwiched between transparent electrodes. A bias voltage is applied across the electrodes, which causes an electric field across the liquid crystal layer that depends on the local conductivity of the photoconductor. The intensity of the input image causes the local conductivity of the photoconductor to change and therefore the electric field across the liquid crystal change as well. The readout beam passes through the liquid crystal and sees the spatial pattern in the index and is modulated in phase or intensity depending on the setup.

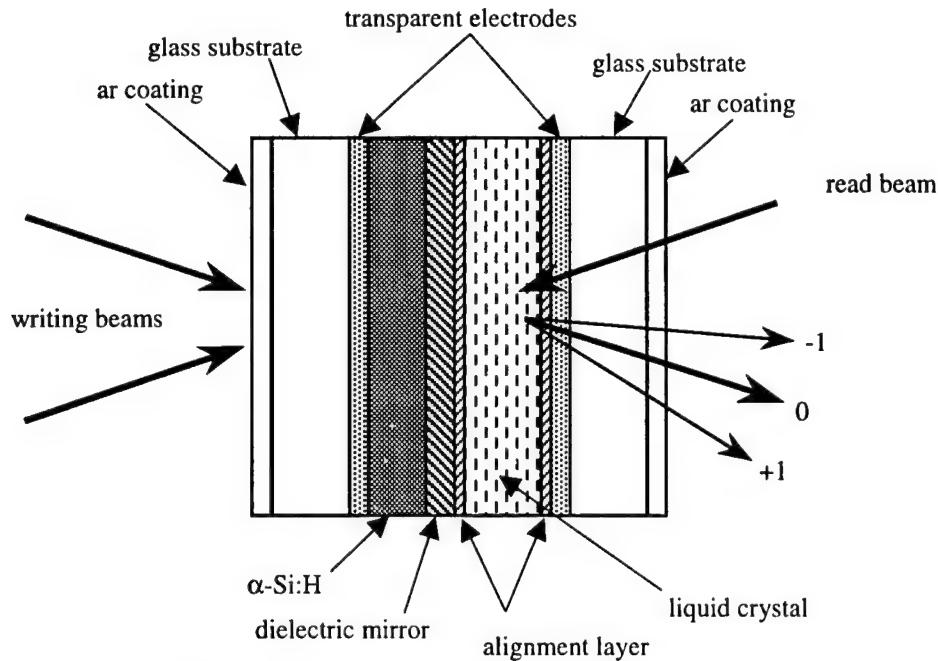


Figure 1. Schematic depiction of an optically addressed spatial light modulator.

By far the most common use of SLM is in display technology. An OASLM can be used as a liquid crystal light valve (LCLV) in conjunction with a cathode ray tube in order to project an image onto a screen. A typical LCLV is similar to the OASLM shown in fig. 1. The CRT can either be tight up against the input side of the OASLM, or be imaged onto it. This use of the LCLV is monochromatic. Full color projection can be achieved by using a LCLV each for red, green, and blue and then combining them into a full color output. Another common use for a SLM is as a flat panel display such as an active matrix liquid crystal display (AMLCD) on laptop computers. The AMLCD is an EASLM where each pixel has its own circuitry to store the information on whether the pixel is on or off. These are just two examples of the many ways that SLMs are used in displays.

The previous examples demonstrate another classification to the SLM technology, the difference between a transmission and reflection system. A transmission system is usually (but not always) an EASLM, where the light travels in a single direction through the SLM. This is the type of configuration used in filter systems, conjugation systems, and many others, including back-lit LCD systems such as the AMLCD. In the reflection SLM, light passes through the liquid crystal layer, bounces off a mirror and then travels through the liquid crystal again. The reflective type includes nearly all OASLMs, as well as most LCDs.

Another application that uses the SLM extensively is the field of optical computing. The use of optics in computing has the benefit of parallel processing, many interconnections, and very high speed performance. The SLM can be used as a signal filter in an optical system to achieve either the convolution

or correlation of the input image with the function that is displayed on the SLM. The system operates on the entire image simultaneously so its speed is limited only by the refresh rate of the SLM and is much faster than performing the same operation in with a computer. The SLM can also be used in a joint transform optical correlator to do pattern recognition or target tracking. Another application of the SLM in optical computing is the formation of neural networks where the SLM forms the weighted interconnects between neurons.

In this paper the application of interest is adaptive optics. SLMs can be used to correct for the OPD of a system directly or, as is the case in this paper, for phase subtraction via real-time holography. For real-time holography the SLM transfers the phase information of an input image to the liquid crystal where it can be read by the output beam. With this technique, the SLM can be used in a system to correct for undesired aberrations. Either the EASLM or the OASLM can be used as an adaptive optical element; however, the EASLM has the requirement of needing a driving computer with some form of image detector attached. The OASLM by its very nature already incorporates the image detection into the unit itself, simplifying the system architecture.

Telescope aberration compensation

Modern telescope designs require the use of large primary mirrors to achieve the high-resolution images desired. In order to maintain the high optical quality necessary for these mirrors, they are generally manufactured as a heavy, monolithic component. Fabrication of such a component is very costly, and transporting it is very difficult. Because of these factors, the size of ground- and space-based telescopes is limited. By using an adaptive optics technique, the optical requirements for the primary mirror can be relaxed so a large, low optical quality primary mirror can be used in conjunction with some compensation optics to achieve high-resolution images with a considerably reduced cost.

One proposed method of adaptive optic compensation for low quality primary mirrors is by using real-time holography with an optically addressed spatial light modulator^{1,3}. This technique uses holographic phase subtraction to remove the aberration of the low quality mirror. Figure 2 show a conceptual set-up of the holographic phase subtraction technique. A beacon laser probes the mirror and picks up the aberration of the primary mirror, ϕ_a , where $\phi_a = \left(2\pi/\lambda\right)(\text{OPD})$ with λ is the wavelength of the beacon laser and OPD is the optical path difference. The aberrated beacon, $Be^{i\phi_a}$, is interfered with a reference plane wave, B , from the beacon laser to form a hologram. For an amplitude hologram the transmission is proportional to the squared modulus of the illuminating field, given by:

$$T \sim 2 + e^{i\phi_a} + e^{-i\phi_a}$$

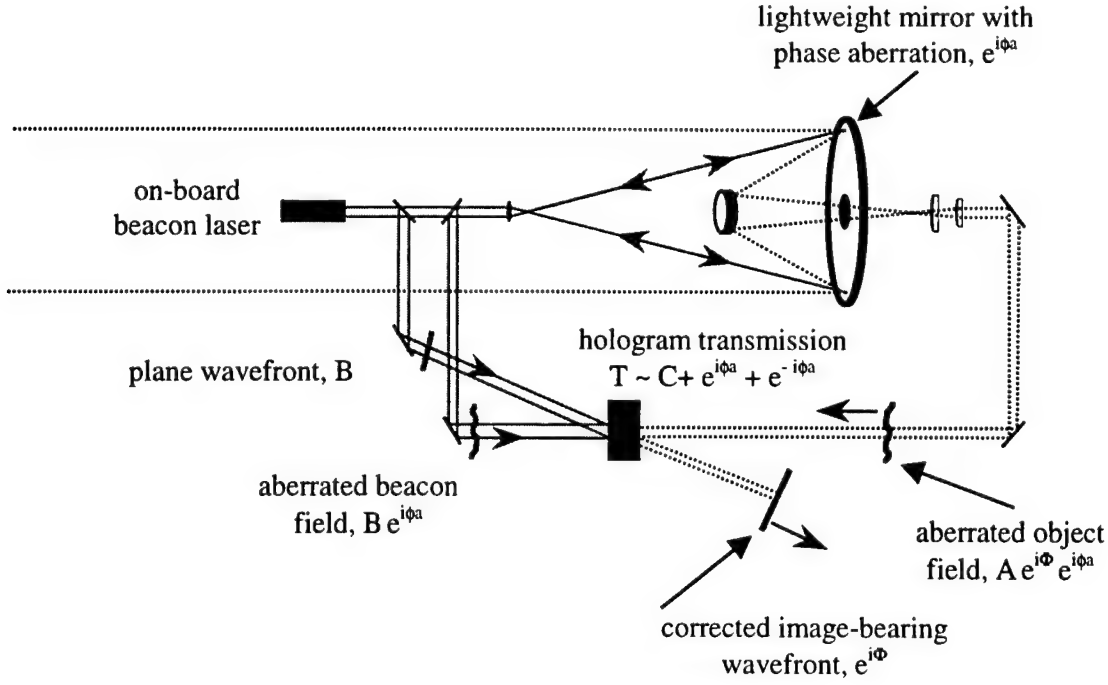


Figure 2. Schematic of an adaptive optical technique for phase subtraction.

This hologram is then illuminated by the aberrated object field, $A e^{i\Phi} e^{i\phi_a}$ where $A e^{i\Phi}$ is the undistorted object field. Multiplying the aberrated object beam with the transmission function of the hologram:

$$A e^{i\Phi} e^{i\phi_a} T \sim 2e^{i\Phi} e^{i\phi_a} + A e^{i\Phi} e^{2i\phi_a} + A e^{i\Phi}$$

The three terms represent the zero, plus one, and minus one diffracted orders, respectively. The zero order, proportional to $e^{i\Phi} e^{i\phi_a}$, is the original aberrated object beam transmitted through the hologram. The plus one order, proportional to $e^{i\Phi} e^{2i\phi_a}$, is the addition of the aberrated phases, creating further distortion. The minus one order, proportional to $e^{i\Phi}$, is the subtraction of the aberrated phases, leaving only the unaberrated phase information, Φ .

Real-time holographic element

The key component to this whole procedure is the real-time holographic element, the OASLM. There are several properties of the OASLM that need to be addressed in order to make it a good adaptive optical device; speed, sensitivity, optical efficiency, diffraction efficiency, and resolution. The speed of OASLMs can range from ~ 30 Hz for nematic liquid crystal to >1 kHz for ferroelectric liquid crystal.

Aberration compensation requires that the OASLM react at a speed greater than that at which the aberration is changing and is very dependant on the specific application. The need for sensitivity can easily be met by an OASLM device, they can typically react to write beam intensities less than $50 \mu\text{W}/\text{cm}^2$ in a standard setup.

For a real-time holography application, the optical efficiency of an OASLM can be defined as the percentage of aberrated, unpolarized image light that is converted into unaberrated image light. This definition takes into account any absorption or other losses that take place within the OASLM itself. One detractor from the optical efficiency is the dielectric mirror. High reflectivity dielectric coatings generally reduce the resolution and degrade the switching capabilities of OASLMs due to the added capacitance. However, new techniques have made high reflectivity photoconductors suitable for use in high performance OASLMs.

Since the compensated image is found in the first order diffraction, the diffraction efficiency of the OASLM is also a source of loss. For a phase only sinusoidal modulation the refractive index profile can be written as $\tilde{n} = n + \Delta\tilde{n} \cos qx$. The diffraction efficiency of this index profile is⁶:

$$\eta = |J_1(2\pi\Delta\tilde{n}d/\lambda)|^2$$

where $2\pi\Delta\tilde{n}d/\lambda$ is the phase associated with the transmittance, or half the total phase modulation. With a nematic OASLM operating in the phase modulation mode the largest theoretical diffraction efficiency achievable is only about 34% at a phase modulation of about 3.7. In addition, phase modulation occurs for only one polarization direction, so for unpolarized readout light the diffraction efficiency is reduced to about 15%

The resolution of the OASLM is limited by the diffusion of charges in the photoconductor and by electric field fringing effects in the photosensor, reflecting layer, and liquid crystal layer. The resolution of the OASLM limits the severity of distortion that can be corrected for. It is desirable to have a resolution of greater than 100 lines per mm while maintaining maximum diffraction efficiency, however, current OASLMs have greatly reduced diffraction efficiencies at spatial resolutions above 30 lines per mm.

Hamamatsu SLM

In this report, an OASLM is characterized for use as an adaptive optical real-time holographic element for aberration correction in a lightweight telescope system. The OASLM being characterized is a Hamamatsu X5641 series parallel aligned nematic liquid crystal spatial light modulator (PAL-SLM). The structure of the PAL-SLM is shown in figure 1⁴. The photoconductor layer is made of amorphous silicon, which has extremely high impedance when it is in the dark state. The impedance of the photoconductor

decreases approximately in proportion to the logarithm of the write light intensity, and the electric field across the liquid crystal layer increases accordingly.

Due to the alignment of the liquid crystal, the Hamamatsu PAL-SLM can be used either in phase modulation mode or, with a polarizer/analyzer combination, in intensity modulation mode. For phase modulation, the liquid crystal molecular axis should be set parallel to the polarization direction of the readout laser. Intensity modulation requires that the molecular axis is tilted 45° to the direction of polarization of the readout laser and that the readout be taken through a polarizer oriented 90° to the readout laser. Figure 3 shows the PAL-SLM in both the phase modulation mode and the intensity modulation mode assuming that the readout laser polarization is vertical. For identification purposes the lower left corner of the active area on the readout side is the only corner that is not rounded off, this corner should be aligned with the lower scribe mark for phase modulation and the upper scribe mark for intensity modulation.

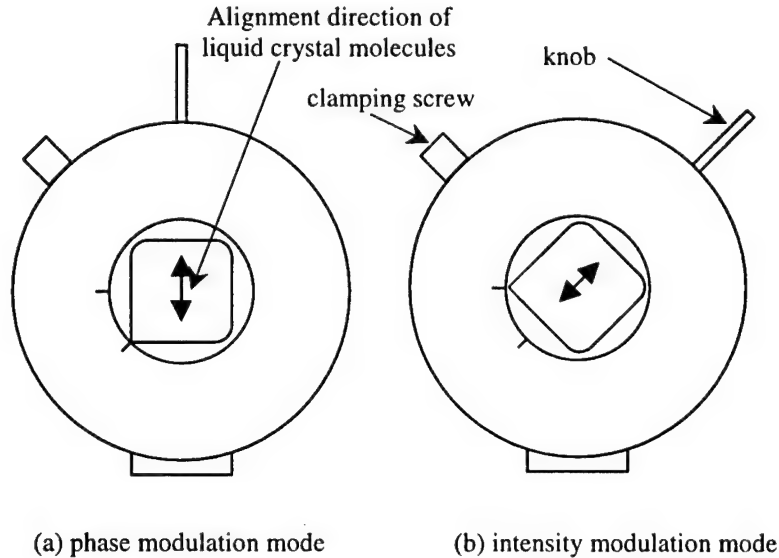


Figure 3. Rotational settings for the PAL-SLM

The PAL-SLM is driven by a 1 kHz bipolar square wave with an amplitude of about $\pm 2.5V$. The voltage of the driving signal can be anything up to a maximum of $\pm 5V$. Larger voltages result in faster response times but they decrease the amount of phase modulation achievable and therefore the diffraction efficiency.

Characterization

During the course of this investigation the diffraction efficiency of the Hamamatsu X5641 OASLM was measured as several parameters were varied. The spatial resolution, writing intensity and driving voltage were varied in an attempt to achieve the near 30% diffraction efficiency that is given in the unit's instruction manual. All the measurements were done in the phase modulation mode with a vertically polarized laser and the PAL-SLM aligned as shown in Fig. 3a. The alignment of the polarization with the liquid crystal molecular axis was tested by using a cross-nicol polarizer and tweaking the angle of the PAL-SLM to get a minimum readout, ensuring pure phase modulation.

The set-up for measuring the diffraction efficiency of the PAL-SLM is shown in figure 4. The half-wave plate and polarizer combinations labeled as 1 and 3 are used as variable beam splitters, 1 splits the main beam into the write beam and read beam, 3 splits the write beam into two beams which are interfered on the photoconductor to write a grating whose spatial frequency depends on the crossing angle between the two write beams. The intensity of both of the writing beams can be controlled simultaneously by the use of the half-wave plate and polarizer combination labeled as 2. The crossing angle of the writing beams is accurately controlled by using the rotation stage that the PAL-SLM is mounted on. The PAL-SLM is rotated until one of the beams is retro-reflecting, the rotation stage is then turned to the desired crossing angle and the other writing beam is adjusted to be retro-reflected. The PAL-SLM is then set so the normal to the surface bisects the angle between the writing beams.

For small crossing angles, the spatial frequency of the grating written on the photoconductor is related to the crossing angle of the writing beams by:

$$f_0 = \frac{\theta}{\lambda}$$

Where f_0 is the spatial frequency, θ is the crossing angle in radians, and λ is the writing beam frequency, 543 nm for green helium-neon. For the spatial frequencies used, 5, 10, and 15, the crossing angles are

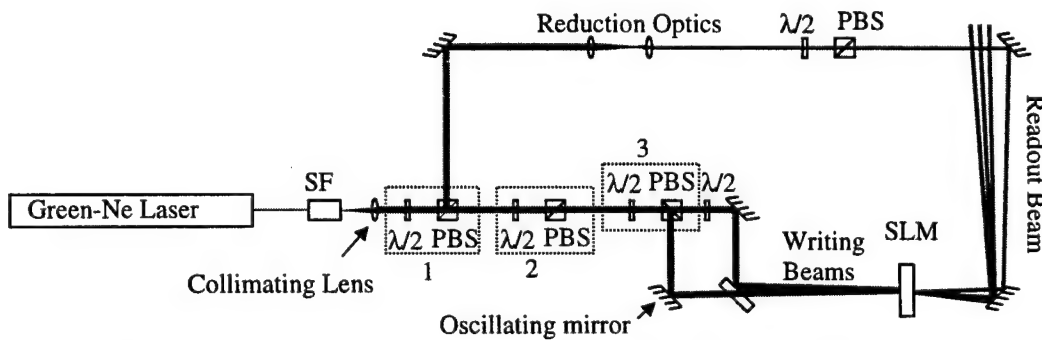


Figure 4. Schematic of the set-up for measuring the diffraction efficiency

0.155°, 0.31°, and 0.465°, respectively.

An initial test was done to ensure that the diffraction existed and that the diffraction efficiency responded to differing write intensities. The PAL-SLM was in the phase modulation mode with a driving voltage of $\pm 2.5\text{V}$ and the trial was performed at three different spatial frequencies, 5, 10, and 15 lines per mm. The writing beam diameter was 0.6 cm and the readout beam diameter was 0.3 cm. The results indicated that the diffraction efficiency does respond to the writing intensity and that there was a maximum in the diffraction efficiency at a combined writing power of about $14\text{ }\mu\text{W}$, which corresponds to a peak writing intensity of $100\text{ }\mu\text{W}/\text{cm}^2$. The diffraction efficiency also had a dependence on the spatial frequency of the writing pattern, the peak efficiency dropped off from a value of 15% at a resolution of 5 lines per mm to 13.6% at 10 lines per mm and 8.5% at 15 lines per mm.

As an attempt to maximize the diffraction efficiency, the diameter of both the writing beams and the of read beam was increased. The read beam's diameter was increased to 0.5 cm in order to satisfy the condition that $f_0 d \gg 2$, where f_0 is the spatial frequency and d is the diameter of the readout beam⁷. Satisfying this condition ensures that there is negligible overlap of the diffracted orders. The writing beams' diameter was increased to 2.5 cm so that the writing pattern was uniform over the area of the readout beam.

The results for this modified setup are shown in figure 5. A peak diffraction efficiency can be seen, this time a much higher value of nearly 22% for a resolution of 5 lines per mm. The diffraction efficiency also increased for resolutions for 10 and 15 lines per mm. The peak values of efficiency occur

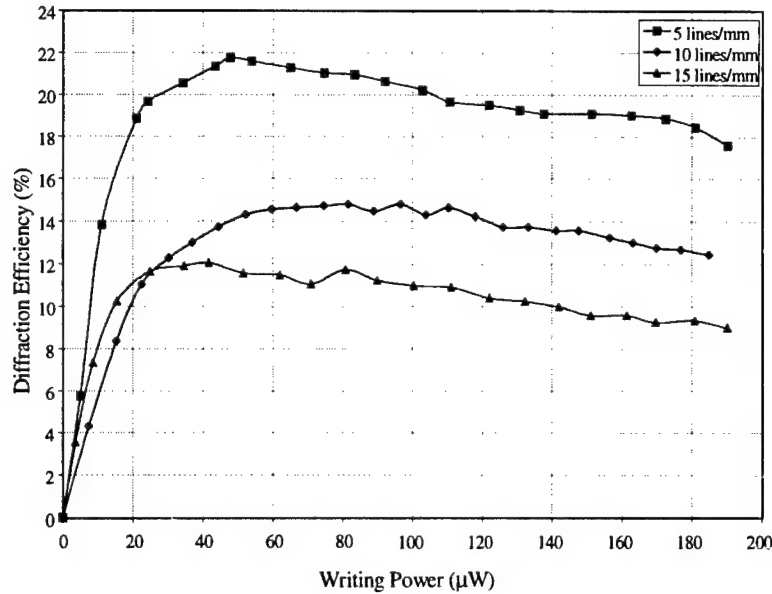


Figure 5. Diffraction efficiency vs. writing beam intensity for three spatial frequencies using a 2.5cm diameter writing beam.

around a writing power of $50 \mu\text{W}$ with a corresponding peak writing intensity of $20 \mu\text{W}/\text{cm}^2$. The fact that the efficiency increased while the corresponding writing intensity decreased shows that this is indeed a better system architecture. Even though the efficiency has improved, it is still not at the level of near 30% that is given in the Hamamatsu instruction manual.

With the writing intensity set to yield the maximum diffraction efficiency, the Driving voltage was varied in order to determine the optimum value to maximize the diffraction efficiency. The writing beams were set at a resolution of 10 lines per mm with a writing beam intensity of $\sim 25 \mu\text{W}/\text{cm}^2$. The results of this test are shown in figure 6. Figure 6 shows that there are several local efficiency maxima, but the peak diffraction efficiency of 16.7% occurs at $\sim 2.6 \text{ V}$, an improvement over the 14.8% efficiency measured previously for a resolution of 10 lines per mm.

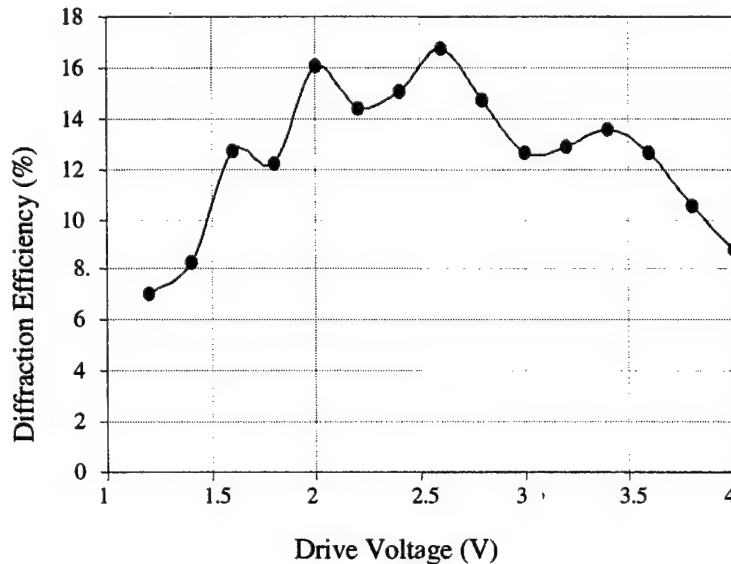


Figure 6. Diffraction efficiency vs. Drive Voltage with a writing beam of $25 \mu\text{W}/\text{cm}^2$ and a resolution of 10 lines/mm.

Even with optimization of all the controllable variables, the diffraction efficiency remains well below the value given in the Hamamatsu instruction manual. One possible reason for this discrepancy may be the amount of phase modulation that is actually produced by the PAL-SLM. In order to measure the phase modulation of the PAL-SLM, the setup from figure 4 was modified to form an interferometer. This modification is shown in figure 7a. The output side of the PAL-SLM was used as a mirror in one of the arms of the interferometer, with half of the input side illuminated by a uniform beam and the other half remaining dark. Figure 7b shows a resulting interferogram. The phase difference between the dark input and the illuminated input can be easily seen. With the PAL-SLM in this configuration and using a readout wavelength of 543 nm, the maximum phase modulation was measured to be approximately $\frac{3\pi}{4}$, or about

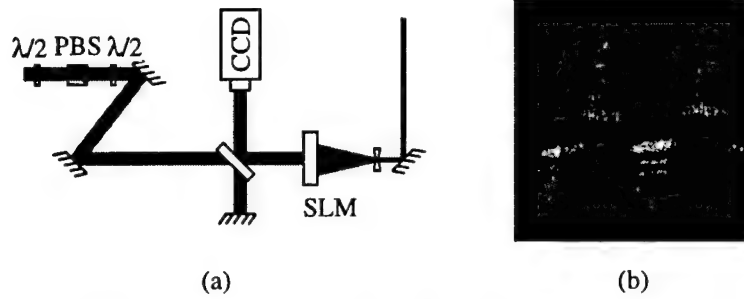


Figure 7. (a) Setup modification to measure the phase modulation of the SLM. The input side of the SLM is on the right. (b) Interferogram from this setup.

2.4. For this phase modulation the theoretical maximum diffraction efficiency is about 24%, much closer to the measured maximum diffraction efficiency of 22% than the value of near 30% given in the Hamamatsu instruction manual.

Another area of interest for the PAL-SLM is its response time to a changing input pattern. In order to test this, the setup was returned to what is shown in figure 4 and an oscillating mirror was used. The oscillating mirror was simply a mirror attached to a piezo-electric cell which is driven by a variable frequency triangle wave in order to apply a 2π phase shift on one of the writing beams and therefore shift the position of the fringes on the PAL-SLM. With a 2π phase shift, the time average of the writing image on the surface of the photoconductor over an integer number of periods is uniform. If the liquid crystal responds fast enough to the moving image, there will be little or no change in the diffraction efficiency. However, if the liquid crystal cannot respond fast enough to keep up with the image, the diffraction efficiency will decrease. Figure 8 shows the results for this trial with a resolution of 5 lines per mm and a

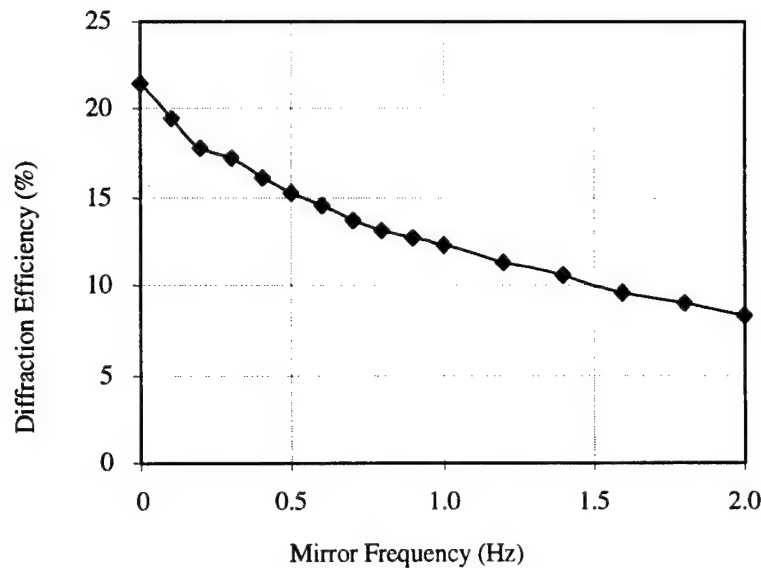


Figure 8. Diffraction efficiency vs. mirror frequency for a moving input grating.

driving voltage of 2.6V. The diffraction efficiency started at an initial value of 21% and dropped to a value of less than 10% at an oscillating frequency as below 2 Hz. This was completely unexpected since the Hamamatsu instruction manual lists a response time of around 50 ms, corresponding to a frequency of 20 Hz.

Conclusion

The results of the characterization of the Hamamatsu PAL-SLM were somewhat disappointing, however, the diffraction efficiency of 22% is better than the efficiency of less than 1% from the SLM currently being used. The maximum diffraction efficiency obtained (22%) was well below the efficiency of about 30% given in the Hamamatsu instruction manual. The speed of the device was surprisingly slow, the Hamamatsu instruction manual claims the speed to be 20 Hz, however, the diffraction efficiency drops off significantly when the input is changing at a speed of just 1 Hz. Another big disagreement between the Hamamatsu instruction manual and the results is the phase modulation, according to the Hamamatsu instruction manual, there should be over 2π phase modulation for the green helium neon's wavelength, but the actual measurement was less than π . The Hamamatsu PAL-SLM represents a significant increase in the optical efficiency, but the surprisingly slow response time may limit its usefulness in adaptive optics imaging systems.

References

1. M.T. Gruneisen, K.W. Peters, J.M. Wilkes, "Compensated Imaging By Real-Time Holography With Optically Addressed Liquid Crystal Spatial Light Modulators," SPIE Annual Meeting, San Diego, CA, 17 July-1 Aug 1997.
2. U. Efron, *Spatial Light Modulator technology materials, devices, and applications*, Marcel Dekker Inc., New York, NY. 1995
3. M.T. Gruneisen, J.M. Wilkes, "Compensated Imaging By Real-Time Holography With Optically Addressed Spatial Light Modulators," Spring Topical Meeting on Spatial Light Modulators, Lake Tahoe, NV, March 17-19, 1997, Paper StuB5.
4. Hamamatsu technical instruction manual for model X5641 PAL-SLM parallel aligned nematic liquid crystal spatial light modulator.
5. J. Munch R. Wuerker, "Holographic Technique for correcting aberrations in a telescope," Appl. Opt. **28**, pp. 1312-1317, 1989
6. H.J. Eichler, P. Günter, D.W. Pohl, *Laser-induced dynamic gratings*, Springer-Verlag, New York, NY, 1986
7. J.W. Goodman, *Introduction to fourier optics*, McGraw-Hill, Inc. New York, NY. 1968

**A LIBRARY OF THE NATURAL FREQUENCY RESPONSES FOR
CYLINDRICAL AND RECTANGULAR SHAPED PLASTIC MINES**

**Mark C. Worthy
Graduate Student
Department of Environmental Engineering**

**University of Alabama in Huntsville
Huntsville, AL 35899**

**Final Report for:
Graduate Student Research Program
Phillips Laboratory**

**Sponsored by:
Air Force Office of Scientific Research
Bolling Air Force Base, DC**

and

Phillips Laboratory

August 1997

A LIBRARY OF THE NATURAL FREQUENCY RESPONSES FOR CYLINDRICAL AND RECTANGULAR SHAPED PLASTIC MINES

Mark C. Worthy
Graduate Student
Department of Environmental Engineering
University of Alabama in Huntsville

Abstract

The dielectric mine problem is presented. An approximate approach for finding the natural frequencies of dielectric targets in a dielectric medium is presented. This approach is applied to (and demonstrated for) dielectric, rectangular and cylindrical cavities. A region where this approach is “accurate” is shown. A library of dielectric, rectangular and cylindrical shaped mines is presented. The library gives the name, country of origin, countries using, and electromagnetic information about 94 different plastic anti-personnel and anti-tank mines. A method for using this library to find the natural frequencies is presented and demonstrated. If this library proves effective it is suggested that the user input all of the data into software for real time (and easier) manipulation.

A LIBRARY OF THE NATURAL FREQUENCY RESPONSES FOR CYLINDRICAL AND RECTANGULAR SHAPED PLASTIC MINES

Mark C. Worthy

Introduction

Successfully detecting buried dielectric land mines has proven to be a technical nightmare. Former war zone areas like Bosnia, Iraq, and Afghanistan have demonstrated just how lacking in technology we are in finding buried plastic targets. One common cry from the scientist and military personnel working on this problem has been to establish a library of the natural frequency responses for each and every plastic land mine. With such a library a user could know if what has been detected is of interest. It is the purpose of this report to establish such a library for cylindrical and rectangular shaped, plastic land mines.

This task will be accomplished using Dr. Carl E. Baum's perturbation formula method for finding the signatures of dielectric targets in a dielectric medium [Baum, 1994]. In my 1996 final report (for RDL) I established an "effective" region for using this perturbation method. With this effective region one can decide whether or not to use the method by simply entering in their soil conditions (ϵ and σ) and the size of their target into an equation and see if the result of this equation falls within an acceptable percent error [Worthy, 1997].

This report will supply the radar user with all of the tools needed to quickly find the pole locations of 94 different plastic anti-tank and anti-personnel mines. These are mines that are approximately rectangular or cylindrical in shape. The names, country of origin, countries known to use, and important electromagnetic information about each of these mines is provided.

Definitions & Equations

Before we look at the perturbed functions its important that we define some necessary terms. The relative dielectric constant, ϵ_r , will be defined as

$$\epsilon_r \equiv \frac{\text{target}}{\text{medium}} = \frac{\epsilon_2}{\epsilon_1}$$

We will define the ratio of the propagation constants, ξ , as:

$$\xi(s) \equiv \frac{\gamma_1}{\gamma_2} = \epsilon_r^{-\frac{1}{2}} \left[1 + \frac{\sigma_1}{s\epsilon_1} \right]^{\frac{1}{2}}$$

where $s = \Omega + j\omega \equiv$ the complex frequency.

We will define the natural frequencies as

$$s_\alpha = s_{\alpha,0} + \Delta s_\alpha$$

For the cylinder (where r is the radius) we will have a normalization factor T_a such that:

$$T_a = \sqrt{\mu_o \epsilon_2} r$$

Therefore:

$$s_\alpha T_a = s_{\alpha,0} T_a + \Delta s_\alpha T_a$$

Now we are ready for the perturbation formulas.

The Perturbation Method

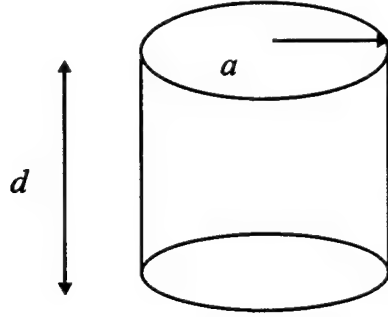
An approximate method for finding the natural frequencies of dielectric targets in a dielectric medium was first presented by Dr. Carl Baum in 1994 (Interaction Note 504). In 1996 Dr. George Hanson (a fellow SRP worker, for RDL) developed a more general formula and applied it to a finite cylindrical shaped target (Interaction Note 520).

The general method for the perturbed functions involves solving for two terms $s_{\alpha,0}$, and Δs_α . The $s_{\alpha,0}$ term is found from the exact theoretical equations by applying the limiting case when $\xi \rightarrow \infty$. The Δs_α term is found from the following equation [Hanson, 1996]:

$$\Delta s_\alpha = \frac{-1}{2\xi(s_{\alpha,0})\sqrt{\mu_o \epsilon_2}} \left[\frac{\oint_s |\vec{H}_0|^2 ds}{\int_v |\vec{H}_0|^2 dv} \right]$$

The Finite Cylinder

For the following cylindrical cavity:



George found that for the E-modes [Hanson, 1996]:

$$s_{\alpha,0}T_a = i\sqrt{x_{n,p}^2 + \left[\frac{q\pi a}{d}\right]^2}$$

Where a is the radius and d is the height of the cylinder. q describes the variation along the height of the cylinder and $x_{n,p}$ is the p -th resonance of the n -th order Bessel function [Hanson, 1996].

Therefore, $x_{n,p}$ is found from $J_n(x_{n,p}) = 0$. Similarly, for the H-modes:

$$s_{\alpha,0}T_a = i\sqrt{x_{n,p}'^2 + \left[\frac{q\pi a}{d}\right]^2}$$

where $x_{n,p}'$ is found from $J_n'(x_{n,p}') = 0$. Note that all of the $s_{\alpha,0}T_a$ values will be imaginary.

After applying the surface and volume integrals to the cavity George found the following Δs_α terms. Where for the E-modes [Hanson, 1996]:

$$\Delta s_\alpha T_a = -\xi^{-1}(s_{\alpha,0}) \left[1 + \frac{2a}{(1 + \delta_{q,0})d} \right]$$

and for the H-modes:

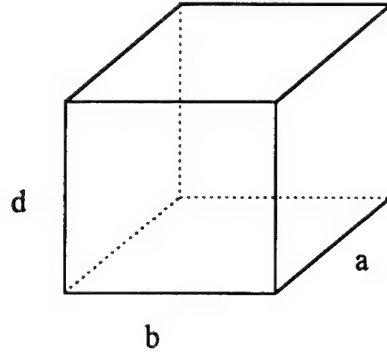
$$\Delta s_\alpha T_a = -\xi^{-1}(s_{\alpha,0}) \left[\frac{\left(\frac{nq\pi a}{d}\right)^2 + x_{n,p}'^4 + \frac{2a}{d} \left(\frac{q\pi a}{d}\right)^2 (x_{n,p}'^2 - n^2)}{(s_{\alpha,0}T_a)^2 (n^2 - x_{n,p}'^2)} \right]$$

where $\delta_{q,0}$ is the Kronecker delta function. n corresponds to the Bessel functions ($n = 0, 1, 2$, etc.). As for q , $q = 0, 1, 2$, etc. for the E-modes and $q = 1, 2, 3$, etc. for the H-modes; however, $q > 2$ corresponds to $a \ll d$ or $a \gg d$.

For the case of the dielectric mine we are only concerned with the dominant poles. So we will only solve for $n = 0, 1$, and 2 . Similarly since a and d are so close (not varying by more than say a factor of 3) we will only need to look at $q = 0$ and 1 for the dominant poles.

The Rectangular Cavity

The resonant frequency, $s_{\alpha,0}$, of a rectangular cavity has been found (and discussed) by Harrington, Dearholt, Collin, Kong, and others. Where for the rectangular cavity:



we have:

$$s_{\alpha,0} = \frac{j}{\sqrt{\mu_0 \epsilon_2}} \left[\left(\frac{m\pi}{a} \right)^2 + \left(\frac{n\pi}{b} \right)^2 + \left(\frac{p\pi}{d} \right)^2 \right]^{\frac{1}{2}}$$

Where $m = 0, 1, 2$, etc., $n = 0, 1, 2$, etc., and $p = 0, 1, 2$, etc.. Since these integers m , n , and p represent the half-wave periodicity in the y , x , and z directions respectively, “the lowest resonant frequency (the dominant mode) occurs when the integer associated with the smallest dimension is zero and the other two are unity” [Dearholt, 1973]. Therefore, if d is the smallest dimension then the most dominant frequency will take the following form.

$$s_{\alpha,0} = \frac{j}{\sqrt{\mu_0 \epsilon_2}} \left[\left(\frac{\pi}{a} \right)^2 + \left(\frac{\pi}{b} \right)^2 \right]^{\frac{1}{2}}$$

The next dominant mode depends upon the shape of the target. Where (assuming d is still the smallest dimension) if $a > b$ then the next dominant mode will be found by letting $m = 2$ and $n = 1$. However, if $a \cong b$ then the next dominant mode will be found by letting $m = 2$ and $n = 2$.

After applying the surface and volume integrals to the rectangular cavity (assuming that the thickness, d , was the smallest dimension) I found Δs_a to be:

$$\Delta s_a = \frac{-1}{\xi(s_{a,0})\sqrt{\mu_0\epsilon_2}} \left[\frac{2a^3d + 2b^3d + ab^3 + a^3b}{abd(a^2 + b^2)} \right]$$

If, however, the width, b , had been the smallest dimension then we would use:

$$\Delta s_a = \frac{-1}{\xi(s_{a,0})\sqrt{\mu_0\epsilon_2}} \left[\frac{2a^3b + 2d^3b + ad^3 + a^3d}{abd(a^2 + d^2)} \right]$$

From these two equations one could easily predict Δs_a for the case when the length, a , is the smallest dimension.

The Effective Region

Now that we have established the perturbation functions it becomes important to know when they will give good results. In last years final report for RDL I established an effective region for the perturbation functions. I accomplished this by finding the “exact” pole locations (from the theoretical equations) for a dielectric slab, sphere, and infinite cylinder. I investigated 42 different situations (different σ_1 , ϵ_1 , and ϵ_2). I found the percent errors for all 42 cases between the exact versus perturbed poles.

Then I established two unit-less parameters, τ and ϵ_r , for graphing the effective region.

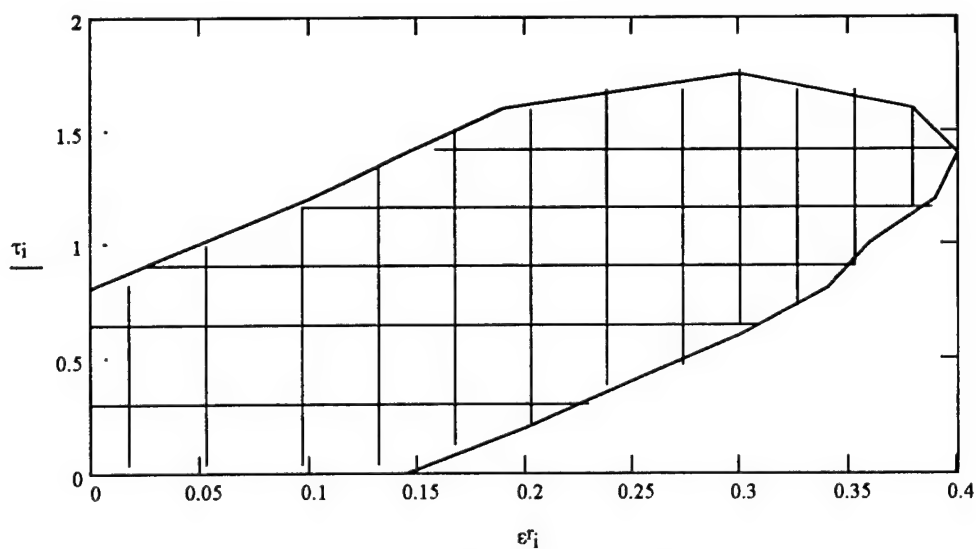
Such that:

$$\tau = \frac{r\sigma_1\sqrt{\mu_0\epsilon_2}}{\epsilon_1} \quad \text{and} \quad \epsilon_r = \frac{\epsilon_2}{\epsilon_1}$$

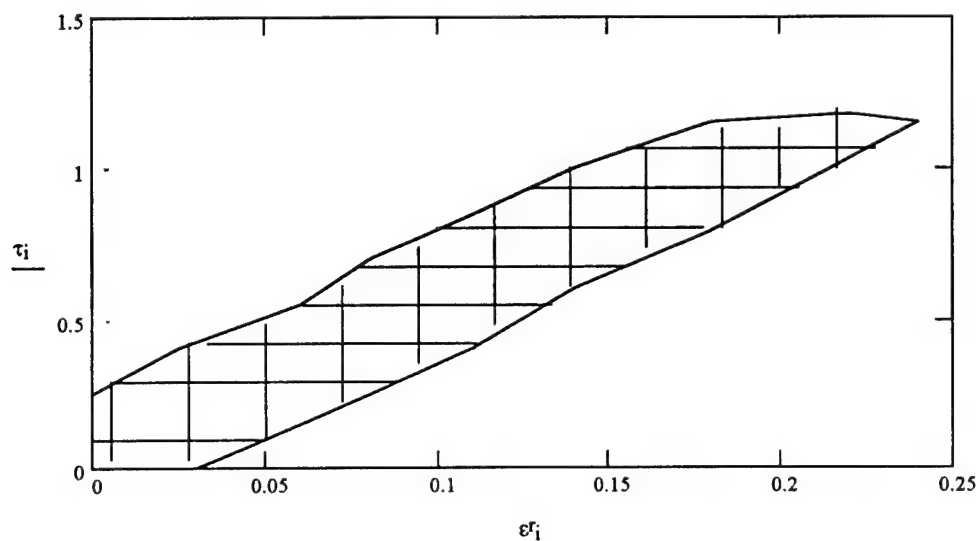
Where we let r be either the radius of the cylinder or the smallest dimension of the rectangular cavity. For the mine problem $\epsilon_2 \approx 2.5\epsilon_0$.

In the following graphs everything inside the curves represents a “good” region. In the first graph the perturbed functions were less than 6% off for the region inside the curve, and in the

second graph (below) the perturbed functions were less than 2% off. (See Interaction Note 529 for a more extensive discussion of this problem.)



Graph 1: < 6% error for perturbed functions



Graph 2: < 2% error for perturbed functions

In order to use these graphs you must first know your soil conditions, σ_1 and ε_1 . Then you will simply enter σ_1 and ε_1 , and the r and ε_2 values for the mine into the equations for τ and ε_r . Finally, check these values to see if they fall into the “good” region on the graphs.

A Library of Cylindrical and Rectangular Shaped Plastic Land Mines

The following five pages contain a list of all of the plastic land mines that are approximately cylindrical or rectangular in shape. Three of the pages list the name of the mine by category, the country who makes the mine, and the country(s) who are known to use the mine. There is one page of the electromagnetic (and pole) information for all of the rectangular mines. However, the electromagnetic information for all of the cylindrical mines is 41 pages long. Therefore, since I have a 20 page limit for this report I will only provide a one page excerpt from my cylindrical mine report. For a complete list of the cylindrical mines I refer you to Phillips Laboratories' Interaction Note 530.

Cylindrical-Plastic-Mines List

I. Anti-Personnel Mines

<i>Mine</i>	<i>Made By</i>	<i>Counties Used By</i>
AP NM M14	India	India
AUPS	Italy	Italy
CP-X.01	Spain	Spain
DM-11	Sweden & Former West Germany	Sweden, Switzerland, Germany, Angola, Zambia, Eritrea, Ethiopia
DM-39	Former West Germany	Former West Germany
FMK-1	Argentina	Argentina, Falkland Islands
LBA Type A&B	Italy	Italy
M14	USA, India, & Vietnam	USA, India, Vietnam, Malawi, Angola, Iraq, Iran, Zambia, Somalia, Eritrea, Ethiopia, Cambodia
MAP II	Chile	Chile
MD-82-B	Vietnam	Vietnam, Cambodia
MGP.30	Peru	Peru
MN-79	Vietnam	Vietnam, Cambodia
NR22C1	France	Netherlands
P5	Spain	Spain
P4 MK1	Pakistan	Pakistan, Somalia, Afghanistan
PATVAG 59	Switzerland	Switzerland, Egypt, Portugal
PATVAG M3	Switzerland	Unknown
PM 79	Bulgaria	Bulgaria
PMA-3	Former Yugoslavia	Former Yugoslavia, Namibia, South Africa, Cambodia
PMP 71	Former East Germany	Germany, Somalia, Ethiopia, Eritrea
PP M1-SR II	Former Czechoslovakia	Afghanistan, Czech & Slovak Republics, Nicaragua, South Africa, Mozambique, Zambia, Somalia, Eritrea, Ethiopia
PPM-2 (variant)	China	China
PRB BAC H-28	Belgium	Belgium
PRB M409	Belgium & Portugal	Belgium, Portugal, Angola, Zambia, Iraq, Namibia, South Africa, Somalia
R2M2	South Africa	South Africa, Namibia, Zimbabwe, Zambia
TM-100	Former Yugoslavia	Former Yugoslavia
TRUPPMINA-10	Sweden	Sweden, Germany, Switzerland, Austria

TYPE 68	China	China
TYPE 72	China & South Africa	Afghanistan, Cambodia, China, Iraq, Pakistan, South Africa, Angola, Zambia, Somalia, Eritrea, Ethiopia
TYPE 72B	China	China, Cambodia
TYPE 72C	China	China
U/I TH AP.1&.2	Thailand	Thailand
(SD/AD)	China	China
VS-MK2-EL	Italy	Unknown

II. Anti-Tank Mines

<i>Mine</i>	<i>Made By</i>	<i>Counties Used By</i>
AT-1A	India	India
B MK1	Egypt & Italy	Egypt, Somalia
BAT/7	Italy	Unknown
K-1	Former East Germany	Former East Germany
L-3	United Kingdom	United Kingdom
M/52	Denmark	Denmark
M453	Portugal	Portugal
MAT F5	Chile	Chile
MAT-62B	Romania	Romania
MAT-87	Romania	Romania
MAT-U-9-10,20,30	Unknown	Romania
MAT/5	Italy	Italy
MATS/2.6	Italy	Italy
MGP.31	Peru	Peru
MPP-B	Poland	Poland
NA-MI-BA	Former Czechoslovakia	Former Czechoslovakia
No. 22	Israel	Israel
P3 MK1	Pakistan	Pakistan, Somalia, Afghanistan
P3 MK2	Pakistan	Pakistan
PT M1-BA III	Former Czechoslovakia	Czech & Slovak Republics, Iraq, Poland, South Africa, Namibia, Mozambique, Angola, Zambia, Somalia, Eritrea, Ethiopia
PTM 80P	Bulgaria	Bulgaria
SACI 54/7	Italy & Egypt	Italy, Egypt, Somalia
SACI 54/9	Italy	Italy
SACI IMAC-10,5,7	Italy	Unknown
SB-81 & 81/AR	Italy & Spain	Italy, Egypt, Somalia
SBMV/1	Italy	Unknown
T.C. 6	Egypt	Egypt, Somalia, Afghanistan
TC/2.4	Italy	Italy, Iraq
TM-62P	Former Soviet Union, Bulgaria, & Poland	Former USSR, Poland, Germany, Egypt, Bulgaria, Zambia, Mozambique, South Africa
TM-62P3	Former USSR & Germany	Former USSR, Poland, Egypt
TMA-1	Former Yugoslavia	Former Yugoslavia
TYPE 69	China	China
TYPE 72	China, South Africa	China, Iraq, Jordan, South Africa, Angola, Zambia
TYPE 81	China	China
U/I TH	Thailand	Thailand
VS-1.6	Italy	Italy, Iraq
VS-HCT	Italy	Italy

A One Page Excerpt of the Pole Parameters for the Cylindrical Shaped Plastic Mines:

SACI 54/9

radius height
a = 0.141 d = 0.191

	n=0:	n=1:	n=2:
These are the $s_o T_a$ values for the E modes for q = 0:	sEoT _{0,p}	sEoT _{1,p}	sEoT _{2,p}
	2.404825i	3.83171i	5.13562i
	5.520078i	7.01559i	8.41724i
	8.653727i	10.17347i	11.61984i

	n=0:	n=1:	n=2:
These are the $s_o T_a$ values for the E modes for q = 1:	sET _{0,p}	sET _{1,p}	sET _{2,p}
	3.3409291986i	4.4789090361i	5.6349993269i
	5.9874774117i	7.3889869182i	8.7308965088i
	8.9591079701i	10.4344677138i	11.8490213205i

	n=0:	n=1:	n=2:
These are the $s_o T_a$ values for the H modes for q = 1:	sHT _{0,p}	sHT _{1,p}	sHT _{2,p}
	4.4789047586i	2.9611768643i	3.8349715262i
	7.3889831203i	5.8140241746i	7.0958300576i
	10.4344579639i	8.8457551273i	10.2356707992i

The C values for the E modes for:

q=0 and q=1
CE₀ = 1.7382198953 CE_q = 2.4764397906

These are the C values for the H modes for q=1:

	n=0:	n=1:	n=2:
	CH _{0,p}	CH _{1,p}	CH _{2,p}
	1.1277425573	1.7106672216	1.9249397845
	1.0469364147	1.1122739176	1.1485219544
	1.0235363695	1.0466641107	1.0663924182

SACI IMAC-10

radius height
a = 0.145 d = 0.16

	n=0:	n=1:	n=2:
These are the $s_o T_a$ values for the E modes for q = 0:	sEoT _{0,p}	sEoT _{1,p}	sEoT _{2,p}
	2.404825i	3.83171i	5.13562i
	5.520078i	7.01559i	8.41724i
	8.653727i	10.17347i	11.61984i

	n=0:	n=1:	n=2:
These are the $s_o T_a$ values for the E modes for q = 1:	sET _{0,p}	sET _{1,p}	sET _{2,p}
	3.7267923777i	4.7736568446i	5.8720005901i
	6.211043332i	7.5712813443i	8.8857035379i
	9.110037823i	10.5643404899i	11.9635479592i

	n=0:	n=1:	n=2:
These are the $s_o T_a$ values for the H modes for q = 1:	sHT _{0,p}	sHT _{1,p}	sHT _{2,p}
	4.7736528312i	3.3905371165i	4.1754257416i
	7.5712776378i	6.044009482i	7.2854634528i
	10.5643308599i	8.998586405i	10.3680340579i

Rectangular-Plastic-Mines List

I. Anti-Personnel Mines

<i>Mine</i>	<i>Made By</i>	<i>Counties Used By</i>
M-62	Hungary	Hungary, Cambodia
MI AP ID 48	France	France, Nigeria, Iceland
NR 15	France	Netherlands
PP-56	Former Yugoslavia	Former Yugoslavia
TM-200	Former Yugoslavia	Former Yugoslavia
TM-500	Former Yugoslavia	Former Yugoslavia

II. Anti-Tank Mines

<i>Mine</i>	<i>Made By</i>	<i>Counties Used By</i>
AT 3A	India	India
L9	United Kingdom	United Kingdom
M-19	USA, Chile, Iran, South Korea, Turkey	USA, Chile, South Korea, Angola, Zambia, Iran, Turkey
P2 MK3	Pakistan	Pakistan, Somalia, Eritrea, Ethiopia, Afghanistan
PT-56	Former Yugoslavia	Former Yugoslavia
PT MI-BA II	Former Czechoslovakia	Czech and Slovak Republics, Poland, South Africa, Namibia, Somalia, Eritrea, Ethiopia
TMA-2	Former Yugoslavia	Former Yugoslavia, Angola, Zambia, Namibia, South Africa
TMA-5	Former Yugoslavia	Former Yugoslavia, Angola, Zambia, Namibia, South Africa, Afghanistan
VS-AT4	Italy	Unknown

Pole Parameters for Rectangular, Plastic Mines

I. Anti-Personnel Mines

<i>Mine</i>	<i>a</i>	<i>b</i>	<i>d</i>	mode-1 $S_{\alpha,0} (Rad/s)$	mode-2 $S_{\alpha,0} (Rad/s)$	<i>CS</i> (1/s)
M-62	.187m	.05m	.065m	$9.7018622 \times 10^9 j$	$1.1160900 \times 10^{10} j$	-9.2158222×10^9
MI AP ID 48	.11m	.099m	.066m	$8.0947672 \times 10^9 j$	$1.6189534 \times 10^{10} j$	-6.5318004×10^9
NR 15	.095m	.088m	.065m	$9.2267250 \times 10^9 j$	$1.8453450 \times 10^{10} j$	-7.0795822×10^9
TM-200	.059m	.032m	.109m	$1.1480099 \times 10^{10} j$	$1.4878998 \times 10^{10} j$	$-1.1684382 \times 10^{10}$
TM-500	.07m	.05m	.108m	$1.0140540 \times 10^{10} j$	$1.3931592 \times 10^{10} j$	-8.6455364×10^9

II. Anti-Tank Mines

<i>Mine</i>	<i>a</i>	<i>b</i>	<i>d</i>	mode-1 $S_{\alpha,0} (Rad/s)$	mode-2 $S_{\alpha,0} (Rad/s)$	<i>CS</i> (1/s)
AT 3A	1.21m	.108m	.08m	$5.5373197 \times 10^9 j$	$5.6025831 \times 10^9 j$	-5.8559999×10^9
L-9	1.2m	.108m	.082m	$5.5376859 \times 10^9 j$	$5.6040308 \times 10^9 j$	-5.7977948×10^9
M-19	.332m	.332m	.094m	$2.5373313 \times 10^9 j$	$5.0746627 \times 10^9 j$	-3.1592777×10^9
P2 MK3	.262m	.262m	.12m	$3.2152443 \times 10^9 j$	$6.4304886 \times 10^9 j$	-3.0274123×10^9
PT MI-BA II	.395m	.23m	.135m	$2.9968882 \times 10^9 j$	$3.9753727 \times 10^9 j$	-2.8788417×10^9
TMA-2	.26m	.2m	.14m	$3.7575352 \times 10^9 j$	$5.4649105 \times 10^9 j$	-3.0877178×10^9
TMA-5	.312m	.275m	.113m	$2.8873346 \times 10^9 j$	$5.7746692 \times 10^9 j$	-2.9853724×10^9
VS-AT4	.28m	.188m	.104m	$3.8163538 \times 10^9 j$	$5.3048672 \times 10^9 j$	-3.6342654×10^9

How the library works

A complete library of pole locations of dielectric mines in a dielectric medium would be an impossible task since there are infinite different possible values for σ_1 and ϵ_1 (even within the values for common soils and our effective region). Therefore, what I've done is compile a library of parameters for each land mine such that the user can quickly calculate the poles for the mine by simply inputting their particular soil conditions.

The Cylinder:

For the cylinder you can see that I've listed the radius, length, $s_{\alpha,0}T_a$ values, and two parameters CE for the E-modes and CH for the H-modes. Such that:

$$CE_q = \left[1 + \frac{2a}{(1 + \delta_{q,0})d} \right]$$

for the E-modes, and

$$CH_q = \left[\frac{\left(\frac{nq\pi a}{d} \right)^2 + x'_{n,p}{}^4 + \frac{2a}{d} \left(\frac{q\pi a}{d} \right)^2 (x'_{n,p}{}^2 - n^2)}{(s_{\alpha,0}T_a)^2 (n^2 - x'_{n,p}{}^2)} \right]$$

for the H-modes. Therefore:

$$\Delta s_{\alpha} T_a = -\xi^{-1}(s_{\alpha,0}) CE_q$$

for the E-modes and

$$\Delta s_{\alpha} T_a = -\xi^{-1}(s_{\alpha,0}) CH_q$$

for the H-modes.

Hence, in order to find the pole locations for a particular mine the user will only have to calculate

$$\xi(s_{\alpha,0}) = \epsilon_r^{-\frac{1}{2}} \left[1 + \frac{\sigma_1}{s_{\alpha,0} \epsilon_1} \right]^{\frac{1}{2}}.$$

Since, however, this is a repeated calculation (there are 27 s_{α} values we are solving for, for each mine) the user might wish to enter the tabulated (library) values in a math software program. This

could potentially allow for real time identification (if a user had all of the library data entered in their computer).

The Rectangular Cavity:

For the rectangular cavity pole parameter page I've listed the dimensions of each mine and the two most dominant $s_{\alpha,0}$ values. I've also listed a parameter CS such that:

$$CS = \frac{-1}{\sqrt{\mu_0 \epsilon_2}} \left[\frac{2a^3b + 2d^3b + ad^3 + a^3d}{abd(a^2 + d^2)} \right]$$

Therefore:

$$\Delta s_{\alpha} = \frac{CS}{\xi(s_{\alpha,0})}$$

Hence, recalling that $s_{\alpha} = s_{\alpha,0} + \Delta s_{\alpha}$, in order to find the pole locations for a particular mine the user will first calculate

$$\xi(s_{\alpha,0}) = \epsilon_r^{-\frac{1}{2}} \left[1 + \frac{\sigma_1}{s_{\alpha,0} \epsilon_1} \right]^{\frac{1}{2}}.$$

Then the user will input this value into the Δs_{α} equation above, and, finally, add this to the corresponding $s_{\alpha,0}$ value. Note that the CS equation used in the library is not necessarily the equation above. The CS equation used depended upon which dimension was the smallest (a, b, or d) in that particular mine (the CS equation above is for the case when d is the smallest).

Again, since repeatedly calculating these poles with this method can be a monotonous task (though much faster and easier than the exact method) the user might wish to enter the tabulated (library) values (along with the values for the cylindrical shaped mines) into a math software program.

Example

As an example lets say you have radar of a suspected mine field laid by the Polish army. You've eliminated all the metallic mine choices. Unfortunately at this time radar technology can't tell

you if the remaining “blips” on the screen are plastic mines or a child’s toy. What do you do?

Assuming that you don’t already have the library data in your computer, you should first (if you know the soil conditions) go to the cylindrical and rectangular mine lists (pages 9, 10, and 12). From these lists you can see that the only cylindrical plastic land mines used by the Polish army are four anti-tank mines: the MPP-B, the PT M1-BA III, the TM-62P, and the TM-62P3, and the only rectangular plastic land mine is the anti-tank mine PT MI-BA II.

Next you will want to calculate the natural frequencies of these mines to see if they could possibly be the “blips” on your screen. For the cylindrical mines we will only look the MPP-B.

Before we can start this we must first see if the soil conditions will allow you to use the perturbations formulas (i.e. check the effective region). Lets say that the soil in the mine field has a permittivity of $\epsilon_1 = 12\epsilon_0$ and a conductivity of $\sigma_1 = 0.05 \text{ S/m}$. From the pole parameter pages we see that the radius of the MPP-B is 0.16m and the smallest dimension for the PT MI-BA II is 0.135m. This means that $\epsilon r = 0.2083333333$ and $\tau = 0.3971083449$ for the MPP-B, and $\tau = 0.335060166$ for the PT MI-BA II. Upon looking at the “effective region” graph (page 8) we see that these values do lie within the < 6% error region.

So, lets see what the pole parameter page says about the MPP-B (see IN 530):

MPP-B

radius height
a = 0.16 d = 0.128

	n=0:	n=1:	n=2:
These are the $s_o T_a$ values for the E modes for q = 0: $sEoT_{0,p}$	$sEoT_{0,p}$	$sEoT_{1,p}$	$sEoT_{2,p}$
	2.404825i	3.83171i	5.13562i
	5.520078i	7.01559i	8.41724i
	8.653727i	10.17347i	11.61984i
These are the $s_o T_a$ values for the E modes for q = 1: $sET_{0,p}$	$sET_{0,p}$	$sET_{1,p}$	$sET_{2,p}$
	4.6048279183i	5.4866436371i	6.4649709714i
	6.7744016712i	8.0398855666i	9.2882283614i
	9.5030651827i	10.905079033i	12.265477508i
These are the $s_o T_a$ values for the H modes for q = 1: $sHT_{0,p}$	$sHT_{0,p}$	$sHT_{1,p}$	$sHT_{2,p}$
	5.4866401453i	4.3371881063i	4.9749008889i
	8.0398820763i	6.6215941699i	7.7713214097i
	10.905069704i	9.3962767104i	10.7150169835i

The C values for the E modes for:

$$q=0 \quad \text{and} \quad q=1$$

$$CE_0 = 2.25 \quad CE_1 = 3.5$$

These are the C values for the H modes for $q=1$:

$CH_{0,p}$	$CH_{1,p}$	$CH_{2,p}$
1.7684189682	2.6481066907	2.6853321983
1.3578587765	1.5640411441	1.4806470759
1.1945154663	1.2759131317	1.2434098906

Now, recall the necessary equations:

$$s_\alpha T_a = s_{\alpha,0} T_a + \Delta s_\alpha T_a$$

$$\Delta s_\alpha T_a = -\xi^{-1}(s_{\alpha,0}) CE_q, \quad \Delta s_\alpha T_a = -\xi^{-1}(s_{\alpha,0}) CH_q$$

$$\xi(s_{\alpha,0}) = \epsilon_r^{-\frac{1}{2}} \left[1 + \frac{\sigma_1}{s_{\alpha,0} \epsilon_1} \right]^{\frac{1}{2}}$$

$$T_a = \sqrt{\mu_o \epsilon_2} a$$

$$s_\alpha = s_{\alpha,0} + \Delta s_\alpha$$

Calculating T_a we find that $T_a = 8.43858 \times 10^{-10}$. Notice that the $s_{\alpha,0} T_a$ values are given.

Now, in order to solve for s_α we must solve for all of the $\Delta s_\alpha T_a$ values for the E and H modes.

This means calculating $-\xi(s_{\alpha,0})^{-1}$ for all 27 $s_{\alpha,0} T_a$ values and multiplying by the corresponding CE and CH values.

Next, add these $\Delta s_\alpha T_a$ values to the corresponding $s_{\alpha,0} T_a$ values, and finally divide all of these numbers by T_a .

Doing so gives the following results:

Poles for the **E-modes**:

$q=0$	$q=1$
$n=0$:	$n=0$:
$s_\alpha = -1.20480 \times 10^9 \pm 2.75099 \times 10^9 i \text{ Rad/s}$	$s_\alpha = -1.88786 \times 10^9 \pm 5.37562 \times 10^9 i \text{ Rad/s}$
$s_\alpha = -1.21465 \times 10^9 \pm 6.49784 \times 10^9 i \text{ Rad/s}$	$s_\alpha = -1.89068 \times 10^9 \pm 7.97252 \times 10^9 i \text{ Rad/s}$
$s_\alpha = -1.21604 \times 10^9 \pm 1.02270 \times 10^{10} i \text{ Rad/s}$	$s_\alpha = -1.89188 \times 10^9 \pm 1.12219 \times 10^{10} i \text{ Rad/s}$
$n=1$:	$n=1$:
$s_\alpha = -1.21214 \times 10^9 \pm 4.47805 \times 10^9 i \text{ Rad/s}$	$s_\alpha = -1.88941 \times 10^9 \pm 6.43356 \times 10^9 i \text{ Rad/s}$

$$\begin{aligned} s_{\alpha} &= -1.21554 \times 10^9 \pm 8.27933 \times 10^9 i \text{ Rad/s} & s_{\alpha} &= -1.89138 \times 10^9 \pm 9.48084 \times 10^9 i \text{ Rad/s} \\ s_{\alpha} &= -1.21631 \times 10^9 \pm 1.20321 \times 10^{10} i \text{ Rad/s} & s_{\alpha} &= -1.89217 \times 10^9 \pm 1.28884 \times 10^{10} i \text{ Rad/s} \end{aligned}$$

n = 2:

$$\begin{aligned} s_{\alpha} &= -1.21428 \times 10^9 \pm 6.03900 \times 10^9 i \text{ Rad/s} \\ s_{\alpha} &= -1.21599 \times 10^9 \pm 9.94603 \times 10^9 i \text{ Rad/s} \\ s_{\alpha} &= -1.21647 \times 10^9 \pm 1.37491 \times 10^{10} i \text{ Rad/s} \end{aligned}$$

n = 2:

$$\begin{aligned} s_{\alpha} &= -1.89044 \times 10^9 \pm 7.60319 \times 10^9 i \text{ Rad/s} \\ s_{\alpha} &= -1.89182 \times 10^9 \pm 1.09664 \times 10^{10} i \text{ Rad/s} \\ s_{\alpha} &= -1.89237 \times 10^9 \pm 1.45043 \times 10^{10} i \text{ Rad/s} \end{aligned}$$

Poles for the **H-modes**:

q = 1

n = 0:

$$\begin{aligned} s_{\alpha} &= -9.54650 \times 10^8 \pm 6.46734 \times 10^9 i \text{ Rad/s} \\ s_{\alpha} &= -7.33782 \times 10^8 \pm 9.50941 \times 10^9 i \text{ Rad/s} \\ s_{\alpha} &= -6.45781 \times 10^8 \pm 1.29111 \times 10^{10} i \text{ Rad/s} \end{aligned}$$

n = 1:

$$\begin{aligned} s_{\alpha} &= -1.42786 \times 10^9 \pm 5.07448 \times 10^9 i \text{ Rad/s} \\ s_{\alpha} &= -8.44837 \times 10^8 \pm 7.82149 \times 10^9 i \text{ Rad/s} \\ s_{\alpha} &= -6.89668 \times 10^8 \pm 1.11203 \times 10^{10} i \text{ Rad/s} \end{aligned}$$

n = 2:

$$\begin{aligned} s_{\alpha} &= -1.44901 \times 10^9 \pm 5.83768 \times 10^9 i \text{ Rad/s} \\ s_{\alpha} &= -8.00086 \times 10^8 \pm 9.18884 \times 10^9 i \text{ Rad/s} \\ s_{\alpha} &= -6.72203 \times 10^8 \pm 1.26851 \times 10^{10} i \text{ Rad/s} \end{aligned}$$

Next, lets look at the much easier rectangular mine case where we can see from the pole parameter page (page 13):

II. Anti-Tank Mines

<i>Mine</i>	<i>a</i>	<i>b</i>	<i>d</i>	mode-1	mode-2	<i>CS (1/s)</i>
				$s_{\alpha,0} \text{ (Rad/s)}$	$s_{\alpha,0} \text{ (Rad/s)}$	
PT MI-BA II	.395m	.23m	.135m	$2.9968882 \times 10^9 j$	$3.9753727 \times 10^9 j$	-2.8788417×10^9

Now, recall the necessary equations:

$$\xi(s_{\alpha,0}) = \varepsilon_r^{-\frac{1}{2}} \left[1 + \frac{\sigma_1}{s_{\alpha,0} \varepsilon_1} \right]^{\frac{1}{2}}$$

$$\Delta s_{\alpha} = \frac{CS}{\xi(s_{\alpha,0})}$$

$$s_{\alpha} = s_{\alpha,0} + \Delta s_{\alpha}$$

Calculating for mode-1 we find:

$$\xi(s_{\alpha,0}) = 2.191160 - .0343982j \text{ per Rad, and}$$

$$\Delta s_{\alpha} = -1.3135198 \times 10^9 - 2.0620465 \times 10^7 j \text{ Rad/s.}$$

Therefore, the most dominant pole will be:

$$s_{\alpha} = s_{\alpha,0} + \Delta s_{\alpha} = -1.3135198 \times 10^9 \pm 2.9762677 \times 10^9 j \text{ Rad/s}$$

Calculating for mode-2 we find:

$$\xi(s_{\alpha,0}) = 2.1910437 - .0259329j \text{ per Rad, and}$$

$$\Delta s_{\alpha} = -1.3137293 \times 10^9 - 1.5549149 \times 10^7 j \text{ Rad/s.}$$

Therefore, the next most dominant pole will be:

$$s_{\alpha} = s_{\alpha,0} + \Delta s_{\alpha} = -1.3137293 \times 10^9 \pm 3.9598236 \times 10^9 j \text{ Rad/s}$$

Conclusions

The dielectric mine problem was presented. An approximate approach for finding the natural frequencies of dielectric, cylindrical and rectangular shaped targets in a dielectric medium was presented. A region where this approach is “accurate” was presented.

A library (list) of dielectric, cylindrical and rectangular shaped mines is presented. The library gives the name, country of origin, countries using, and electromagnetic information about 94 different cylindrical and rectangular shaped anti-personnel and anti-tank mines.

A method for using this library is presented and demonstrated. If this library proves effective it is suggested that the user input all of the data into software for real time (and easier) manipulation.

Acknowledgments

I would to recognize Carl E. Baum for his guidance in this project. I would also like to most graciously thank AFOSR and Phillips Laboratory for their sponsorship in this work.

References

- Baum, C.E., Concerning the identification of buried dielectric targets, Phillips Laboratory's Interaction Note 504, July, 1994.
- Collin, R.E., Foundations for Microwave Engineering, McGraw-Hill, Inc., New York, 1966.
- Dearholt, D.W., Electromagnetic Wave Propagation, McGraw-Hill, Inc., New York, 1973.
- Hanson, G., C.E. Baum, Perturbation formula for the internal resonances of a dielectric object embedded in a low-impedance medium, Phillips Laboratory's Interaction Note 520, August 1996.
- Harrington, R.F., Time-Harmonic Electromagnetic Fields, McGraw-Hill, Inc., New York, 1961.
- Kong, J.A., Electromagnetic Wave Theory (second ed.), John Wiley & Sons, Inc., New York, 1990.
- Worthy, M.C., A comparison of exact versus perturbed pole locations of dielectric objects in dielectric medium, Phillips Laboratory's Interaction Note 529, July, 1997.
- Worthy, M.C., A library of the natural frequency responses for cylindrical shaped buried plastic mines, Phillips Laboratory's Interaction Note 530, July, 1997.
- Worthy, M.C., A library of the natural frequency responses for rectangular shaped buried plastic mines, Phillips Laboratory's Interaction Note 531, July, 1997.
- The information about the names of, country made in, countries used by, and dimensions of the mines in the "library" came from "Mine Facts," a CD-ROM developed by the Essex Corporation for the Department of Defense in 1996.

Simulating Transient Temperature Distributions in Optically Pumped Multilayer Laser Structures

**John Yoon
Department of Electrical and Computer Engineering**

**University of Florida
127 Larsen
Gainesville, FL 32611**

**Final Report for:
Graduate Student Research Program**

**Sponsored by:
Air Force Office of Scientific Research
Bolling Air Force Base, DC**

and

**Phillips Laboratory
Kirtland AFB, NM**

October 1997

Simulating Transient Temperature Distributions in Optically Pumped Multilayer Laser Structures

John Yoon

Department of Electrical and Computer Engineering

University of Florida

Abstract

A numerical method for simulating the temperature distribution in an optically pumped multilayer semiconductor laser is presented in a tutorial form. The model uses the Implicit Crank-Nicolson method in a one dimensional case. The temperature distribution is calculated assuming that the power in the optical pump beam is absorbed in the active region of the laser structure. The pulse width is 0.1 ms at a duty cycle of 1%. The result of the computation is in a good agreement with that of a commercial thermal modeling tool.

Simulating Transient Temperature Distributions in Optically Pumped Multilayer Laser Structures

John Yoon

Introduction

Optically pumped mid-IR semiconductor lasers have great potential for use in IR-countermeasure applications. It has been shown recently, [1,2], that the performance of such lasers is very sensitive to the temperature rise caused by absorption of the pump beam in the active region. The goal of this work is to contribute to the development of a comprehensive model capable of simulating these transient temperature distributions. In future work, the model will be used to design improved laser structure with reduced temperature sensitivity.

An analytical method for the transient problem in a multilayer structure can be found in the paper by Zommer et al. [3]. However, the major difficulty in using this scheme is that the analytical solution changes every time the number of the layers in the structure is changed. In order to circumvent this problem, a numerical technique was used.

The boundary conditions used in the numerical method of this study take into account the presence of a pulsed heat source in one of the layers in the structure. It is assumed that the pump beam is absorbed in the active region of the laser and that the absorbed beam results in the heat generation in the structure. It should be noted that the heat source is pulsed, not continuous since the mid-IR semiconductor laser under consideration in this report is operated in pulse mode, not CW.

The simulation uses a one dimensional model, where the temperature distribution in the transverse direction in the structure is computed. A one dimensional model can be used provided that the temperature change in the lateral direction is negligible compared to that in the transverse direction. However, the complete analysis of the temperature distribution in the laser requires a two dimensional model in order to compare the transverse temperature gradient with the lateral temperature gradient. The comparison can determine which temperature change in a system is responsible for the temperature problem in the laser. The one dimensional model presented in this report can be extended to a two dimensional model and is currently under development.

This report consists of the following four sections: (1)brief review of heat conduction theory and numerical methods, (2)description of the temperature problem in the optically pumped mid-IR semiconductor laser, (3) simulation, and (4)conclusions.

Brief Review of Heat Conduction Theory and Numerical Methods

The classical heat conduction theory based on the Fourier heat flux model can be found in a number of references[4,5,6,7]. The general heat conduction equation is

$$\frac{\partial}{\partial x} \left(k \frac{\partial T}{\partial x} \right) + \frac{\partial}{\partial y} \left(k \frac{\partial T}{\partial y} \right) + \frac{\partial}{\partial z} \left(k \frac{\partial T}{\partial z} \right) + q' = \rho C \frac{\partial T}{\partial t} \quad (1)$$

where T is temperature, q is the rate of heat flow per sec per volume, q' is the rate of heat generation per volume inside, k is the thermal conductivity(W/m K), ρ is the density(g/cm³), and C is the specific heat (J/g °C). Heat capacity is defined as ρC in unit of J/(cm³ K).

The analytical solutions of various kinds of heat conduction problems are well presented in other references[8,9]. Most of those works are for regular geometries and well-behaved boundary conditions. However, there are many other practical heat conduction problems involving irregular geometries and complicated boundary conditions, where their analytical solutions would be so complicated to use.

Several numerical analyses were studied: the finite difference method, the Laplace transformation method, and the fast Fourier transformation(FFT) method. To the author's knowledge, there are only very few studies done about the numerical Laplace transformation[10]. In contrary, the FFT algorithm [11,12] is widely utilized for a wide range of engineering problems. However, the FFT method still requires the equation (1) to be analytically solved for a given geometry and boundary conditions in the frequency domain, and its algebra is very laborious. The finite difference method was employed in the model for an unsteady conduction problem in a one dimensional case. In the finite difference method, the equation (1) and boundary conditions are modeled by a set of simultaneous algebraic equations with discrete approximation of derivatives to predict temperatures at certain nodal points in the system for a given time[13,14,15,16].

The simulation in this study uses the implicit Crank -Nicolson method. Although this method is well discussed in other references[4,15,16,17,18], it is briefly discussed below for the completeness.

The approximation of the first and the second derivative using the central difference equation is given by

$$\left. \frac{\partial T}{\partial x} \right|_{i,j} = \frac{T_{i+1,j} - T_{i-1,j}}{2 \Delta x} \quad (2)$$

$$\left. \frac{\partial^2 T}{\partial x^2} \right|_{i,j} \cong \frac{T_{i+1,j} - 2 T_{i,j} + T_{i-1,j}}{(\Delta x)^2} \quad (3)$$

where

$$T_{i,j} \equiv T(x_i, t_j) \text{ and } \Delta x \equiv x_{i+1} - x_i.$$

Equation (1) can be rewritten for a one dimension case(e.g. x) if thermal parameters are constant and the internal heat generation is equal to zero.

$$\alpha \frac{\partial^2 T}{\partial x^2} = \frac{\partial T}{\partial t} \quad (4)$$

where α is the thermal diffusivity(cm^2/s) which is defined as $\alpha = k/\rho C$. Then equation (4) can be expressed in terms of the difference equation by substituting (2) and (3) into (4). It becomes

$$T_{i,j+1} = \gamma T_{i+1,j} + (1-2\gamma) T_{i,j} + \gamma T_{i-1,j} \quad (5)$$

$$\text{where } \gamma \equiv \frac{\alpha \Delta t}{(\Delta x)^2} \text{ and } \gamma < \frac{1}{2}.$$

This can be rewritten with the central difference expressions for both $\frac{\partial^2 T}{\partial x^2}$ and $\frac{\partial T}{\partial t}$, representing the derivation

at the midpoint between j and j+1. Then (4) is given by

$$\alpha \frac{1}{2} \left[\frac{T_{i+1,j+1} - 2 T_{i,j+1} + T_{i-1,j+1}}{(\Delta x)^2} + \frac{T_{i+1,j} - 2 T_{i,j} + T_{i-1,j}}{(\Delta x)^2} \right] = \frac{T_{i,j+1} - T_{i,j}}{\Delta t} \quad (6)$$

Arranging terms,

$$\frac{\gamma}{2} T_{i+1,j} + (1-\gamma) T_{i,j} + \frac{\gamma}{2} T_{i-1,j} = -\frac{\gamma}{2} T_{i+1,j+1} + (1+\gamma) T_{i,j+1} - \frac{\gamma}{2} T_{i-1,j+1} \quad (7)$$

(7) was derived using the Crank-Nicolson method and is shown to be stable for all the values of γ [16,18].

However, according to author's modeling results, γ appears to have to be between 0 and 1 for (7) to be stable. This problem led the author to use the implicit Crank-Nicolson method instead. The second derivative is evaluated along the j+1 line instead of using the known values along the j line. Then (4) becomes

$$\alpha \frac{T_{i+1,j+1} - 2T_{i,j} + T_{i-1,j}}{(\Delta x)^2} = \frac{T_{i,j+1} - T_{i,j}}{\Delta t} \quad (7)$$

After arranging terms,

$$-\gamma T_{i+1,j+1} + (1+2\gamma) T_{i,j+1} - \gamma T_{i-1,j+1} = T_{i,j} \quad (8)$$

Equation (8) is stable for all values of γ , and the truncation errors are first order in time and second order in space .

This difference equation can be expressed in a matrix equation as follows.

$$\tilde{A} \tilde{T}_{j+1} = \tilde{T}_j \quad (9)$$

where

$$\tilde{A} = \begin{pmatrix} 1+2\gamma & -\gamma & 0 & \cdot & \cdot & \cdot & 0 \\ -\gamma & 1+2\gamma & -\gamma & \cdot & \cdot & \cdot & 0 \\ 0 & -\gamma & 1+2\gamma & -\gamma & \cdot & \cdot & \cdot \\ 0 & 0 & -\gamma & 1+2\gamma & -\gamma & \cdot & \cdot \\ \cdot & \cdot & \cdot & \cdot & \cdot & \cdot & \cdot \\ \cdot & \cdot & \cdot & \cdot & \cdot & \cdot & \cdot \\ 0 & \cdot & \cdot & \cdot & \cdot & -\gamma & 1+2\gamma \end{pmatrix} \quad \text{and} \quad \tilde{T}_j = \begin{pmatrix} T_{1,j} \\ T_{2,j} \\ T_{3,j} \\ \cdot \\ \cdot \\ \cdot \\ T_{N,j} \end{pmatrix}$$

Description of Temperature Problem in the Optically Pumped mid-IR Laser

The thermal model in this report is designed to work particularly for lasers. Figure 1 shows the general structure diagram of an optically pumped laser. The mid-IR laser under consideration in this study are optically pumped, and it is assumed that the pump beam is absorbed in the active region of the laser. It should be noted that the active region in the laser under consideration is composed of multi-quantum wells, that is, a multilayer structure. In this study, these multilayers in the active region are represented by one layer that simulates the averaged characteristics of those layers in the active region.

The heat generation is assumed to take place in the center of the active region and to dissipate into the adjacent layers. The heat transfer by conduction from the active region up to the contact layer through the clad layer and the heat transfer by convection and radiation through the top surface of the contact layer are assumed to be negligible. The heat flow is allowed only downward from the active region to the heat sink by conduction. A pulsed heat source in the active region is assumed because the laser under consideration are operated in pulse

mode. Thus the temperature problem in the mid-IR laser is a unsteady-state conduction problem, in which the temperature in the system varies with time.

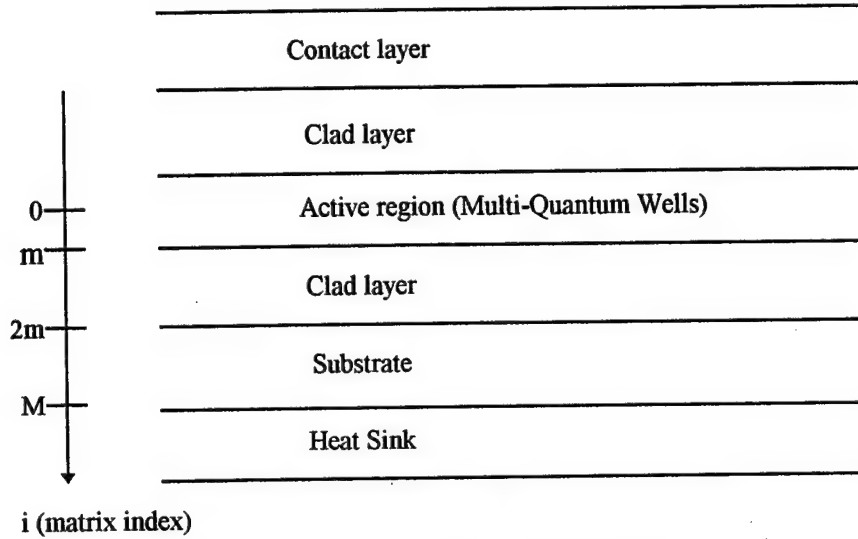


Fig. 1. Structure of an optically pumped laser

From (1) and (4), the governing heat conduction equations in the laser are given by

$$\frac{\partial^2 T}{\partial x^2} - \frac{1}{\alpha} \frac{\partial T}{\partial t} = -\frac{Q}{k}, \quad \text{for the active region} \quad (10)$$

$$\frac{\partial^2 T}{\partial x^2} = \frac{1}{\alpha} \frac{\partial T}{\partial t}, \quad \text{everywhere else} \quad (11)$$

where Q is the heat generation rate per time per volume (W/cm^3). The boundary conditions are as follows:

a) initial condition: $T_i = T_a$, $t = 0$, $i = 0, 1, \dots, M$

b) $\frac{\partial T_i}{\partial x} = 0$, at the center of the active region (i.e. $i = 0$), $t > 0$

c) $T_M = T_b$, $t > 0$, $i = M$

d) temperature continuity: $T_i = T_{i+1}$, at the interface of two different layers (e.g. $i = m$), $t > 0$

e) heat flow continuity:

$$k_1 \frac{\partial {}^1T_i}{\partial x} = k_2 \frac{\partial {}^2T_i}{\partial x}, \quad \text{at the interface of two different layers (e.g. } i = m), t > 0$$

where ${}^lT_{i,j} = T(x_i, t_j)$ for the l th layer, T_a is the initial temperature of the structure for $t < 0$, and T_b is the temperature of the heat sink. In order to solve the differential equations (10) and (11), the boundary conditions a) through e) should be expressed in terms of the difference equations to be substituted in (10) and (11). Then, for a given time t , (10) and (11) become as follows:

$$(1+2\gamma_1) {}^1T_{0,j+1} - 2\gamma_1 {}^1T_{1,j+1} = {}^1T_{0,j} + C_q Q_{0,j}, \quad \text{when } i = 0 \quad (12)$$

$$-\gamma_1 {}^1T_{i-1,j+1} + (1+2\gamma_1) {}^1T_{i,j+1} - \gamma_1 {}^1T_{i+1,j+1} = {}^1T_{i,j} + C_q Q_{i,j}, \quad \text{when } i = 1, \dots, m-1 \quad (13)$$

$$-2\gamma_1 {}^1T_{m-1,j+1} + (1+2\gamma_1 + \chi) {}^1T_{m,j+1} - 2\gamma_1 \kappa {}^2T_{m+1,j+1} = (1 + \kappa \frac{\gamma_1}{\gamma_2}) {}^1T_{m,j} + C_q Q_{m,j}, \quad \text{when } i = m \quad (14)$$

$$-\gamma_2 {}^2T_{i-1,j+1} + (1+2\gamma_2) {}^2T_{i,j+1} - \gamma_2 {}^2T_{i+1,j+1} = {}^2T_{i,j}, \quad \text{when } i = m+1, \dots, M-1 \quad (15)$$

$$T_{M,j} = T_b, \quad \text{when } i = M \quad (16)$$

where

$$\gamma_i \equiv \frac{\alpha_i \Delta t}{(\Delta x)^2}, \quad C_q \equiv \frac{\alpha_1 \Delta t}{k_1}, \quad \kappa \equiv \left(\frac{k_2}{k_1} \right) \left(\frac{\Delta x_1}{\Delta x_2} \right), \quad \chi \equiv \gamma_1 \kappa \left(\frac{1+2\gamma_2}{\gamma_2} \right)$$

It should be noted that the elements of the matrix $Q_{i,j}$ are adjusted as the pulse turns on and off with time.

The thermal model is implemented using Matlab 4.2. The next section will discuss the simulation for a two-layer structure, using (12) through (16) in a matrix equation as (9).

Simulation

The structure used in the model is shown in Fig 2. For the simplicity, a two-layer structure is chosen. The position $x = 0$ in Fig. 2 corresponds to the position $i = 0$ in Fig. 1. Therefore, the top surface of the layer I is assumed to be insulated. That is, no heat transfer is assumed from the top surface to air. The layer I is considered as the active region of the laser structure and the heat source is assumed to be in the layer I.

The heat flow is allowed only from the layer I to the heat sink by conduction. The initial temperature T_a and the heat sink temperature T_b are set to zero.

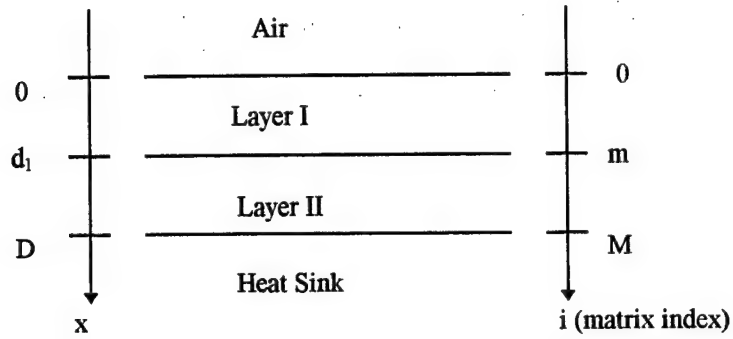


Fig 2. Structure Diagram of Two layers. $D = d_1 + d_2$, $M = 2m$

The materials in this example are chosen same as those used by Zommer et al.[3]. The layer I in Fig. 2 is the Si chip and the layer II is the soft solder (e.g. 95-percent Pb 5-percent Sn). Thermal properties of the materials are listed in Table 1. Table 2 shows the dimension of each layer and the information on the pulsed heat source used in the computation.

TABLE I

Thermal properties of materials at 300K

Material	k (W/°C cm)	C (J/g °C)	ρ (g/cm ³)
Si	1.42	0.691 @273 K	2.33
95%Pb 5%Sn	0.356	0.135	11.0

TABLE II

Dimension of layers

	Layer I	Layer II
thickness (μm)	150	500

Pulse information

Period (ms)	Pulse Width (ms)	Power (W/cm ³)
10	0.1	6.7×10^5

The temperature distribution with time at the bottom of the layer I (i.e. $x = 150 \mu\text{m}$) is shown in Fig.3. The heat generation occurs between 4.95ms and 5.05ms on the scale of the plot. It is observed from the plot that the temperature at the bottom of the layer I rapidly rises from 0 °C to 28 °C while the pulse is on and then the temperature dissipates as the pulse turns off. The result is compared with that from the commercial thermal program, PC3D, and they are in a very good agreement. The programs are given in Appendix I through III.

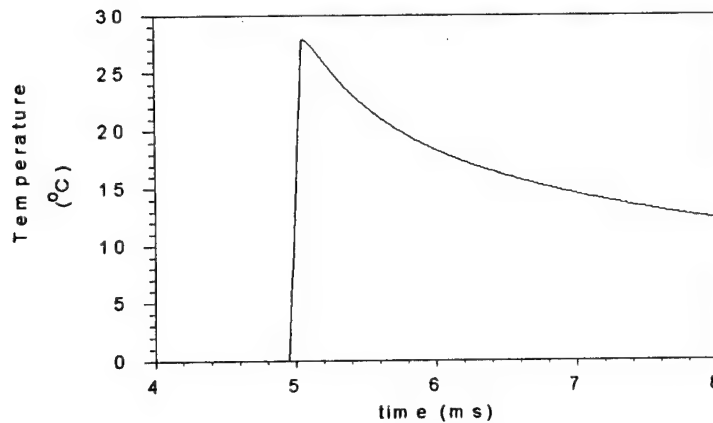


Fig. 3. Temperature distribution at the bottom of layer I, computed for the structure of Fig. 2

Conclusion

The difference equations are derived for the transient temperature problem in a multilayer structure using the Implicit Crank-Nicolson method. A numerical analysis is better from the practical point of a view when compared with the analytical analysis. The advantage of the numerical modeling is that the user can perform the computation for any multilayer system once the model is established. An analytical method requires an analytical

solution to be found every time the number of the layers in a system is changed and the mathematical derivation of finding an analytical solution usually takes even more time and effort.

The boundary conditions of the derived difference equations are set as required for the pulsed optically-pumped laser. A pulsed heat source is assumed to be in one of the layers, that is, the active region. For the simplicity, the heat transfer by convection and radiation is ignored. The heat flow is assumed only from the active region down to the heat sink by conduction.

The thermal model is implemented using MATLAB 4.2. A soft soldered power transistor is chosen in the calculation. The heat source is given as $6.7 \times 10^5 \text{ W/cm}^3$ with the pulse width of 0.1ms at a duty cycle of 1% in the computation. Although the model is designed for the laser and the device chosen in the calculation is irrelevant to the laser, the presence of the pulsed heat source in one of the layers makes the example case similar to the laser model from the point of a view of the boundary conditions for a multilayer structure and a pulsed heat source in the active region. Also, the computation is intended to prove that the developed thermal model works correctly, not to give the analysis of the temperature problem in the laser. The computation by the model is compared with that calculated by the commercial thermal modeling tool, PC3D, and they are in a good agreement. The presented difference equations for the given boundary conditions and the programs given in Appendices should serve as good tutorial materials for the interested readers to create their own thermal modeling tool.

Acknowledgment

This work was supported by a grant from the AFOSR Summer Research Program. The author wishes to thank Captain Michael Gregg for continuous encouragement and support throughout the course of the work and Dr. Chi Yan for suggesting the topic and for many helpful discussions. He also wishes to acknowledge the support and hospitality of many other researchers at PL/LIDA. He thanks Carl Miester at the University of Florida, Gainesville for running the commercial thermal modeling tool, PC3D, for the comparison of the computation.

Appendix I

% KK.m

% Associated with "Im7283.m"

% John Yoon

```
function z = KK(j,k,dx)
```

```
z = k(j+1)*dx(j)/( k(j)*dx(j+1) );
```

Appendix II

```
% Psi.m
```

```
% Must run with "Im7283.m"
```

```
% John Yoon
```

```
function z = Psi(j, r, k, dx)
```

```
z = r(j)*KK(j,k,dx)*((1+2*r(j+1))/r(j+1));
```

Appendix III

```
% Script file to solve the diffusion equation by simple IMPLICIT method.
```

```
% No requirement for the value of r for convergence reliability.
```

```
% Must run with KK.m and Psi.m
```

```
% Model: One dimensional, multi-layer, unsteady heat conduction
```

```
%
```

```
% John Yoon
```

```
% Note: Top layer has a heat source.
```

```
%%%%%%%%%
```

```
clear all;
```

```
Nxx = 25; % step # in space for each region
```

```
Nt = 2000; % 5000; % step # in time
```

```
ss = input('1 for x, 2 for t: ');
```

```
if ss == 1
```

```
prt = Nt/10; % print T vs. x at every prt time
```

```
else
```

```
prt = 1; % print T vs. t at every prt time
```

```
end
```

```
% thermal parameters from gain region (in cm)
```

```
Aph = [1.42/(0.691*2.33) 0.356/(0.135*11)];
```

```
k = [1.42 0.356];
```

```
% Layer thickness downward from heat source, cm
```

```
L = [150e-4 500e-4];
```

```
Xd = L(1); % position(meter) for T vs. t
```

```
% Note: xd is index of matrix x for Xd.
```

```
% Figure out # regions downward from active region
```

```
[rL cL] = size(L); % L must be row vector
```

```
Rgn = cL; % # of Regions downward from active region
```

```
Nx = Rgn * Nxx + 1; % total step #
```

```
% Temperature Boundary Conditions
```

```
T0 = 0; % heat sink, degree C
```

```
% Pulse Information
```

```
P_P = 0.01; % pulse period (sec);
```

```
dc = 0.01; % duty cycle
```

```
P_W = P_P * dc; % pulse width
```

```
Qq = 6.7e5; % W/cm^3
```

```
% increment for computation
```

```
dx = L / Nxx
```

```
dt = P_P/Nt % time step (in seconds)
```

```
n = 1: Nt; % index for time
```

```
tt = (n-1)*dt;
```

```
t = [tt (tt(Nt) + dt)]; % construction of vector t
```

```
% Construct matrix of x
```

```
x = zeros(Nx,1);
```

```
for j = 1:Rgn
```

```
if j == 1
```

```
    L0 = 0;
```

```
else
```

```
    L0 = L0 + L(j-1);
```

```
end
```

```
if j == 1
```

```
    xx = linspace(0, L(j), Nxx+1);
```

```
    for nn = 1:Nxx+1
```

```
        x(nn) = xx(nn);
```

```
    end
```

```
else
```

```
    xx = linspace(L0, L0+L(j), Nxx+1);
```

```
    for nn = 2:Nxx+1
```

```
        x(nn+(j-1)*Nxx) = xx(nn);
```

```
    end
```

```
end
```

```
end % for j = 1:Rgn
```

```
% Figure the size of matrices
```

```
M = length(x);
```

```
MT = length(t);
```

```
% Find index of x for the position of interest
```

```
xd = -1; % initialization
```

```
for rcnt = 1:M-1
```

```
    if( Xd >= x(rcnt) & Xd < x(rcnt+1) )
```

```
        xd = rcnt;
```

```
        break;
```

```
    elseif( Xd > x(rcnt) & Xd <= x(rcnt+1) )
```

```
        xd = rcnt+1;
```

```
        break;
```

```
    end
```

```
end
```

```
if( xd < 0 )
```

```
    disp('Invalid position of x entered. '); break;
```

```
end
```

```
% Construct matrix for Q (Pulse)
```

```
Pi = 0; % index for start of pulse
```

```
Pf = 0; % index for end of pulse
```

```
Q = zeros(M, MT);
```



```

for tcnt = 1:MT
    if( t(tcnt) >= (P_P-P_W)/2 ) & ( t(tcnt) <= (P_P+P_W)/2 )
        Q(:,tcnt) = Qq*ones(M,1);
        if( (Pi+Pf) == 0 )
            Pi = tcnt;
            Pf = tcnt;
        else
            Pf = tcnt;
        end
    else
        Q(:,tcnt) = zeros(M,1);
    end
end % for tcnt = 1:MT
xQT = 1; % requirement for xQT: 1 <= xQT <= M
plot(t, Q(xQT,:)); xlabel('t (sec)'); ylabel('W/vol. ');
title('Pulse Profile: Please press any button to continue..');
pause; tic;

% Some initializations
r = Aph*dt./(dx.*dx);
r
cQ = Aph(1)*dt/k(1)
cq = cQ*Qq

% KK = (k(2)/k(1))*(dx(1)/dx(2));
% Psi = r(1)*KK*((1+2*r(2))/r(2));

% Construct the matrices A and B
A = zeros(M,M); B = eye(M,M);
A(1,1) = 1 + 2*r(1); A(1,2) = -2*r(1); A(M,M) = 1;

j = 1; % index of region
for rcnt = 2:(M-1)
    if( rcnt <= j*Nxx )
        A(rcnt, rcnt-1) = -r(j);
        A(rcnt, rcnt) = 1 + 2*r(j);
        A(rcnt, rcnt+1) = -r(j);

    elseif( rcnt == j*Nxx+1 ) % interface between different regions
        A(rcnt, rcnt-1) = -2*r(j);
        A(rcnt, rcnt) = 1 + 2*r(j) + Psi(j,r,k,dx);
        A(rcnt, rcnt+1) = -2*r(j)*KK(j,k,dx);
        B(rcnt, rcnt) = 1 + KK(j,k,dx)*r(j)/r(j+1);
        j = j + 1;
        if j > Rgn
            j = Rgn; % to prevent index from
                    % exceeding matrix dimension
        end % if j > Rgn
    end % if

end % if

end % for rcnt = 2:(M-1)

A = sparse(A); B = sparse(B);

```

```

% Construct matrix G
G = zeros(M,1);
for rcnt = 1:Nxx+1
    G(rcnt) = cQ; % heat source in active region only
end

% Initialization of T (Temperature Matrix)
T = T0*ones(M,1);

if ss == 1 % plot of T vs. x
    plot(x, T);
else % plot of T vs. t
    pt(1) = 0; pT(1) = T(xd);
end

% Calculation in time for each region
ptcnt = 2;

for tcnt = 1:Nt
    temp_G = zeros(M,1);
    if( tcnt >= Pi & tcnt <= Pf )
        temp_G = G*Q(xQT,tcnt);
    end
    T = A \ ( B*T + temp_G );
    T(M) = T0;
    if (fix(tcnt/prt) == tcnt/prt) % plot every prt counts
        pt(ptcnt) = tcnt;
        if ss == 1
            plot(x,T); hold on
        end
        pT1(ptcnt) = T(xd);
        ptcnt = ptcnt+1;
    end % if fix
end % for tcnt
X_pos = x(xd)

if ss == 1
    disp(['T vs.x printed ' num2str(ptcnt-1) ' times at every ' num2str(t(prt)) ' seconds']);
    xlabel('x');
    title(['Implicit method program result at every ' num2str(t(prt)) ' sec']);
elseif(ss == 2) % ss == 2
    plot(pt*dt, pT1); xlabel('t');
    title(['Temperature distribution at the bottom of the active layer']);
    ss2 = fopen('Tt.txt', 'w');
    pT = [(pt*dt)' pT1']; clear pT1;
    fprintf(ss2, '%5e %5e\n', pT);
    disp(' Output file "Tt.TXT" created. ');
end

hold off
ylabel('Temperature (K)'); grid;
toc;
% end of program

```

References

1. C. Yan, D.L. McDaniel, Jr., C.E. Moeller, M.D. Falcon, and D.M. Gianardi, Jr., "Observing Lateral Temperature and Refractive Index Profiles in an Optically Pumped Mid-Infrared Laser Through Temporally and Spatially Resolved Spectra", submitted to Applied Physics Letters.
2. C. Yan, S.J. Murry, C. Lin, J. Yoon, D.M. Gianardi, C.E. Moeller, D.L. McDaniel, Jr., M. Falcon, and S.S. Pei, "Thermally Induced Waveguide Mode Variations in Optically Pumped Mid-IR Type II Semiconductor Lasers", submitted to Photonics West 1998 Conference
3. N. Zommer, d.L. Feucht, "Analytical Thermal Response of a Multi-Layer Device Under the Semi-Infinite Approximation", *IEEE Transactions on Electron Devices*, Vol. ED-25, No. 4, April 1978, pp.441-448
4. M. N. Özisik, Basic Heat Transfer, McGraw-Hill, 1977
5. F. Kreith, Principles of Heat Transfer, 3rd ed., Intext Educational Publishers, 1973
6. S. Kakac, and Y. Yener, Heat Conduction, 3rd ed., Taylor & Francis, 1993
7. F. M. White, Heat and Mass Transfer, Addison-Wesley, 1988
8. J.R. Cannon, The One-Dimensional Heat Equation, Addison-Wesley, 1984
9. H.S. Carslaw and J.C. Jaeger, Conduction of Heat in Solids, 2nd ed., Oxford Press, London, 1959
10. H. Inoue, M. Kamibayashi, K. Kishimoto, T. Shibuya, and T. Koizumi, "Numerical Laplace Transformation and Inversion using Fast Fourier Transform", *JSME International Journal*, Series I, Vol.35, No.3, 1992, pp.319-324
11. W.H. Press, S.A. Teukolsky, W.T. Vetterling, and B.P. Flannery, Numerical Recipes in C, Cambridge, 1992
12. S.A. Hovanessian and L.A. Pipes, Digital Computer Methods in Engineering, McGraw-Hill, 1969
13. V. Vemuri and W.J. Karplus, Digital Computer Treatment of Partial Differential Equations, Prentice-Hall, 1981
14. J.H. Ferziger, Numerical Methods for Engineering Application, John Wiley & Sons, 1981
15. Y. Jaluria and K.E. Torrance, Computational Heat Transfer, Hemisphere Publishing Corp., 1986
16. M. N. Özisik, Finite Difference Methods in Heat Transfer, CRC Press, 1994
17. A. Biran and M. Breiner, Matlab for Engineers, Addison-Wesley, 1995
18. G.J. Borse, Numerical Methods with Matlab, PWS Publishing Company, 1997